



1-1-2013

Modeling the Anisotropic Resolution and Noise Properties of Digital Breast Tomosynthesis

Raymond Joseph Acciavatti

University of Pennsylvania, racci@seas.upenn.edu

Follow this and additional works at: <http://repository.upenn.edu/edissertations>

 Part of the [Radiology Commons](#)

Recommended Citation

Acciavatti, Raymond Joseph, "Modeling the Anisotropic Resolution and Noise Properties of Digital Breast Tomosynthesis" (2013).
Publicly Accessible Penn Dissertations. 605.
<http://repository.upenn.edu/edissertations/605>

This paper is posted at ScholarlyCommons. <http://repository.upenn.edu/edissertations/605>
For more information, please contact libraryrepository@pobox.upenn.edu.

Modeling the Anisotropic Resolution and Noise Properties of Digital Breast Tomosynthesis

Abstract

Digital breast tomosynthesis (DBT) is a 3D imaging modality in which a reconstruction of the breast is generated from various x-ray projections. Due to the newness of this technology, the development of an analytical model of image quality has been on-going. In this thesis, a more complete model is developed by addressing the limitations found in the previous linear systems (LS) model [Zhao, Med. Phys. 2008, 35(12): 5219-32].

A central assumption of the LS model is that the angle of x-ray incidence is approximately normal to the detector in each projection. To model the effect of oblique x-ray incidence, this thesis generalizes Swank's calculations of the transfer functions of x-ray fluorescent screens to arbitrary incident angles. In the LS model, it is also assumed that the pixelation in the reconstruction grid is the same as the detector; hence, the highest frequency that can be resolved is the detector alias frequency. This thesis considers reconstruction grids with smaller pixelation to investigate super-resolution, or visibility of higher frequencies. A sine plate is introduced as a conceptual test object to analyze super-resolution. By orienting the long axis of the sine plate at various angles, the feasibility of oblique reconstruction planes is also investigated. This formulation differs from the LS model in which reconstruction planes are parallel to the breast support.

It is shown that the transfer functions for arbitrary angles of x-ray incidence can be modeled in closed form. The high frequency modulation transfer function (MTF) and detective quantum efficiency (DQE) are degraded due to oblique x-ray incidence. In addition, using the sine plate, it is demonstrated that a reconstruction can resolve frequencies exceeding the detector alias frequency. Experimental images of bar patterns verified the existence of super-resolution. Anecdotal clinical examples showed that super-resolution improves the visibility of microcalcifications. The feasibility of oblique reconstructions was established theoretically with the sine plate and was validated experimentally with bar patterns.

This thesis develops a more complete model of image quality in DBT by addressing the limitations of the LS model. In future studies, this model can be used as a tool for optimizing DBT.

Degree Type

Dissertation

Degree Name

Doctor of Philosophy (PhD)

Graduate Group

Bioengineering

First Advisor

Andrew D. Maidment

Keywords

Digital Breast Tomosynthesis (DBT), Image Quality, Image Reconstruction, Oblique Reconstruction, Optimization, Super-Resolution

Subject Categories

Radiology

MODELING THE ANISOTROPIC RESOLUTION AND NOISE
PROPERTIES OF DIGITAL BREAST TOMOSYNTHESIS

Raymond Joseph Acciavatti

A DISSERTATION

in

Bioengineering

Presented to the Faculties of the University of Pennsylvania

in

Partial Fulfillment of the Requirements for the

Degree of Doctor of Philosophy

2013

Supervisor of Dissertation

Andrew D. A. Maidment, Ph.D., FAAPM
Associate Professor of Radiology

Graduate Group Chairperson

Daniel A. Hammer, Ph.D.
Professor of Bioengineering

Dissertation Committee

Daniel K. Bogen, M.D., Ph.D., Professor of Bioengineering
Mitchell D. Schnall, M.D., Ph.D., Eugene P. Pendergrass Professor of Radiology
Jeremy F. Magland, Ph.D., Research Assistant Professor of Radiology

MODELING THE ANISOTROPIC RESOLUTION AND NOISE
PROPERTIES OF DIGITAL BREAST TOMOSYNTHESIS

COPYRIGHT

2013

Raymond Joseph Acciavatti

Dedicated to
Mom, Dad, and my Grandparents

Acknowledgements

I would like to express my gratitude to the following individuals who helped to shape my research:

- First and foremost, my parents and grandparents, who have always been there to guide me in the right direction.
- My advisor, Andrew Maidment, who has been a tremendous source of motivation and encouragement throughout my research in his lab.
- The members of my thesis committee (Daniel Bogen, Mitchell Schnall, and Jeremy Magland) for providing valuable feedback during my progress meetings.
- James Gee, Peter Davies, and Ann Tiao – the leadership faculty of my graduate program (the HHMI-NIBIB Integrated Graduate Training Program in Biomedical Imaging and Informational Sciences).
- Ann-Katherine Carton, who helped me to get started in the field of Medical Physics in Andrew Maidment's lab during the 2006 Summer Undergraduate Fellowship Program of the American Association of Physicists in Medicine (AAPM).
- Predrag Bakic for getting me involved in various projects pertaining to anthropomorphic computer phantom simulation for mammography and tomosynthesis.

- Johnny Kuo, Susan Ng, and Peter Ringer of Real Time Tomography for guidance with the reconstruction software that I used for experimental validation of various concepts.
- Baorui Ren, Chris Ruth, and various collaborators at Hologic for providing useful background information on the acquisition geometry for tomosynthesis.
- Despina Kontos and various members of her lab for offering feedback on my work and for always being open to collaborative research projects.
- David Pokrajac for helpful discussions on MATLAB coding.
- Joseph Chui for sharing his expertise in computer science.
- Roshan Karunamuni for offering input on my x-ray experiments.
- Mike O'Shea and Scott Cupp, medical physicists at the Hospital of the University of Pennsylvania, for various background discussions in medical physics and for sharing their expertise in experimental techniques.
- Denny Lee for sharing his insights on the design of detectors for various medical imaging systems.
- Jim Delikatny for getting me involved in teaching the medical imaging laboratory course for graduate students.
- Aldo Badano, Kish Chakrabarti, and other researchers at the United States Food and Drug Administration (FDA) for useful discussions on detector theory and medical physics.

- X-ray technicians and radiologists who helped to train me in the use of clinical tomosynthesis systems at the Hospital of the University of Pennsylvania.
- Members of Andrew Maidment's lab with whom I worked throughout my time at Penn.
- And finally, others with whom I came in contact at Penn, conferences, and lectures, but are too numerous to mention.

In addition, I would like to acknowledge the support provided by the following grant sources:

- The Howard Hughes Medical Institute (HHMI).
- The National Institute of Biomedical Imaging and Bioengineering (NIBIB).
- The Department of Defense (DOD) Breast Cancer Research Program.

The content of this thesis is solely the responsibility of the author and does not necessarily reflect the official views of the funding agencies.

ABSTRACT

MODELING THE ANISOTROPIC RESOLUTION AND NOISE PROPERTIES OF DIGITAL BREAST TOMOSYNTHESIS

Raymond Joseph Acciavatti

Dr. Andrew D. A. Maidment

Digital breast tomosynthesis (DBT) is a 3D imaging modality in which a reconstruction of the breast is generated from various x-ray projections. Due to the newness of this technology, the development of an analytical model of image quality has been on-going. In this thesis, a more complete model is developed by addressing the limitations found in the previous linear systems (LS) model [Zhao, Med. Phys. 2008, **35**(12): 5219-32].

A central assumption of the LS model is that the angle of x-ray incidence is approximately normal to the detector in each projection. To model the effect of oblique x-ray incidence, this thesis generalizes Swank's calculations of the transfer functions of x-ray fluorescent screens to arbitrary incident angles. In the LS model, it is also assumed that the pixelation in the reconstruction grid is the same as the detector; hence, the highest frequency that can be resolved is the detector alias frequency. This thesis considers reconstruction grids with smaller pixelation to investigate super-resolution, or visibility of higher frequencies. A sine plate is introduced as a conceptual test object to analyze super-resolution. By orienting the long axis of the sine plate at various angles, the feasibility of oblique reconstruction planes is also investigated. This formulation differs from the LS model in which reconstruction planes are parallel to the breast support.

It is shown that the transfer functions for arbitrary angles of x-ray incidence can be modeled in closed form. The high frequency modulation transfer function (MTF) and detective quantum efficiency (DQE) are degraded due to oblique x-ray incidence. In addition, using the sine plate, it is demonstrated that a reconstruction can resolve frequencies exceeding the detector alias frequency. Experimental images of bar patterns verified the existence of super-resolution. Anecdotal clinical examples showed that super-resolution improves the visibility of microcalcifications. The feasibility of oblique reconstructions was established theoretically with the sine plate and was validated experimentally with bar patterns.

This thesis develops a more complete model of image quality in DBT by addressing the limitations of the LS model. In future studies, this model can be used as a tool for optimizing DBT.

Table of Contents

CHAPTER 1. Thesis Introduction.....	1
1. SCOPE OF THIS THESIS.....	2
2. REVIEW OF ZHAO’S LINEAR SYSTEMS MODEL FOR TOMOSYNTHESIS.....	5
3. TRANSFER FUNCTIONS FOR TOMOSYNTHESIS.....	8
4. LIMITATIONS OF ZHAO’S MODEL THAT ARE EXPLORED IN THIS THESIS.....	12
5. DYNAMIC RECONSTRUCTION AND RENDERING.....	15
6. THESIS ROADMAP.....	16
7. REFERENCES.....	19
 CHAPTER 2. Optimization of Phosphor-Based Detector Design for Oblique X-Ray Incidence in Digital Breast Tomosynthesis.....	 21
1. INTRODUCTION.....	22
2. METHODS.....	24
2.1. Transfer Functions for Front-Screen Configuration.....	24
2.2. Transfer Functions for Back-Screen Configuration.....	30
3. RESULTS FOR A MODEL DETECTOR.....	30
3.1. Transfer Functions for Front- and Back-Screen Configurations.....	30
3.2. Anisotropy of the Transfer Functions over the Detector Area.....	38
3.3. Optimization of Phosphor Thickness for Oblique Incidence.....	40
4. COMPARISON WITH RESULTS IN THE LITERATURE.....	46
5. DISCUSSION.....	49
6. CONCLUSION.....	53
7. REFERENCES.....	54
 GLOSSARY OF TERMS: Chapter 2.....	 58
 LIST OF SYMBOLS.....	 59

CHAPTER 3. Observation of Super-Resolution in Digital Breast Tomosynthesis.....	62
1. INTRODUCTION.....	63
2. METHODS.....	65
2.1. Input Object and Acquisition Geometry.....	65
2.2. Detector Signal.....	70
2.3. Filtered Backprojection (FBP) Reconstruction from the Projections.....	75
2.4. Formulation of the Reconstruction Filter.....	78
2.5. Fourier Transform of the DBT Images.....	80
3. THEORETICAL RESULTS.....	83
3.1. Input Frequency Directed Parallel to the Chest Wall Side of the Breast Support.....	83
3.1.1. <i>Individual Projections</i>	85
3.1.2. <i>SBP Reconstruction</i>	88
3.1.3. <i>FBP Reconstruction</i>	88
3.2. Input Frequency Directed Perpendicular to the Chest Wall.....	91
3.3. Dependency of Super-Resolution on Reconstruction Depth.....	96
4. EXPERIMENTAL RESULTS.....	99
5. DISCUSSION.....	105
6. CONCLUSION.....	110
7. APPENDIX: DETECTOR SIGNAL FOR AN INPUT FREQUENCY DIRECTED PERPENDICULAR TO THE CHEST WALL.....	111
8. REFERENCES.....	113

CHAPTER 4. Oblique Reconstructions in Tomosynthesis: I. Proof-of-Principle Justification.....	117
1. INTRODUCTION.....	118
2. METHODS.....	124
2.1. Reconstruction Formula for Incomplete Angular Data.....	124
2.2. Reconstruction of a Pitched Sine Plate.....	130
2.2.1. <i>Case 1</i>	134
2.2.2. <i>Case 2</i>	138
2.3. Reconstruction of a Pitched Rod.....	139
3. RESULTS.....	143
3.1. Sine Plate.....	143
3.1.1. <i>Visualization of the Reconstruction</i>	143
3.1.2. <i>Modulation Transfer Function (MTF)</i>	147
3.2. Rod.....	152
4. COMPARISON WITH RESULTS IN THE LITERATURE.....	156
5. DISCUSSION.....	158
6. CONCLUSION.....	161

7. APPENDIX A: RADON TRANSFORM OF PITCHED SINE PLATE.....	162
8. APPENDIX B: RADON TRANSFORM OF PITCHED ROD.....	164
9. APPENDIX C: OPTICAL TRANSFER FUNCTION IDENTITY.....	167
10. REFERENCES.....	169

CHAPTER 5. Oblique Reconstructions in Tomosynthesis: II. Super-Resolution.....	171
---	------------

1. INTRODUCTION.....	172
2. METHODS.....	173
2.1. Pitched Sine Plate.....	173
2.2. Digital Detector Signal.....	175
2.3. Fourier Transform of the Pitched Reconstruction Slice.....	181
3. THEORETICAL RESULTS.....	185
3.1. Projection Images.....	185
3.2. SBP and FBP Reconstruction.....	190
3.3. Effect of Object Thickness on the Modulation Transfer Function (MTF).....	192
3.4. Limiting Resolution of an Oblique Reconstruction.....	194
3.4.1. <i>Loss of Resolution with Increasing Object Thickness</i>	194
3.4.2. <i>Aliasing at Large Object Thicknesses</i>	195
3.5. Depth Dependence of Super-Resolution.....	197
4. EXPERIMENTAL RESULTS.....	200
5. CLINICAL RESULTS.....	204
6. DISCUSSION.....	207
7. CONCLUSION.....	211
8. REFERENCES.....	213

GLOSSARY OF TERMS: Chapters 3, 4, and 5.....	215
---	------------

LIST OF SYMBOLS.....	216
-----------------------------	------------

CHAPTER 6. Thesis Summary and Future Work.....	224
---	------------

1. THESIS SUMMARY.....	225
1.1. Chapter 2.....	225
1.2. Chapter 3.....	226
1.3. Chapter 4.....	227
1.4. Chapter 5.....	228
2. AREAS FOR FUTURE RESEARCH.....	229
2.1. Points of Future Investigation with Super-Resolution.....	230
2.1.1. <i>Quantifying the Clinical Benefits of Super-Resolution</i>	230

2.1.2. <i>Development of an Acquisition Geometry that Optimizes Super-Resolution</i>	230
2.1.3. <i>Geometric Accuracy Requirements for Super-Resolution</i>	234
2.1.4. <i>Effect of Reducing the Detector Element Size</i>	234
2.2. Development of Optimal Design Strategies for Continuous X-Ray Tube Motion.....	237
2.2.1. <i>Optimization of Scan Time</i>	237
2.2.2. <i>Optimization of the X-Ray Tube Velocity</i>	238
3. THESIS CONCLUSION.....	239
4. REFERENCES.....	241

List of Tables

5.1. Summary of the modeling assumptions in chapters 4 and 5.....	208
---	-----

List of Illustrations

CHAPTER 1. Thesis Introduction.....	1
1.1. Diagram of tomosynthesis acquisition geometry.....	3
1.2. Linear systems theory for tomosynthesis.....	6
1.3. Illustration of the Central Slice Theorem.....	9
1.4. Comparison of resolution in the reconstruction and in the detector.....	10
1.5. Thesis roadmap.....	18
 CHAPTER 2. Optimization of Phosphor-Based Detector Design for Oblique X-Ray Incidence in Digital Breast Tomosynthesis.....	 21
2.1. Illustration of oblique x-ray incidence in a phosphor.....	25
2.2. Modulation transfer function (MTF) at various incident angles.....	33
2.3. Normalized noise power spectra (NNPS) at various incident angles.....	34
2.4. Detective quantum efficiency (DQE) at various incident angles.....	36
2.5. Variation in Swank factor and DQE(0) with incident angle.....	37
2.6. Variation in the incident angle over the detector area.....	39
2.7. Variation in DQE over the detector area at a fixed frequency.....	40
2.8. Effect of phosphor thickness on DQE(0).....	41
2.9. Effect of phosphor thickness on the high-frequency DQE.....	43
2.10. Optimization of phosphor thickness at various frequencies.....	44
2.11. Generalization of the optimal phosphor thickness to various incident angles and frequencies.....	45
 CHAPTER 3. Observation of Super-Resolution in Digital Breast Tomosynthesis.....	 62
3.1. Diagram of a sine plate for tomosynthesis reconstruction.....	67
3.2. Diagram of backprojection angles for tomosynthesis reconstruction.....	69
3.3. Reconstruction filters from linear systems theory.....	84
3.4. Simulated projections of a high-frequency sine plate.....	86
3.5. Simulated reconstruction of a high-frequency sine plate.....	90
3.6. Translational shift in the image of an object between projections along the posteroanterior (PA) direction.....	92
3.7. Simulated reconstruction of a high-frequency sine plate oriented along the posteroanterior (PA) direction.....	93
3.8. Depth-dependency of super-resolution in the reconstruction.....	97

3.9. Experimental projection image of a bar pattern phantom.....	100
3.10. Experimental reconstruction of a bar pattern phantom showing super-resolution.....	102
3.11. Experimental reconstruction of a bar pattern phantom oriented along the posteroanterior (PA) direction.....	103
3.12. A clinical image of microcalcifications with super-resolution.....	104
 CHAPTER 4. Oblique Reconstructions in Tomosynthesis: I. Proof-of-Principle Justification	 117
4.1. Thought experiments in the reconstruction of a thick object along oblique planes.....	119
4.2. Illustration of the effect of thickness on the Fourier transform of a pitched sine plate.....	121
4.3. Experimental reconstructions of a bar pattern phantom along oblique planes.....	123
4.4. Illustration of two test objects and their Radon transforms.....	126
4.5. Illustration of the sampling of Fourier space for a pitched sine plate.....	134
4.6. Reconstruction of a pitched sine plate in the plane of x-ray tube motion...	144
4.7. Tomographic slices for a pitched sine plate.....	146
4.8. Modulation transfer function (MTF) for oblique reconstructions.....	151
4.9. Reconstruction of a pitched rod in the plane of x-ray tube motion.....	152
4.10. Tomographic slices for a pitched rod.....	154
4.11. Measurement accuracy in oblique reconstructions.....	156
 CHAPTER 5. Oblique Reconstructions in Tomosynthesis: II. Super-Resolution	 171
5.1. Diagram of a pitched sine plate for tomosynthesis reconstruction.....	174
5.2. Simulated projections of a pitched sine plate.....	187
5.3. Illustration of the projection of a pitched sine plate onto the detector.....	189
5.4. Simulated reconstruction of a pitched sine plate.....	191
5.5. Dependency of the modulation transfer function (MTF) on frequency and object thickness.....	193
5.6. Effect of object thickness on the limit of resolution.....	196
5.7. Aliasing in the reconstruction of a thick sine plate.....	197
5.8. Depth dependency of super-resolution in oblique reconstructions.....	199
5.9. Experimental image of a bar pattern phantom in a plane parallel to the breast support.....	201
5.10. Experimental reconstructions of a bar pattern phantom along various pitches.....	202
5.11. Effect of pitch on the limit of resolution.....	203

5.12. An anecdotal clinical image of microcalcifications using oblique reconstructions.....	205
5.13. Illustration of microcalcifications oriented along various pitches.....	206
5.14. Visualization of a complex cancer using oblique reconstructions.....	207
CHAPTER 6. Thesis Summary and Future Work.....	224
6.1. Optimization of super-resolution along the posteroanterior (PA) direction using a newly proposed acquisition geometry.....	231
6.2. Modulation transfer function (MTF) for various phosphor blurring parameters.....	236

CHAPTER 1

Thesis Introduction

1. SCOPE OF THIS THESIS

In the United States, breast cancer is one of the leading causes of cancer death in women (second to lung cancer). It is estimated that a woman's risk of being diagnosed with breast cancer is one in eight.¹ As more individuals live longer due to refinements in medical therapies, it is projected that breast cancer incidence will increase by as much as one-third over the next 20 years.²

The gold standard for breast cancer screening in women is digital mammography (DM). In DM, an x-ray source projects x rays onto a compressed breast to create a 2D image. Compression lowers the path length of x rays to reduce the radiation dose, and immobilizes the breast to reduce motion artifacts. Although the breast can be imaged with multiple views, the two views that are used for screening are cranial-caudal (CC) and mediolateral oblique (MLO).

The American Cancer Society recommends all women aged 40 and older to have an annual mammography exam.¹ Over the past twenty years, mammography has helped to reduce breast cancer mortality by detecting cancer in its early stages.³ However, one shortcoming of mammography is that superposition of dense tissue over a tumor may obscure the cancer. It is reported that 17% of breast cancers are not successfully visualized by DM and that 70-90% of DM radiographs which are initially believed to be suggestive of malignancy are falsely positive.⁴

Digital breast tomosynthesis (DBT) is being investigated as a 3D alternative to DM in which tomographic sections of the breast are generated from x-ray projections taken over a limited range of angles (Figure 1.1). The tomographic nature of DBT filters

out adjacent anatomical structures, thereby reducing the possibility for overlap of dense tissue over a cancer. Preliminary studies have shown that DBT has improved sensitivity and specificity for the early detection of breast cancer relative to DM.^{5,6}

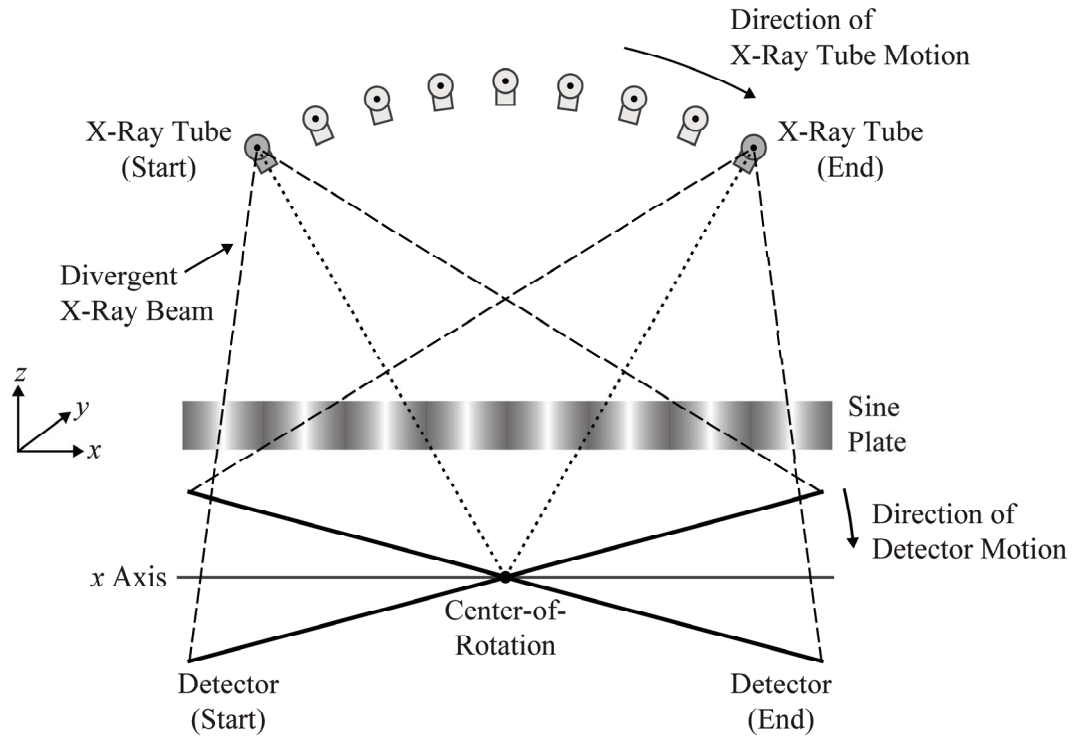


Figure 1.1: Diagram of tomosynthesis acquisition geometry. A schematic diagram of the Selenia Dimensions acquisition geometry (Hologic Inc., Bedford, MA) is shown. The sine plate is a conceptual test object used for analyzing image quality throughout this thesis. Increasing the frequency of the sine plate simulates small closely-spaced structures such as microcalcifications, which are early indicators of breast cancer.

The Perelman School of Medicine at the University of Pennsylvania is one of a small number of major medical centers in the world to convert its screening practices to DBT. Since September of 2011, Penn has used DBT to screen all patients. The Perelman Center for Advanced Medicine at Penn has four Selenia Dimensions DBT units (Hologic Inc., Bedford, MA) for this purpose. Although DBT systems produced by other

manufacturers are being used in clinical trials, the Hologic system is currently the only DBT unit with FDA-approval (as of April 2013).

Penn has found that DBT offers many benefits relative to DM. One notable improvement is reducing the call-back rate (CBR) without reducing the positive predictive value of biopsies. Conant *et al.* reported that the average CBR at Penn decreased from 10.33% (2010-2011) to 8.7% (2011-2012).⁷ A reduction in CBR was observed for all readers and was not dependent upon their experience. The change in CBR was statistically significant when controlled for variable-reader volumes ($p = 0.004$). In addition, Penn observed that the cancer detection rate increased from 4.25 per 1000 women screened to 5.58 per 1000; this change was not statistically significant ($p = 0.161$). Many researchers believe that the benefits of DBT may ultimately fuel its widespread dissemination as an upgrade or adjunct to DM in screening centers throughout the United States.

Although the potential benefits of tomosynthesis over conventional mammography have been identified, the technology is still in its early stages of development and a platform for optimizing DBT has not yet been identified. A prerequisite for optimizing DBT is the development of a rigorous model of image quality. Although Zhao has developed a preliminary model using linear systems theory, simplifying assumptions are made in that work in order to keep the mathematics tractable.⁸ One limitation of Zhao's work is the presumption that image quality is isotropic throughout the reconstructed volume. An additional assumption is that the angle of incidence is approximately normal to the detector in all projections. In this

thesis, I develop a more complete model of image quality by carefully examining the limitations of Zhao's work. Since the model is developed in closed form, it can ultimately be used as a tool for optimizing the design of DBT systems. The final chapter of this thesis gives early thoughts for optimizing DBT.

2. REVIEW OF ZHAO'S LINEAR SYSTEMS MODEL FOR TOMOSYNTHESIS

Two metrics of image quality that are introduced in Zhao's work are the 3D optical transfer function (OTF) and 3D noise power spectra (NPS). The cascaded approach for calculating these transfer functions is summarized in Figure 1.2 and is reviewed in this section. The OTF and NPS of the detector provide the input to the first stage of the cascade. Zhao's earlier work proposed a model for these transfer functions in amorphous selenium (*a*-Se).⁹⁻¹¹ In this detector, an absorbed x ray ionizes a Se atom and creates an electron-hole pair. As a result of an electric field applied along the thickness of the photoconductor, the electron and hole migrate to two different ends of the detector and an image is formed.¹² Using the transfer functions of the detector, the first stage of the cascade in Figure 1.2 models focal spot blurring (FSB) due to continuous x-ray tube motion during the image acquisition.¹³ Although FSB has no effect on NPS,⁹ it has an important impact on OTF. Continuous tube motion introduces a multiplicative factor to the input OTF (T_p) of each projection which is given by $\text{sinc}(a_1 f_r)$, where a_1 is the distance traveled by the focal spot during a projection and f_r is frequency measured perpendicular to the ray of each projection.⁸ In Figure 1.2, the output OTF and NPS of this stage of the cascade are denoted T_f and W_f , respectively.

At the second stage of Figure 1.2, the logarithm of the projections is calculated to determine the line integral of x-ray attenuation. The OTF and NPS are found from

$$T_l = \frac{T_f}{\Gamma} \quad (1.1)$$

$$W_l = \frac{W_f}{\Gamma^2}, \quad (1.2)$$

where Γ is a constant converting x-ray intensity to digital values.⁸

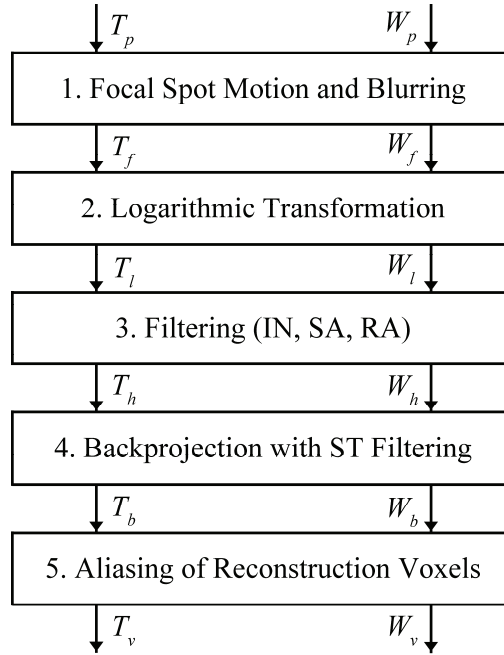


Figure 1.2: Linear systems theory for tomosynthesis. In Zhao's model of image quality for tomosynthesis, the 3D optical transfer function (OTF) and 3D noise power spectra (NPS) are calculated using a cascaded multi-step approach. This figure is adapted from Zhao's paper.⁸

In the third stage of the cascade, the two transfer functions are filtered. Filters which lower the high frequency detector response include an interpolation (IN) filter and a spectrum apodization (SA) filter. The IN filter is given by $\text{sinc}^2(a_x f_r) \times \text{sinc}^2(a_y f_y)$,

where a_x and a_y denote the detector element sizes in the x and y directions. By contrast, the SA filter is a Hanning window function applied along the r direction. To reduce the low frequency detector response, an additional filter must be applied along the r direction. In computed tomography (CT), the conventional low frequency filter is a ramp (RA) filter which increases linearly with frequency from zero.¹⁴

In the fourth stage of the cascade, the OTF and NPS are backprojected along the ray of incidence. The OTF and NPS are thus

$$T_b(f_x, f_y, f_z) = T_h(f_x, f_y, f_z) \cdot \sum_n \delta[f_x \sin \theta_n - f_z \cos \theta_n] \cdot H_{ST}(f_z) \quad (1.3)$$

$$W_b(f_x, f_y, f_z) = W_h(f_x, f_y, f_z) \cdot \sum_n \delta[f_x \sin \theta_n - f_z \cos \theta_n] \cdot H_{ST}^2(f_z), \quad (1.4)$$

where (f_x, f_y, f_z) is a point in frequency space and where H_{ST} is a slice thickness (ST) filter applied along the source-to-detector direction (z). In Zhao's model, H_{ST} is a Hanning window function.¹⁵ In addition, the index n denotes the projection number, which ranges between $n = -(N-1)/2$ and $n = (N-1)/2$ for a system with an odd number of N total projections.

To take into account the size of voxels in the reconstruction, the OTF and NPS are aliased in stage 5 of Figure 1.2

$$T_v(f_x, f_y, f_z) = \sum_{j_z} T_b(f_x, f_y, f_z) \delta\left(f_z - \frac{j_z}{d_z}\right) \quad (1.5)$$

$$W_v(f_x, f_y, f_z) = \sum_{j_x, j_y, j_z} W_b(f_x, f_y, f_z) \delta\left(f_x - \frac{j_x}{d_x}, f_y - \frac{j_y}{d_y}, f_z - \frac{j_z}{d_z}\right), \quad (1.6)$$

where d_x , d_y , and d_z are the dimensions of each voxel and where j_x , j_y , and j_z are integers.⁸ In this formulation, the aliased OTF is found by summing the output of stage 4 over frequencies given by integer multiples of d_z^{-1} . By contrast, the aliased NPS is calculated by analogous summations over all three directions.

3. TRANSFER FUNCTIONS FOR TOMOSYNTHESIS

One assumption made in Zhao's work is that the x rays in each projection form a parallel beam. In such a geometry, the sampling of Fourier space is determined from the Central Slice Theorem. As illustrated in Figure 1.3, Fourier space is sampled along the direction perpendicular to the x-ray beam of each projection. Defining the xz plane as the plane of the chest wall (*i.e.*, the plane of x-ray tube motion in Figure 1.1), one can show that the sampling of Fourier space is identical in cross sections for which f_y is constant. In these cross sections (the f_x - f_z planes of Fourier space), the sampled area resembles a double cone whose opening angle matches the angular range of the scan (Figure 1.3). Zhao demonstrated that cross sections of the 3D OTF [Eq. (1.5)] are non-zero in analogous regions of Fourier space.⁸

By convention, slices in a tomosynthesis reconstruction are created using planes parallel to the breast support (*i.e.*, the xy plane). To calculate the in-plane OTF for such a slice, the 3D OTF given by Eq. (1.5) is integrated along the z direction. The z direction is chosen since it is perpendicular to the slice. This line integral yields a 2D OTF measuring modulation within the plane of reconstruction. As Zhao demonstrated in a

separate paper, the in-plane OTF can be measured experimentally using the edge technique.¹⁶

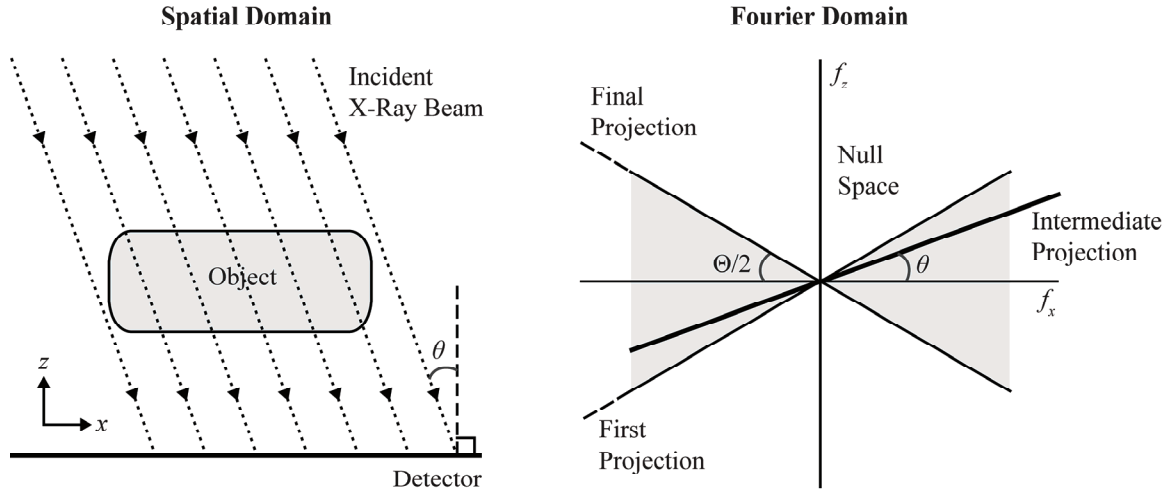


Figure 1.3: Illustration of the Central Slice Theorem. According to the Central Slice Theorem, a parallel projection samples Fourier space perpendicular to the direction of the incident x-ray beam. Since the x-ray tube motion occurs within the xz plane, the sampling of Fourier space is identical in cross sections for which f_y is constant. In these cross sections (the $f_x f_z$ planes of Fourier space), the sampled area resembles a double cone. This sampled area is termed the “*Fourier double cone*” (FDC) throughout this thesis. The opening angle (Θ) of the FDC matches the angular range of the DBT scan.

Figure 1.4(a) illustrates the effect of filtering on the in-plane OTF for frequency measurements along the x direction (*i.e.*, $f_y = 0$). This direction corresponds to the tube travel direction as shown in Figure 1.1. It is useful to interpret the in-plane OTF conceptually as a measurement of the relative amplitude of a sinusoidal test object in the plane of reconstruction. At each frequency, the in-plane OTF compares the amplitude of the reconstruction against the amplitude of the attenuation coefficient of the sinusoidal object. Figure 1.4(a) has been generated using the reconstruction of a sine plate that is explicitly calculated in Chapter 3 of this thesis; although the figure is not taken directly

from Zhao's paper, the trends shown are qualitatively concordant with Figure 14 of that paper.⁸

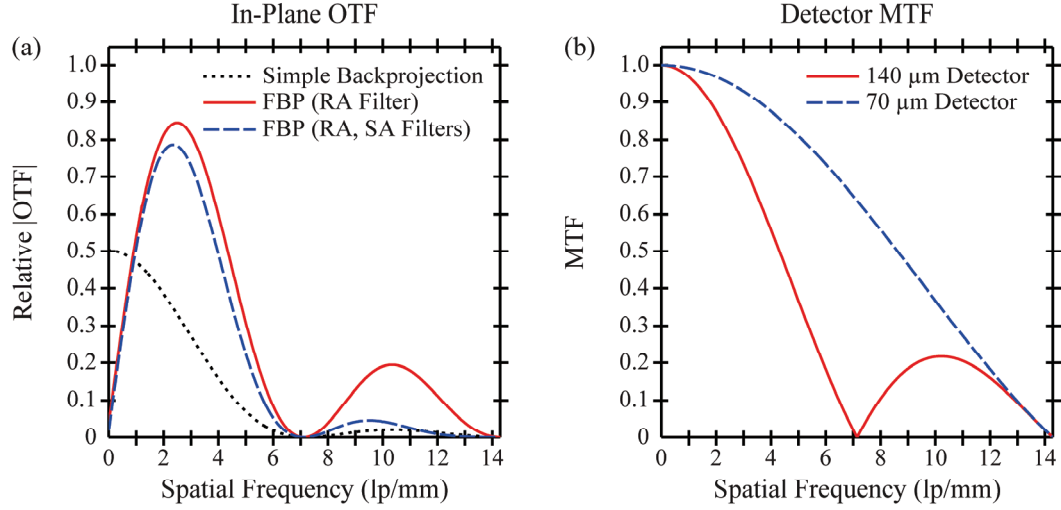


Figure 1.4: Comparison of resolution in the reconstruction and in the detector. (a) The in-plane OTF is studied as a function of frequency (f_x) in a DBT system with 140 μm detector elements. In SBP reconstruction, modulation decreases with frequency up to the first zero of the OTF. Conversely, in FBP reconstruction, modulation increases linearly at low frequencies, following the ramp filter. Incorporating SA filtering reduces the high frequency signal. (b) Regardless of the reconstruction filter, the first zero of the in-plane OTF can be recovered from the MTF of the detector sampling process.

In a simple backprojection (SBP) reconstruction with no filtering, Figure 1.4(a) demonstrates that the in-plane OTF decreases with frequency. This trend is monotonic up to the first zero of the plot (7.14 lp/mm). The first zero arises from the MTF of the detector sampling process; the MTF is the normalized modulus of the OTF¹⁷⁻¹⁹

$$\text{MTF}(f_x, f_y) = \left| \text{sinc}(a_x f_x) \text{sinc}(a_y f_y) \right|, \quad (1.7)$$

where

$$\text{sinc}(u) \equiv \frac{\sin(\pi u)}{\pi u}. \quad (1.8)$$

For measurements along the x direction, the first zero of Eq. (1.7) occurs at the frequency a_x^{-1} , or 7.14 mm^{-1} for $140 \text{ }\mu\text{m}$ detector elements [Figure 1.4(a)]. As the size of the detector elements is reduced, the first zero is shifted to a higher frequency. Figure 1.4(b) illustrates this property using a $70 \text{ }\mu\text{m}$ detector; the first zero of the MTF is 14.3 mm^{-1} .

If RA filtering is incorporated into the reconstruction, Figure 1.4(a) demonstrates that the in-plane OTF increases linearly at low frequencies. In contrast to the plot for SBP reconstruction, this trend arises from the frequency dependence of the filter. At high frequencies, the RA filter and the detector MTF have competing influences on modulation. Although the RA filter increases with frequency, the detector MTF decreases to zero at the frequency a_x^{-1} (7.14 lp/mm for $140 \text{ }\mu\text{m}$ detector elements). Consequently, there is an intermediate frequency at which the in-plane OTF is maximized.

Since noise tends to occur at high frequencies, an SA filter is often applied in addition to the RA filter in order to reduce the high frequency signal in the reconstruction. As shown in Figure 1.4(a), this additional filter does not change the in-plane OTF considerably at low frequencies. However, at higher frequencies approaching the first zero of the OTF, the reconstruction with the RA and SA filters has less modulation than the reconstruction with the RA filter alone.

To analyze the noise properties in the reconstruction, the in-plane NPS can be calculated by integrating the 3D NPS along z . Zhao showed that the in-plane NPS decreases with frequency in an SBP reconstruction. The degradation with frequency is less pronounced than the in-plane OTF. By contrast, if RA filtering is incorporated into

the reconstruction, Zhao demonstrated that the in-plane NPS is proportional to f_x^2 at low frequencies. This trend is observed regardless of whether SA filtering is applied.

In order to validate the in-plane NPS calculation, Zhao determined the 3D NPS experimentally. In that paper, the reconstruction of a Lucite phantom was divided into multiple sub-images consisting of uniform noise. An individual realization of the 3D NPS was then determined from the 3D Fourier transform of the mean subtracted image. By calculating the ensemble average of the NPS realizations of various sub-images, the final NPS was determined experimentally and its dependence on reconstruction filter was shown to match the qualitative trends found from the theoretical calculations.

While the NPS of the reconstruction is colored, it should be pointed out that the NPS of a single projection is white (*i.e.*, frequency-independent). My earlier work has shown that the NPS of a parallel projection is $\overline{\Phi} a_x^2 a_y^2$, where $\overline{\Phi}$ is the mean number of x-ray photons per unit area on the detector.¹⁹ This NPS formula assumes that the x-ray photons are Poisson-distributed across the detector and that the x-ray converter has an MTF of unity at all frequencies. An amorphous selenium (*a*-Se) photoconductor operated in drift mode is a good approximation for an x-ray converter with this property.²⁰

4. LIMITATIONS OF ZHAO'S MODEL THAT ARE EXPLORED IN THIS THESIS

One trade-off of DBT is resolution loss in the projection images as a result of oblique x-ray incidence. Zhao's model possesses an important limitation in making the

assumption that the MTF and NPS of each projection can be approximated by their value at normal incidence. In calculating the 3D transfer functions in stage 4 of the cascade, this assumption is evident in Eqs. (1.3) and (1.4), as T_h and W_h are factored out of the summation over all projections. This step is justified only if the transfer functions for each projection are identical. In order to model the consequences of oblique x-ray incidence in this thesis, I extend Swank's analytical formulation of the transfer functions of x-ray fluorescent screens to oblique incidence (Chapter 2).²¹ This approach differs from previous research on oblique incidence in that closed form solutions for the transfer functions are obtained, providing greater insight into the underlying detector physics than empirical studies²² or Monte Carlo simulations.²³

Because x rays are emitted from the focal spot in all directions, the incident angle is spatially variant at each point on the detector. In this thesis, I demonstrate that the transfer functions for each projection vary at each point on the detector as a result of this property.²¹ Unlike Zhao's paper which modeled a parallel beam geometry, I analyze the spatial anisotropy of the transfer functions by modeling a divergent beam geometry.

In Zhao's model, the x and y dimensions of the voxels in the reconstruction are chosen to match the detector element size. Hence, the highest frequency that can be resolved in each slice is the alias frequency of the detector. This thesis considers reconstruction grids with much smaller pixelation in order to visualize higher frequencies (Chapter 3).²⁴ Because oblique x-ray incidence shifts the image of an object in sub-pixel detector element increments with each increasing projection angle, it is demonstrated that DBT is capable of super-resolution (*i.e.*, sub-pixel resolution). For analytical proof of

super-resolution, a theoretical framework is developed in which the reconstruction of a high frequency sinusoidal input is calculated. The feasibility of super-resolution is also validated experimentally by acquiring images of a bar pattern phantom with frequencies higher than the detector alias frequency. Super-resolution cannot be demonstrated using Zhao's work, since it does not model the sub-pixel shifts in the image of an object between projections.

This thesis shows that the existence of super-resolution is dependent on position in the reconstruction and on the directionality of the input frequency. Super-resolution is feasible over a broad range of positions if the test frequency is oriented along the tube travel direction (x), but is achievable at fewer positions if the test frequency is oriented along the chest wall-to-nipple direction (y).²⁴ In Zhao's model, the spatial anisotropy of image quality within the plane of reconstruction is not demonstrated.

Following convention, Zhao's paper assumes that slices in a DBT reconstruction should only be created using planes parallel to the breast support. This thesis demonstrates that slices can also be generated along oblique directions through the same volume, analogous to multiplanar reconstructions in CT. To investigate the visibility of individual frequencies in oblique planes, the reconstruction of a sinusoidal input is calculated. Unlike Chapter 3 in which the sinusoidal input is parallel to the breast support, the object is oriented at an angle (*i.e.*, "pitch") in the following two chapters on oblique reconstructions (Chapters 4 and 5). By comparing the signal in the reconstruction against the attenuation coefficient of the sine plate, this thesis generalizes Zhao's calculation of in-plane OTF to a slice along any pitch in the reconstructed

volume. This formulation differs from Zhao's model, which is limited to the 0° pitch parallel to the breast support.

As demonstrated by Zhao, a cross section of the 3D OTF resembles a double cone [Figure 1.3(b)] in any plane perpendicular to the f_y axis (namely, the f_x - f_z planes of Fourier space). This region is termed the Fourier double cone (FDC) throughout this thesis, even though it is not 3D in the strict sense of a cone. The opening angle of the FDC matches the angular range of the scan. Although the 3D OTF is zero along pitches outside the opening angle of the FDC, the in-plane OTF is not zero along these pitches. This thesis demonstrates that the in-plane OTF can be calculated by integrating the 3D OTF along the direction perpendicular to the plane of the slice. In Zhao's work, the in-plane OTF is found by integrating the 3D OTF along the z direction; this formulation presumes that the slice is parallel to the breast support (*i.e.*, the xy plane).

5. DYNAMIC RECONSTRUCTION AND RENDERING

In order to demonstrate the existence of super-resolution in experimental images (Chapters 3 and 5), it is necessary to perform the reconstruction on a grid with smaller pixelation than the detector. In this thesis, I use a state-of-the-art commercial prototype reconstruction solution (BrionaTM, Real Time Tomography, Villanova, PA) for this purpose.²⁵ This software allows the user to magnify a region in the reconstruction in real-time at higher resolution than the detector. Although it is possible to interpolate a reconstruction performed with the same resolution as the detector, the magnified image that results does not support super-resolution.

The BrionaTM software uses a backprojection filtering reconstruction algorithm in which the backprojection transformation is performed using a Graphics Processing Unit (GPU). This approach allows the user to change the depth and tilt angle of the reconstruction plane in real-time, analogous to how a radiologist would dynamically view a 3D reconstruction for CT. Backprojection filtering is implemented instead of filtered backprojection in order to minimize computation time. Since filtering and backprojection are linear operations, their order can be switched with no impact on the final result. The BrionaTM software is an important tool for validating oblique reconstructions in experimental images in Chapters 4 and 5 of this thesis.

In Zhao's model, the reconstruction consists of a stack of slices with 1.0 mm thickness. As a result, a small object that spans two adjacent slices (*e.g.*, a calcification) will appear blurry. Bakic *et al.* demonstrated that the size of a small object is determined with 50% error if it is 0.6 mm from the plane of focus.²⁶ In order to minimize blurring, the BrionaTM software can generate a slice at a depth corresponding to the precise position at which the object is in focus. The slice thickness is effectively zero in contrast to Zhao's work.

6. THESIS ROADMAP

In this thesis, I develop a model of image quality for DBT by carefully examining the limitations of Zhao's linear systems formulation (Figure 1.5). My thesis begins by analyzing image quality in individual projections (**Chapter 2**). Although degradation in image quality due to oblique x-ray incidence has been studied in cesium iodide (CsI)

phosphors with empirical data²² and amorphous selenium (*a*-Se) direct converting detectors using Monte Carlo simulations,²³ no one has performed a theoretical analysis of the consequences of oblique x-ray incidence. The purpose of **Chapter 2** is to extend Swank's analytical formulation of the transfer functions of x-ray fluorescent screens to oblique x-ray incidence.²¹

In assessing image quality in the reconstruction (**Chapters 3-5**), a significant component of the remainder of my thesis is to analyze a conceptual test object known as a "*sine plate*". This object is a thin strip whose attenuation coefficient varies sinusoidally (Figure 1.1). Increasing the frequency of the object simulates small closely-spaced structures such as microcalcifications, which are early indicators of cancer. The sine plate has led to two important discoveries in DBT. In my work on super-resolution (**Chapter 3**), I show that a reconstruction can resolve higher frequencies than each 2D projection.²⁴ The clinical impact of this finding is improving the visibility of microcalcifications; an early variant of this work earned the Best Student Paper Award at the 2011 SPIE Medical Imaging Conference.²⁷ By orienting the long axis of the sine plate along various angles, I later demonstrate that reconstructions are achievable in obliquely pitched planes (**Chapters 4-5**). This work shows that some objects are more easily visualized in oblique planes instead of conventional planes that are parallel to the breast support.

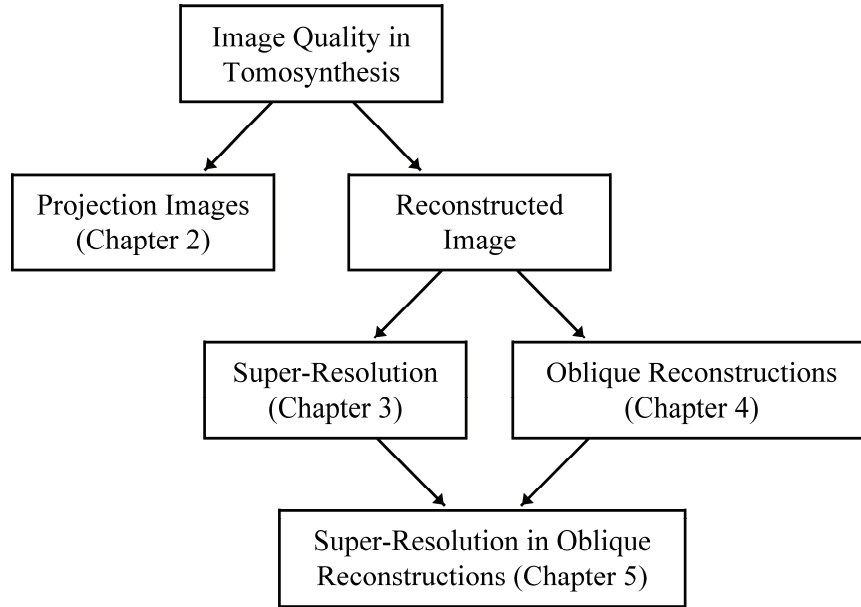


Figure 1.5: Thesis roadmap. In this thesis, image quality in DBT is analyzed separately in projection images (Chapter 2) and in the reconstruction (Chapters 3-5).

Finally, **Chapter 6** discusses avenues for future research by focusing on how the model of image quality developed in this thesis can be used to optimize DBT systems. One area for future research is investigating the trade-offs between long and short scan time in DBT systems with continuous tube motion and patient motion. My preliminary research on this topic earned the Runner-Up to the Best Student Paper Award at the 2012 SPIE Medical Imaging Conference.

7. REFERENCES

- ¹Society AC. Breast Cancer Facts & Figures 2011-2012. Atlanta; 2011. p. 1-32.
- ²Kumar V, Abbas A, Fausto N. Robbins and Cotran Pathologic Basis of Disease. 7th ed. Philadelphia: Elsevier; 2005.
- ³Institute of Medicine NRC. *Mammography and Beyond - Developing Technologies for the Early Detection of Breast Cancer*. Washington, DC: National Academy Press; 2001.
- ⁴Mushlin AI, Kouides RW, Shapiro DE. Estimating the Accuracy of Screening Mammography: A Meta-analysis. *American Journal of Preventive Medicine*. 1998;14(2):143-53.
- ⁵Rafferty EA. Tomosynthesis: New weapon in breast cancer fight. *Decisions in Imaging Economics*. 2004;17(4).
- ⁶Poplack SP, Tosteson TD, Kogel CA, Nagy HM. Digital breast tomosynthesis: initial experience in 98 women with abnormal digital screening mammography. *American Journal of Roentgenology*. 2007;189(3):616-23.
- ⁷Conant EF, Gavenonis SC, Weinstein SP, Schnall M, Kontos D. Early Implementation of Digital Breast Tomosynthesis: Comparison of Call-back and Cancer Detection Rates in a Clinical Screening Practice. *RSNA*; 2012; Chicago, Illinois; 2012.
- ⁸Zhao B, Zhao W. Three-dimensional linear system analysis for breast tomosynthesis. *Medical Physics*. 2008;35(12):5219-32.
- ⁹Zhao W, Rowlands JA. Digital radiology using active matrix readout of amorphous selenium: Theoretical analysis of detective quantum efficiency. *Medical Physics*. 1997;24(12):1819-33.
- ¹⁰Zhao W, Ji WG, Rowlands JA. Effects of characteristic x rays on the noise power spectra and detective quantum efficiency of photoconductive x-ray detectors. *Medical Physics*. 2001;28:2039-49.
- ¹¹Zhao W, Ji WG, Debie A, Rowlands JA. Imaging performance of amorphous selenium based flat-panel detectors for digital mammography: Characterization of a small area prototype detector. *Medical Physics*. 2003;30:254-63.
- ¹²Rowlands JA, Yorkston J. Chapter 4: Flat Panel Detectors for Digital Radiography. In: Beutel J, Kundel HL, Van Metter RL, editors. *Handbook of Medical Imaging Volume 1 Physics and Psychophysics*. Bellingham, WA: SPIE - The International Society for Optical Engineering; 2000. p. 223-328.
- ¹³Zhao B, Zhou J, Zhao W. Focal spot blur in tomosynthesis systems. *RSNA*; 2005; 2005.
- ¹⁴Mertelmeier T, Orman J, Haerer W, Dudam MK. Optimizing filtered backprojection reconstruction for a breast tomosynthesis prototype device. In: Flynn MJ, Hsieh J, editors. *Physics of Medical Imaging*; 2006; San Diego: SPIE; 2006.
- ¹⁵Kijewski MF, Judy PF. The noise power spectrum of CT images. *Physics in Medicine & Biology*. 1987;32(5):565-75.
- ¹⁶Zhao B, Zhou J, Hu Y-H, Mertelmeier T, Ludwig J, Zhao W. Experimental validation of a three-dimensional linear system model for breast tomosynthesis. *Medical Physics*. 2009;36(1):240-51.

- ¹⁷Albert M, Maidment ADA. Linear response theory for detectors consisting of discrete arrays. *Medical Physics*. 2000;27(10):2417-34.
- ¹⁸Acciavatti RJ, Maidment ADA. An Analytical Model of NPS and DQE Comparing Photon Counting and Energy Integrating Detectors. In: Samei E, Pelc NJ, editors. *SPIE Medical Imaging*; 2010; San Diego, CA: SPIE; 2010. p. 76220I-1 - I-12.
- ¹⁹Acciavatti RJ, Maidment ADA. A Comparative Analysis of OTF, NPS, and DQE in Energy Integrating and Photon Counting Digital X-ray Detectors. *Medical Physics*. 2010;37(12):6480-95.
- ²⁰Lee DL, Cheung LK, Rodricks B, Powell GF. Improved imaging performance of a 14 x 17-inch Direct Radiography (TM) System using Se/TFT detector. In: James T. Dobbins I, Boone JM, editors. *SPIE Conference on Physics of Medical Imaging*; 1998; San Diego, CA: SPIE; 1998. p. 14-23.
- ²¹Acciavatti RJ, Maidment ADA. Optimization of phosphor-based detector design for oblique x-ray incidence in digital breast tomosynthesis. *Medical Physics*. 2011;38(11):6188-202.
- ²²Mainprize JG, Bloomquist AK, Kempston MP, Yaffe MJ. Resolution at oblique incidence angles of a flat panel imager for breast tomosynthesis. *Medical Physics*. 2006;33(9):3159-64.
- ²³Hajdok G, Cunningham IA. Penalty on the detective quantum efficiency from off-axis incident x rays. In: Yaffe MJ, Flynn MJ, editors. *Medical Imaging 2004: Physics of Medical Imaging*; 2004; San Diego, CA: SPIE; 2004. p. 109-18.
- ²⁴Acciavatti RJ, Maidment ADA. Observation of super-resolution in digital breast tomosynthesis. *Medical Physics*. 2012;39(12):7518-39.
- ²⁵Kuo J, Ringer PA, Fallows SG, Bakic PR, Maidment ADA, Ng S. Dynamic Reconstruction and Rendering of 3D Tomosynthesis Images. In: Pelc NJ, Samei E, Nishikawa RM, editors. *SPIE Medical Imaging*; 2011; Lake Buena Vista, FL: SPIE; 2011. p. 796116-1 - 11.
- ²⁶Bakic PR, Ringer P, Kuo J, Ng S, Maidment ADA. Analysis of Geometric Accuracy in Digital Breast Tomosynthesis Reconstruction. *Lecture Notes in Computer Science*. 2010;6136:62-9.
- ²⁷Acciavatti RJ, Maidment ADA. Investigating the Potential for Super-Resolution in Digital Breast Tomosynthesis. In: Pelc NJ, Samei E, Nishikawa RM, editors. *SPIE Medical Imaging*; 2011; Lake Buena Vista, FL: SPIE; 2011. p. 79615K-1 - K-12.

CHAPTER 2

Optimization of Phosphor-Based Detector Design for Oblique X-Ray Incidence in Digital Breast Tomosynthesis

This chapter is based on a peer-reviewed article published in Medical Physics **38**(11), 6188-202 (2011).

1. INTRODUCTION

In many radiographic studies, non-normally (*i.e.*, obliquely) incident x rays provide a source of blurring at the periphery of the detector due to the divergence of the x-ray beam emitted from the focal spot. Que and Rowlands proposed an analytical model of the resolution loss due to oblique incidence by deriving an expression for the modulation transfer function (MTF) of amorphous selenium (*a*-Se) detectors from first principles.¹ Their work assumes that the detector is operated in drift mode, so that the point spread function (PSF) for normal incidence is a delta function and hence the MTF for normal incidence is unity at all frequencies.²

Oblique incidence is more readily observed in digital mammography (DM) than many other imaging studies. A DM detector is placed closer to the focal spot than most modalities³ to counteract the loss in x-ray penetration resulting from the use of relatively low energies (~ 20 keV).⁴⁻⁶ The drawback of decreasing the source-to-detector distance is increasing the angle of incidence relative to the normal, especially at the edges of the detector. For example, the maximum angle of incidence is 25° for a DM system with a detector field-of-view (FOV) of $24\text{ cm} \times 30\text{ cm}$ and a source-to-image distance of 70 cm measured at the midpoint of the chest wall.

In digital breast tomosynthesis (DBT), low dose x-ray projection images are acquired over a limited range of angles around the breast, and sharply in-focus slices at all depths of the breast volume are generated using image reconstruction techniques. Preliminary studies indicate that DBT provides increased sensitivity and specificity relative to DM for the early detection of breast cancer in women.⁷ One shortcoming of

DBT, however, is that it is more directly impacted by the resolution loss due to oblique incidence than DM. The maximum projection angle in DBT can be as large as 20° or 30° , and the angle of incidence at the edges of the detector is even higher if one takes into account the divergent x-ray beam geometry. While some DBT systems incorporate a rotating detector to counteract changes in obliquity, many systems employ a stationary detector.

Mainprize *et al.* experimentally demonstrated the resolution loss due to oblique incidence in cesium iodide doped with thallium (CsI:Tl), a structured phosphor-based detector, using the slanted edge technique to measure MTF.⁸ The authors showed that at 10° incidence, the MTF degradation becomes comparable to the resolution loss associated with other common sources of image blurring, such as the blurring of the focal spot and the lateral spread of visible light within the scintillator. At 40° incidence, the MTF is reduced considerably; for example, at 5 line pairs per mm (lp/mm), the MTF is degraded by 35% to 40% over a broad range of kVp and target-filter combinations.

While Mainprize *et al.* did not measure noise power spectra (NPS), Hajdok and Cunningham have calculated NPS using Monte Carlo simulations of *a*-Se.³ Their work demonstrated that unlike MTF, NPS has minimal angular dependence. Since the detective quantum efficiency (DQE) is dependent upon the square of the MTF, Hajdok and Cunningham have shown that the DQE degradation with oblique incidence at high frequencies is more pronounced than the MTF degradation.

Although oblique incidence has been studied experimentally and using Monte Carlo simulations, a theoretical treatment has been lacking. For this reason, the purpose

of this chapter is to extend Swank's calculations⁹ of the transfer functions of turbid granular phosphors to oblique incidence. Building off our previous work on oblique incidence,¹⁰ we analyze the light diffusion equations in a non-structured scintillator such as gadolinium oxysulfide doped with terbium ($\text{Gd}_2\text{O}_2\text{S:Tb}$), which is commonly used in breast imaging and which can reasonably approximate other detector materials. The theoretical formulation of this work differs from the one proposed by Que and Rowlands in not making the assumption that the PSF for normal incidence is a delta function. Ultimately, the analytical model is used as a tool for optimizing the design of the phosphor for oblique incidence.

2. METHODS

2.1. Transfer Functions for Front-Screen Configuration

The optical transfer function (OTF), NPS, and DQE of a turbid granular phosphor are derived here from first principles for all angles of incidence. The Boltzmann transport equation may be used to model the spread of visible light in a turbid phosphor. A first-order, steady state solution to the Boltzmann transport equation is a diffusion equation of the form¹¹

$$-\nabla^2 \phi(\mathbf{r}) + \sigma^2 \phi(\mathbf{r}) = S(\mathbf{r}), \quad (2.1)$$

where $\phi(\mathbf{r})$ is the product of the density of the secondary carriers (*i.e.*, the optical photons) with the diffusion constant, σ is the reciprocal of the mean diffusion length of the secondary carriers, and $S(\mathbf{r})$ is the source function. The diffusion equation is a useful approximation to the Boltzmann transport equation provided that three criteria are met:

(1) solutions for $\phi(\mathbf{r})$ are determined far from the x-ray source $S(\mathbf{r})$ relative to the mean free path of optical scatter; (2) the optical properties of the phosphor possess no discontinuities; and (3) the probability of optical absorption is small compared against the probability of optical scatter.¹² This model has been used by Swank for normal incidence⁹ and has shown good agreement with experimental data.^{12, 13}

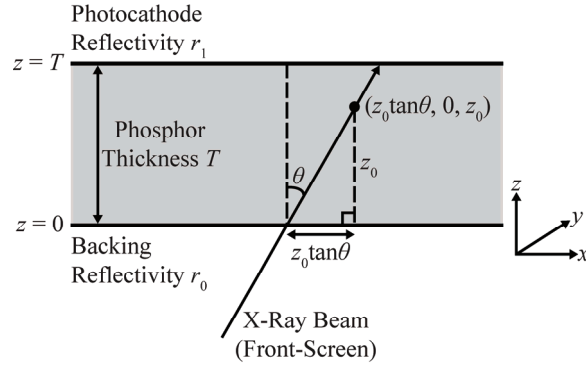


Figure 2.1: Illustration of oblique x-ray incidence in a phosphor. In terms of delta functions, the source function $S(\mathbf{r})$ at the depth z_0 of the phosphor is found from trigonometry to be $\delta(x - z_0 \tan \theta) \delta(y) \delta(z - z_0)$, where θ is the angle of x-ray incidence relative to the normal. The figure assumes a front-screen configuration in which x rays are incident on the backing at $z = 0$ before striking the photocathode at $z = T$. Reversing the direction of the arrowhead of the x-ray beam converts the front-screen configuration to a back-screen configuration.

As shown in Figure 2.1, the source function $S(\mathbf{r})$ in Eq. (2.1) may be modeled as the point $(z_0 \tan \theta, 0, z_0)$ along the x-ray path length, where z_0 is depth within the scintillator of total thickness T and where θ is the angle of incidence relative to the normal. In terms of delta functions, $S(\mathbf{r})$ can be written as

$$S(\mathbf{r}) = \delta(x - z_0 \tan \theta) \delta(y) \delta(z - z_0). \quad (2.2)$$

Using the Fourier representation of the delta function,¹⁴ the source function can equivalently be expressed as the integral

$$S(\mathbf{r}) = \delta(z - z_0) \int_{-\infty}^{\infty} \int_{-\infty}^{\infty} e^{2\pi i[(x-z_0 \tan \theta)v_x + yv_y]} dv_x dv_y. \quad (2.3)$$

Defining \mathbf{v} as the 2D spatial frequency vector with components v_x and v_y , solutions to Eq. (2.1) can be written in the form

$$\phi(x, y, z) = \int_{-\infty}^{\infty} \int_{-\infty}^{\infty} \psi_{\mathbf{k}}(z) e^{2\pi i(xv_x + yv_y)} dv_x dv_y. \quad (2.4)$$

Substituting Eqs. (2.3)-(2.4) into Eq. (2.1), it can be shown that

$$-\frac{d^2 \psi_{\mathbf{k}}}{dz^2} + q^2 \psi_{\mathbf{k}} = e^{-ik_x z_0 \tan \theta} \delta(z - z_0), \quad (2.5)$$

where

$$q^2 = \sigma^2 + k_x^2 + k_y^2, \quad (2.6)$$

$$\mathbf{k} = 2\pi \mathbf{v}. \quad (2.7)$$

To solve Eq. (2.5) for $\psi_{\mathbf{k}}(z)$, one can apply integral transform techniques.^{15, 16} Denoting the Laplace transform of $\psi_{\mathbf{k}}(z)$ as $\mathcal{L}\psi_{\mathbf{k}}(p)$, the transform of the differential equation is

$$(-p^2 + q^2) \cdot \mathcal{L}\psi_{\mathbf{k}}(p) + C_1 p + C_2 = e^{-ik_x z_0 \tan \theta} e^{-pz_0}, \quad (2.8)$$

where C_1 and C_2 are the constants of integration. Solving for $\mathcal{L}\psi_{\mathbf{k}}(p)$ and taking the inverse transform generates the following piece-wise expression for $\psi_{\mathbf{k}}(z)$.

$$\psi_{\mathbf{k}}(z) = \begin{cases} C_1 \cosh(qz) + \frac{C_2}{q} \sinh(qz), & 0 \leq z \leq z_0 \\ C_1 \cosh(qz) + \frac{C_2}{q} \sinh(qz) - \frac{e^{-ik_x z_0 \tan \theta}}{q} \sinh[q(z - z_0)], & z_0 < z \leq T \end{cases} \quad (2.9)$$

The constants C_1 and C_2 can now be determined from boundary conditions concerning secondary carrier currents directed toward the planes at $z = 0$ and $z = T$. In terms of the inverse relaxation length τ , the secondary carrier currents across any plane of constant z are

$$j_{\text{left}}(z) = \frac{1}{2} \left[\phi \tau + \frac{d\phi}{dz} \right], \quad (2.10)$$

$$j_{\text{right}}(z) = \frac{1}{2} \left[\phi \tau - \frac{d\phi}{dz} \right]. \quad (2.11)$$

In the right-hand side of the two equations, the first term models the effusion current, while the second term comes from Fick's law. The first boundary condition is determined by the reflectivity r_0 of the plane at $z = 0$. Noting that $j_{\text{right}}(0) = r_0 j_{\text{left}}(0)$, one finds

$$\left. \frac{d\phi}{dz} \right|_{z=0} = \tau \rho_0 \phi|_{z=0}, \quad (2.12)$$

where

$$\rho_0 \equiv \frac{1 - r_0}{1 + r_0}. \quad (2.13)$$

The second boundary condition is determined from the reflectivity r_1 of the boundary at $z = T$, as stipulated by the expression $j_{\text{left}}(T) = r_1 j_{\text{right}}(T)$. Defining ρ_1 similar to ρ_0 and noting that the boundary conditions hold for each Fourier component $\psi_{\mathbf{k}}$ of ϕ , it can be shown that

$$C_1 = \left[\frac{(q + \tau \rho_1) e^{q(T-z_0)} + (q - \tau \rho_1) e^{-q(T-z_0)}}{(q + \tau \rho_0)(q + \tau \rho_1) e^{qT} - (q - \tau \rho_0)(q - \tau \rho_1) e^{-qT}} \right] e^{-ik_x z_0 \tan \theta}, \quad (2.14)$$

$$C_2 = \tau\rho_0 C_1 . \quad (2.15)$$

Consistent with Swank's approach, the photocathode is defined by the plane $z = T$ and the backing is defined by the plane $z = 0$, as diagrammed schematically in Figure 2.1. The OTF of the scattering process, $G(\mathbf{v}, z_0)$, is then determined for a point source from the expression

$$G(\mathbf{v}, z_0) = \left[\frac{\rho_1}{1 + \rho_1} \right] \left[\psi_{\mathbf{k}} \tau - \frac{d\psi_{\mathbf{k}}}{dz} \right] \Big|_{z=T} . \quad (2.16)$$

Hence,

$$G(\mathbf{v}, z_0) = \tau\rho_1 \left[\frac{(q + \tau\rho_0)e^{(q - ik_x \tan \theta)z_0} + (q - \tau\rho_0)e^{-(q + ik_x \tan \theta)z_0}}{(q + \tau\rho_0)(q + \tau\rho_1)e^{qT} - (q - \tau\rho_0)(q - \tau\rho_1)e^{-qT}} \right] . \quad (2.17)$$

To calculate the OTF of the entire phosphor, one multiplies Eq. (2.17) by the relative x-ray signal as a function of the depth z_0

$$N_F(z_0) = \frac{\mu e^{-\mu z_0 \sec \theta} \sec \theta}{1 - e^{-\mu T \sec \theta}} , \quad (2.18)$$

where μ is the linear attenuation coefficient of the phosphor, and then integrates over the phosphor thickness. Assuming a front-screen (F) configuration in which x rays are first incident on the backing at $z = 0$ before striking the photocathode at $z = T$, the OTF is thus

$$G_F(\mathbf{v}) = \int_0^T N_F(z_0) G(\mathbf{v}, z_0) dz_0 \quad (2.19)$$

$$= \frac{\beta \mu \sec \theta}{1 - e^{-\mu T \sec \theta}} \left[\frac{(q + \tau\rho_0)(e^{(\gamma_- - ik_x \tan \theta)T} - 1)}{\gamma_- - ik_x \tan \theta} - \frac{(q - \tau\rho_0)(e^{-(\gamma_+ + ik_x \tan \theta)T} - 1)}{\gamma_+ + ik_x \tan \theta} \right] , \quad (2.20)$$

where

$$\beta \equiv \frac{\tau\rho_1}{(q + \tau\rho_0)(q + \tau\rho_1)e^{qT} - (q - \tau\rho_0)(q - \tau\rho_1)e^{-qT}} , \quad (2.21)$$

$$\gamma_{\pm} \equiv q \pm \mu \sec \theta. \quad (2.22)$$

The MTF is found from the normalized modulus of the OTF.¹⁷

In the absence of outside noise sources, the quantum NPS or $W_F(\mathbf{v})$ is calculated by integrating the product of $N_F(z_0)$ with $|G(\mathbf{v}, z_0)|^2$ from $z_0 = 0$ to $z_0 = T$.

$$W_F(\mathbf{v}) = \int_0^T N_F(z_0) |G(\mathbf{v}, z_0)|^2 dz_0 \quad (2.23)$$

$$= \frac{\beta^2 \mu \sec \theta}{1 - e^{-\mu T \sec \theta}} \left[\frac{(q + \tau \rho_0)^2 (e^{(q + \gamma_-)T} - 1)}{q + \gamma_-} + \frac{2(q^2 - \tau^2 \rho_0^2)(1 - e^{-\mu T \sec \theta})}{\mu \sec \theta} + \frac{(q - \tau \rho_0)^2 (1 - e^{-(q + \gamma_+)T})}{q + \gamma_+} \right] \quad (2.24)$$

With the OTF and quantum NPS known, it is now possible to determine the DQE. From the work of Nishikawa, DQE can be formulated as the product of four terms¹²

$$\text{DQE}(\mathbf{v}) = A_Q A_S R_C(\mathbf{v}) R_N(\mathbf{v}), \quad (2.25)$$

where A_Q is the x-ray quantum detection efficiency (QDE) determined by the Lambert-Beer Law as

$$A_Q = 1 - e^{-\mu T \sec \theta}, \quad (2.26)$$

A_S is the Swank information factor

$$A_S = \frac{G_F^2(\mathbf{0})}{W_F(\mathbf{0})}, \quad (2.27)$$

$R_C(\mathbf{v})$ is the Lubberts fraction

$$R_C(\mathbf{v}) = \frac{1}{A_S} \cdot \frac{|G_F(\mathbf{v})|^2}{W_F(\mathbf{v})}, \quad (2.28)$$

and $R_N(\mathbf{v})$ is the ratio of the x-ray quantum noise power to the total noise power.

Assuming a quantum-limited imaging system, $R_N(\mathbf{v})$ is taken to be unity in this work.

2.2. Transfer Functions for Back-Screen Configuration

In a similar fashion, the transfer functions for a back-screen (B) configuration can be calculated. Unlike the front-screen configuration, x rays first strike the photocathode at $z = T$ before passing through the backing at $z = 0$. This modification reverses the direction of the x-ray beam in Figure 2.1 without further altering the diagram. Hence

$$N_B(z_0) = \frac{\mu e^{-\mu(T-z_0)\sec\theta} \sec\theta}{1 - e^{-\mu T \sec\theta}}, \quad (2.29)$$

so that the OTF and quantum NPS are found to be

$$G_B(\mathbf{v}) = \frac{\beta \mu \sec\theta}{e^{\mu T \sec\theta} - 1} \left[\frac{(q + \tau \rho_0)(e^{(\gamma_+ - ik_x \tan\theta)T} - 1)}{\gamma_+ - ik_x \tan\theta} - \frac{(q - \tau \rho_0)(e^{-(\gamma_- + ik_x \tan\theta)T} - 1)}{\gamma_- + ik_x \tan\theta} \right], \quad (2.30)$$

$$W_B(\mathbf{v}) = \frac{\beta^2 \mu \sec\theta}{e^{\mu T \sec\theta} - 1} \left[\frac{(q + \tau \rho_0)^2 (e^{(q + \gamma_+)T} - 1)}{q + \gamma_+} + \frac{2(q^2 - \tau^2 \rho_0^2)(e^{\mu T \sec\theta} - 1)}{\mu \sec\theta} + \frac{(q - \tau \rho_0)^2 (1 - e^{-(q + \gamma_-)T})}{q + \gamma_-} \right]. \quad (2.31)$$

Eqs. (2.30) and (2.31) follow from Eqs. (2.19) and (2.23); the subscript “ B ” is used to denote a back-screen.

3. RESULTS FOR A MODEL DETECTOR

3.1. Transfer Functions for Front- and Back-Screen Configurations

The OTF, NPS, and DQE calculations are now illustrated for a phosphor with a reflective backing ($r_0 = 1$), a non-reflective photocathode ($r_1 = 0$), and optical scatter at the diffusion limit ($\tau \rightarrow \infty$). In view of the limitations of Swank’s model, a large value of τ has been chosen. As Swank demonstrated in his original paper,⁹ the MTF of a scattering phosphor ($\tau > 0$) is always higher than the MTF a non-scattering phosphor

($\tau = 0$) at low frequencies, but the opposite trend arises at high frequencies. The crossover point of the scattering and non-scattering MTF curves corresponds to the frequency beyond which Swank's model becomes inaccurate. For very small values of τ , the crossover point occurs at relatively low frequencies. However, for infinite τ , the scattering MTF curve never crosses the non-scattering MTF curve between 0 and 10 lp/mm. Hence, Swank's model is increasingly accurate in approaching the diffusion limit.

In calculating the transfer functions, we assume 20 keV monoenergetic x rays⁴⁻⁶ and a porous, 100 μm thick $\text{Gd}_2\text{O}_2\text{S:Tb}$ phosphor with 50% packing density. The attenuation coefficient μ for the porous phosphor is determined by halving the value for a crystalline phosphor.¹² Since crystalline $\text{Gd}_2\text{O}_2\text{S}$ has a mass density of 7.34 g/cm^3 and a mass attenuation coefficient of $36.9 \text{ cm}^2/\text{g}$ for 20 keV x rays,¹⁸ the attenuation coefficient for porous $\text{Gd}_2\text{O}_2\text{S}$ is 13.5 mm^{-1} .

In Figure 2.2, cross sections of the MTF surface are plotted versus frequency at two polar angles (α) of the frequency vector (0° and 90°) for multiple angles of incidence and two optical absorption parameters. The value of the high optical absorption parameter ($\sigma = 20 \text{ mm}^{-1}$) was chosen to match Swank's example⁹ in which $\sigma T = 2$. In practice, the optical absorption can be increased by adding an optical dye to the phosphor. Following convention, the polar angle is defined as the angle of the frequency vector relative to the x axis, so that the 0° polar angle is only perpendicular to the x-ray beam for normal incidence and the 90° polar angle is always perpendicular to the x-ray beam (Figure 2.1).

Consistent with Swank's work at normal incidence, Figure 2.2 demonstrates that increasing the optical absorption increases the MTF. Figure 2.2(a) indicates that increasing the angle of incidence decreases the MTF, giving rise to poorer spatial resolution in the front-screen configuration. For example, comparing 30° incidence to normal incidence at 5.0 lp/mm ($\alpha = 0^\circ$), the MTF decreases by 17% in a phosphor with no optical absorption and by 15% in a phosphor with high optical absorption. As expected, the MTF has minimal angular dependence orthogonal to the ray of incidence [Figure 2.2(c)].

Figures 2.2(b) and 2.2(d) demonstrate that the back-screen configuration has superior MTF to the front-screen configuration for all projection angles. This result has been well-established for normal incidence.^{19, 20} More significantly, Figures 2.2(b) and 2.2(d) further show that the angular dependence of the MTF is much less pronounced in the back-screen configuration than in the front-screen configuration. For example, comparing 30° incidence to normal incidence at 5.0 lp/mm along a 0° polar angle, the back-screen MTF decreases by a mere 3%. Unlike the front-screen, the back-screen MTF increases slightly with projection angle for measurements orthogonal to the incident ray.

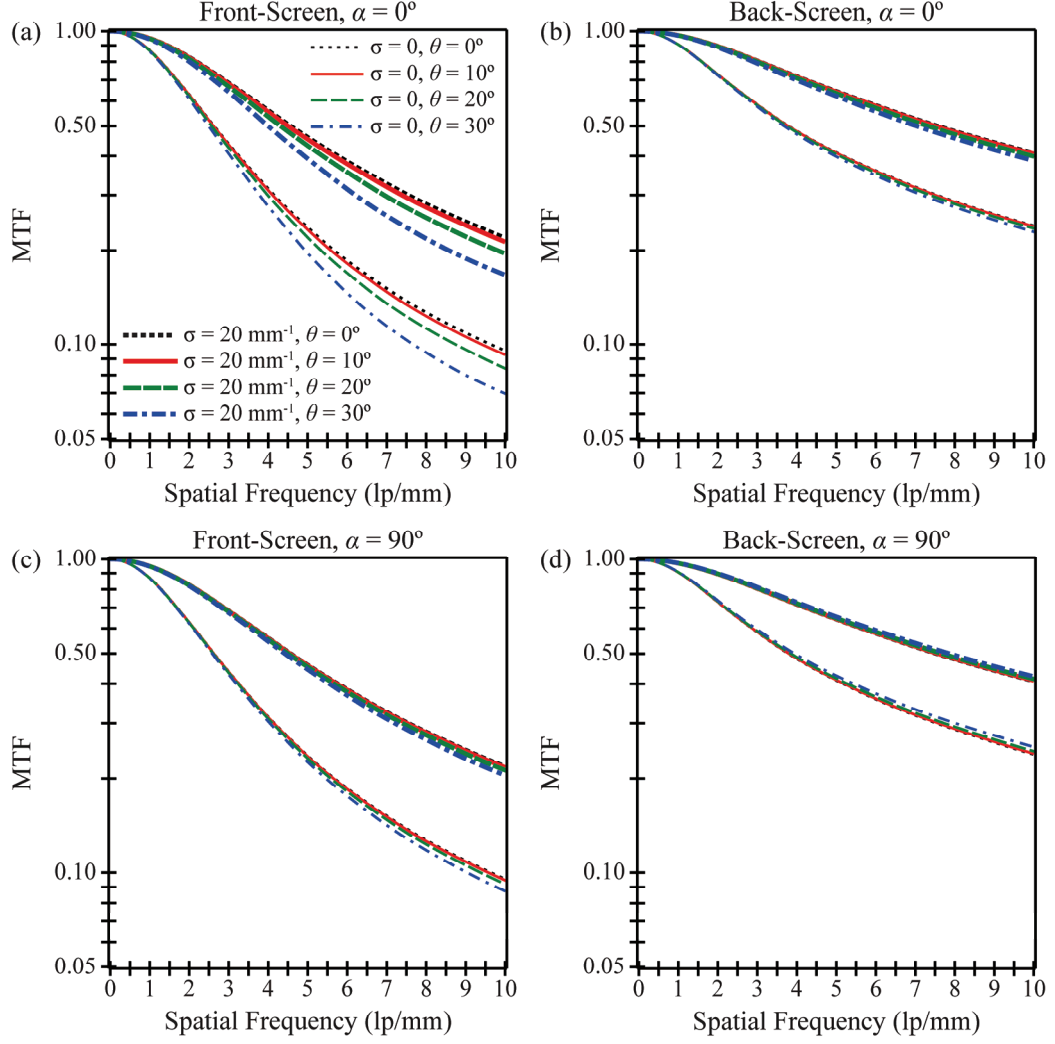


Figure 2.2: Modulation transfer function (MTF) at various incident angles. The modulation transfer function (MTF) of a porous $\text{Gd}_2\text{O}_2\text{S:Tb}$ phosphor is plotted versus frequency measured along 0° and 90° polar angles for multiple incident angles ($\theta = 0^\circ, 10^\circ, 20^\circ, 30^\circ$) and two optical absorption parameters ($\sigma = 0, 20 \text{ mm}^{-1}$). The scintillator possesses a reflective backing, a non-reflective photocathode, optical scatter at the diffusion limit, and quantum-limited noise. Also, the phosphor thickness is $100 \mu\text{m}$, and the incident x-ray energy is 20 keV . As shown, the front-screen configuration has considerably more angular dependence than the back-screen configuration.

In Figure 2.3, normalized NPS (NNPS) is plotted versus frequency for the same scintillator. Like MTF, NNPS increases with increasing optical absorption for all angles of incidence. Unlike MTF, NNPS is independent of the directionality of the frequency

vector. Over projection angles typical of DBT, the angular dependence of the NNPS is minimal. For example, comparing 30° incidence to normal incidence at 5.0 lp/mm in a front-screen configuration, NNPS decreases by 8% in a phosphor with no optical absorption and by 4% in a phosphor with high optical absorption. In a back-screen configuration, NNPS increases slightly by 5% and 2%, respectively.

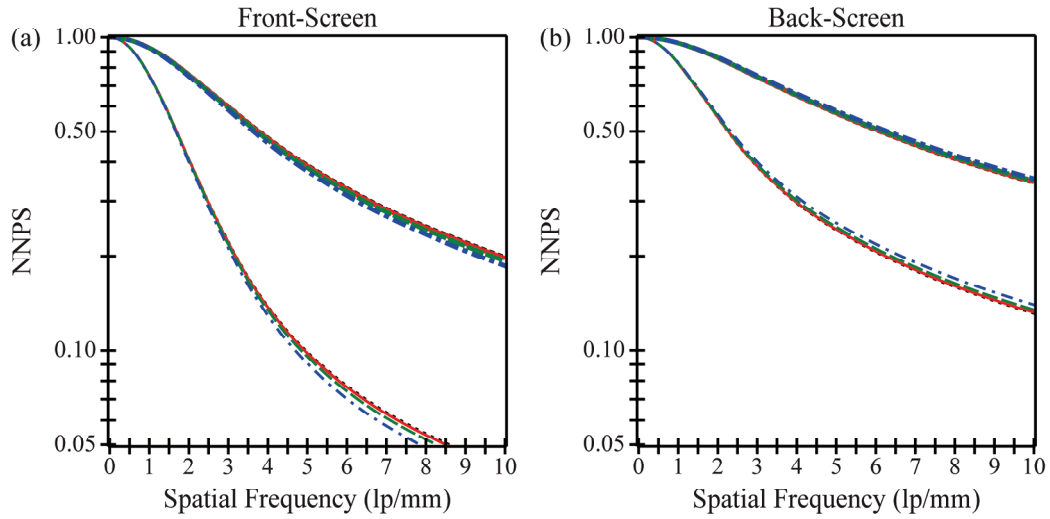


Figure 2.3: Normalized noise power spectra (NNPS) at various incident angles. Normalized noise power spectra (NNPS) is plotted versus frequency. NNPS is independent of the directionality of the frequency vector. While front-screen NNPS decreases with projection angle, back-screen NNPS increases slightly with projection angle. The plots implicitly share a legend with Figure 2.2.

Figure 2.4 shows DQE versus frequency. In both a front- and back-screen configuration, Figures 2.4(a) and 2.4(b) demonstrate that for measurements made along a 0° polar angle, DQE increases with projection angle at low frequencies and decreases with projection angle at high frequencies. At low frequencies, the angular dependence of the x-ray quantum detection efficiency (A_Q) is responsible for the DQE increase. In calculating A_Q using Eq. (2.26), the x-ray path length increases from the phosphor

thickness T with normal incidence to $T\sec\theta$ with oblique incidence; hence a greater number of x rays are converted to visible light. At high frequencies, the degradation in DQE with increasing projection angle arises from the combined angular dependencies of the OTF and NPS. The high frequency DQE for the front-screen configuration is lower than that of the back-screen configuration, and its degradation with projection angle is much more pronounced. For example, at 5.0 lp/mm in a front-screen irradiated at a 30° angle, the DQE decreases by 20% relative to normal incidence. In the back-screen configuration, the relative decrease in DQE is less than 5%.

In the direction orthogonal to the incident ray, DQE increases with projection angle over a very broad range of frequencies [Figures 2.4(c) and 2.4(d)]. Comparing 30° incidence with normal incidence at 5.0 lp/mm in a front-screen configuration, DQE increases by 6% in a phosphor with no optical absorption and by 4% in a phosphor with high optical absorption. Using a back-screen configuration, the relative increase in DQE is approximately twice as high.

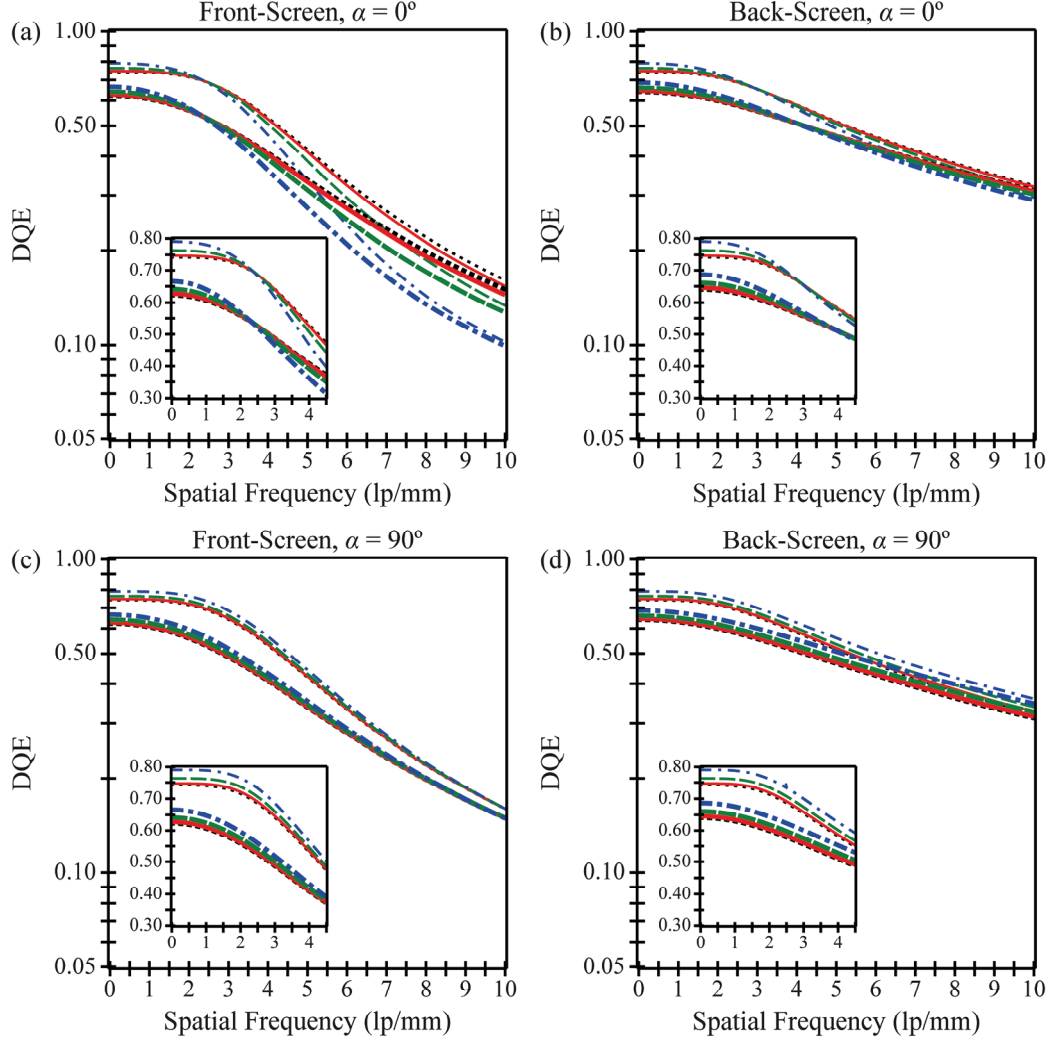


Figure 2.4: Detective quantum efficiency (DQE) at various incident angles. Detective quantum efficiency (DQE) is plotted versus frequency. Along a 0° polar angle, DQE increases with projection angle at low frequencies and only decreases with projection angle at high frequencies. The front-screen has much more angular dependence than the back-screen at very high frequencies. For measurements orthogonal to the incident ray (90° polar angle), DQE increases with projection angle over a very broad range of frequencies in both configurations. The plots implicitly share a legend with Figure 2.2.

In Figure 2.5, the angular dependence of the Swank factor (A_S) used for calculating the DQE is studied. Swank has shown that A_S provides a measure of the fluctuation in signal generated from each x-ray photon due to variability in the absorbed

energy of each interacting x ray and in the number of secondary carriers generated from each interacting x ray.²¹ Figure 2.5 demonstrates that in a phosphor with no optical absorption, the Swank factor is unity at all projection angles for either the front- or back-screen configuration. By contrast, in a phosphor with high optical absorption, the Swank factor has slight angular dependence over projection angles typical of DBT. For example, comparing 30° incidence to normal incidence, A_S increases by 0.3% in a front-screen configuration and by 0.5% in a back-screen configuration. At very oblique angles approaching shearing incidence ($\theta = 90^\circ$), the Swank factor increases sharply to unity.

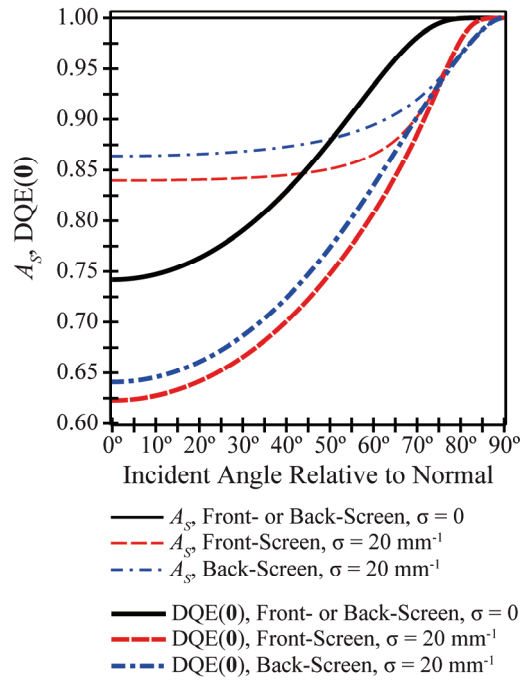


Figure 2.5: Variation in Swank factor and DQE(0) with incident angle. The Swank information factor (A_S) has no angular dependence in a phosphor lacking optical absorption and slight angular dependence over typical incident angles in a phosphor with high optical absorption. $DQE(0)$ has greater relative variation with incident angle. Both A_S and $DQE(0)$ increase sharply to unity at angles approaching shearing incidence ($\theta = 90^\circ$).

Unlike A_s , $DQE(\mathbf{0})$ is projection angle dependent for all possible optical absorption parameters. For both configurations, the relative increase in $DQE(\mathbf{0})$ comparing 30° incidence to normal incidence is 6% in a phosphor with no optical absorption and 7% in a phosphor with high optical absorption. The angular dependence of $DQE(\mathbf{0})$ is therefore more pronounced than the Swank factor.

3.2. Anisotropy of the Transfer Functions over the Detector Area

Because the focal spot of a DBT system emits x rays in all directions, the angle of incidence is spatially variant at each point on the detector. Assuming a stationary detector whose center-of-rotation (COR) coincides with the midpoint of the chest wall, the angle of incidence relative to the normal at each point (x, y) on the detector may be determined from the expression

$$\theta = \arctan \left[\frac{\sqrt{(x - h \sin \Delta)^2 + y^2}}{h \cos \Delta} \right], \quad (2.32)$$

where h is the source-to-COR distance and Δ is the nominal projection angle (*i.e.*, the angle of the x-ray tube arc relative to the normal at the COR). In deriving this result, the phosphor thickness (T) is taken to be negligible compared against the source-to-COR distance (h). Also, the chest wall defines the x axis of the detector and its midpoint the origin. For a $24 \text{ cm} \times 30 \text{ cm}$ field-of-view (FOV) and a source-to-COR distance of 70 cm, the angle θ is plotted versus the length (x) and the width (y) of the detector for the central projection ($\Delta = 0^\circ$) and an oblique projection ($\Delta = 20^\circ$) in Figure 2.6. In the central projection [Figure 2.6(a)], the angle of incidence relative to the normal varies

between 0° and 25° , and in the oblique projection [Figure 2.6(b)], it varies between 10° and 35° . For either case, the maximum angle is found at a corner of the FOV opposite the chest wall.

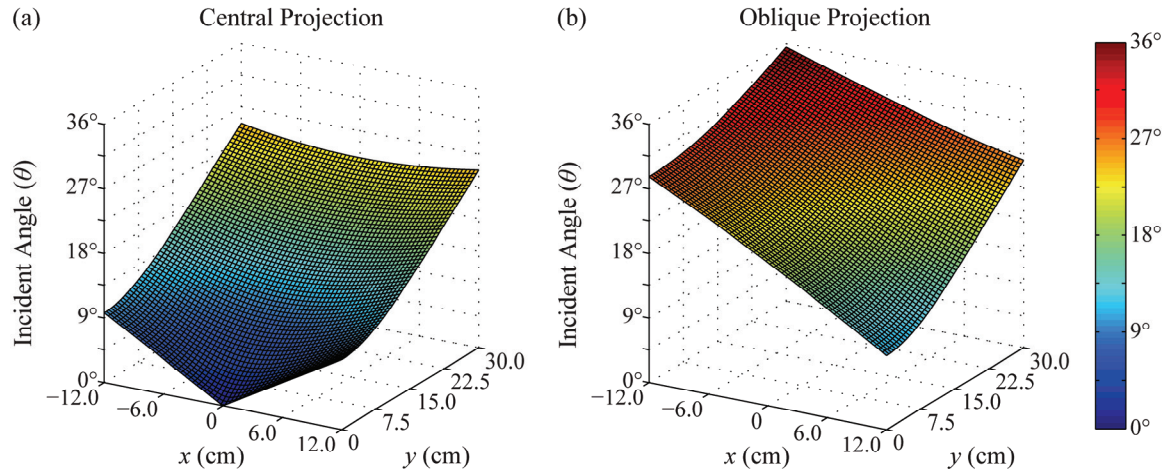


Figure 2.6: Variation in the incident angle over the detector area. The angle of incidence relative to the normal is plotted versus position along the detector for (a) the central projection and (b) an oblique projection. The DBT system has a source-to-COR distance of 70 cm, and the nominal projection angle in (b) is 20° .

Like the angle of incidence, the transfer functions of the phosphor are spatially variant across the detector area (Figure 2.7). To illustrate the spatial anisotropy of one of the transfer functions, a surface plot of front-screen DQE versus position along the detector is shown for the frequency 5.0 lp/mm in a phosphor with high optical absorption assuming a 0° polar angle for the frequency vector. In the central projection [Figure 2.7(a)], the front-screen DQE varies between 0.34 and 0.30 (12% decrease), and in the oblique projection [Figure 2.7(b)], it varies between 0.33 and 0.24 (27% decrease). Although not plotted in the figure, one can show that the back-screen DQE has much less variation over the detector area in either projection ($< 4\%$ decrease).

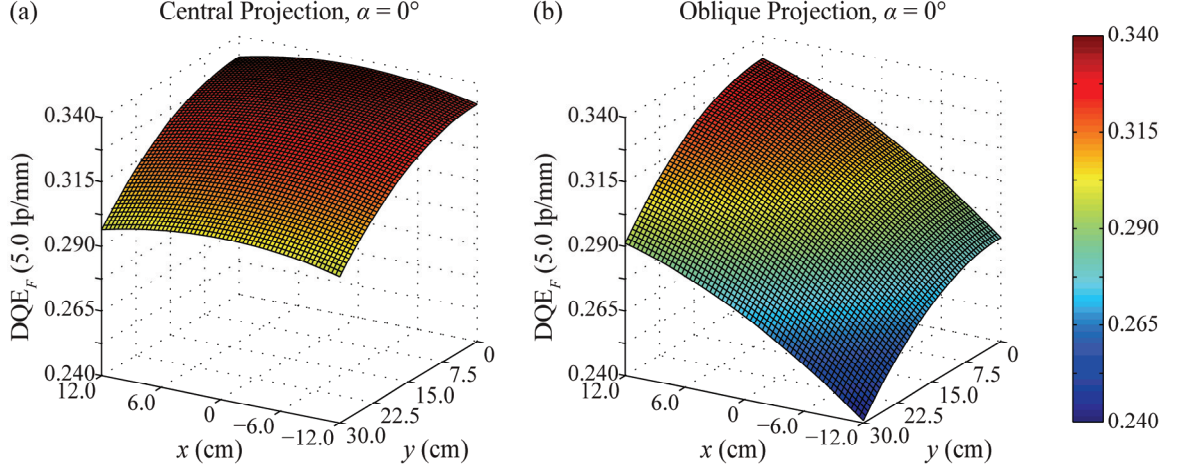


Figure 2.7: Variation in DQE over the detector area at a fixed frequency. The anisotropy of the transfer functions over the detector is illustrated by plotting the front-screen DQE at a fixed spatial frequency (5.0 lp/mm) versus areal position, assuming high optical absorption ($\sigma = 20 \text{ mm}^{-1}$) and frequency measurements along a 0° polar angle. The oblique projection has greater variation in DQE over the detector area than the central projection. The directionalities of the x and y axes are flipped relative to Figure 2.6 to improve visualization of the surfaces.

3.3. Optimization of Phosphor Thickness for Oblique Incidence

In addition to illustrating the impact of oblique incidence on the transfer functions of a phosphor, the analytical models developed in this work can be used as a platform for optimizing detector design over the range of projection angles used in DBT. One important element in the design of a phosphor is its x-ray quantum detection efficiency (QDE). In Figures 2.8-2.9, DQE at a fixed frequency is plotted versus QDE at normal incidence to investigate whether DQE can be maximized by varying QDE. Both figures have been generated using the same phosphor parameters analyzed in Figures 2.2-2.5, except the phosphor thickness T is now left as a variable which allows QDE at normal incidence to vary.

$$T = \frac{1}{\mu} \cdot \ln \left(\frac{1}{1 - A_{Q0}} \right) \quad (2.33)$$

In Eq. (2.33), A_{Q0} denotes the QDE at normal incidence.

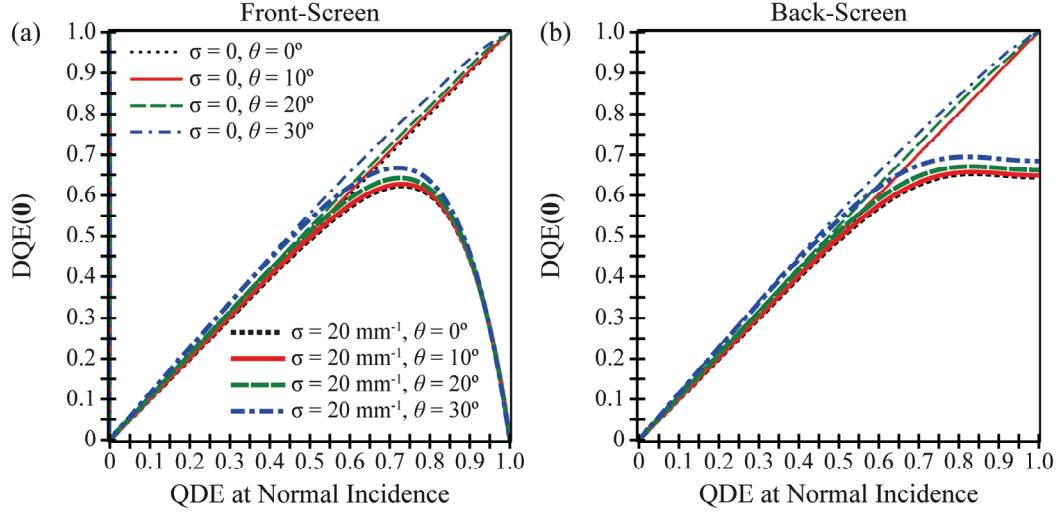


Figure 2.8: Effect of phosphor thickness on $DQE(0)$. For four angles of incidence and two optical absorption parameters, the dependency of $DQE(0)$ on QDE at normal incidence is analyzed. With no optical absorption, $DQE(0)$ for both front- and back-screen configurations is optimized by large QDE. With high optical absorption, the maximum $DQE(0)$ for the front-screen occurs at intermediate QDE, while relatively high $DQE(0)$ for the back-screen occurs over a broad range of large QDE. The optimal QDE for the front-screen is angularly dependent.

Figure 2.8 illustrates that in a front- or back-screen configuration with no optical absorption, $DQE(0)$ can be optimized by manufacturing a phosphor with a very large thickness (100% QDE). By contrast, in a phosphor with high optical absorption, the dependency of $DQE(0)$ on QDE is quite different for the two configurations. In a front-screen, $DQE(0)$ is maximized by an intermediate QDE which is projection angle dependent, favoring smaller thicknesses at larger angles. For example, in the 0° and 30°

projections, the optimal QDE at normal incidence are 0.73 and 0.72 corresponding to 97 μm and 94 μm thicknesses, respectively. By contrast, the back-screen $\text{DQE}(\mathbf{0})$ attains relatively high values over a broader range of QDE. With 100% QDE, $\text{DQE}(\mathbf{0})$ plateaus to 0.64 and 0.68 for the 0° and 30° projections, respectively.

In Figure 2.9, the dependency of DQE on QDE is analyzed at a higher frequency (5.0 lp/mm). The high frequency DQE for the front-screen is maximized at an intermediate QDE for both optical absorption parameters. For measurements made along the 0° polar angle in a front-screen with no optical absorption, the optimal QDE values at normal incidence are 0.60 for the 0° projection and 0.54 for the 30° projection, corresponding to 68 μm and 58 μm thicknesses, respectively [Figure 2.9(a)]. With high optical absorption, the respective QDE optima are 0.55 and 0.51 (59 μm and 52 μm thicknesses). In the direction orthogonal to the incident ray, the optimal QDE have less projection angle dependence [Figure 2.9(c)].

Unlike the front-screen configuration, the back-screen configuration supports relatively high DQE over large QDE values at 5.0 lp/mm. For measurements made along the 0° polar angle [Figure 2.9(b)], the back-screen DQE plateaus to 0.51 and 0.48 for the 0° and 30° projections, respectively, in a phosphor with no optical absorption (0.46 and 0.45 with high optical absorption). For measurements made along the orthogonal direction, the back-screen DQE attains a higher plateau; also, the asymptote actually increases slightly with projection angle [Figure 2.9(d)].

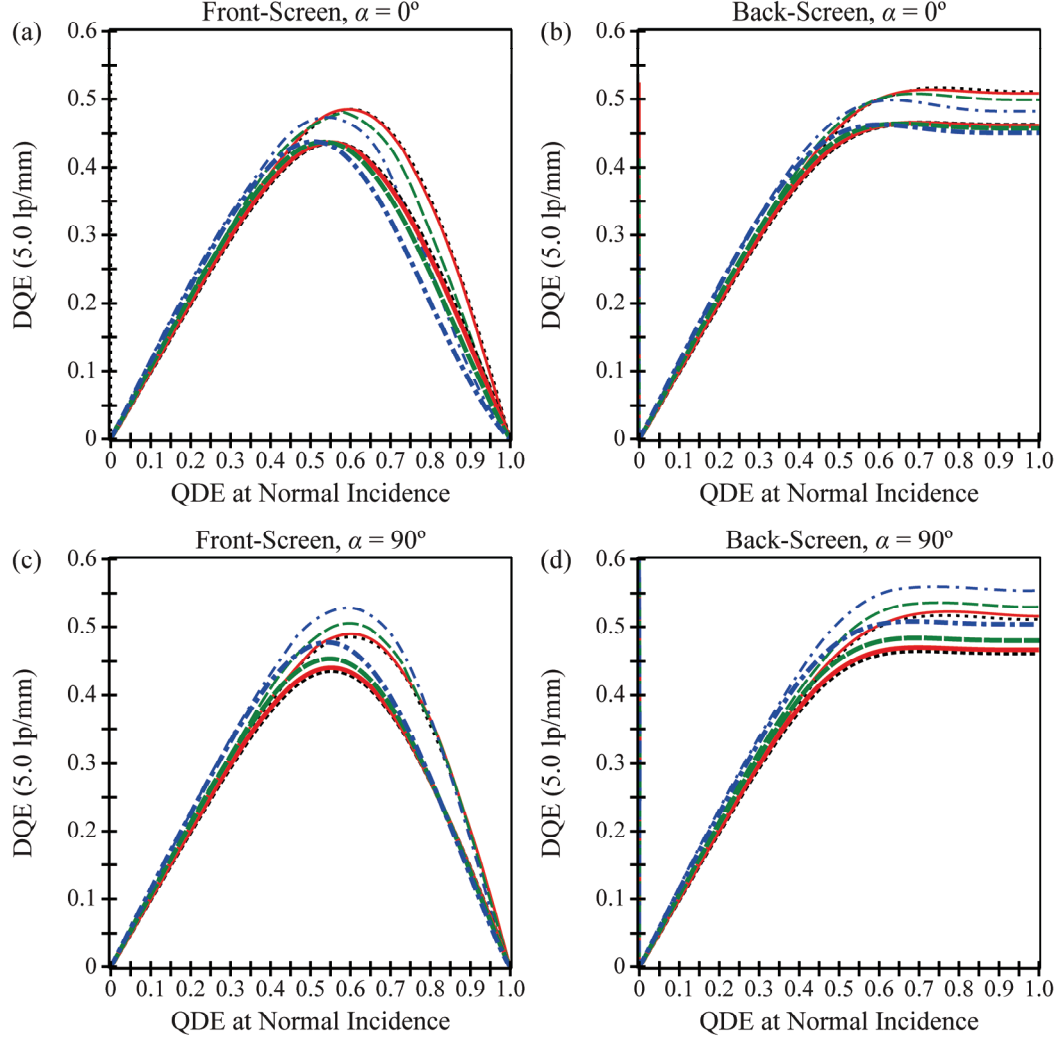


Figure 2.9: Effect of phosphor thickness on the high-frequency DQE. At 5.0 lp/mm, DQE is plotted versus QDE at normal incidence. In the front-screen configuration, DQE is optimized by an intermediate QDE. The optimal QDE is projection angle dependent, shifting to lower values (thinner phosphors) at larger angles. By contrast, in the back-screen configuration, relatively high DQE is supported over large QDE values for all projection angles. The plots implicitly share a legend with Figure 2.8.

To illustrate the dependence of DQE on both frequency and QDE, a surface plot is shown in Figure 2.10 assuming 30° incidence, high optical absorption, and frequency measurements along the 0° polar angle. The curvature of the front-screen surface demonstrates that the value of QDE which maximizes DQE decreases with frequency.

By contrast, the back-screen surface shows that DQE is not optimized by a single QDE value. Instead, at all frequencies, the back-screen supports relatively high DQE over very large QDE.

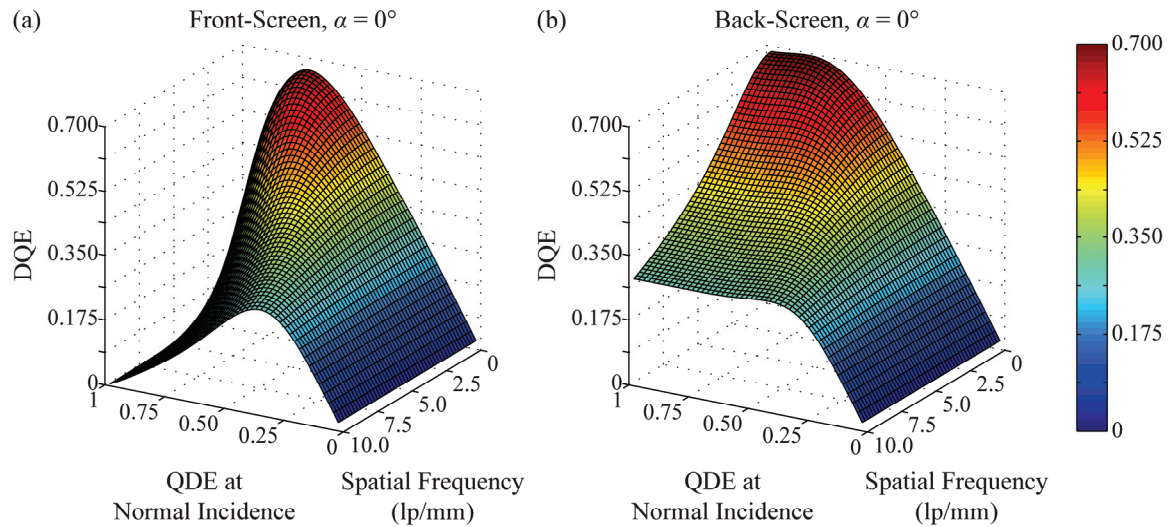


Figure 2.10: Optimization of phosphor thickness at various frequencies. A surface plot shows the dependence of DQE on both frequency and QDE at normal incidence, assuming $\theta = 30^\circ$, $\sigma = 20 \text{ mm}^{-1}$, and a 0° polar angle for the frequency vector. At all frequencies, the front-screen DQE is optimized by an intermediate QDE. By contrast, the back-screen DQE attains relatively high values over a broad range of large QDE (thick phosphors).

Figures 2.8-2.10 demonstrate that the optimal thickness of a front-screen is both projection angle dependent and frequency dependent. In Figure 2.11, the combined dependence is shown explicitly in a surface plot, assuming a 0° polar angle and high optical absorption. The graph was generated in MATLAB R2010b by discretizing a grid (60×60) of incident angles and frequencies from 0° to 45° and 0 lp/mm to 10 lp/mm, respectively. The optimal thickness which maximizes DQE was determined by the zero of the first partial derivative of DQE with respect to phosphor thickness. Because the

zeros of the first DQE derivative cannot be easily solved in closed form, Newton's method was implemented to find the zeros numerically

$$T_{n+1} = T_n - \frac{\partial D_F}{\partial T} \bigg|_{T=T_n} \cdot \left[\frac{\partial^2 D_F}{\partial T^2} \bigg|_{T=T_n} \right]^{-1}, \quad n \in \mathbb{N}, \quad (2.34)$$

where D_F is the symbolic abbreviation for front-screen DQE. For all projection angles and frequencies investigated in the plot, the initial guess (25 μm) and the number of iterations (9) provided convergence exceeding ten decimal places. Figure 2.11 demonstrates that the optimal phosphor thickness for the front-screen configuration is a decreasing function of both incident angle and frequency, ranging from 97 μm (0° incidence, 0 lp/mm) to 25 μm (45° incidence, 10 lp/mm).

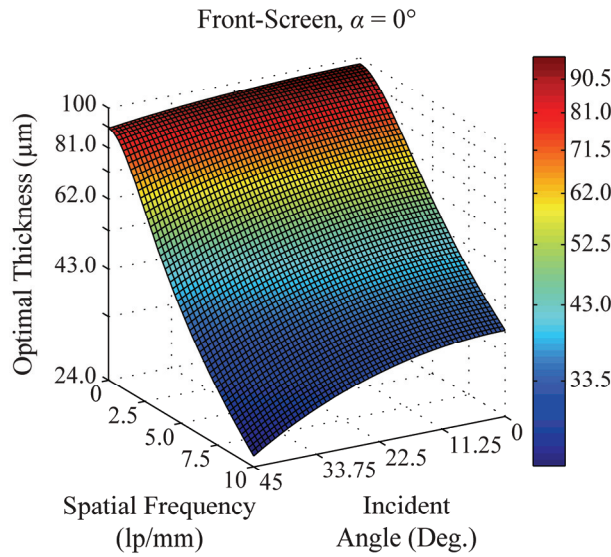


Figure 2.11: Generalization of the optimal phosphor thickness to various incident angles and frequencies. For a front-screen configuration, the dependence of the optimal phosphor thickness on both the angle of incidence and frequency is analyzed, assuming $\sigma = 20 \text{ mm}^{-1}$ and a 0° polar angle for the frequency vector.

4. COMPARISON WITH RESULTS IN THE LITERATURE

This chapter extends Swank's calculations⁹ of the transfer functions of turbid phosphors to oblique x-ray incidence. In the limiting case of normal incidence, the formulas presented in this chapter exactly reduce to Swank's results. Our work is unique in modeling the transfer functions for oblique incidence in closed form without making the assumption that the PSF of normal incidence is a delta function.¹ One benefit of this approach is unifying many prior results on oblique incidence under one model. For example, in a front-screen configuration, we demonstrate that oblique incidence degrades the MTF, and that the resultant loss in resolution becomes more pronounced with increasing frequency and increasing angle. Although these findings are derived for a turbid phosphor such as $\text{Gd}_2\text{O}_2\text{S:Tb}$, they are consistent with experimental data on CsI:Tl presented by Mainprize *et al.*⁸ as well as analytical modeling of *a*-Se proposed by Que and Rowlands.¹ On a similar note, we have observed that NPS is degraded with increasing projection angle, though to a lesser degree than MTF. This finding is concordant with the prior work of Hajdok and Cunningham,³ who performed Monte Carlo simulations of *a*-Se. As a final point, we have shown that DQE increases with incident angle at low frequencies but only decreases with incident angle at high frequencies. Consistent with the findings of Hajdok and Cunningham, the DQE degradation with projection angle at high frequencies is more pronounced than the MTF degradation, reflecting the dependency of DQE on the square of MTF.

In this work, it has been observed that the Swank factor is angularly dependent, but that its variation is small over projection angles typical of DBT. In particular, it has

been shown that the Swank factor changes by no more than 0.5% comparing 0° and 30° incidence. This observation is consistent with Monte Carlo simulations of CsI:Tl phosphors conducted by Badano *et al.*, who demonstrated that the variation in the Swank factor over projection angles typical of DBT is minimal.²² While the relative change in the Swank factor with projection angle is small, the relative increase in DQE(0) is more substantial, as it includes the effect of increasing x-ray quantum detection efficiency with increasing projection angle.

Although our work demonstrates consistency with other studies on oblique incidence, it is important to identify fundamental differences between the detectors addressed in the comparison. This work models a turbid phosphor in which visible light spreads by optical scatter. By contrast, prior studies on CsI:Tl^{8, 22} assume a structured phosphor in which needlelike crystals approximately 10 μm in diameter transmit the optical photons to the photocathode by total internal reflection, thereby minimizing the lateral spread of visible light.^{19, 23} At a given incident angle, structured phosphors should have higher MTF than turbid phosphors for this reason. Although the transfer functions of turbid phosphors are different from structured phosphors, this work demonstrates that their angular dependence follows comparable trends. On a similar note, our model has shown concordance with prior studies on oblique incidence in *a*-Se.^{1, 3} In *a*-Se, an absorbed x ray ionizes a Se atom, freeing an electron and a hole which migrate to different ends of the detector due to an applied electric field.¹⁹ In drift mode, the electric field is small enough so that the electron and hole do not have sufficient kinetic energy to ionize Se atoms and create an avalanche of electron-hole pairs. Because the electron and

hole migrate in a nearly perfect orthogonal path to opposite ends of the detector, the MTF of a -Se at normal incidence is approximately unity for all frequencies.² At higher incident angles, the MTF of a -Se decreases with frequency, but is expected to be superior to a turbid phosphor since there is no lateral spread of visible light. The analytical model of a -Se developed by Que and Rowlands¹ can effectively be derived by using Eq. (2.2) for the source function but by eliminating Eq. (2.1) for the diffusion of secondary carriers.

To our knowledge, this work is the first to investigate the angular dependence of the transfer functions of the back-screen configuration. The consistency of our back-screen model with expected trends at normal incidence helps to suggest its validity. For example, in accord with experimental data in turbid phosphors,²⁰ we demonstrate that the back-screen has higher MTF than the front-screen. Because optical photons are predominately generated near the x-ray entrance surface of the phosphor, visible light exhibits less lateral spread before reaching the photocathode if the back-screen configuration is used.

Consistent with prior authors, this chapter demonstrates that the Swank factor of the back-screen is greater than the front-screen. In experimental measurements on $\text{Gd}_2\text{O}_2\text{S:Tb}$ phosphors at 20 keV, Trauernicht and Van Metter demonstrated that a back-screen has approximately 5% higher Swank factor than a comparable front-screen.²⁴ Such a relative change in A_S with screen configuration matches the results presented in Figure 2.5. It is evident from Figure 2.5 that the benefits of the back-screen over the front-screen should hold with higher incident angles.

5. DISCUSSION

This chapter develops an analytical model of the transfer functions of turbid phosphors for oblique x-ray incidence. The results of the model are consistent with prior observations on oblique incidence in a range of detector types. Having an analytical model of the transfer functions has in turn led to the development of optimization strategies for improving detector design in DBT.

One area for optimizing detector design is the choice of a front- or back-screen configuration. Although it is well known that the back-screen has greater MTF than the front-screen at normal incidence, back-screen transfer functions have not yet been analyzed for oblique incidence. In this work, it is suggested that the back-screen transfer functions should have much less angular dependence than the front-screen, and consequently, exhibit less variation with position along the detector. As a result, a back-screen configuration may be chosen to optimize the design of a phosphor for oblique incidence. Initially, this result would seem to have no practical impact, since back-screens are not currently used clinically due to the glass substrate of the thin-film transistor (TFT) array for digital signal readout.²⁵⁻²⁷ If these detectors were operated as back-screens, the high attenuation of glass (~ 0.7 mm thick) would prevent a large percentage of x rays from reaching the phosphor itself,¹⁹ and hence both QDE and DQE would be compromised. Based on new research on flexible organic light-emitting diode (OLED) displays, however, TFT arrays may soon be manufactured on a plastic substrate.²⁸⁻³⁴ Because plastic is much less attenuating than glass, operating such a detector in a back-screen configuration would not be prohibitive. Detectors

manufactured with plastic have many benefits such as being bendable, light-weight, and easy to transport. These future phosphor-based detectors should preferentially be operated as back-screens in order to optimize detector performance for oblique incidence.

The analytical model of the transfer functions was ultimately used as a platform for optimizing the QDE of the detector for oblique incidence. This work provides a method for determining the QDE that maximizes DQE at any frequency of interest, such as the frequency of small microcalcifications or fine cancerous lesions within the breast. To our knowledge, this work is the first to show that the optimal QDE is projection angle dependent in a front-screen, tending toward lower values (thinner phosphors) with increasing projection angle. Because the incident angle is greatest at the periphery of the detector opposite the chest wall, a corollary of this finding is that one beneficial design feature would be to reduce thickness at the edges and corners of the phosphor. Although it is beyond the scope of this work to determine a single value for the optimum thickness at each point on a DBT detector, future work should be directed at modeling the transfer functions of the reconstruction³⁵ and optimizing thickness to maximize the 3D DQE for a fixed frequency of interest. In experimental practice, the optimal thickness should be calculated on a case-by-case basis for each detector under consideration, taking into account the unique characteristics of the imaging system.

In this chapter, it was demonstrated that the back-screen DQE is not optimized by a single QDE but instead attains reasonably high values over a broad range of phosphor thicknesses. Hence, the back-screen configuration has an important benefit over the front-screen configuration: future detectors with a plastic TFT substrate can be

manufactured with very large thickness without degradation in high frequency DQE at any projection angle.

A discussion of the limitations of this work and directions for future modeling are now noted. One assumption made in the Section 3 is that the incident x-ray beam is monoenergetic. Since the phosphor attenuation coefficient μ is energy-dependent, it is important to model polyenergetic x-ray spectra³⁶⁻³⁸ when studying the phosphor thickness which maximizes DQE in a front-screen (Figure 2.11). Future work should be aimed at determining if the angular dependence of the optimal thickness becomes more or less pronounced upon varying the kVp and the target-filter combination. Since Figure 2.11 was generated assuming a monoenergetic x-ray beam, the reader should take caution against directly applying the optimal thickness calculations to any real imaging system.

Although a relatively low energy (~ 20 keV) is conventionally chosen to maximize contrast between glandular tissue and cancer,⁴⁻⁶ it would be useful to simulate higher energies found in dual-energy contrast-enhanced DBT (DE CE-DBT).³⁹⁻⁴⁴ In DE CE-DBT, low and high energy images are acquired below and above the K edge of iodine (33.2 keV) after iodinated contrast is injected into the blood stream,^{45, 46} and contrast uptake is determined using weighted logarithmic subtraction. Contrast uptake can be used to quantify blood flow at the site of a tumor, which exceeds healthy tissue.⁴⁷

Another extension of this work would be to model detector pixelation due to the TFT array in which the phosphor is placed in optical contact.²⁵⁻²⁷ In this setting, the PSF is the convolution of the phosphor blurring function with the detector element sampling function.⁴⁸⁻⁵⁰ An additional subtlety that may be modeled is the blurring of the focal spot.

The MTF of the focal spot is degraded with increasing focal spot size,⁵¹ as well as with increasing focal spot motion during a continuous DBT scan.^{35, 52} Our model can also be refined by taking into account detector lag and ghosting.⁵³⁻⁵⁵ In addition, one can incorporate the possibility for an NPS that is not quantum-limited but possesses outside noise sources.¹³

A final point of investigation would be to extend this work to a structured phosphor, such as CsI:Tl. In structured phosphors, needlelike crystals transmit the optical photons to the photocathode by total internal reflection to minimize the lateral spread of visible light. Structured phosphors have superior spatial resolution to non-structured phosphors for this reason.^{19, 23} To model a structured phosphor, the boundary conditions for the secondary carrier currents would no longer be determined exclusively by the reflectivities of the backing and the photocathode. Instead, boundary conditions would also exist for the reflectivities of the walls of the needlelike crystals. Recently, Freed *et al.* have proposed an analytical model^{56, 57} of the PSF of CsI:Tl using a competing approach; their model was later generalized to direct-converting detectors.⁵⁸ A key step in the derivation of their PSF formula is considering three different functional forms (Gaussian, exponential, Lorentzian) to quantify the spread of secondary carriers or electron-hole pairs at each depth of the detector material. Empirically, the authors find that the Lorentzian provides the best match to data generated from Monte Carlo simulations. The authors then determine optimal values for the parameters in their model by minimizing the normalized differences between the analytical technique and Monte Carlo simulations. Although useful in providing a closed form solution for the PSF, their

model is limited in not being derived from first principles. By contrast, in our current work, all results are derived from first principles, and the value of each parameter has physical significance. It would be intriguing to determine whether this chapter could be generalized to model the boundary conditions of a structured phosphor and have agreement with Freed *et al.*

6. CONCLUSION

This work develops analytical models of OTF, NPS, and DQE for a turbid phosphor irradiated obliquely. Our analysis differs from much of the previous work on oblique incidence in that closed form solutions are obtained from first principles, thereby providing greater insight into the underlying detector physics.

Ultimately, the model provides a platform for optimizing the design of DBT detectors. For example, in a conventional front-screen configuration, the model is a useful tool for optimizing phosphor thickness at various angles of incidence. Because the incident angle is spatially variant across the detector area, the potential merit of designing a phosphor with reduced thickness near its periphery has been proposed.

This work demonstrates that the transfer functions of the back-screen have less angular dependence than the front-screen, and that high DQE is supported over a broader range of thicknesses for all incident angles. As a result, future DBT detectors manufactured on a plastic substrate instead of glass should preferentially be operated in the back-screen configuration.

7. REFERENCES

- ¹Que W, Rowlands JA. X-ray imaging using amorphous selenium: Inherent spatial resolution. *Medical Physics*. 1995;22(4):365-74.
- ²Lee DL, Cheung LK, Rodricks B, Powell GF. Improved imaging performance of a 14 x 17-inch Direct Radiography (TM) System using Se/TFT detector. *SPIE Conference on Physics of Medical Imaging*; 1998: SPIE; 1998. p. 14-23.
- ³Hajdok G, Cunningham IA. Penalty on the detective quantum efficiency from off-axis incident x rays. In: Yaffe MJ, Flynn MJ, editors. *Medical Imaging 2004: Physics of Medical Imaging*; 2004; San Diego: SPIE; 2004. p. 109-18.
- ⁴Johns PC, Yaffe MJ. X-ray Characterization of normal and neoplastic breast tissues. *Physics in Medicine and Biology*. 1987;32(6):675-95.
- ⁵Yaffe MJ. Chapter 5: Digital Mammography. In: Beutel J, Kundel HL, Metter RLV, editors. *Handbook of Medical Imaging Volume 1 Physics and Psychophysics*. Bellingham, WA: SPIE Press; 2000. p. 329-72.
- ⁶Bushberg JT, Seibert JA, Edwin M. Leidholdt J, Boone JM. Chapter 8: Mammography. In: John J-R, Snyder A, DeGeorge T, editors. *The Essential Physics of Medical Imaging*. 2 ed. Philadelphia, PA: Lippincott Williams and Wilkins; 2002. p. 191-229.
- ⁷Rafferty EA. Tomosynthesis: New Weapon in Breast Cancer Fight. *Decisions in Imaging Economics*. 2004 April 2004;17(4).
- ⁸Mainprize JG, Bloomquist AK, Kempston MP, Yaffe MJ. Resolution at oblique incidence angles of a flat panel imager for breast tomosynthesis. *Medical Physics*. 2006;33(9):3159-64.
- ⁹Swank RK. Calculation of Modulation Transfer Functions of X-Ray Fluorescent Screens. *Appl Opt*. 1973;12(8):1865-70.
- ¹⁰Acciavatti RJ, Maidment ADA. Calculation of OTF, NPS, and DQE for Oblique X-Ray Incidence on Turbid Granular Phosphors. In: Marti J, editor. *IWDM 2010*; 2010 16-18 June 2010; Girona, Spain: Springer-Verlag; 2010. p. 436-43.
- ¹¹Marshak RE, Brooks H, Hurwitz Jr. H. Introduction to the Theory of Diffusion and Slowing Down of Neutrons - I. *Nucleonics*. 1949;4:10-22.
- ¹²Nishikawa RM, Yaffe MJ. Model of the spatial-frequency-dependent detective quantum efficiency of phosphor screens. *Medical Physics*. 1990;17(5):894-904.
- ¹³Nishikawa RM, Yaffe MJ. Effect of various noise sources on the detective quantum efficiency of phosphor screens. *Medical Physics*. 1990;17(5):887-93.
- ¹⁴Lea SM. Chapter 6: Generalized Functions in Physics. *Mathematics for Physicists*. Belmont, CA: Brooks/Cole - Thomson Learning; 2004. p. 287-322.
- ¹⁵Barrett HH, Myers KJ. Chapter 4: Series Expansions and Integral Transforms. In: Saleh BEA, editor. *Foundations of Image Science*. New York, NY: John Wiley & Sons; 2004. p. 175-214.
- ¹⁶Lea SM. Chapter 5: Laplace Transforms. *Mathematics for Physicists*. Belmont, CA: Brooks/Cole - Thomson Learning; 2004. p. 251-86.
- ¹⁷Dainty JC, Shaw R. Chapter 6: Fourier Transforms, and the Analysis of Image Resolution and Noise. *Image Science*. London, England: Academic Press; 1974. p. 190-231.

- ¹⁸Berger MJ, Hubbell JH, Seltzer SM, Chang J, Coursey JS, Sukumar R, et al. XCOM: Photon Cross Section Database. [cited 2010 December 30]; Available from: <http://physics.nist.gov/xcom>
- ¹⁹Rowlands JA, Yorkston J. Chapter 4: Flat Panel Detectors for Digital Radiography. In: Beutel J, Kundel HL, Van Metter RL, editors. Handbook of Medical Imaging Volume 1 Physics and Psychophysics. Bellingham, WA: SPIE - The International Society for Optical Engineering; 2000. p. 223-328.
- ²⁰Kandarakis I, Cavouras D, Kanellopoulos E, Nomicos CD, Panayiotakis GS. Image Quality Evaluation of YVO₄:Eu Phosphor Screens for Use in X-Ray Medical Imaging Detectors. Radiation Measurements. 1998;29(5):481-6.
- ²¹Swank RK. Absorption and noise in x-ray phosphors. J Appl Phys. 1973;44(9):4199-203.
- ²²Badano A, Kyprianou IS, Sempau J. Anisotropic imaging performance in indirect x-ray imaging detectors. Medical Physics. 2006;33(8):2698-713.
- ²³Samei E. Image quality in two phosphor-based flat panel digital radiographic detectors. Medical Physics. 2003;30(7):1747-57.
- ²⁴Trauernicht DP, Metter RV. Conversion noise measurement for front and back x-ray intensifying screens. SPIE. 1990;1231:262-70.
- ²⁵Jing T, Goodman CA, Drewery J, Cho G, Hong WS, Lee H, et al. Amorphous silicon pixel layers with cesium iodide converters for medical radiography. IEEE Trans Nucl Sci. 1994;41(4):903-9.
- ²⁶Cowen AR, Kengyelics SM, Davies AG. Solid-state, flat-panel, digital radiography detectors and their physical imaging characteristics. Clin Radiol. 2008;63:487-98.
- ²⁷Nagarkar VV, Gupta TK, Miller SR, Klugerman Y, Squillante MR, Entine G. Structured CsI(Tl) scintillators for x-ray imaging applications. IEEE Trans Nucl Sci. 1998;45(3):492-6.
- ²⁸He Y, Kanicki J. High-efficiency organic polymer light-emitting heterostructure devices on flexible plastic substrates. Applied Physics Letters. 2000;76(6):661-3.
- ²⁹Weaver MS, Michalski LA, Rajan K, Rothman MA, Silvernail JA, Brown JJ, et al. Organic light-emitting devices with extended operating lifetimes on plastic substrates. Applied Physics Letters. 2002;81(16):2929-31.
- ³⁰Sarma KR, Chanley C, Dodd S, Roush J, Schmidt J, Srdanov G, et al. Active Matrix OLED Using 150C a-Si TFT Backplane Built on Flexible Plastic Substrate. In: Hopper D, editor. SPIE; 2003; Orlando, FL; 2003. p. 180-91.
- ³¹Sugimoto A, Ochi H, Fujimura S, Yoshida A, Miyadera T, Tsuchida M. Flexible OLED Displays Using Plastic Substrates. IEEE Journal of Selected Topics in Quantum Electronics. 2004;10(1):107-14.
- ³²Forrest SR. The path to ubiquitous and low-cost organic electronic appliances on plastic. Nature. 2004;428:911-8.
- ³³Nathan A, Kumar A, Sakariya K, Servati P, Sambandan S, Striakhilev D. Amorphous Silicon Thin Film Transistor Circuit Integration for Organic LED Displays on Glass and Plastic. IEEE Journal of Solid-State Circuits. 2004;39(9):1477-86.

- ³⁴Tsukagoshi K, Tanabe J, Yagi I, Shigeto K, Yanagisawa K, Aoyagi Y. Organic light-emitting diode driven by organic thin film transistor on plastic substrates. *Journal of Applied Physics*. 2006;99(6):064506-1-5.
- ³⁵Zhao B, Zhao W. Three-dimensional linear system analysis for breast tomosynthesis. *Medical Physics*. 2008;35(12):5219-32.
- ³⁶Tucker DM, Barnes GT, Chakraborty DP. Semiempirical model for generating tungsten target x-ray spectra. *Medical Physics*. 1991;18(2):211-8.
- ³⁷Boone JM, Fewell TR, Jennings RJ. Molybdenum, rhodium, and tungsten anode spectral models using interpolating polynomials with application to mammography. *Medical Physics*. 1997;24(12):1863-74.
- ³⁸Blough MM, Waggener RG, Payne WH, Terry JA. Calculated mammographic spectra confirmed with attenuation curves for molybdenum, rhodium, and tungsten targets. *Medical Physics*. 1998;25(9):1605-12.
- ³⁹Carton A-K, Li J, Chen SC, Conant EF, Maidment ADA. Optimization of Contrast-Enhanced Digital Breast Tomosynthesis Lecture Notes in Computer Science. 2006;4046:183-9.
- ⁴⁰Chen SC, Carton AK, Albert M, Conant EF, Schnall MD, Maidment ADA. Initial clinical experience with contrast-enhanced digital breast tomosynthesis. *Academic Radiology*. 2007;14(2):229-38.
- ⁴¹Carton AK, Lindman K, Ullberg C, Francke T, Maidment ADA. Dual-Energy Subtraction for Contrast-Enhanced Digital Breast Tomosynthesis. In: Hsieh J, Flynn MJ, editors. *Medical Imaging 2007: Physics of Medical Imaging*; 2007; San Diego, CA: SPIE; 2007. p. 1-12.
- ⁴²Puong S, Patoureaux F, Iordache R, Bouchevreau X, Muller S. Dual-energy contrast enhanced digital breast tomosynthesis: concept, method and evaluation on phantoms. In: Hsieh J, Flynn MJ, editors. *Medical Imaging 2007: Physics of Medical Imaging*; 2007; San Diego, CA: SPIE; 2007. p. 1-12.
- ⁴³Puong S, Bouchevreau X, Duchateau N, Iordache R, Muller S. Optimization of beam parameters and iodine quantification in Dual-Energy Contrast Enhanced Digital Breast Tomosynthesis. In: Hsieh J, Samei E, editors. *Medical Imaging 2008: Physics of Medical Imaging*; 2008; San Diego, CA: SPIE; 2008. p. 1-11.
- ⁴⁴Carton AK, Gavenonis SC, Currivan JA, Conant EF, Schnall MD, Maidment ADA. Dual-energy contrast-enhanced digital breast tomosynthesis - a feasibility study. *British Journal of Radiology*. 2010;83:344-50.
- ⁴⁵Carton A-K, Ullberg C, Lindman K, Acciavatti R, Francke T, Maidment ADA. Optimization of a dual-energy contrast-enhanced technique for a photon-counting digital breast tomosynthesis system: I. A theoretical model. *Medical Physics*. 2010;37(11):5896-907.
- ⁴⁶Carton A-K, Ullberg C, Maidment ADA. Optimization of a dual-energy contrast-enhanced technique for a photon-counting digital breast tomosynthesis system: II. An experimental validation. *Medical Physics*. 2010;37(11):5908-13.
- ⁴⁷Weidner N, Semple JP, Welch WR, Folkman J. Tumor Angiogenesis and Metastasis - Correlation in Invasive Breast Carcinoma. *New England Journal of Medicine*. 1991;324:1-8.

- ⁴⁸Albert M, Maidment ADA. Linear response theory for detectors consisting of discrete arrays. *Medical Physics*. 2000;27(10):2417-34.
- ⁴⁹Acciavatti RJ, Maidment ADA. An Analytical Model of NPS and DQE Comparing Photon Counting and Energy Integrating Detectors. In: Samei E, Pelc NJ, editors. *Physics of Medical Imaging*; 2010; San Diego, CA: SPIE; 2010. p. 1-12.
- ⁵⁰Acciavatti RJ, Maidment ADA. A Comparative Analysis of OTF, NPS, and DQE in Energy Integrating and Photon Counting Digital X-ray Detectors. *Medical Physics*. 2010;37(12):6480-95.
- ⁵¹Johns HE, Cunningham JR. Chapter 16: Diagnostic Radiology. *The Physics of Radiology*. 4th ed. Springfield, IL: Charles C Thomas; 1983. p. 557-669.
- ⁵²Ren B, Ruth C, Stein J, Smith A, Shaw I, Jing Z. Design and performance of the prototype full field breast tomosynthesis system with selenium based flat panel detector. In: Flynn MJ, editor. *SPIE*; 2005; San Diego, CA: (SPIE, Bellingham, WA, 2005); 2005. p. 550-61.
- ⁵³Bloomquist AK, Yaffe MJ, Mawdsley GE, Hunter DM. Lag and ghosting in a clinical flat-panel selenium digital mammography system. *Medical Physics*. 2006;33(8):2998-3005.
- ⁵⁴Siewerdsen JH, Jaffray DA. A ghost story: Spatio-temporal response characteristics of an indirect-detection flat-panel imager. *Medical Physics*. 1999;26(8):1624-41.
- ⁵⁵Zhao W, DeCrescenzo G, Kasap SO, Rowlands JA. Ghosting caused by bulk charge trapping in direct conversion flat-panel detectors using amorphous selenium. *Medical Physics*. 2005;32(2):488-500.
- ⁵⁶Freed M, Park S, Badano A. A fast, angle-independent, analytical model of CsI detector response for optimization of 3D x-ray breast imaging systems. *Medical Physics*. 2010;37(6):2593-605.
- ⁵⁷Freed M, Park S, Badano A. Erratum: "A fast, angle-dependent, analytical model of CsI detector response for optimization of 3D x-ray breast imaging systems" [*Med. Phys.* 37, 2593-2605 (2010)]. *Medical Physics*. 2011;38(4):2307.
- ⁵⁸Badano A, Freed M, Fang Y. Oblique incidence effects in direct x-ray detectors: A first-order approximation using a physics-based analytical model. *Medical Physics*. 2011;38(4):2095-8.

GLOSSARY OF TERMS:

Chapter 2

LIST OF SYMBOLS

Symbol	Meaning
∂	Partial derivative operator.
∇^2	Laplacian operator.
\in	Set membership.
\mathcal{L}	Laplace transform operator.
\mathbb{N}	Set of natural numbers.
α	Polar angle of the 2D spatial frequency vector \mathbf{v} .
β	A term defined by Eq. (2.21) to simplify intermediate calculations.
γ_{\pm}	A term defined by Eq. (2.22) to simplify intermediate calculations.
Δ	Nominal projection angle.
δ	Delta function.
θ	Angle of x-ray incidence relative to the normal to the detector.
μ	X-ray linear attenuation coefficient of the phosphor.
\mathbf{v}	Spatial frequency vector with components v_x and v_y .
ρ_j	A quantity defined by Eq. (2.13) that is related to surface reflectivity. The subscripts $j = 0, 1$ correspond to the phosphor backing and photocathode, respectively.
σ	Reciprocal of the mean diffusion length of optical photons.
τ	Inverse relaxation length (the diffusion limit occurs with $\tau \rightarrow \infty$).
$\phi(\mathbf{r})$	Product of photon density and the diffusion constant.
$\psi_{\mathbf{k}}(z)$	Fourier transform of $\phi(\mathbf{r})$ in a plane of constant z .

A_Q	X-ray quantum detection efficiency.
A_{Q0}	X-ray quantum detection efficiency at normal incidence.
A_S	Swank information factor.
B	Back-screen configuration (often used as a subscript).
C_1, C_2	Constants of integration used in intermediate calculations.
CE	Contrast-enhanced.
COR	Center-of-rotation of x-ray tube, corresponding to the midpoint of the chest wall side of the detector.
D	Symbolic abbreviation for detective quantum efficiency.
DBT	Digital breast tomosynthesis.
DE	Dual energy.
DM	Digital mammography.
DQE	Detective quantum efficiency.
F	Front-screen configuration (often used as a subscript).
FOV	Field-of-view.
$G(\mathbf{v})$	Optical transfer function found by summing the contributions of each depth z_0 of the phosphor.
$G(\mathbf{v}, z_0)$	Optical transfer function associated with the depth $0 \leq z_0 \leq T$ of the phosphor.
h	Source-to-COR distance for rotating x-ray tube.
i	Imaginary unit given as $\sqrt{-1}$.
$j(z)$	Photon current across plane of constant z .
\mathbf{k}	A quantity equivalent to $2\pi\mathbf{v}$.

MTF	Modulation Transfer Function.
n	Iteration number for Newton's Method.
NPS	Noise power spectra.
$N(z_0)$	Relative x-ray signal at the depth z_0 of the phosphor.
OLED	Organic light-emitting diode.
OTF	Optical transfer function.
p	Independent variable of the Laplace transform of a function.
PSF	Point spread function.
q	A quantity defined in Eq. (2.6) to simplify intermediate calculations.
QDE	Quantum detection efficiency.
r_j	Reflectivity of a surface, where $j = 0, 1$ correspond to the phosphor backing and photocathode, respectively.
$R_C(\mathbf{v})$	Lubberts fraction.
$R_N(\mathbf{v})$	Ratio of the quantum noise power to the total noise power.
$S(\mathbf{r})$	Source function, modeled as point-like.
T	Phosphor thickness.
TFT	Thin-film transistor.
$W(\mathbf{v})$	Noise power spectra.
x	Position along the chest wall side of the detector.
y	Position perpendicular to the chest wall side of the detector.
z_0	Depth within a phosphor (with or without the subscript).

CHAPTER 3

Observation of Super-Resolution in Digital Breast Tomosynthesis

This chapter is based on a peer-reviewed article published in Medical Physics **39**(12), 7518-39 (2012).

1. INTRODUCTION

Digital breast tomosynthesis (DBT) is a 3D imaging modality in which low dose x-ray projections are acquired over a limited angular range about the breast. Using digital image reconstruction techniques, tomographic sections at all depths of the breast volume are subsequently generated. Unlike 2D digital mammography (DM), DBT can filter out overlapping anatomical structures which may hide a tumor. Preliminary studies indicate that DBT has greater sensitivity and specificity for cancer detection relative to DM.^{1,2}

In conventional practice, the reconstructed slices are generated on planes parallel to the breast support. In order to have the same in-plane resolution in the reconstruction as the detector, the pixel size in each reconstructed slice should match that of the detector elements. Using this approach, the highest frequency that can be resolved in the plane of reconstruction is the alias frequency of the detector. This chapter considers the possibility for reconstruction grids with much smaller pixelation so that higher frequencies can be visualized. Because non-normal x-ray incidence causes the image of an object to be translated in sub-pixel detector element increments with each increasing projection angle, it is demonstrated in this work that DBT is capable of super-resolution (*i.e.*, sub-pixel resolution).

Super-resolution has been well-described in a number of applications involving reconstruction from projections,³ including forensics, satellite imaging, computed tomography (CT), and magnetic resonance imaging (MRI); however, to our knowledge, its potential in DBT has not yet been demonstrated. An understanding of super-

resolution and an analysis of how to optimize its presence may prove to be useful for designing the highest quality DBT systems. Although it is possible to improve spatial resolution simply by reducing the pixel size of the detector, there are practical lower limits on the sizes that can be manufactured. In addition, one drawback of reducing the pixel size is decreasing the mean number of photons incident on each detector element and hence decreasing the signal-to-noise ratio (SNR) per pixel according to Poisson statistics⁴ for x-ray distributions. Clinically, super-resolution should be beneficial to diagnostic radiologists by improving the visibility of microcalcifications and other subtle signs of breast cancer with no increased radiation dose to the patient.

In this chapter, a theoretical framework for investigating super-resolution in DBT is developed by calculating the reconstruction of a sine input whose frequency is greater than the alias frequency of the detector. For optimal visualization of high frequencies in the 3D image, an infinitesimally fine (*i.e.*, non-pixelated) reconstruction grid is considered. The reconstruction techniques include both simple backprojection (SBP) and filtered backprojection (FBP). In order to investigate the experimental feasibility of super-resolution using a commercial DBT system, images of a bar pattern phantom with frequencies higher than the alias frequency of the detector were acquired and subsequently reconstructed.

2. METHODS

2.1. Input Object and Acquisition Geometry

An analytical framework for investigating the potential for super-resolution in DBT is now developed by calculating the reconstruction of a high frequency sinusoidal input. Accordingly, suppose that a rectangular prism with infinite extent in the x and y directions has a linear attenuation coefficient $\mu(x, y, z)$ which varies sinusoidally along the x direction with frequency f_0 . Throughout the remainder of this manuscript, the input object will be termed a “*sine plate*”. With the xz plane defining the chest wall, the frequency vector is therefore oriented parallel to the chest wall side of the breast support. Figure 3.1 illustrates a cross section of the sine plate in the xz plane. As shown, the rectangular prism is positioned between $z = z_0 + \varepsilon/2$ and $z = z_0 - \varepsilon/2$, where z_0 is the central height of the prism and ε is the prism’s thickness. Defining the origin O as the midpoint of the chest wall side of the detector, the attenuation coefficient may be written as

$$\mu(x, y, z) = C \cdot \cos[2\pi f_0(x - x_0)] \cdot \text{rect}\left(\frac{z - z_0}{\varepsilon}\right), \quad (3.1)$$

where C is a constant denoting the amplitude of the waveform, x_0 is a translational shift in the waveform relative to the origin, and the rect function is defined by the expression

$$\text{rect}(u) \equiv \begin{cases} 1 & , |u| \leq 1/2 \\ 0 & , |u| > 1/2 \end{cases}. \quad (3.2)$$

By setting the amplitude C to $1/\varepsilon$, $\mu(x, y, z)$ may be normalized⁵ so that the total attenuation found by integrating along the z direction is simply $\cos[2\pi f_0(x - x_0)]$ for all ε .

Provided that $|z - z_0| \leq \varepsilon$, the 1D Fourier transform (\mathcal{F}_1) of Eq. (3.1) along the x direction peaks at the frequencies $f_x = \pm f_0$, and vanishes at all other frequencies.⁶

$$\mathcal{F}_1\mu(f_x, y, z) = \int_{-\infty}^{\infty} \mu(x, y, z) \cdot e^{-2\pi i f_x x} dx \quad (3.3)$$

$$= \frac{C}{2} \left[e^{-2\pi i f_0 x_0} \delta(f_x - f_0) + e^{2\pi i f_0 x_0} \delta(f_x + f_0) \right] \cdot \text{rect}\left(\frac{z - z_0}{\varepsilon}\right) \quad (3.4)$$

Typically, only the positive frequency $f_x = +f_0$ is of interest in a physical measurement. Thus, although it is non-physical for an attenuation coefficient to vary between negative and positive values, formulating $\mu(x, y, z)$ by Eq. (3.1) is helpful for a thought experiment in interrogating the reconstruction of a single input frequency. An analysis of the case for which the input frequency is oriented along the y direction (*i.e.*, perpendicular to the chest wall) is considered separately in the appendix (Section 7).

The most general DBT acquisition geometry with a divergent x-ray beam and a rotating detector is now modeled. In acquiring the n^{th} projection, the focal spot emits x rays at the nominal projection angle ψ_n relative to the center-of-rotation (COR) of the DBT system. The COR and the focal spot lie in the plane of the chest wall. In addition, the detector rotates about the y axis at the angle γ_n relative to the x direction. The two parameters ψ_n and γ_n are determined from the nominal angular spacing $\Delta\psi$ and the detector gear ratio g by the relations

$$\psi_n = n \cdot \Delta\psi \quad (3.5)$$

$$\gamma_n = \frac{\psi_n}{g}. \quad (3.6)$$

For an odd number of N total projections, the index n varies between $-(N - 1)/2$ and $(N - 1)/2$, and the special case $n = 0$ defines the central projection.

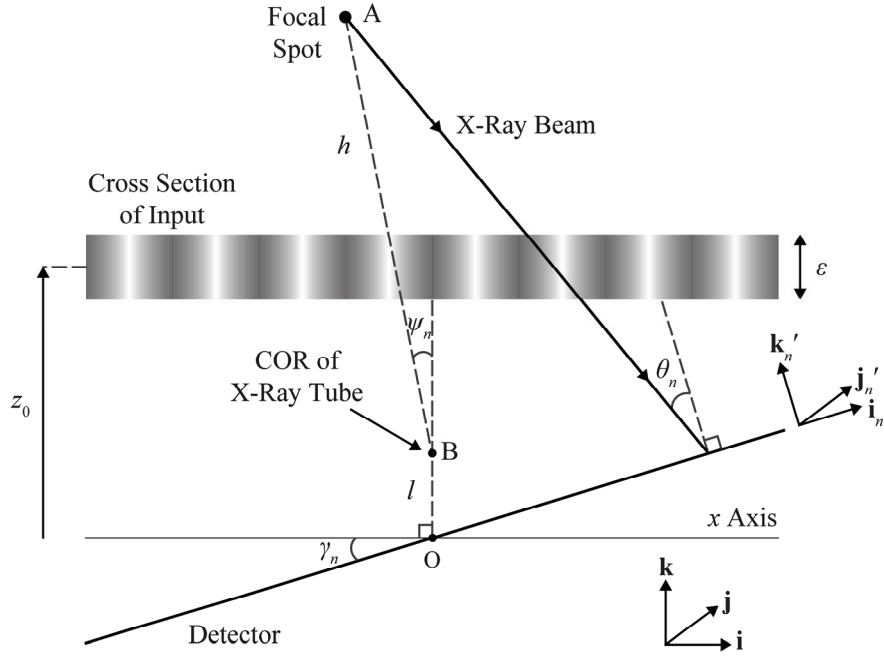


Figure 3.1: Diagram of a sine plate for tomosynthesis reconstruction. The 3D input object is a rectangular prism whose linear attenuation coefficient varies sinusoidally with position x parallel to the chest wall side of the breast support. A 2D cross section of the input object through the plane of the chest wall is shown (figure not to scale). In acquiring projection images, the x-ray tube rotates within the xz plane about point B, and the detector simultaneously rotates about the y axis. The primed unit vectors \mathbf{i}'_n and \mathbf{j}'_n define the coordinate axes of the plane of the detector for the n^{th} projection.

As a final step in this section, it is useful to calculate the incident angle at each point on the detector. Following Figure 3.2, the vector from O to an arbitrary point C on the detector for the n^{th} projection is

$$\overrightarrow{OC} = u_1 \mathbf{i}'_n + u_2 \mathbf{j}'_n \quad (3.7)$$

$$= (u_1 \cos \gamma_n) \mathbf{i} + u_2 \mathbf{j} + (u_1 \sin \gamma_n) \mathbf{k} . \quad (3.8)$$

The matrix transformation between the primed and unprimed coordinate systems supports the transition from Eq. (3.7) to Eq. (3.8).

$$\begin{pmatrix} \mathbf{i}'_n \\ \mathbf{j}'_n \\ \mathbf{k}'_n \end{pmatrix} = \begin{pmatrix} \cos \gamma_n & 0 & \sin \gamma_n \\ 0 & 1 & 0 \\ -\sin \gamma_n & 0 & \cos \gamma_n \end{pmatrix} \begin{pmatrix} \mathbf{i} \\ \mathbf{j} \\ \mathbf{k} \end{pmatrix} \quad (3.9)$$

Additional vectors from O to the COR at point B and from the COR to the focal spot at point A are

$$\overrightarrow{OB} = l\mathbf{k} \quad (3.10)$$

$$\overrightarrow{BA} = (-h \sin \psi_n)\mathbf{i} + (h \cos \psi_n)\mathbf{k}, \quad (3.11)$$

where l is the COR-to-origin distance and where h is the source-to-COR distance. In Eq. (3.11), it is assumed that for positive values of ψ_n , the x coordinate of the focal spot at A is negative. This sign convention is chosen so that positive values of ψ_n cause the x component of the trajectory from A to C to be positive for positive values of u_1 (Figure 3.2). By the summation rules for vectors, the net vector from point C on the detector to the focal spot at A is

$$\overrightarrow{CA} = -\overrightarrow{OC} + \overrightarrow{OB} + \overrightarrow{BA} \quad (3.12)$$

$$= -(u_1 \cos \gamma_n + h \sin \psi_n)\mathbf{i} - u_2\mathbf{j} + (l + h \cos \psi_n - u_1 \sin \gamma_n)\mathbf{k}. \quad (3.13)$$

Thus the angle of incidence is found from the expression

$$\cos \theta_n = \frac{\overrightarrow{CA} \cdot \mathbf{k}'_n}{|\overrightarrow{CA}| |\mathbf{k}'_n|}, \quad (3.14)$$

giving

$$\theta_n = \arccos \left[\frac{h \cos(\psi_n - \gamma_n) + l \cos \gamma_n}{\sqrt{(u_1 \cos \gamma_n + h \sin \psi_n)^2 + u_2^2 + (l + h \cos \psi_n - u_1 \sin \gamma_n)^2}} \right]. \quad (3.15)$$

The dot product in Eq. (3.14) has been computed using Eq. (3.9) to write \mathbf{k}'_n in terms of the unprimed unit vectors.

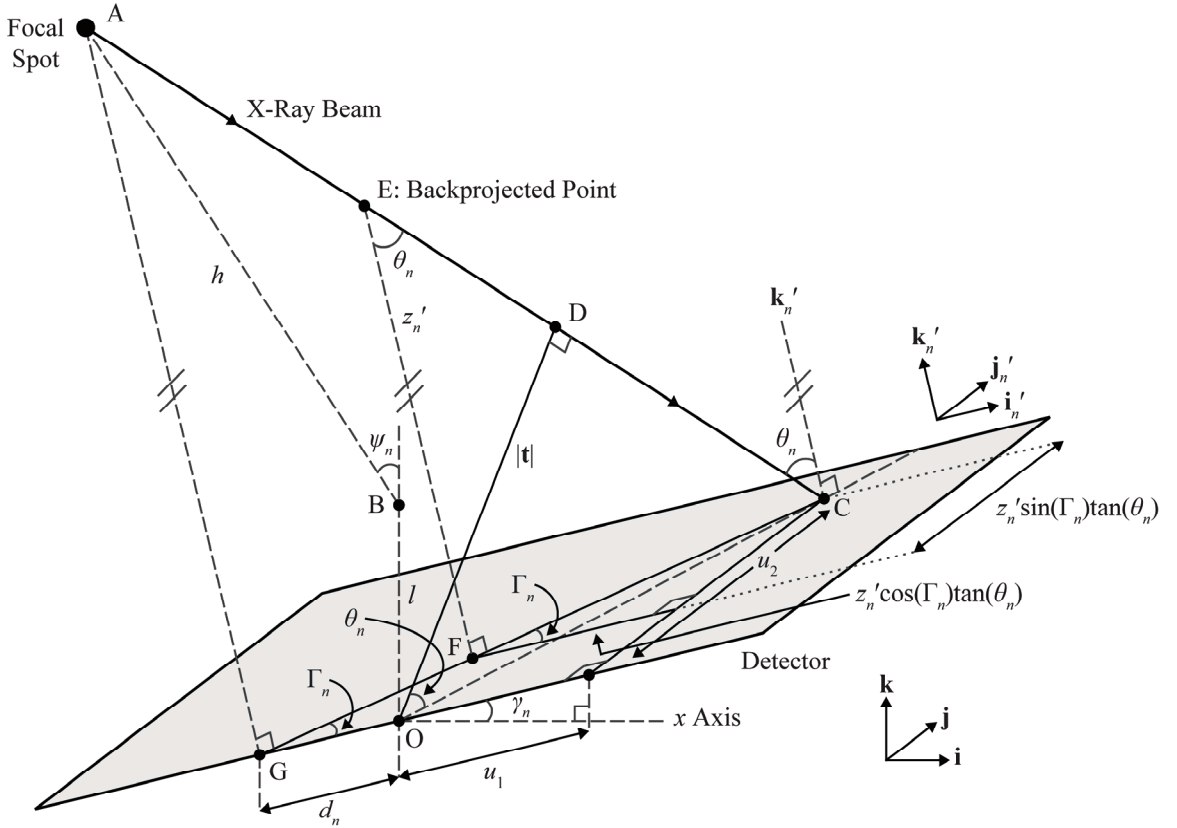


Figure 3.2: Diagram of backprojection angles for tomosynthesis reconstruction. A schematic diagram of the DBT acquisition geometry is shown (figure not to scale). The x-ray beam strikes point C at the angle θ_n relative to the normal to the detector. In FBP reconstruction, signal at C is backprojected to an arbitrary point E along the incident ray. Within the plane of the detector, backprojection is directed toward point F along the angle Γ_n relative to the \mathbf{i}'_n axis.

2.2. Detector Signal

To calculate the detector signal for each projection, it is useful to perform ray tracing through the input object. We begin by defining the line from the focal spot at A to the incident point on the detector at C for the n^{th} projection. This line can be expressed as the parametric equation

$$\begin{pmatrix} x \\ y \\ z \end{pmatrix} = w \begin{pmatrix} u_1 \cos \gamma_n + h \sin \psi_n \\ u_2 \\ u_1 \sin \gamma_n - l - h \cos \psi_n \end{pmatrix} + \begin{pmatrix} -h \sin \psi_n \\ 0 \\ l + h \cos \psi_n \end{pmatrix}, \quad (3.16)$$

where (x, y, z) is a point in \mathbb{R}^3 and w is a free parameter. The focal spot at A has been defined to correspond with $w = 0$, while the incident point at C has been defined to correspond with $w = 1$. The x-ray path length \mathcal{L}_n through the input object for the n^{th} projection image is determined from the intersection of Eq. (3.16) with the planes $z = z_0 + \varepsilon/2$ and $z = z_0 - \varepsilon/2$. The values of w for these two points are

$$w_n^+ = \frac{z_0 + (\varepsilon/2) - l - h \cos \psi_n}{u_1 \sin \gamma_n - l - h \cos \psi_n} \quad (3.17)$$

$$w_n^- = \frac{z_0 - (\varepsilon/2) - l - h \cos \psi_n}{u_1 \sin \gamma_n - l - h \cos \psi_n}, \quad (3.18)$$

where w_n^+ and w_n^- correspond to the entrance and exit points of the x-ray beam through the input, respectively. For the n^{th} projection image, total x-ray attenuation $\mathcal{A}\mu(n)$ is now found by integrating $\mu(x, y, z)$ along \mathcal{L}_n .

$$\mathcal{A}\mu(n) = \int_{\mathcal{L}_n} \mu ds \quad (3.19)$$

The differential arc length ds along \mathcal{L}_n is

$$ds = \sqrt{\left(\frac{dx}{dw}\right)^2 + \left(\frac{dy}{dw}\right)^2 + \left(\frac{dz}{dw}\right)^2} dw \quad (3.20)$$

$$= \sqrt{(u_1 \cos \gamma_n + h \sin \psi_n)^2 + u_2^2 + (l + h \cos \psi_n - u_1 \sin \gamma_n)^2} dw \quad (3.21)$$

$$= [h \cos(\psi_n - \gamma_n) + l \cos \gamma_n] \sec(\theta_n) \cdot dw. \quad (3.22)$$

Eq. (3.22) follows from Eq. (3.15). Substituting Eq. (3.22) into Eq. (3.19) yields the total x-ray attenuation

$$\mathcal{A}\mu(n) = \kappa_n \int_{w_n^+}^{w_n^-} \cos[2\pi f_0(u_1 \cos \gamma_n + h \sin \psi_n)w + \lambda_n] dw \quad (3.23)$$

$$= \frac{\kappa_n \left(\sin[2\pi f_0(u_1 \cos \gamma_n + h \sin \psi_n)w_n^- + \lambda_n] - \sin[2\pi f_0(u_1 \cos \gamma_n + h \sin \psi_n)w_n^+ + \lambda_n] \right)}{2\pi f_0(u_1 \cos \gamma_n + h \sin \psi_n)} \quad (3.24)$$

where

$$\kappa_n = C[h \cos(\psi_n - \gamma_n) + l \cos \gamma_n] \sec \theta_n \quad (3.25)$$

$$\lambda_n = -2\pi f_0(h \sin \psi_n + x_0). \quad (3.26)$$

Using a sum-to-product trigonometric identity for real numbers b_1 and b_2

$$\sin(b_1) - \sin(b_2) = 2 \cos\left(\frac{b_1 + b_2}{2}\right) \sin\left(\frac{b_1 - b_2}{2}\right), \quad (3.27)$$

one may rewrite Eq. (3.24) as

$$\begin{aligned} \mathcal{A}\mu(n) &= \kappa_n (w_n^- - w_n^+) \cos[\pi f_0(u_1 \cos \gamma_n + h \sin \psi_n)(w_n^+ + w_n^-) + \lambda_n] \\ &\quad \cdot \text{sinc}\left[f_0(u_1 \cos \gamma_n + h \sin \psi_n)(w_n^- - w_n^+)\right] \end{aligned} \quad (3.28)$$

$$= \frac{\left(\varepsilon \kappa_n \cos \left[\frac{2\pi f_0 (l + h \cos \psi_n - z_0)(u_1 \cos \gamma_n + h \sin \psi_n)}{l + h \cos \psi_n - u_1 \sin \gamma_n} + \lambda_n \right] \right) \cdot \text{sinc} \left[\frac{\varepsilon f_0 (u_1 \cos \gamma_n + h \sin \psi_n)}{l + h \cos \psi_n - u_1 \sin \gamma_n} \right]}{l + h \cos \psi_n - u_1 \sin \gamma_n} \quad (3.29)$$

where

$$\text{sinc}(u) \equiv \frac{\sin(\pi u)}{\pi u}. \quad (3.30)$$

The transition from Eq. (3.28) to (3.29) follows from Eqs. (3.17) and (3.18). Eq. (3.29) possesses a singularity at $u_1 = (l + h \cos \psi_n) \csc \gamma_n$, the point at which the denominator vanishes. For typical acquisition geometries, this singularity is not expected to correspond to a position on the detector, since neither the attenuation coefficient $\mu(x, y, z)$ nor the path length \mathcal{L}_n should have an infinity.

Eq. (3.29) provides an expression for signal intensity versus position along the detector, assuming that the detector is non-pixelated and possesses an x-ray converter whose modulation transfer function (MTF) is unity at all frequencies. An amorphous selenium (*a*-Se) photoconductor operated in drift mode is a good approximation for an x-ray converter with these properties.⁷ In a clinical setting, *a*-Se is placed in contact with a plate of amorphous silicon (*a*-Si) in which a thin-film transistor (TFT) array samples detector signal in pixels (*i.e.*, detector elements).⁸⁻¹⁰ The logarithmically-transformed signal in the \mathbf{m}^{th} detector element for the n^{th} projection is

$$\mathcal{D}\mu(\mathbf{m}, n) = \int_{a_y m_y}^{a_y(m_y+1)} \int_{a_x(m_x-1/2)}^{a_x(m_x+1/2)} \mathcal{A}\mu(n) \cdot \frac{du_1}{a_x} \frac{du_2}{a_y}. \quad (3.31)$$

In Eq. (3.31), m_x and m_y are integers used for labeling detector elements, and a_x and a_y denote detector element lengths in the directions parallel and perpendicular to the chest wall, respectively. In the special case of square detector elements, it is assumed that $a_x = a_y = a$. Detector elements are centered on $u_1 = m_x a_x$ and $u_2 = (m_y + 1/2)a_y$, where $m_x \in \mathbb{Z}$ and $m_y \in \mathbb{Z}^*$.

It is important to note that the integrand in Eq. (3.31) is dependent on both u_1 and u_2 due to the dependency of κ_n [Eq. (3.25)] on the incident angle θ_n [Eq. (3.15)]. However, because θ_n should vary minimally within the area of a single detector element, total attenuation can be well approximated by the expression

$$\tilde{\mathcal{A}}\mu(n) = \mathcal{A}\mu(n) \Big|_{\theta_n = \theta_{\mathbf{mn}}}, \quad (3.32)$$

where $\theta_{\mathbf{mn}}$ is the evaluation of θ_n at the centroid of the \mathbf{m}^{th} detector element

$$\theta_{\mathbf{mn}} \equiv \theta_n \Big|_{(u_1, u_2) = (m_x a_x, [m_y + 1/2] a_y)}, \quad (3.33)$$

so that

$$\mathcal{D}\mu(\mathbf{m}, n) \cong \int_{a_x(m_x - 1/2)}^{a_x(m_x + 1/2)} \tilde{\mathcal{A}}\mu(n) \cdot \frac{du_1}{a_x}. \quad (3.34)$$

Because it would be difficult to evaluate Eq. (3.34) in closed form, it is appropriate to apply approximate integration techniques. One such method is the midpoint formula¹¹

$$\mathcal{D}\mu(\mathbf{m}, n) \cong \lim_{J_x \rightarrow \infty} \frac{1}{J_x} \sum_{j_x=1}^{J_x} \tilde{\mathcal{A}}\mu(j_x, n), \quad (3.35)$$

where

$$\tilde{\mathcal{A}}\mu(j_x, n) \equiv \tilde{\mathcal{A}}\mu(n) \Big|_{u_1 = a_x \left(\frac{j_x - 1/2}{J_x} + m_x - \frac{1}{2} \right)}. \quad (3.36)$$

The raw signal $\mathcal{S}\mu(u_1, u_2)$ across the detector can now be determined for the n^{th} projection as

$$\mathcal{S}\mu(u_1, u_2) = \sum_{\mathbf{m}} \mathcal{D}\mu(\mathbf{m}, n) \cdot \text{rect}\left(\frac{u_1 - m_x a_x}{a_x}\right) \cdot \text{rect}\left(\frac{u_2 - (m_y + 1/2)a_y}{a_y}\right). \quad (3.37)$$

Using this expression for raw signal, it is now possible to calculate the x-ray transform¹² $\mathcal{X}\mu(t_1, t_2)$.

$$\begin{aligned} \mathcal{X}\mu(t_1, t_2) = \sum_{\mathbf{m}} \mathcal{D}\mu(\mathbf{m}, n) \cdot \text{rect}\left(\frac{t_1 \sec \theta_{\mathbf{m}n} - m_x a_x}{a_x}\right) \\ \cdot \text{rect}\left(\frac{t_2 \sec \theta_{\mathbf{m}n} - (m_y + 1/2)a_y}{a_y}\right) \end{aligned} \quad (3.38)$$

To justify the transition from Eq. (3.37) to Eq. (3.38), one must determine the affine parameters t_1 and t_2 in terms of u_1 and u_2 by considering a line segment \overline{OD} which is orthogonal to \overline{AC} and which connects the origin with the x-ray beam (Figure 3.2). From trigonometry, the length $|\mathbf{t}| = \sqrt{t_1^2 + t_2^2}$ of \overline{OD} is

$$|\mathbf{t}| = |\mathbf{u}| \cos \theta_n. \quad (3.39)$$

By generalizing Eq. (3.39) to components, one finds $t_1 = u_1 \cos \theta_n$ and $t_2 = u_2 \cos \theta_n$. In Eq. (3.38), the incident angle across the area of the \mathbf{m}^{th} detector element for the n^{th} projection has been approximated by its value at the centroid.

2.3. Filtered Backprojection (FBP) Reconstruction from the Projections

The reconstructed attenuation coefficient can now be determined by filtering the x-ray transform with the function $\phi(t_1, t_2)$ and backprojecting the result along the ray of incidence.¹³ It is customary to apply filtering exclusively to frequencies within the plane of the x-ray tube motion, so that the filter's 2D Fourier transform $\mathcal{F}_2\phi(f_1, f_2)$ is independent of f_2

$$\mathcal{F}_2\phi(f_1, f_2) = \mathcal{F}_1\phi(f_1), \quad (3.40)$$

and hence

$$\phi(t_1, t_2) = \phi(t_1)\delta(t_2). \quad (3.41)$$

The specific formula for $\phi(t_1)$ will be addressed in Section 2.4. Assuming that the reconstruction grid is infinitesimally fine (*i.e.*, non-pixelated), the filtered backprojection (FBP) reconstruction is

$$\mu_{\text{FBP}} = \sum_{\mathbf{m}, n} \frac{\mathcal{D}\mu(\mathbf{m}, n)}{N} \cdot \left[\phi(t_1) * \text{rect}\left(\frac{t_1 \sec \theta_{\mathbf{m}n} - m_x a_x}{a_x}\right) \right]_{l_1 = x'_n \cos \theta_{\mathbf{m}n} + z'_n \cos(\Gamma_{\mathbf{m}n}) \sin(\theta_{\mathbf{m}n})} \cdot \left[\text{rect}\left(\frac{t_2 \sec \theta_{\mathbf{m}n} - (m_y + 1/2) a_y}{a_y}\right) \right]_{l_2 = y'_n \cos \theta_{\mathbf{m}n} + z'_n \sin(\Gamma_{\mathbf{m}n}) \sin(\theta_{\mathbf{m}n})}, \quad (3.42)$$

where μ_{FBP} is the reconstructed attenuation coefficient and $*$ is the convolution operator. Within the plane of the detector, backprojection of signal in the \mathbf{m}^{th} detector element for the n^{th} projection is directed azimuthally along the angle $\Gamma_{\mathbf{m}n}$ relative to the \mathbf{i}'_n axis (Figure 3.2). As shown in Eq. (3.42), backprojection may be performed for each of the N projections using the primed coordinate system. To evaluate Eq. (3.42) at the point

(x, y, z) in the unprimed coordinate system, one applies the matrix transformation given in Eq. (3.9).

It is now important to illustrate how the azimuthal backprojection angle Γ_{mn} is calculated. Begin by considering an arbitrary point E along the x-ray beam at which signal is backprojected from the incident point C (Figure 3.2). A line segment along the \mathbf{k}_n' direction may then be drawn from E to the point F on the detector for the n^{th} projection. As a result, within the plane of the detector, backprojection is directed from C to F at the angle Γ_n relative to the \mathbf{i}_n' axis. Point G may now be defined as the position at the chest wall side of the detector which is collinear with points C and F. A derivation of the formula for Γ_n requires knowledge of the distance d_n between G and O, which is now calculated.

$$\overrightarrow{GO} = d_n \mathbf{i}_n' \quad (3.43)$$

$$= (d_n \cos \gamma_n) \mathbf{i} + (d_n \sin \gamma_n) \mathbf{k} \quad (3.44)$$

Since ACG and ECF are similar triangles, \overrightarrow{GA} is parallel to \overrightarrow{FE} and is in turn parallel to \mathbf{k}_n' . Denoting \times as the cross product operator, it follows that

$$\overrightarrow{GA} \times \mathbf{k}_n' = \mathbf{0}, \quad (3.45)$$

where

$$\overrightarrow{GA} = \overrightarrow{GO} + \overrightarrow{OA} \quad (3.46)$$

$$= (d_n \cos \gamma_n - h \sin \psi_n) \mathbf{i} + (d_n \sin \gamma_n + l + h \cos \psi_n) \mathbf{k}. \quad (3.47)$$

To calculate $\overrightarrow{\text{OA}}$ in Eq. (3.46), Eqs. (3.10) and (3.11) have been summed. Substituting Eqs. (3.9) and (3.47) into the cross product of Eq. (3.45) gives

$$\overrightarrow{\text{GA}} \times \mathbf{k}_n' = \begin{vmatrix} \mathbf{i} & \mathbf{j} & \mathbf{k} \\ d_n \cos \gamma_n - h \sin \psi_n & 0 & d_n \sin \gamma_n + l + h \cos \psi_n \\ -\sin \gamma_n & 0 & \cos \gamma_n \end{vmatrix} \quad (3.48)$$

$$= -[d_n + l \sin \gamma_n - h \sin(\psi_n - \gamma_n)] \mathbf{j}. \quad (3.49)$$

By combining Eqs. (3.45) and (3.49), one can solve for d_n .

$$d_n = h \sin(\psi_n - \gamma_n) - l \sin \gamma_n \quad (3.50)$$

Using this result, it follows from trigonometry that

$$\cos \Gamma_n = \frac{u_1 + d_n}{\sqrt{(u_1 + d_n)^2 + u_2^2}} \quad (3.51)$$

$$\sin \Gamma_n = \frac{u_2}{\sqrt{(u_1 + d_n)^2 + u_2^2}}. \quad (3.52)$$

Substituting the coordinates of the detector element centroid into Eqs. (3.51)-(3.52), one finds that the azimuthal backprojection angle for the \mathbf{m}^{th} detector element in the n^{th} projection satisfies the properties

$$\cos \Gamma_{mn} = \frac{m_x a_x + d_n}{\sqrt{(m_x a_x + d_n)^2 + (m_y + 1/2)^2 a_y^2}} \quad (3.53)$$

$$\sin \Gamma_{mn} = \frac{(m_y + 1/2) a_y}{\sqrt{(m_x a_x + d_n)^2 + (m_y + 1/2)^2 a_y^2}}. \quad (3.54)$$

These relations are the expressions needed for FBP reconstruction in Eq. (3.42). One special case of Eq. (3.42) is simple backprojection (SBP) reconstruction

$$\mathcal{B}(\mathcal{X}\mu) = \sum_{\mathbf{m},n} \frac{\mathcal{D}\mu(\mathbf{m},n)}{N} \cdot \text{rect}\left(\frac{x'_n + z'_n \cos(\Gamma_{\mathbf{m}n}) \tan(\theta_{\mathbf{m}n}) - m_x a_x}{a_x}\right) \cdot \text{rect}\left(\frac{y'_n + z'_n \sin(\Gamma_{\mathbf{m}n}) \tan(\theta_{\mathbf{m}n}) - (m_y + 1/2) a_y}{a_y}\right), \quad (3.55)$$

where \mathcal{B} denotes the backprojection operator. With SBP, the filter $\phi(t_1, t_2)$ effectively becomes the product $\delta(t_1)\delta(t_2)$. According to Eq. (3.55), backprojection in the primed coordinate system occurs by translating x'_n and y'_n by $-z'_n \cos(\Gamma_{\mathbf{m}n}) \tan(\theta_{\mathbf{m}n})$ and $-z'_n \sin(\Gamma_{\mathbf{m}n}) \tan(\theta_{\mathbf{m}n})$, respectively, where z'_n is the height of the backprojected point (E) above the plane of the detector. These translational shifts are illustrated in Figure 3.2.

2.4. Formulation of the Reconstruction Filter

Following Zhao's linear systems theory for DBT,¹⁴ a ramp (RA) filter should be applied to the x-ray transform of each projection to reduce the low frequency detector response.¹⁵ The filter is truncated at the spatial frequencies $f_1 = -\xi$ and $f_1 = +\xi$ in the Fourier domain.

$$\mathcal{F}_1 \phi_{\text{RA}}(f_1) = \begin{cases} |f_1| & , |f_1| \leq \xi \\ 0 & , |f_1| > \xi \end{cases} \quad (3.56)$$

The spatial representation $\phi_{\text{RA}}(t_1)$ of the RA filter is determined by its inverse Fourier transform.⁶

$$\phi_{\text{RA}}(t_1) = \int_{-\infty}^{\infty} \mathcal{F}_1 \phi_{\text{RA}}(f_1) \cdot e^{2\pi i t_1 f_1} df_1 \quad (3.57)$$

$$= \xi^2 [2\text{sinc}(2\xi t_1) - \text{sinc}^2(\xi t_1)] \quad (3.58)$$

Using this result, the convolution in Eq. (3.42) can be calculated.

$$\begin{aligned} \phi_{\text{RA}}(t_1) * \text{rect}\left(\frac{t_1 \sec \theta_{\text{m}} - m_x a_x}{a_x}\right) \\ = \frac{\left[a_x \cos(\theta_{\text{m}}) \left[\cos(\pi a_x \xi \cos \theta_{\text{m}}) \cos[2\pi \xi (t_1 - m_x a_x \cos \theta_{\text{m}})] - 1 \right] \right. \\ \left. + 2(t_1 - m_x a_x \cos \theta_{\text{m}}) \sin(\pi a_x \xi \cos \theta_{\text{m}}) \sin[2\pi \xi (t_1 - m_x a_x \cos \theta_{\text{m}})] \right]}{2\pi^2 [t_1 - (m_x - 1/2)a_x \cos \theta_{\text{m}}][t_1 - (m_x + 1/2)a_x \cos \theta_{\text{m}}]} \end{aligned} \quad (3.59)$$

Since noise tends to occur at high frequencies, a spectrum apodization (SA) filter is often applied in addition to the RA filter in order to reduce the high frequency detector response. Following Zhao's approach, a Hanning window function is the SA filter.

$$\mathcal{F}_1 \phi_{\text{SA}}(f_1) = \begin{cases} \frac{1}{2} \left[1 + \cos\left(\frac{\pi f_1}{\xi}\right) \right] & , |f_1| \leq \xi \\ 0 & , |f_1| > \xi \end{cases} \quad (3.60)$$

$$\phi_{\text{SA}}(t_1) = \frac{\xi \text{sinc}(2\xi t_1)}{1 - 4\xi^2 t_1^2} \quad (3.61)$$

According to the convolution theorem,⁶ the net filter is thus

$$\begin{aligned} \phi_{\text{SA}}(t_1) * \phi_{\text{RA}}(t_1) \\ = \frac{\xi^2 \left[\pi^2 (12\xi^2 t_1^2 - 1) \text{sinc}^2(\xi t_1) - 2\pi^2 (4\xi^2 t_1^2 - 1) \text{sinc}(2\xi t_1) - 4(4\xi^2 t_1^2 + 1) \right]}{2\pi^2 (4\xi^2 t_1^2 - 1)^2} \end{aligned} \quad (3.62)$$

The convolution of the net filter in Eq. (3.62) with the rect function in Eq. (3.42) can be performed in closed form similar to Eq. (3.59). This expression is omitted as it is lengthy.

2.5. Fourier Transform of the DBT Images

According to Eq. (3.4), the Fourier transform of the input along the x direction peaks at the frequencies $f_x = \pm f_0$. To determine whether the frequency spectra of the DBT images possess this expected dependency on f_0 , their continuous Fourier transforms may be considered. Within the plane of the detector, the 2D Fourier transform of the n^{th} projection is

$$\mathcal{F}_2(\mathcal{S}\mu)(f_1, f_2) = \int_{-\infty}^{\infty} \int_{-\infty}^{\infty} \mathcal{S}\mu(u_1, u_2) \cdot e^{-2\pi i(f_1 u_1 + f_2 u_2)} du_1 du_2 \quad (3.63)$$

$$= a_x a_y \cdot \text{sinc}(a_x f_1) \text{sinc}(a_y f_2) \cdot \sum_{\mathbf{m}} \mathcal{D}\mu(\mathbf{m}, n) \cdot e^{-2\pi i[m_x a_x f_1 + (m_y + 1/2) a_y f_2]} \cdot \quad (3.64)$$

The 2D Fourier transform of the reconstruction along the x and y directions may now be calculated by considering a fixed height z . Because this chapter only considers input frequencies parallel to the xy plane, it is unnecessary to transform along the z direction. Although filtered backprojection reconstruction in Eq. (3.42) is performed in the primed coordinate system, it is important to take the Fourier transform in the unprimed coordinate system. As such, the reconstructed attenuation coefficient can be written in the form

$$\mu_{\text{FBP}}(x, y, z) = \sum_{\mathbf{m}, n} \frac{\mathcal{D}\mu(\mathbf{m}, n)}{N} \cdot [\rho_1(t_1)] \Big|_{t_1 = \sigma_1 \mathbf{m}_x x + \sigma_2 \mathbf{m}_y z} \cdot [\rho_2(t_2)] \Big|_{t_2 = \sigma_3 \mathbf{m}_x x + \sigma_4 \mathbf{m}_y y + \sigma_5 \mathbf{m}_z z}, \quad (3.65)$$

where

$$\rho_1(t_1) = \phi(t_1) * \text{rect}\left(\frac{t_1 \sec \theta_{\mathbf{m}} - m_x a_x}{a_x}\right) \quad (3.66)$$

$$\rho_2(t_2) = \text{rect}\left(\frac{t_2 \sec \theta_{\mathbf{m}n} - (m_y + 1/2)a_y}{a_y}\right), \quad (3.67)$$

and

$$\sigma_{1\mathbf{m}n} = \cos(\gamma_n) \cos(\theta_{\mathbf{m}n}) - \cos(\Gamma_{\mathbf{m}n}) \sin(\gamma_n) \sin(\theta_{\mathbf{m}n}) \quad (3.68)$$

$$\sigma_{2\mathbf{m}n} = \sin(\gamma_n) \cos(\theta_{\mathbf{m}n}) + \cos(\Gamma_{\mathbf{m}n}) \cos(\gamma_n) \sin(\theta_{\mathbf{m}n}) \quad (3.69)$$

$$\sigma_{3\mathbf{m}n} = -\sin(\Gamma_{\mathbf{m}n}) \sin(\gamma_n) \sin(\theta_{\mathbf{m}n}) \quad (3.70)$$

$$\sigma_{4\mathbf{m}n} = \cos \theta_{\mathbf{m}n} \quad (3.71)$$

$$\sigma_{5\mathbf{m}n} = \sin(\Gamma_{\mathbf{m}n}) \cos(\gamma_n) \sin(\theta_{\mathbf{m}n}). \quad (3.72)$$

According to the convolution theorem, the Fourier transform of Eq. (3.66) under the frequency variable f_1 is

$$\mathcal{F}_1 \rho_1(f_1) = \mathcal{F}_1 \phi(f_1) \cdot a_x \cos(\theta_{\mathbf{m}n}) \text{sinc}(a_x f_1 \cos \theta_{\mathbf{m}n}) e^{-2\pi i m_x a_x f_1 \cos \theta_{\mathbf{m}n}}. \quad (3.73)$$

In the special case of SBP reconstruction, the filter in Eq. (3.73) is unity. In a similar fashion, the Fourier transform of Eq. (3.67) may be written

$$\mathcal{F}_1 \rho_2(f_2) = a_y \cos(\theta_{\mathbf{m}n}) \text{sinc}(a_y f_2 \cos \theta_{\mathbf{m}n}) e^{-2\pi i (m_y + 1/2) a_y f_2 \cos \theta_{\mathbf{m}n}}. \quad (3.74)$$

The 2D Fourier transform of Eq. (3.65) at the fixed depth z is now determined from the expression

$$\mathcal{F}_2 \mu_{\text{FBP}}(f_x, f_y, z) = \sum_{\mathbf{m}, n} \frac{\mathcal{D}\mu(\mathbf{m}, n)}{N} \cdot \int_{-\infty}^{\infty} \rho_1(\sigma_{1\mathbf{m}n} x + \sigma_{2\mathbf{m}n} z) \cdot I_{y\mathbf{m}n}(x) \cdot e^{-2\pi i f_x x} dx, \quad (3.75)$$

where $I_{y\mathbf{m}n}(x)$ is given by the integral

$$I_{y\mathbf{m}n}(x) = \int_{-\infty}^{\infty} \rho_2(\sigma_{3\mathbf{m}n} x + \sigma_{4\mathbf{m}n} y + \sigma_{5\mathbf{m}n} z) \cdot e^{-2\pi i f_y y} dy. \quad (3.76)$$

To evaluate Eq. (3.76), one can make the change of variables

$\eta_{y\mathbf{m}n} = \sigma_{3\mathbf{m}n}x + \sigma_{4\mathbf{m}n}y + \sigma_{5\mathbf{m}n}z$. Since $\sigma_{4\mathbf{m}n} > 0$, it follows that

$$I_{y\mathbf{m}n}(x) = \int_{-\infty}^{\infty} \rho_2(\eta_{y\mathbf{m}n}) e^{\frac{-2\pi i f_y (\eta_{y\mathbf{m}n} - \sigma_{3\mathbf{m}n}x - \sigma_{5\mathbf{m}n}z)}{\sigma_{4\mathbf{m}n}}} \frac{d\eta_{y\mathbf{m}n}}{\sigma_{4\mathbf{m}n}} \quad (3.77)$$

$$= \frac{e^{\frac{2\pi i f_y (\sigma_{3\mathbf{m}n}x + \sigma_{5\mathbf{m}n}z)}{\sigma_{4\mathbf{m}n}}}}{\sigma_{4\mathbf{m}n}} \int_{-\infty}^{\infty} \rho_2(\eta_{y\mathbf{m}n}) e^{-2\pi i \left(\frac{f_y}{\sigma_{4\mathbf{m}n}} \right) \eta_{y\mathbf{m}n}} d\eta_{y\mathbf{m}n} \quad (3.78)$$

$$= \frac{e^{\frac{2\pi i f_y (\sigma_{3\mathbf{m}n}x + \sigma_{5\mathbf{m}n}z)}{\sigma_{4\mathbf{m}n}}}}{\sigma_{4\mathbf{m}n}} \mathcal{F}_1 \rho_2 \left(\frac{f_y}{\sigma_{4\mathbf{m}n}} \right), \quad (3.79)$$

where $\mathcal{F}_1 \rho_2$ has been previously calculated in Eq. (3.74). Using Eq. (3.79), Eq. (3.75)

can now be rewritten as

$$\mathcal{F}_2 \mu_{\text{FBP}}(f_x, f_y, z) = \sum_{\mathbf{m}, n} \frac{\mathcal{D}\mu(\mathbf{m}, n)}{N} \frac{e^{\frac{2\pi i f_y \sigma_{5\mathbf{m}n} z}{\sigma_{4\mathbf{m}n}}}}{\sigma_{4\mathbf{m}n}} I_{x\mathbf{m}n} \mathcal{F}_1 \rho_2 \left(\frac{f_y}{\sigma_{4\mathbf{m}n}} \right), \quad (3.80)$$

where

$$I_{x\mathbf{m}n} = \int_{-\infty}^{\infty} \rho_1(\sigma_{1\mathbf{m}n}x + \sigma_{2\mathbf{m}n}z) e^{-2\pi i \left(f_x - \frac{\sigma_{3\mathbf{m}n} f_y}{\sigma_{4\mathbf{m}n}} \right) x} dx. \quad (3.81)$$

To evaluate Eq. (3.81), it is helpful to perform the substitution $\eta_{x\mathbf{m}n} = \sigma_{1\mathbf{m}n}x + \sigma_{2\mathbf{m}n}z$,

$$I_{x\mathbf{m}n} = \int_{-\infty}^{\infty} \rho_1(\eta_{x\mathbf{m}n}) e^{-2\pi i \left(f_x - \frac{\sigma_{3\mathbf{m}n} f_y}{\sigma_{4\mathbf{m}n}} \right) \left(\frac{\eta_{x\mathbf{m}n} - \sigma_{2\mathbf{m}n}z}{\sigma_{1\mathbf{m}n}} \right)} \frac{d\eta_{x\mathbf{m}n}}{|\sigma_{1\mathbf{m}n}|} \quad (3.82)$$

$$= \frac{e^{\frac{2\pi i \sigma_{2\mathbf{m}n} z (\sigma_{4\mathbf{m}n} f_x - \sigma_{3\mathbf{m}n} f_y)}{\sigma_{1\mathbf{m}n} \sigma_{4\mathbf{m}n}}}}{|\sigma_{1\mathbf{m}n}|} \int_{-\infty}^{\infty} \rho_1(\eta_{x\mathbf{m}n}) e^{-2\pi i \left(\frac{\sigma_{4\mathbf{m}n} f_x - \sigma_{3\mathbf{m}n} f_y}{\sigma_{1\mathbf{m}n} \sigma_{4\mathbf{m}n}} \right) \eta_{x\mathbf{m}n}} d\eta_{x\mathbf{m}n} \quad (3.83)$$

$$= \frac{e^{\frac{2\pi i \sigma_{2mn} z (\sigma_{4mn} f_x - \sigma_{3mn} f_y)}{\sigma_{1mn} \sigma_{4mn}}}}{|\sigma_{1mn}|} \mathcal{F}_1 \rho_1 \left(\frac{\sigma_{4mn} f_x - \sigma_{3mn} f_y}{\sigma_{1mn} \sigma_{4mn}} \right) \quad (3.84)$$

where $\mathcal{F}_1 \rho_1$ is given by Eq. (3.73). The final expression for the 2D Fourier transform of the reconstruction can now be derived by combining Eqs. (3.80) and (3.84).

$$\begin{aligned} \mathcal{F}_2 \mu_{\text{FBP}}(f_x, f_y, z) = \sum_{\mathbf{m}, n} \frac{\mathcal{D}\mu(\mathbf{m}, n)}{N} \frac{e^{\frac{2\pi i z}{\sigma_{1mn} \sigma_{4mn}} [\sigma_{2mn} \sigma_{4mn} f_x + (\sigma_{1mn} \sigma_{5mn} - \sigma_{2mn} \sigma_{3mn}) f_y]}}{|\sigma_{1mn}| \sigma_{4mn}} \\ \cdot \mathcal{F}_1 \rho_1 \left(\frac{\sigma_{4mn} f_x - \sigma_{3mn} f_y}{\sigma_{1mn} \sigma_{4mn}} \right) \mathcal{F}_1 \rho_2 \left(\frac{f_y}{\sigma_{4mn}} \right) \end{aligned} \quad (3.85)$$

A special case of this result is important to consider.

$$\mathcal{F}_2 \mu_{\text{FBP}}(f_x, 0, z) = \sum_{\mathbf{m}, n} \frac{\mathcal{D}\mu(\mathbf{m}, n)}{N} \frac{e^{\frac{2\pi i \sigma_{2mn} z f_x}{\sigma_{1mn}}} a_y \cos \theta_{mn}}{|\sigma_{1mn}| \sigma_{4mn}} \mathcal{F}_1 \rho_1 \left(\frac{f_x}{\sigma_{1mn}} \right) \quad (3.86)$$

Eq. (3.86) is useful for analyzing the reconstruction of an input frequency oriented along the x direction; that is, $f_y = 0$.

3. THEORETICAL RESULTS

3.1. Input Frequency Directed Parallel to the Chest Wall Side of the Breast Support

Image acquisition is now simulated for a Selenia Dimensions integrated multi-mode mammography and tomosynthesis x-ray system (Hologic Inc., Bedford, MA) having 15 projections, an angular spacing ($\Delta\psi$) of 1.07° between projections, a source-to-COR distance (h) of 70.0 cm, a COR-to-origin distance (l) of 0 cm, and square detector element length ($a_x = a_y = a$) of 140 μm . In addition, the sine plate has a thickness (ε) of 0.5 mm, a translational shift (x_0) of 0 mm along the direction of the chest wall side of the

breast support, and a frequency (f_0) of $0.7a^{-1}$ (5.00 lp/mm) parallel to the x axis. To illustrate the potential for super-resolution in DBT, the input frequency is chosen to be higher than the detector alias frequency $0.5a^{-1}$ (3.57 lp/mm). The sine plate is placed at a depth corresponding to the mid-thickness of a typical breast size (50.0 mm thick) under compression. With the breast support positioned 25.0 mm above the origin of the detector, the sine plate is therefore positioned at the depth $z_0 = 50.0$ mm.

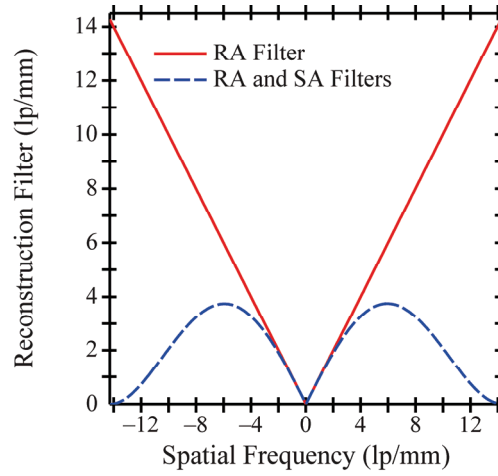


Figure 3.3: Reconstruction filters from linear systems theory. Reconstruction is performed with either the ramp (RA) filter alone or the RA and spectrum apodization (SA) filters together. The SA filter is a Hanning window function.

FBP reconstructions are performed with either the RA filter alone or the RA and SA filters together, assuming a truncation frequency (ξ) of $2a^{-1}$ (14.3 lp/mm). Although ξ is typically chosen to be the detector alias frequency $0.5a^{-1}$, it is necessary to choose a higher value to achieve super-resolution. The specified value of ξ corresponds to the second zero of the MTF of the detector sampling process for frequency measurements along the f_1 direction ($f_2 = 0$).¹⁶⁻¹⁸

$$\text{MTF}(f_1, f_2) = \text{sinc}(a_x f_1) \text{sinc}(a_y f_2) \quad (3.87)$$

Figure 3.3 shows a plot of the reconstruction filters versus frequency. The two filters almost perfectly match each other at low frequencies but diverge at high frequencies, since the SA filter is intended to suppress high frequency noise.

3.1.1. Individual Projections

At a fixed distance (u_2) of 30.0 mm from the chest wall, Figure 3.4(a)-(b) shows a cross section of signal versus detector position u_1 for the central projection ($n = 0$) and an oblique projection ($n = 7$) of the sine plate. The u_2 displacement lies between the chest wall and nipple of a typical breast. In the recent development of a physical 3D anthropomorphic phantom for image quality assessment in DM and DBT,^{19, 20} Carton *et al.* modeled a distance of 65.0 mm between the chest wall and nipple for an average breast size of 450 ml. The u_2 displacement considered in Figure 3.4(a)-(b) thus corresponds to a position approximately halfway between the chest wall and nipple of this phantom.

Detector signal is a discrete function [Eq. (3.31)] due to detector element sampling. To represent this signal graphically, the presence of each detector element can be modeled by a rectangle function, so that the projections appear to be step-like in Figure 3.4(a)-(b). The width of each step matches the detector element length (140 μm).

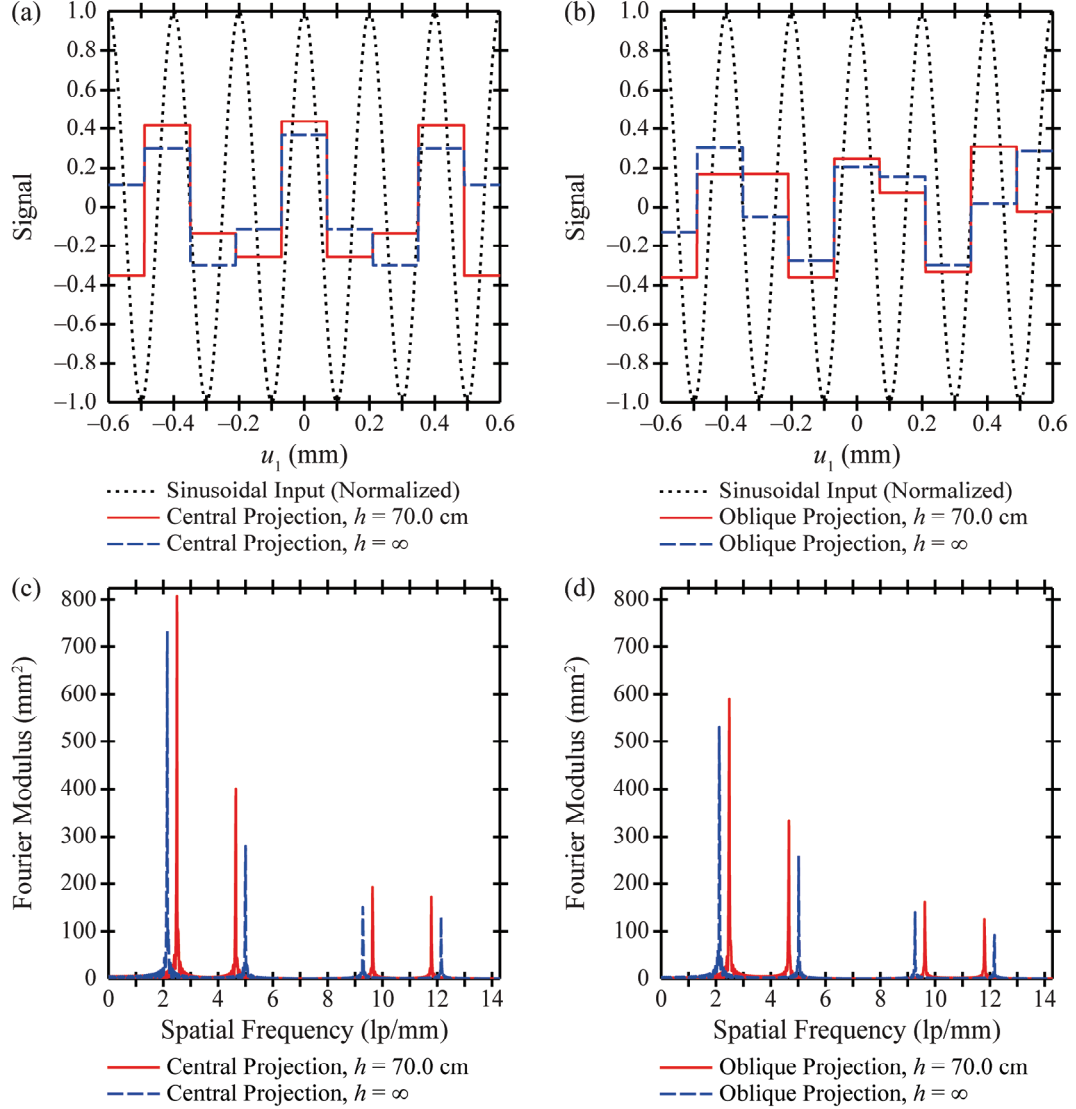


Figure 3.4: Simulated projections of a high-frequency sine plate. At a distance u_2 of 30.0 mm from the chest wall, cross sections of detector signal in the central projection ($n = 0$) and the most oblique projection ($n = 7$) are plotted versus position u_1 . In addition, Fourier transforms are shown versus frequency. The major Fourier peaks do not occur at the input frequency 5.00 lp/mm, illustrating the presence of aliasing. Reducing the source-to-COR distance (h) magnifies the input frequency projected onto the detector.

In Figure 3.4(c)-(d), the modulus of the Fourier transform of detector signal is plotted versus frequency f_1 , assuming $f_2 = 0$ [Eq. (3.64)]. The central and oblique projections are similar in that they both represent a high frequency input as if it were a

lower frequency. The major peak of the Fourier transform of either projection does not occur at the input frequency 5.00 lp/mm but instead occurs at a lower frequency as evidence of aliasing.

The two projections and their frequency spectra are also plotted in Figure 3.4 for an infinite source-to-COR distance (h) with no other changes in the acquisition parameters. This limiting case transforms the divergent beam geometry into a parallel beam geometry. Consequently, the x-ray angle relative to the normal to the detector does not vary with position (u_1, u_2) by Eq. (3.15) but instead is always $\psi_n - \gamma_n$ for the n^{th} projection.

In the parallel beam geometry, the central projection represents the input frequency as if it were $a^{-1} - f_0$, or $0.3a^{-1}$. As a result, the Fourier transform has a major peak at $0.3a^{-1}$ (2.14 lp/mm), and has minor peaks at $0.7a^{-1}$ (5.0 lp/mm), $1.3a^{-1}$ (9.29 lp/mm), and $1.7a^{-1}$ (12.14 lp/mm). Unlike the parallel beam geometry, the divergent beam geometry magnifies the input so that it projects onto the x-ray converter with the frequency f_0/M

$$M = \frac{h}{h - z_0}, \quad (3.88)$$

where M denotes the magnification.²¹ With a source-to-COR distance (h) of 70.0 cm and an object-to-detector distance (z_0) of 50.0 mm, M is 1.077. As a result of the magnification, the peaks in the Fourier transform of detector signal occur at different frequencies than the parallel beam geometry. Accordingly, these Fourier peaks occur at $a^{-1} - f_0/M$ (2.50 lp/mm), f_0/M (4.64 lp/mm), $2a^{-1} - f_0/M$ (9.64 lp/mm), and $a^{-1} + f_0/M$

(11.78 lp/mm). The Fourier transform of the most oblique projection peaks at similar frequencies as the central projection.

3.1.2. SBP Reconstruction

Figure 3.5(a) shows SBP reconstruction versus position (x) measured parallel to the chest wall side of the breast support, performed at the distance $y = 30.0$ mm from the chest wall and at the height $z = z_0 = 50.0$ mm above the detector. Unlike an individual projection, SBP reconstruction can resolve the input frequency 5.00 lp/mm. This property arises because the oblique projections give information about the input which is not present in the central projection alone [Figure 3.4(b)]. Although not explicitly plotted in Figure 3.5(a), it can be shown that super-resolution is present across a broad range of x and y positions in the reconstructed volume.

The SBP Fourier transform [Eq. (3.86)] correctly possesses its major peak at 5.00 lp/mm. The major peak of an individual projection, occurring at 2.50 lp/mm, is now highly suppressed in magnitude [Figure 3.5(c)].

3.1.3. FBP Reconstruction

FBP reconstructions are now performed with either the RA filter alone or the RA and SA filters together. In the spatial domain, these reconstructions are plotted versus position (x) parallel to the chest wall side of the breast support, assuming $y = 30.0$ mm and $z = 50.0$ mm [Figure 3.5(b)]. Figure 3.5(b) demonstrates that reconstruction filters smoothen pixelation artifacts found in the SBP reconstruction. In addition, Figure 3.5(b)

shows that reconstructing with the RA filter alone yields greater modulation than reconstructing with the RA and SA filters together. The modulation for reconstruction with the RA filter alone is 41.0%, yet the modulation for reconstruction with the RA and SA filters together is 29.8%. It is expected that reconstruction with the RA filter alone has greater modulation, since the amplitude of this filter exceeds that of the RA and SA filters together at the input frequency (Figure 3.3). Importantly, the modulation of either FBP reconstruction technique is well above the limit of resolution for typical imaging systems, which is often taken to be 5%. In addition, the modulation of either FBP reconstruction technique is greater than that of SBP reconstruction (18.4%).

Although reconstruction with the RA filter alone has the benefit of greater modulation than reconstruction with the RA and SA filters together, the trade-off is greater spectral leakage at very high frequencies. In fact, the amplitude of the high frequency spectral leakage is greater with the RA filter alone than with SBP. In experimental practice, reconstruction with the RA filter alone also increases the presence of noise, which tends to occur at high frequencies.

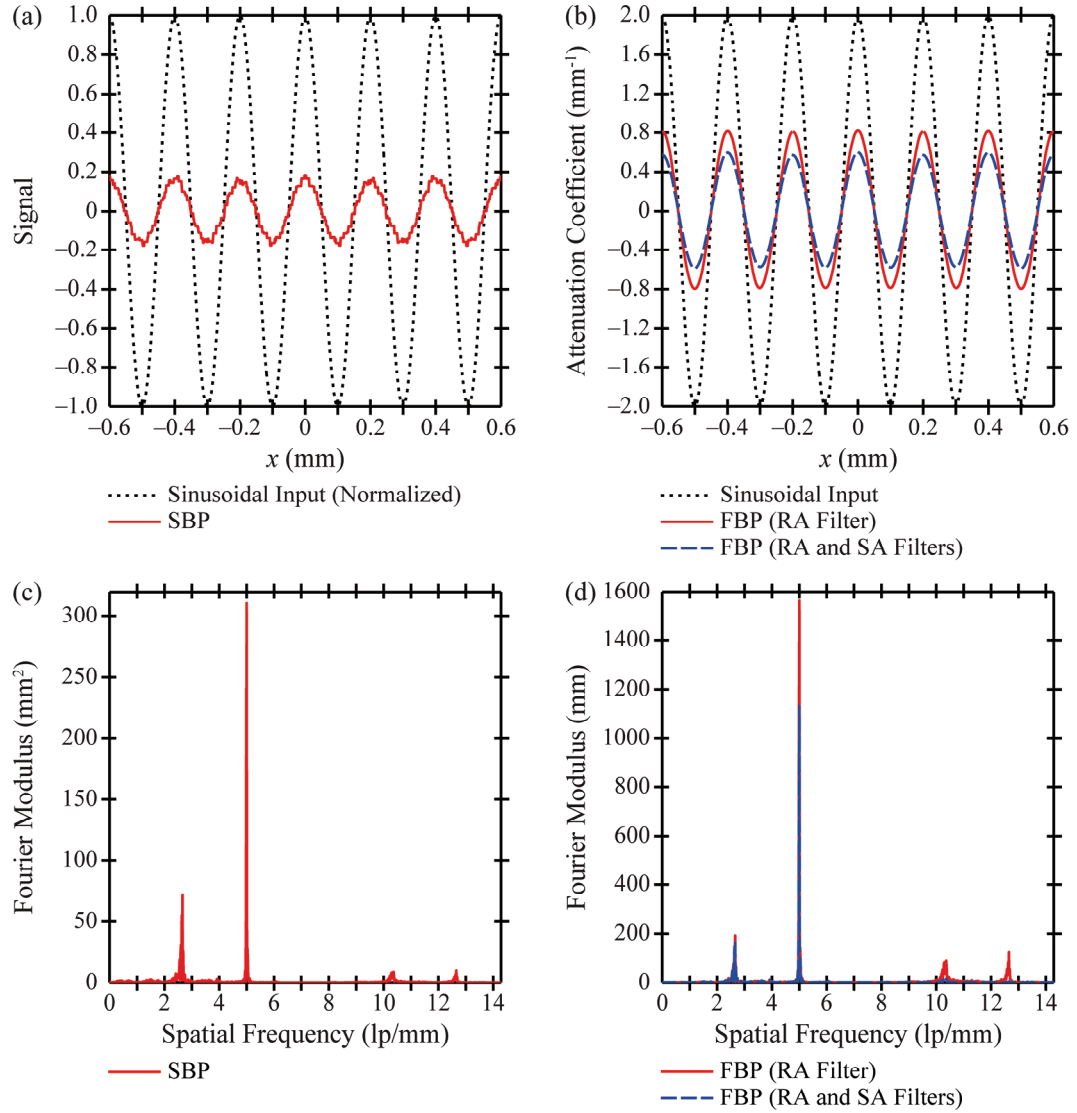


Figure 3.5: Simulated reconstruction of a high-frequency sine plate. Unlike a single projection (Figure 3.4), simple backprojection (SBP) reconstruction can resolve a high frequency input oriented along the x direction. Applying filters to the reconstruction smoothens pixelation artifacts in the spatial domain and reduces low frequency spectral leakage in the Fourier domain. Reconstructing with the ramp (RA) filter alone has the benefit of greater modulation than reconstructing with the RA and spectrum apodization (SA) filters together. The drawback of reconstructing with the RA filter alone is increasing the amplitude of high frequency spectral leakage.

3.2. Input Frequency Directed Perpendicular to the Chest Wall

It is now demonstrated that the existence of super-resolution is dependent on the directionality of the input frequency. Super-resolution arises because of sub-pixel detector element shifts in the image of an object with each increasing projection angle. In order to investigate the feasibility of super-resolution for frequencies oriented along the y direction (*i.e.*, perpendicular to the chest wall), the translational shift in the u_2 position of the incident x ray is now calculated. For the n^{th} projection, an x ray passing from the focal spot through the point (x, y, z) strikes the detector at the u_2 coordinate

$$u_2(n) = \frac{y[l \cos \gamma_n + h \cos(\psi_n - \gamma_n)]}{x \sin \gamma_n + (l - z) \cos \gamma_n + h \cos(\psi_n - \gamma_n)}. \quad (3.89)$$

This expression follows from Eq. (3.16). The translational shift in the u_2 position of the object comparing projection numbers n_1 and n_2 is thus

$$\Delta u_2(n_1, n_2) = u_2(n_2) - u_2(n_1). \quad (3.90)$$

Assuming that $z = 50.0$ mm, Figure 3.6 shows the magnitude of this translational shift versus position y within two planes, $x = 0$ and $x = -30.0$ mm, comparing the central projection and an oblique projection ($n_1 = 0, n_2 = 7$) as well as two oblique projections ($n_1 = -7, n_2 = 7$). Throughout the remainder of this work, a plane defined by a fixed value of x will be termed a PA/SS plane since it has extent in both the posteroanterior (PA) and source-to-support (SS) directions. Although the SS direction technically varies with position on the breast support due to the divergence of the x-ray beam, it is assumed to be equivalent to the z direction for the purpose of this work. As such, the SS direction lies along the same axis as the source-to-image distance (SID), or the length between the focal spot and the origin O for the central projection (Figure 3.1). In a cranial-caudal

(CC) view, a PA/SS plane is thus a sagittal plane through the breast. By contrast, in a mediolateral oblique (MLO) view, the same plane is at an approximately 45° angle relative to the sagittal and transverse planes through the breast.

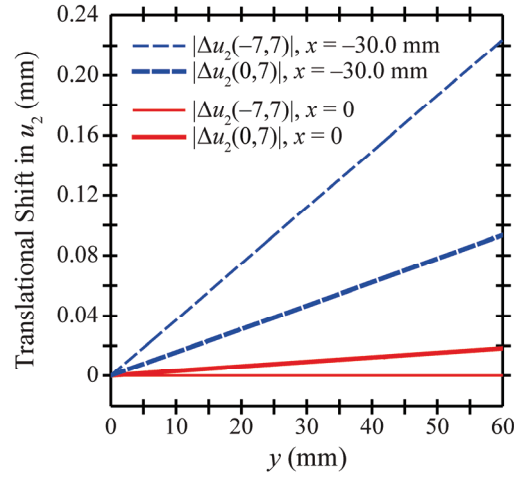


Figure 3.6: Translational shift in the image of an object between projections along the posteroanterior (PA) direction. At a reconstruction depth (z) of 50.0 mm, the magnitude of the translational shift in the u_2 coordinate of the image [Eq. (3.90)] is plotted versus position y measured perpendicular to the chest wall. In the mid PA/SS plane ($x = 0$), translational shifts are minimal comparing the central projection and an oblique projection ($n_1 = 0, n_2 = 7$), and are zero comparing the two most oblique projections ($n_1 = -7, n_2 = 7$). Increasing the magnitude of the distance x relative to the mid PA/SS plane yields a noticeable change in the translational shift.

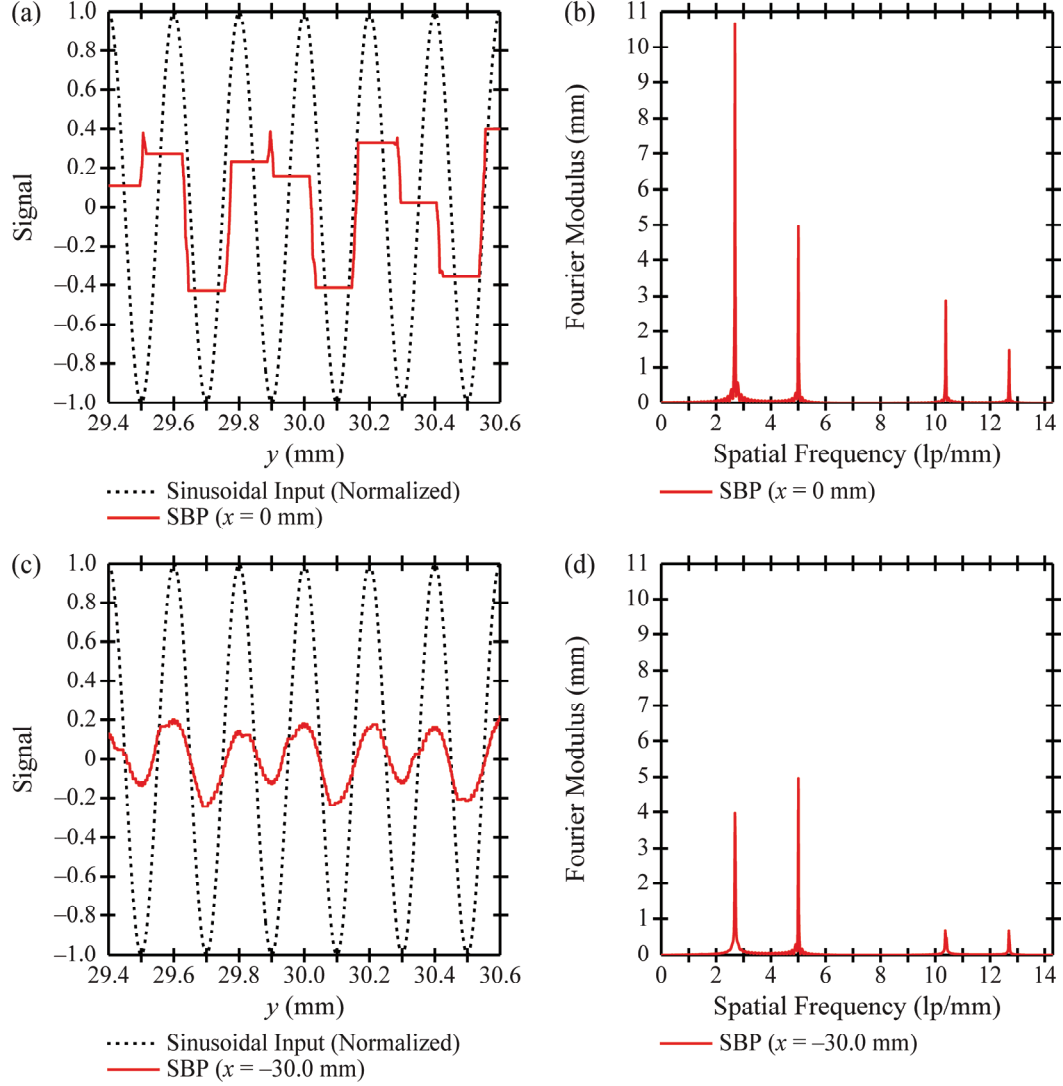


Figure 3.7: Simulated reconstruction of a high-frequency sine plate oriented along the posteroanterior (PA) direction. (a) Within the mid PA/SS plane ($x = 0$), SBP reconstruction resembles a single projection over the region $y \in [29.4 \text{ mm}, 30.6 \text{ mm}]$ for an input frequency oriented along the y direction perpendicular to the chest wall. (b) The 1D Fourier transform of the SBP reconstruction is plotted versus frequency measured along the y direction. Within the mid PA/SS plane of a typical sized breast, the major Fourier peak occurs at a frequency lower than the input frequency, 5.00 lp/mm. (c) With $x = -30.0 \text{ mm}$, super-resolution in an SBP reconstruction is indeed achievable over the region $y \in [29.4 \text{ mm}, 30.6 \text{ mm}]$. (d) For additional proof of super-resolution at $x = -30.0 \text{ mm}$, the major peak of the corresponding Fourier transform occurs at the input frequency, 5.00 lp/mm.

In the mid PA/SS plane ($x = 0$), translational shifts between projections are minimal in a typical sized breast. For example, with $x = 0$, $y = 30.0$ mm, and $z = 50.0$ mm, the translational shift between the central projection and an oblique projection is 0.009 mm (6.52% of detector element length), and the translational shift between the two most oblique projections is zero. For this reason, super-resolution along the y direction is simply not achievable within the mid PA/SS plane. As illustrated in Figure 3.7(a), SBP reconstruction at $x = 0$ in the region $y \in [29.4 \text{ mm}, 30.6 \text{ mm}]$ resembles a single projection.

In Figure 3.6, it is demonstrated that the u_2 translational shift between projections increases as the magnitude of the distance x increases. For example, with $x = -30.0$ mm and $y = 30.0$ mm, the translational shift between the central projection and the oblique projection is 0.047 mm (33.4% of detector element length), and the translational shift between the two most oblique projections is 0.112 mm (80.0% of detector element length). Because these translational shifts are sufficiently large, SBP reconstruction [Figure 3.7(c)] shows super-resolution at $x = -30.0$ mm over the region $y \in [29.4 \text{ mm}, 30.6 \text{ mm}]$. Unlike SBP reconstruction for an input frequency oriented along the x direction [Figure 3.5(a)], the amplitudes of the peaks in Figure 3.7(c) are noticeably different from each other, indicating the presence of reconstruction artifacts. It can be shown that these artifacts are minimized by increasing the distance y from the chest wall, since the u_2 translational shifts between projections increase with y (Figure 3.6).

The SBP reconstructions in Figure 3.7 can be analyzed further by computing their 1D Fourier transform along the y direction. To show differences in these Fourier transforms at fixed values of x , we choose not to transform over both x and y as given by Eq. (3.85).

$$\mathcal{F}_1[\mathcal{B}(\mathcal{X}\mu)](x, f_y, z) = \sum_{\mathbf{m}, n} \frac{\mathcal{D}\mu(\mathbf{m}, n)}{N} \frac{e^{\frac{2\pi i f_y (\sigma_{3\mathbf{m}n}x + \sigma_{5\mathbf{m}n}z)}{\sigma_{4\mathbf{m}n}}}}{\sigma_{4\mathbf{m}n}} \cdot \text{rect}\left[\frac{(\sigma_{1\mathbf{m}n}x + \sigma_{2\mathbf{m}n}z)\sec\theta_{\mathbf{m}n} - m_x a_x}{a_x}\right] \mathcal{F}_1\rho_2\left(\frac{f_y}{\sigma_{4\mathbf{m}n}}\right) \quad (3.91)$$

For additional proof that super-resolution is not achievable within the mid PA/SS plane, Figure 3.7(b) shows that the major Fourier peak at $x = 0$ occurs well below the input frequency. By contrast, the major Fourier peak at $x = -30.0$ mm [Figure 3.7(d)] matches the input frequency, 5.00 lp/mm. Although not shown in the plot, it can be demonstrated that spectral leakage is reduced by increasing the magnitude of the distance x relative to the mid PA/SS plane.

As a final point in this section, it is important to note that by applying the filters in Figure 3.3 to the SBP reconstructions of Figure 3.7, the modulation effectively vanishes (graph not shown). This finding arises because filtering is applied only within the plane of the chest wall [Eq. (3.40)]. An input frequency oriented along the y direction contributes a component of 0 lp/mm within the plane of the chest wall; since the reconstruction filters vanish at 0 lp/mm (Figure 3.3), FBP reconstructions are expected to have no modulation. For this reason, future research on filter optimization is merited as described in the Discussion section.

3.3. Dependency of Super-Resolution on Reconstruction Depth

Using the Fourier transforms calculated in Sections 3.1 and 3.2, one can introduce a metric for assessing the quality of super-resolution in the reconstruction. This metric is the ratio (r) of the amplitude at the highest Fourier peak less than the detector alias frequency (3.57 lp/mm) to the amplitude at the input frequency (5.00 lp/mm). Super-resolution is present if $r < 1$ and is absent if $r \geq 1$. For high quality super-resolution, r should be as close to zero as possible.

To investigate anisotropies in super-resolution along the z direction, r is plotted versus the reconstruction depth (z_0) in Figure 3.8(a), assuming an input frequency oriented along the x direction (Section 3.1). In the Fourier transforms used for calculating r [Eq. (3.86)], the detector field-of-view (FOV) is 56.1 mm \times 84.1 mm, and is centered on the plane $x = 0$. Detector element indices m_x and m_y thus range from -200 to 200 and 0 to 600 , respectively. By centering the FOV on the region $x = 0$, anisotropies in super-resolution can be assessed within the mid PA/SS plane. Super-resolution is not achievable at depths with sharp peaks in the value of r , including $z_0 = 28.7, 35.6, 42.2, 48.8, 55.2, 61.5, 67.6$, and 73.7 mm. The depths considered in the plot span a typical 50.0 mm breast thickness. Because the width of each peak in Figure 3.8(a) is very narrow, super-resolution is present at most depths in the reconstruction. Although only SBP is simulated, similar anisotropies arise if filters are used.

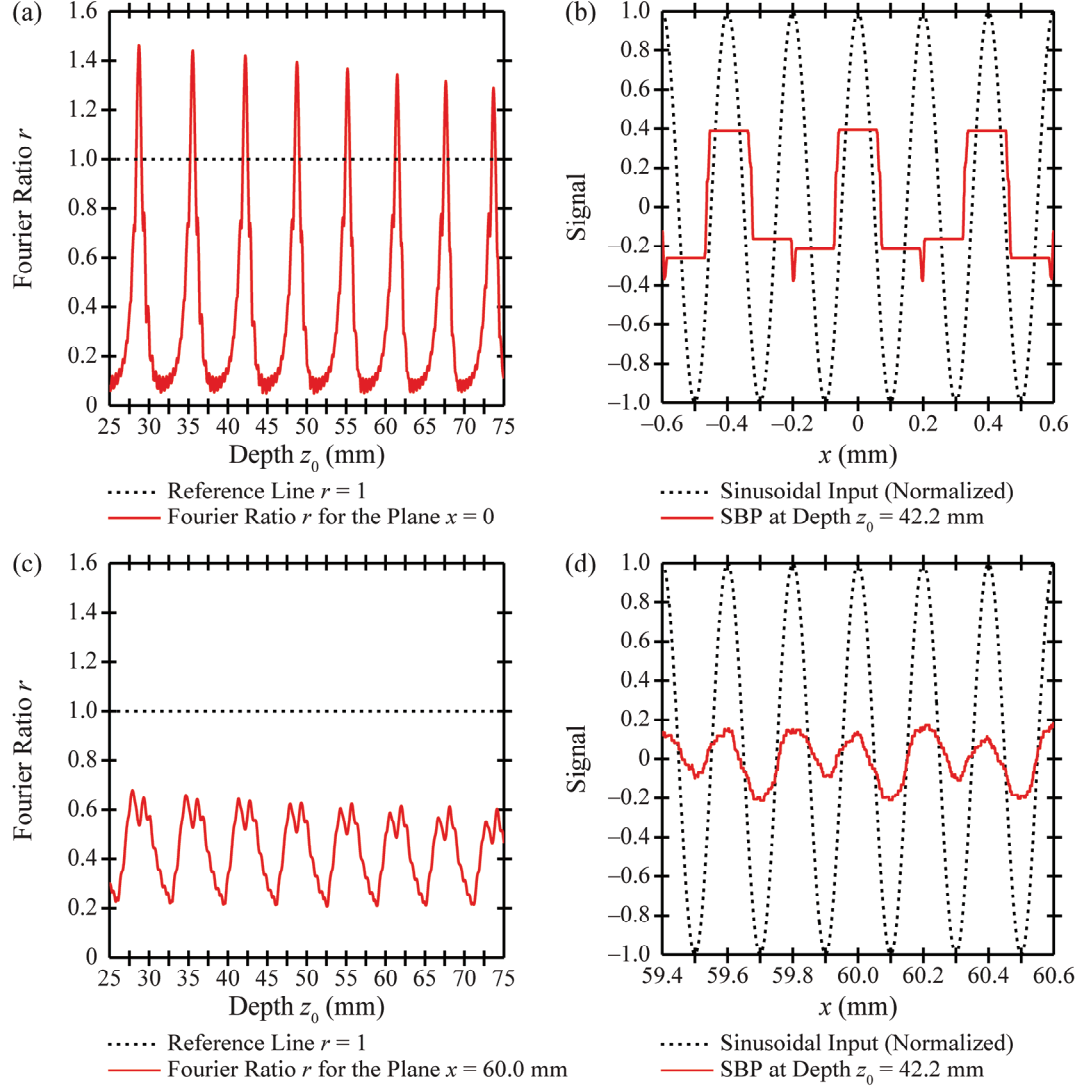


Figure 3.8: Depth-dependency of super-resolution in the reconstruction. For an input frequency oriented along the x direction, the dependency of super-resolution on depth (z_0) is analyzed. The existence of super-resolution is determined from the ratio (r) of the amplitude at the highest peak in the Fourier transform less than the alias frequency of the detector (3.57 lp/mm) to the amplitude at the input frequency (5.00 lp/mm). Super-resolution is present if $r < 1$ and is absent if $r \geq 1$. (a)-(b) Within the mid PA/SS plane ($x = 0$), super-resolution is not achievable at depths with sharp peaks in the value of r , such as $z_0 = 42.2$ mm. (c)-(d) By contrast, within the plane $x = 60.0$ mm, super-resolution is feasible at all depths; r never exceeds unity.

To illustrate the anisotropy of super-resolution along the z direction, Figure 3.8(b) shows an SBP reconstruction at a depth ($z_0 = 42.2$ mm) matching one of the peaks in

Figure 3.8(a). The reconstruction is performed at the distance $y = 30.0$ mm from the chest wall and over a region centered on the mid PA/SS plane (*i.e.*, $x \in [-0.6 \text{ mm}, 0.6 \text{ mm}]$). Signal varies with position in a step-like manner analogous to an individual projection [Figure 3.4(a) and (b)]. Consequently, super-resolution is not achievable at this depth, position, and orientation within the mid PA/SS plane.

A necessary condition for super-resolution is the presence of translational shifts in the image of an object between projections. This condition is not sufficient for super-resolution; the translational shifts must be in increments that maximize sub-pixel sampling gain. If the image of a thin input object is translated between projections in increments that are approximately integer multiples of detector element length, the signal is effectively equivalent in all projections, and super-resolution cannot be achieved. For this reason, anisotropies in super-resolution occur at depths where translational shifts between projections have effectively no sub-pixel sampling differences.

Figure 3.8(c) investigates whether the depth-dependency of super-resolution also exists at positions that are displaced from the mid PA/SS plane ($x = 0$). Similar to Figure 3.8(a), r is plotted versus depth (z_0); however, in the Fourier transforms used for calculating r [Eq. (3.86)], the detector FOV ($56.1 \text{ mm} \times 84.1 \text{ mm}$) is now centered on the plane $x = 60.0$ mm. Detector element indices m_x and m_y thus range from 229 to 629 and 0 to 600, respectively. In Figure 3.8(c), r never exceeds unity, indicating that super-resolution is feasible at all depths within the plane $x = 60.0$ mm. As a result, although Figure 3.8(b) shows that super-resolution is not achievable at the depth $z_0 = 42.2$ mm within the plane $x = 0$, Figure 3.8(d) demonstrates that super-resolution is indeed feasible

at the same depth within the plane $x = 60.0$ mm. The value of r at the depth $z_0 = 42.2$ mm drops from 1.42 to 0.520 in shifting the central axis of the detector FOV from $x = 0$ to $x = 60.0$ mm.

Although Figure 3.8(b) and 3.8(d) are plotted for a fixed value of y (30.0 mm), it can be shown that similar plots hold for all values of y . To explain this finding, it is useful to calculate the translational shift in the object position between projections along the u_1 direction; this direction is chosen because of the orientation of the input frequency in Sections 3.1 and 3.3:

$$\Delta u_1(n_1, n_2) = u_1(n_2) - u_1(n_1), \quad (3.92)$$

where

$$u_1(n) = \frac{x(l + h \cos \psi_n) + zh \sin \psi_n}{x \sin \gamma_n + (l - z) \cos \gamma_n + h \cos(\psi_n - \gamma_n)}. \quad (3.93)$$

There is no y dependency in the formula for the translational shift. Consequently, for an input frequency oriented along the x direction, the existence of super-resolution is dependent only on the x and z coordinates in the reconstruction.

4. EXPERIMENTAL RESULTS

Using a high contrast bar pattern phantom, we have experimentally verified the existence of super-resolution in DBT. The phantom was taped beneath the compression paddle (24 cm \times 29 cm) of the Selenia Dimensions system, and placed 2.5 cm above the breast support. With the alternating light and dark bands of the phantom spanning a 6.0 mm length, the line pairs ranged in frequency from 1.0 lp/mm to 10.0 lp/mm. To match the simulation of Section 3.1, the frequency 5.0 lp/mm was oriented along the x

direction parallel to the chest wall side of the breast support. Also, following the simulation, the bar patterns at 5.0 lp/mm covered the region $x \in [-0.6 \text{ mm}, 0.6 \text{ mm}]$, and the edge of the bar patterns near the numeral “5” (Figure 3.9) was positioned slightly greater than $y = 30 \text{ mm}$ from the chest wall. Using the large (0.3 mm nominal) focal spot and a CC view, 15 projections were acquired at 30 kVp and 14 mAs with a W/AI target-filter combination. The technique for determining the optimal mAs with photo-timing is described in our previous work.⁵

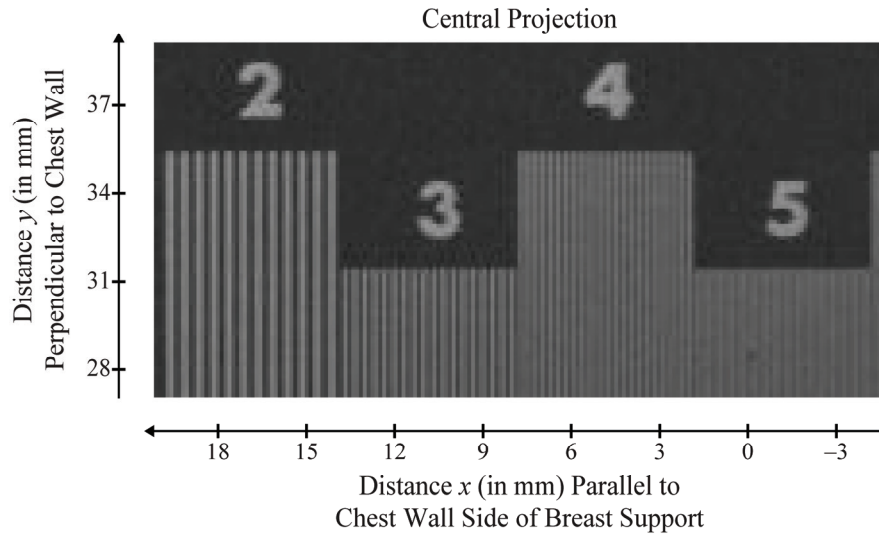


Figure 3.9: Experimental projection image of a bar pattern phantom. The central projection of a bar pattern phantom misrepresents frequencies higher than the detector alias frequency, 3.57 lp/mm for 140 μm detector elements. For example, at 4.0 lp/mm, Moiré patterns are present. At 5.0 lp/mm, fewer than 30 line pairs are observed over a 6.0 mm length.

Reconstruction was subsequently performed using a backprojection filtering (BPF) commercial prototype reconstruction solution (BrionaTM, Real Time Tomography, Villanova, PA).²² Although it is possible to reconstruct on a non-pixelated grid using

analytical modeling, a pixelated grid was required for the experimental data. In order to ensure that high frequencies can be resolved in the plane of the reconstruction, the pixel size of the reconstruction grid (20.44 μm) was chosen to be significantly smaller than that of the detector elements (140 μm). Consequently, the alias frequency of the reconstruction grid (24.46 lp/mm) was substantially higher than the alias frequency of the detector (3.57 lp/mm).

Figure 3.9 shows that the central projection correctly resolves frequencies below the detector alias frequency, 3.57 lp/mm. At the next highest frequency (4.0 lp/mm), one would expect to see 24 line pairs spanning a 6.0 mm length. Instead, less than 24 line pairs are visible, and Moiré patterns²³ are present. Finally, at 5.0 lp/mm, only 16 line pairs are evident within a 6.0 mm length, indicating that the pattern is incorrectly represented as a frequency between 2.0 and 3.0 lp/mm.

Unlike the central projection, BPF reconstruction can resolve frequencies higher than the detector alias frequency (Figure 3.10). In fact, up to 6.0 lp/mm (36 line pairs spanning 6.0 mm) can be observed at the correct orientation with no Moiré patterns. At 7.0 lp/mm, the signal becomes too faint to distinguish bar patterns. This finding arises because the MTF of the reconstruction is reduced with increasing frequency; recall from Eq. (3.87) that the MTF of the detector sampling process vanishes at the frequency $f_1 = a^{-1}$ (7.14 lp/mm), assuming $f_2 = 0$. As expected from the analytical modeling, it should be noted that super-resolution along the x direction was observed over many different x-ray acquisitions in which the bar pattern phantom was placed at various positions in the imaging volume.

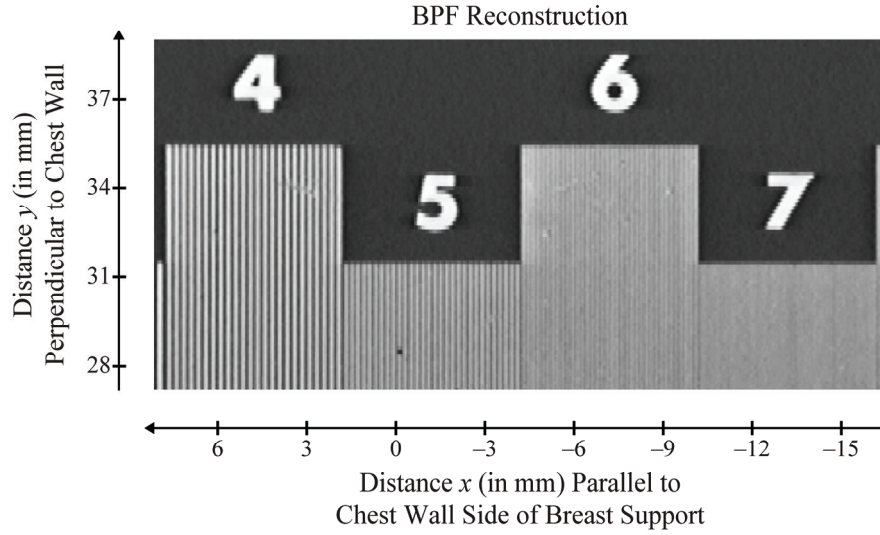


Figure 3.10: Experimental reconstruction of a bar pattern phantom showing super-resolution. Unlike the central projection (Figure 3.9), BPF reconstruction can clearly resolve high frequencies along the x direction parallel to the chest wall side of the breast support. Frequencies up to 6.0 lp/mm are resolved with no Moiré patterns or other evidence of aliasing.

By rotating the bar pattern phantom 90° , the potential for super-resolution orthogonal to the chest wall was also analyzed (Figure 3.11). To orient the reader with the positioning of the phantom, it is important to note that the left edges of the even numerals “4” and “6” were aligned on the mid PA/SS plane ($x = 0$), and that the separation between 4.0 and 5.0 lp/mm was positioned at a displacement $y = 30$ mm from the chest wall. As expected from the analytical modeling (Section 3.2), the extreme left regions of the bar patterns show aliasing of high frequencies due to their proximity to the mid PA/SS plane. Super-resolution is only present at the extreme right of the bar patterns (5.0 and 6.0 lp/mm), where the magnitude of the distance x relative to the mid PA/SS plane is approximately 30 mm or greater.

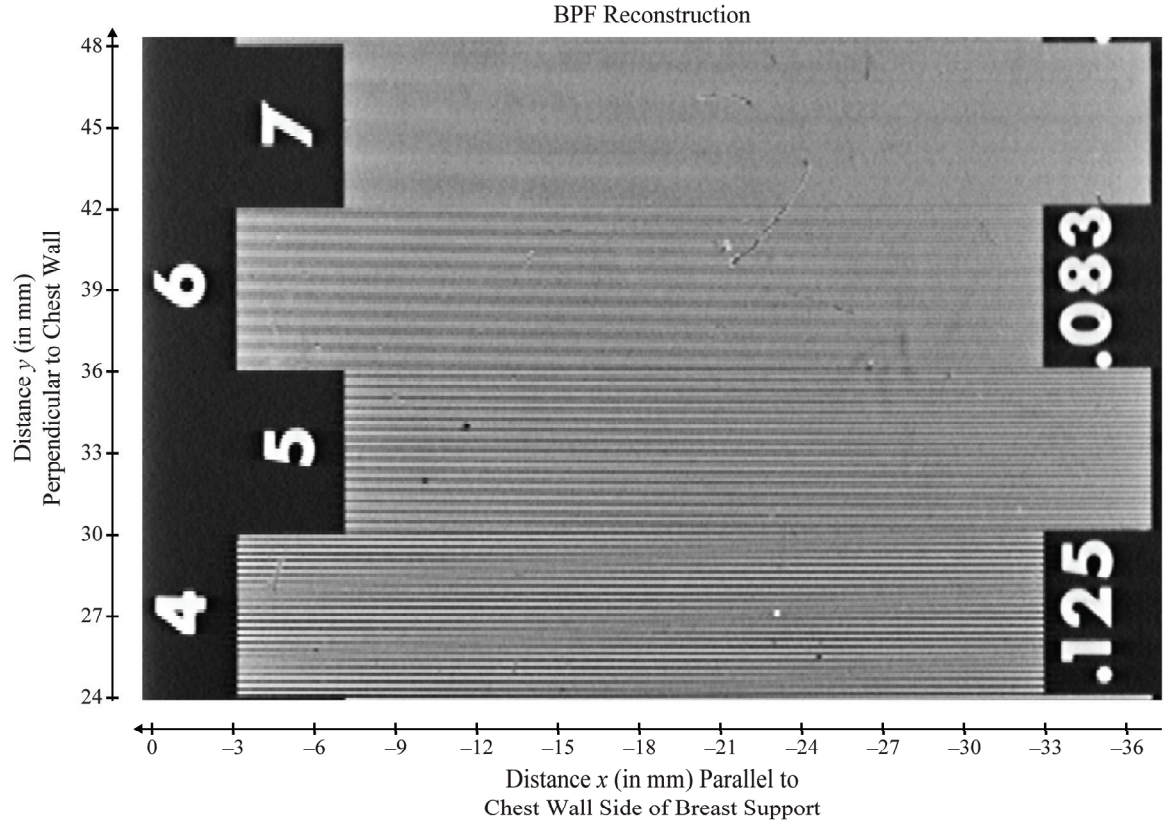


Figure 3.11: Experimental reconstruction of a bar pattern phantom oriented along the posteroanterior (PA) direction. Super-resolution along the y direction is analyzed with bar patterns using a BPF reconstruction. The left edges of the even numerals (“4” and “6”) were aligned on the mid PA/SS plane ($x = 0$), and the separation between 4.0 and 5.0 lp/mm was positioned 30 mm from the chest wall. At the extreme left of the bar patterns, less line pairs are visible than expected, illustrating that super-resolution is not achievable near the plane $x = 0$. In addition, Moiré patterns at 4.0 lp/mm indicate that super-resolution is not possible too close to the chest wall ($y = 0$). Super-resolution is evident only at positions sufficiently displaced from the planes $x = 0$ and $y = 0$; see the extreme right of the bar patterns at 5.0 and 6.0 lp/mm.

It is important to note that the extreme right of the bar patterns at 4.0 lp/mm does not display super-resolution as cleanly as the extreme right of the bar patterns at 5.0 and 6.0 lp/mm due to the presence of Moiré patterns. Recall that the phantom is positioned so that lower frequencies are closer to the chest wall. Because the u_2 translational shift between projections is minimized with decreasing distance from the chest wall

(Figure 3.6), it is expected that super-resolution along the y direction should not be achievable at positions too close to the chest wall.

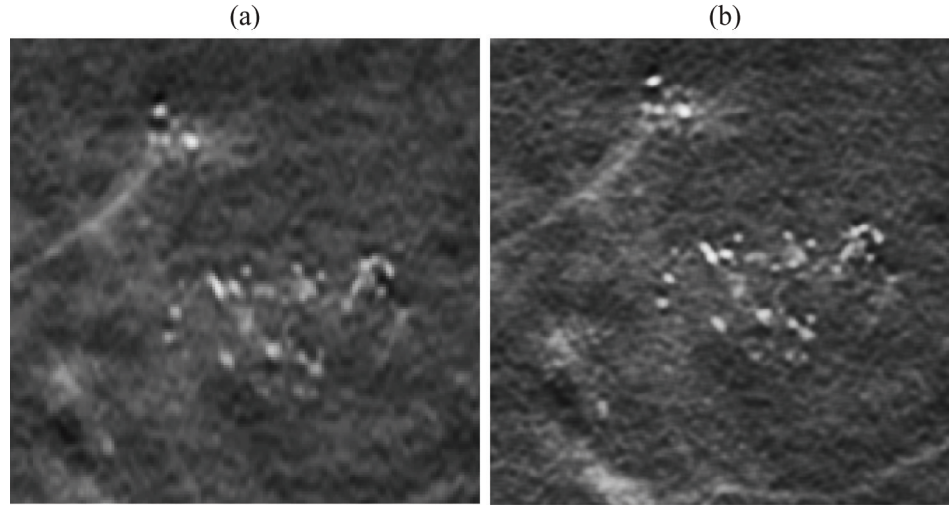


Figure 3.12: A clinical image of microcalcifications with super-resolution. Clinical images of microcalcifications are shown. In (a), BPF reconstruction is performed with pixels matching the detector element size ($140\text{ }\mu\text{m}$), and the result is magnified four-fold to give the image that is shown. In (b), BPF reconstruction is performed using pixels that are much smaller than the detector elements. Image (b) supports super-resolution.

In clinical images, super-resolution should improve the visibility of fine structural details in the breast. This concept is illustrated in Figure 3.12 showing microcalcifications, which are early indicators of breast cancer in many women.²⁴ In the figure, the left image [Figure 3.12(a)] is created by magnifying a BPF reconstruction performed with pixels matching the size of the detector elements ($140\text{ }\mu\text{m}$). The final result has $35\text{ }\mu\text{m}$ pixels (*i.e.*, a four-fold magnification). By contrast, the right image [Figure 3.12(b)] is generated by performing a BPF reconstruction using pixels that are much smaller than the detector elements. As expected from our analysis of bar patterns, the image is sharper in Figure 3.12(b) than in Figure 3.12(a), since Figure 3.12(b) is

capable of resolving high frequency information exceeding the detector alias frequency. Quantifying the clinical impact of this finding is beyond the scope of this work.

5. DISCUSSION

In DBT reconstructions using grids with the same pixel size as the detector elements, the highest frequency that can be resolved in each reconstructed slice is the detector alias frequency. This chapter demonstrates that reconstruction grids with much smaller pixelation display super-resolution, or visibility of higher frequencies. Super-resolution arises because the image of the object is shifted in sub-pixel detector element increments with each increasing projection angle.

Super-resolution was first demonstrated analytically by calculating the reconstruction of a sinusoidal input whose frequency was oriented along the x direction parallel to the chest wall side of the breast support. Using an infinitesimally fine reconstruction grid, it was shown that both SBP and FBP can resolve higher frequencies than a single projection. FBP reconstructions were performed either with the RA filter alone or with the RA and SA filters together. Although reconstruction with the RA filter alone has the benefit of greater modulation in the spatial domain, it presents the trade-off of increased noise and spectral leakage at high frequencies.

In rotating the sine plate by 90° , super-resolution was found to exist at fewer positions in the reconstruction. For an input frequency oriented along the chest wall-to-nipple direction, it was shown that positions with super-resolution must be displaced relative to the chest wall ($y = 0$) and to the mid PA/SS plane ($x = 0$). At these positions,

the translational shifts in the image between projections are sufficiently large to achieve super-resolution. Because increasing the angular range of the scan inherently increases the translational shifts between projections, the exact positions at which super-resolution is feasible are dependent upon the design of the acquisition geometry.

This chapter also demonstrates that the existence of super-resolution is depth-dependent. Considering an input frequency oriented along the x direction for illustration, it was shown that super-resolution is not feasible at certain depths (z) within the mid PA/SS plane. By contrast, super-resolution is achievable at all depths within PA/SS planes that are sufficiently displaced relative to the mid PA/SS plane. The anisotropies in super-resolution along the z direction are dependent upon the number of projections and the angular spacing between projections.

We have experimentally observed super-resolution in images of bar patterns. A single projection showed classical signs of aliasing, including Moiré patterns and the visibility of fewer line pairs than expected. By contrast, reconstructions using very fine grids resolved frequencies higher than the alias frequency of the detector. For the two orientations of the bar patterns, the presence of super-resolution was verified at positions predicted from analytical modeling. The effects observed in the experimental images are not necessarily unique attributes of the commercial DBT system or the commercial reconstruction algorithm used. Super-resolution should be feasible provided the detector has measurable modulation above the alias frequency and the reconstruction algorithm supports finer sampling than the detector in each reconstructed slice.

Super-resolution appears to produce a sharper image of microcalcifications showing more detail. This finding is complementary to prior work on computer breast phantoms demonstrating that fiducial markers can be located with higher precision in a super-sampled reconstruction.²⁵ It is important to determine the effect of super-resolution on noise, and to evaluate the potential benefits of super-resolution using a task-based approach. A future clinical study is also merited to assess the clinical impact of super-resolution in DBT.

Super-resolution is a particularly useful property for x-ray systems that employ binning when switching from 2D to 3D imaging modes. For example, in the Selenia Dimensions system, the DM detector element dimensions are $70\text{ }\mu\text{m} \times 70\text{ }\mu\text{m}$, whereas the DBT detector element dimensions are $140\text{ }\mu\text{m} \times 140\text{ }\mu\text{m}$. Binning has the benefit of lowering the readout time, but presents the drawback of reducing the alias frequency of the detector. Initially, it would seem that binning should make DBT less capable of resolving high frequency information, such as microcalcifications. However, the existence of super-resolution in the reconstruction may counter the trade-offs of binning.

Some of the limitations of this study and directions for future modeling are now noted. In calculating detector signal, this chapter assumes that the MTF of *a*-Se in drift mode is unity. While this assumption is valid for normal x-ray incidence, it is less justifiable with oblique x-ray incidence.²⁶⁻³³ Que and Rowlands proposed the first analytical model of the optical transfer function (OTF) of *a*-Se in drift mode for all incident angles.²⁶ Their work was later validated by Hajdok and Cunningham with

Monte Carlo simulations.²⁷ Denoting μ_{Se} as the attenuation coefficient of Se and L as the thickness of the photoconductor, the OTF at each frequency f is

$$\text{OTF}(f) = \frac{\left[1 - e^{-(\mu_{\text{Se}}L \sec \theta_n + 2\pi i f L \tan \theta_n)}\right] \cos \theta_n}{1 + \frac{2\pi i f \sin \theta_n}{\mu_{\text{Se}}}}. \quad (3.94)$$

The MTF is the normalized modulus of the OTF. For more thorough modeling, signal in the x-ray converter should be convolved with the point spread function (PSF) of α -Se before detector element sampling is performed, where the PSF is determined from the OTF using Fourier theory. It is important to model MTF degradation for measurements near the edge of the detector opposite the chest wall, as the incident angle deviates considerably from the normal. Upon examining θ_n across multiple projections in the Selenia Dimensions detector, it can be shown that the maximum incident angle is approximately 25° . Assuming 200 μm thick α -Se and 20 keV x rays³⁴⁻³⁶ for which μ_{Se} is 20.5 mm^{-1} ,³⁷ the corresponding MTF at 5.0 lp/mm is 85.8%.

While it is important to consider MTF degradation at positions distal to the chest wall, it is less critical for positions close to the chest wall. For example, in the central projection at the position $u_1 = u_2 = 30.0 \text{ mm}$, the incident angle is 3.47° , and the MTF at 5.0 lp/mm is 99.7%. Consequently, for the purpose of this work, an x-ray converter with MTF of unity was assumed.

In addition to modeling the MTF of the x-ray converter, the analytical model of the sine plate can be refined by modeling the MTF of the focal spot. Although this chapter assumes a point-like focal spot that is stationary during each projection, future studies should model MTF degradation with increasing focal spot size³⁸ and increasing

focal spot motion during a continuous scan of the projections.^{14, 39, 40} Our earlier work has shown that continuous x-ray tube motion yields a loss of modulation in the reconstruction.⁴¹ Despite this increase in blurring, super-resolution should still be achievable in the reconstruction of the sine plate (Figures 3.5, 3.7, 3.8). This claim is supported by the presence of super-resolution in bar pattern images (Figures 3.10-3.11), which were acquired on a DBT system with continuous tube motion.

In future studies, detector lag and ghosting⁴²⁻⁴⁴ should also be simulated, and the presence of shot noise⁴⁵ should be modeled at various dose levels. Because this work considers a high contrast input frequency either with the analytical simulation or with the experimental bar patterns, it was not necessary to model the presence of noise at different dose levels. Future studies on super-resolution with low contrast input frequencies will require a noise simulation, as the visibility of the patterns should be influenced by dose. Finally, because the linear attenuation coefficient of an input object is energy dependent, polyenergetic x-ray spectra⁴⁶⁻⁴⁸ should also be simulated in the analytical model. This work implicitly assumes a monoenergetic x-ray beam.

In CT, the conventional low frequency filter is the RA filter^{14, 15} which increases linearly with frequency from zero (Figure 3.3). Assuming that filtering is only applied within the plane of the x-ray tube motion, this work demonstrates that the RA filter is not suited for imaging frequencies perpendicular to the chest wall, since the modulation of the reconstruction vanishes (Section 3.2). The filters used in the experimental reconstructions of bar patterns oriented perpendicular to the chest wall (Figure 3.11) have a nonzero offset at 0 lp/mm, unlike the RA filter used in the analytical modeling. Future

work should consider filters with nonzero offset for analytical modeling of super-resolution, since modulation would not be zero for any orientation of the input frequency.

Because super-resolution has important clinical applications in improving the visibility of microcalcifications, future work should ultimately transition from modeling a sinusoidal input to simulating microcalcifications in a breast background.⁴⁹ Using model observers, improvements in the visibility of microcalcifications should be assessed with image reconstructions at varying grid sizes. It would be useful to determine the coarsest grid size at which the benefits of super-resolution are achieved among observers, as reconstructions on coarser grids require less memory for data storage.

6. CONCLUSION

This work demonstrates the existence of super-resolution in DBT. An analytical model of super-resolution was developed by calculating the reconstruction of a high frequency sinusoidal input. While a single projection cannot resolve frequencies higher than the alias frequency of the detector, a reconstruction on a very fine grid can resolve these frequencies. Super-resolution is made possible by the sub-pixel detector element shifts in the image of the object between projections.

Using a bar pattern phantom, we have experimentally verified the existence of super-resolution in DBT. In considering an input frequency that was oriented either parallel to the chest wall side of the breast support or perpendicular to the chest wall, the experimental images confirmed the presence of super-resolution at positions predicted by

analytical modeling. Super-resolution has the potential to impact the visualization of microcalcifications and other subtle signs of breast cancer.

7. APPENDIX: DETECTOR SIGNAL FOR AN INPUT FREQUENCY DIRECTED PERPENDICULAR TO THE CHEST WALL

This appendix calculates detector signal for an input frequency perpendicular to the chest wall. Under this assumption, the input rectangular prism of thickness ε has a linear attenuation coefficient $\mu(x, y, z)$ which varies sinusoidally along the y direction with frequency f_0

$$\mu(x, y, z) = C \cdot \cos[2\pi f_0(y - y_0)] \cdot \text{rect}\left(\frac{z - z_0}{\varepsilon}\right), \quad [(3.A1): cf. (3.1)]$$

where y_0 is a translational shift in the waveform relative to the origin. The amplitude C of the waveform is equivalent to $1/\varepsilon$ upon normalizing total attenuation along the z direction. The 1D Fourier transform of Eq. (3.A1) along the y direction peaks at the frequencies $f_y = \pm f_0$ and vanishes at all other frequencies, following a formula similar to Eq. (3.4) with the exchange of x_0 for y_0 and f_x for f_y . Using Eqs. (3.17)-(3.19) and Eq. (3.22), total x-ray attenuation versus position (u_1, u_2) along the plane of the rotated detector is calculated for the n^{th} projection as

$$\mathcal{A}\mu(n) = \kappa_n \int_{w_n^+}^{w_n^-} \cos(2\pi f_0 u_2 w + \Lambda) dw \quad [(3.A2): cf. (3.23)]$$

$$= \frac{\kappa_n \left(\sin[2\pi f_0 u_2 w_n^- + \Lambda] - \sin[2\pi f_0 u_2 w_n^+ + \Lambda] \right)}{2\pi f_0 u_2}, \quad [(3.A3): cf. (3.24)]$$

where

$$\Lambda = -2\pi f_0 y_0. \quad [(3.A4): cf. (3.26)]$$

Following the sum-to-product trigonometric identity given in Eq. (3.27), one may rewrite Eq. (3.A3) as

$$\begin{aligned} \mathcal{A}\mu(n) &= \kappa_n (w_n^- - w_n^+) \cos \left[\pi f_0 u_2 (w_n^+ + w_n^-) + \Lambda \right] \\ &\quad \cdot \text{sinc} \left[f_0 u_2 (w_n^- - w_n^+) \right] \end{aligned} \quad [(3.A5): cf. (3.28)]$$

$$= \frac{\left(\varepsilon \kappa_n \cos \left[\frac{2\pi f_0 u_2 (l + h \cos \psi_n - z_0)}{l + h \cos \psi_n - u_1 \sin \gamma_n} + \Lambda \right] \cdot \text{sinc} \left[\frac{\varepsilon f_0 u_2}{l + h \cos \psi_n - u_1 \sin \gamma_n} \right] \right)}{l + h \cos \psi_n - u_1 \sin \gamma_n}. \quad [(3.A6): cf. (3.29)]$$

The logarithmically-transformed signal in the \mathbf{m}^{th} detector element for the n^{th} projection is now determined from Eq. (3.31). The midpoint formula⁵⁰ for approximating this double integral is

$$\mathcal{D}\mu(\mathbf{m}, n) = \lim_{J_y \rightarrow \infty} \frac{1}{J_y} \sum_{j_y=1}^{J_y} \left[\lim_{J_x \rightarrow \infty} \frac{1}{J_x} \sum_{j_x=1}^{J_x} \mathcal{A}\mu(j_x, j_y, n) \right], \quad [(3.A7): cf. (3.35)]$$

where

$$\mathcal{A}\mu(j_x, j_y, n) \equiv \mathcal{A}\mu(n) \Big|_{(u_1, u_2) = \left(a_x \left[\frac{j_x - 1/2}{J_x} + m_x - \frac{1}{2} \right], a_y \left[\frac{j_y - 1/2}{J_y} + m_y \right] \right)}. \quad [(3.A8): cf. (3.36)]$$

FBP reconstruction now follows from Eq. (3.42).

8. REFERENCES

- ¹Rafferty EA. Tomosynthesis: New weapon in breast cancer fight. *Decisions in Imaging Economics*. 2004;17(4).
- ²Poplack SP, Tosteson TD, Kogel CA, Nagy HM. Digital breast tomosynthesis: initial experience in 98 women with abnormal digital screening mammography. *American Journal of Roentgenology*. 2007;189(3):616-23.
- ³Park SC, Park MK, Kang MG. Super-resolution Image Reconstruction: A Technical Overview. *IEEE Signal Processing Magazine*. 2003;20(3):21-36.
- ⁴Bushberg JT, Seibert JA, Edwin M. Leidholdt J, Boone JM. Chapter 10: Image Quality. In: John J-R, Snyder A, DeGeorge T, editors. *The Essential Physics of Medical Imaging*. 2 ed. Philadelphia, PA: Lippincott Williams & Wilkins; 2002. p. 255-91.
- ⁵Acciavatti RJ, Maidment ADA. Investigating the Potential for Super-Resolution in Digital Breast Tomosynthesis. In: Pelc NJ, Samei E, Nishikawa RM, editors. *SPIE Medical Imaging*; 2011; Lake Buena Vista, FL: SPIE; 2011. p. 79615K-1 - K-12.
- ⁶Barrett HH, Myers KJ. Chapter 3: Fourier Analysis. In: Saleh BEA, editor. *Foundations of Image Science*. New York, NY: John Wiley & Sons; 2004. p. 95-174.
- ⁷Lee DL, Cheung LK, Rodricks B, Powell GF. Improved imaging performance of a 14 x 17-inch Direct Radiography (TM) System using Se/TFT detector. In: James T. Dobbins I, Boone JM, editors. *SPIE Conference on Physics of Medical Imaging*; 1998; San Diego, CA: SPIE; 1998. p. 14-23.
- ⁸Jing T, Goodman CA, Drewery J, Cho G, Hong WS, Lee H, et al. Amorphous silicon pixel layers with cesium iodide converters for medical radiography. *IEEE Trans Nucl Sci*. 1994;41(4):903-9.
- ⁹Cowen AR, Kengyelics SM, Davies AG. Solid-state, flat-panel, digital radiography detectors and their physical imaging characteristics. *Clin Radiol*. 2008;63:487-98.
- ¹⁰Nagarkar VV, Gupta TK, Miller SR, Klugerman Y, Squillante MR, Entine G. Structured CsI(Tl) scintillators for x-ray imaging applications. *IEEE Trans Nucl Sci*. 1998;45(3):492-6.
- ¹¹Stewart J. Chapter 7: Techniques of Integration. In: Pirtle B, Green S, editors. *Calculus: Early Transcendentals*. 5e ed. Belmont, CA: Brooks/Cole - Thomson Learning; 2003. p. 474-545.
- ¹²Barrett HH, Myers KJ. Chapter 10: Energy Transport and Photons. In: Saleh BEA, editor. *Foundations of Image Science*. New York, NY: John Wiley & Sons; 2004. p. 551-630.
- ¹³Barrett HH, Myers KJ. Chapter 4: Series Expansions and Integral Transforms. In: Saleh BEA, editor. *Foundations of Image Science*. New York, NY: John Wiley & Sons; 2004. p. 175-214.
- ¹⁴Zhao B, Zhao W. Three-dimensional linear system analysis for breast tomosynthesis. *Medical Physics*. 2008;35(12):5219-32.
- ¹⁵Mertelmeier T, Orman J, Haerer W, Dudam MK. Optimizing filtered backprojection reconstruction for a breast tomosynthesis prototype device. In: Flynn MJ, Hsieh J, editors. *Physics of Medical Imaging*; 2006; San Diego: SPIE; 2006.

- ¹⁶Albert M, Maidment ADA. Linear response theory for detectors consisting of discrete arrays. *Medical Physics*. 2000;27(10):2417-34.
- ¹⁷Acciavatti RJ, Maidment ADA. An Analytical Model of NPS and DQE Comparing Photon Counting and Energy Integrating Detectors. In: Samei E, Pelc NJ, editors. *SPIE Medical Imaging*; 2010; San Diego, CA: SPIE; 2010. p. 76220I-1 - I-12.
- ¹⁸Acciavatti RJ, Maidment ADA. A Comparative Analysis of OTF, NPS, and DQE in Energy Integrating and Photon Counting Digital X-ray Detectors. *Medical Physics*. 2010;37(12):6480-95.
- ¹⁹Carton A-K, Bakic P, Ullberg C, Maidment ADA. Development of a 3D high-resolution physical anthropomorphic breast phantom. In: Samei E, Pelc NJ, editors. *Medical Imaging 2010: Physics of Medical Imaging*; 2010; San Diego, CA: SPIE; 2010. p. 762206-1 - -8.
- ²⁰Carton A-K, Bakic P, Ullberg C, Derand H, Maidment ADA. Development of a physical 3D anthropomorphic breast phantom. *Medical Physics*. 2011;38(2):891-6.
- ²¹Wolbarst AB. Chapter 30: Resolution and Magnification. *Physics of Radiology*. 2nd ed. Madison, WI: Medical Physics Publishing; 2005. p. 333-40.
- ²²Kuo J, Ringer PA, Fallows SG, Bakic PR, Maidment ADA, Ng S. Dynamic Reconstruction and Rendering of 3D Tomosynthesis Images. In: Pelc NJ, Samei E, Nishikawa RM, editors. *SPIE Medical Imaging*; 2011; Lake Buena Vista, FL: SPIE; 2011. p. 796116-1 - 11.
- ²³Albert M, Beideck DJ, Bakic PR, Maidment ADA. Aliasing effects in digital images of line-pair phantoms. *Medical Physics*. 2002;29(8):1716-8.
- ²⁴Lanyi M. Chapter 7: Differential Diagnosis of Microcalcifications. *Diagnosis and Differential Diagnosis of Breast Calcifications*. Berlin: Springer-Verlag; 1988. p. 193-231.
- ²⁵Bakic PR, Ringer P, Kuo J, Ng S, Maidment ADA. Analysis of Geometric Accuracy in Digital Breast Tomosynthesis Reconstruction. *Lecture Notes in Computer Science*. 2010;6136:62-9.
- ²⁶Que W, Rowlands JA. X-ray imaging using amorphous selenium: Inherent spatial resolution. *Medical Physics*. 1995;22(4):365-74.
- ²⁷Hajdok G, Cunningham IA. Penalty on the detective quantum efficiency from off-axis incident x rays. In: Yaffe MJ, Flynn MJ, editors. *Medical Imaging 2004: Physics of Medical Imaging*; 2004; San Diego, CA: SPIE; 2004. p. 109-18.
- ²⁸Mainprize JG, Bloomquist AK, Kempston MP, Yaffe MJ. Resolution at oblique incidence angles of a flat panel imager for breast tomosynthesis. *Medical Physics*. 2006;33(9):3159-64.
- ²⁹Acciavatti RJ, Maidment ADA. Calculation of OTF, NPS, and DQE for Oblique X-Ray Incidence on Turbid Granular Phosphors. *Lecture Notes in Computer Science*. 2010;6136:436-43.
- ³⁰Freed M, Park S, Badano A. A fast, angle-independent, analytical model of CsI detector response for optimization of 3D x-ray breast imaging systems. *Medical Physics*. 2010;37(6):2593-605.

- ³¹Freed M, Park S, Badano A. Erratum: "A fast, angle-dependent, analytical model of CsI detector response for optimization of 3D x-ray breast imaging systems" [Med. Phys. 37, 2593-2605 (2010)]. Medical Physics. 2011;38(4):2307.
- ³²Badano A, Freed M, Fang Y. Oblique incidence effects in direct x-ray detectors: A first-order approximation using a physics-based analytical model. Medical Physics. 2011;38(4):2095-8.
- ³³Acciavatti RJ, Maidment ADA. Optimization of phosphor-based detector design for oblique x-ray incidence in digital breast tomosynthesis. Medical Physics. 2011;38(11):6188-202.
- ³⁴Johns PC, Yaffe MJ. X-ray Characterization of normal and neoplastic breast tissues. Physics in Medicine and Biology. 1987;32(6):675-95.
- ³⁵Yaffe MJ. Chapter 5: Digital Mammography. In: Beutel J, Kundel HL, Metter RLV, editors. Handbook of Medical Imaging Volume 1 Physics and Psychophysics. Bellingham, WA: SPIE - The International Society for Optical Engineering; 2000. p. 329-72.
- ³⁶Bushberg JT, Seibert JA, Edwin M. Leidholdt J, Boone JM. Chapter 8: Mammography. In: John J-R, Snyder A, DeGeorge T, editors. The Essential Physics of Medical Imaging. 2 ed. Philadelphia, PA: Lippincott Williams & Wilkins; 2002. p. 191-229.
- ³⁷Berger MJ, Hubbell JH, Seltzer SM, Chang J, Coursey JS, Sukumar R, et al. XCOM: Photon Cross Sections Database. [cited 2011 November 10]; Available from: <http://physics.nist.gov/xcom>
- ³⁸Johns HE, Cunningham JR. Chapter 16: Diagnostic Radiology. The Physics of Radiology. 4th ed. Springfield, IL: Charles C Thomas; 1983. p. 557-669.
- ³⁹Ren B, Ruth C, Stein J, Smith A, Shaw I, Jing Z. Design and performance of the prototype full field breast tomosynthesis system with selenium based flat panel detector. In: Flynn MJ, editor. SPIE; 2005; San Diego, CA: SPIE; 2005. p. 550-61.
- ⁴⁰Shaheen E, Marshall N, Bosmans H. Investigation of the effect of tube motion in breast tomosynthesis: continuous or step and shoot? In: Pelc NJ, Samei E, Nishikawa RM, editors. SPIE Medical Imaging; 2011; Lake Buena Vista, FL: SPIE; 2011. p. 79611E-1 - E-9.
- ⁴¹Acciavatti RJ, Maidment ADA. Optimization of Continuous Tube Motion and Step-and-Shoot Motion in Digital Breast Tomosynthesis Systems with Patient Motion. In: Pelc NJ, Nishikawa RM, Whiting BR, editors. SPIE Medical Imaging; 2012; San Diego, CA: SPIE; 2012. p. 831306-1 - 12.
- ⁴²Bloomquist AK, Yaffe MJ, Mawdsley GE, Hunter DM. Lag and ghosting in a clinical flat-panel selenium digital mammography system. Medical Physics. 2006;33(8):2998-3005.
- ⁴³Siewerdsen JH, Jaffray DA. A ghost story: Spatio-temporal response characteristics of an indirect-detection flat-panel imager. Medical Physics. 1999;26(8):1624-41.
- ⁴⁴Zhao W, DeCrescenzo G, Kasap SO, Rowlands JA. Ghosting caused by bulk charge trapping in direct conversion flat-panel detectors using amorphous selenium. Medical Physics. 2005;32(2):488-500.
- ⁴⁵Barrett HH, Myers KJ. Chapter 12: Noise in Detectors. In: Saleh BEA, editor. Foundations of Image Science. New York, NY: John Wiley & Sons; 2004. p. 701-800.

- ⁴⁶Tucker DM, Barnes GT, Chakraborty DP. Semiempirical model for generating tungsten target x-ray spectra. *Medical Physics*. 1991;18(2):211-8.
- ⁴⁷Boone JM, Fewell TR, Jennings RJ. Molybdenum, rhodium, and tungsten anode spectral models using interpolating polynomials with application to mammography. *Medical Physics*. 1997;24(12):1863-74.
- ⁴⁸Blough MM, Waggener RG, Payne WH, Terry JA. Calculated mammographic spectra confirmed with attenuation curves for molybdenum, rhodium, and tungsten targets. *Medical Physics*. 1998;25(9):1605-12.
- ⁴⁹Bakic PR, Zhang C, Maidment ADA. Development and characterization of an anthropomorphic breast software phantom based upon region-growing algorithm. *Medical Physics*. 2011;38(6):3165-76.
- ⁵⁰Stewart J. Chapter 15: Multiple Integrals. In: Pirtle B, Green S, editors. *Calculus: Early Transcendentals*. 5e ed. Belmont, CA: Brooks/Cole - Thomson Learning; 2003. p. 980-1053.

CHAPTER 4

Oblique Reconstructions in Tomosynthesis:

I. Proof-of-Principle Justification

This chapter expands upon a conference proceedings manuscript published in Lecture Notes in Computer Science **7361**, 737-744 (2012), and is planned for submission to a peer-reviewed journal.

1. INTRODUCTION

In computed tomography (CT), axial slices of the body are reconstructed successively as the patient is translated in the longitudinal direction. Due to the near isotropic resolution of modern CT scanners, the stack of axial slices can be reformatted to display a multiplanar reconstruction (MPR), or an image of any planar or curved surface in the volume. One application of MPR is visualizing stenosis in coronary arteries with a curved surface following the contour of the vessel. Another example is dental CT, in which an oblique plane can be used to display the jaw and teeth in the same view.¹

In tomosynthesis, projection images are acquired over a small angular range instead of the full 180° arc used in CT. It has been conventionally assumed that tomosynthesis reconstructions should only be created with planes parallel to the detector, since Fourier space is not sampled isotropically.² The sampling of Fourier space is determined from the Central Slice Theorem. As shown in Figure 4.1 using a 2D parallel beam geometry for illustration, the sampled region of Fourier space resembles a double cone whose opening angle matches the angular range of the tomosynthesis scan. This region is termed the “*Fourier double cone*” (FDC) throughout the remainder of this work, even though the region is not 3D in the strict sense of a cone.

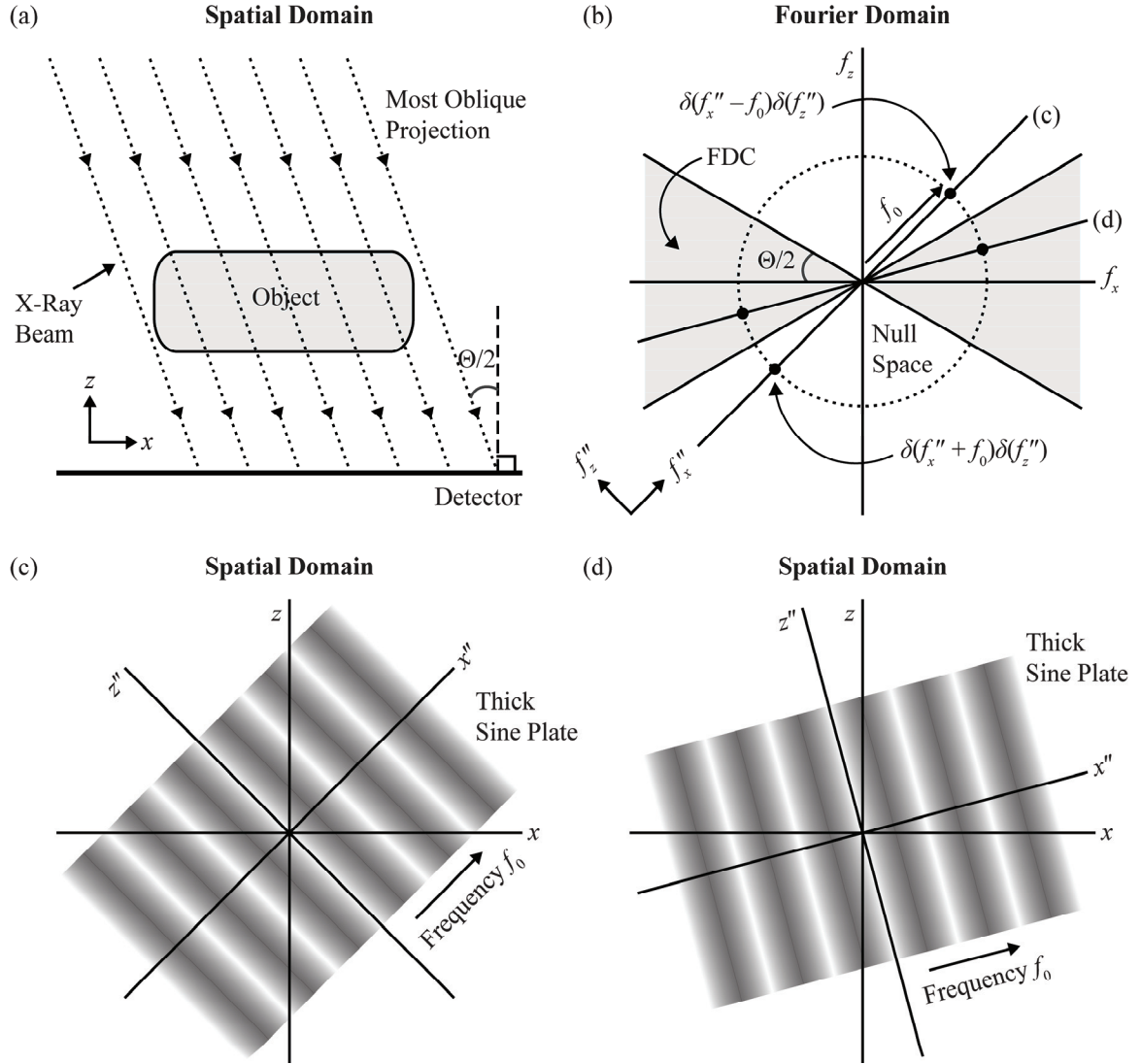


Figure 4.1: Thought experiments in the reconstruction of a thick object along oblique planes. (a) A parallel x-ray beam acquires a projection image for tomosynthesis. (b) According to the Central Slice Theorem, Fourier space is sampled along the direction perpendicular to the x-ray beam of each projection. Thus, the sampled area resembles a double cone whose opening angle matches the angular range (Θ) of the scan. This sampled area is termed the “*Fourier double cone*” (FDC) in this work. (c) A test frequency is oriented along a pitch angle outside the FDC. Since the object is very thick, its Fourier transform consists of two delta functions along the pitch axis. This object is occult to tomosynthesis. (d) The same object is oriented along a pitch within the opening angle of the FDC. This object is sampled perfectly in Fourier space. Since a 0° pitch is always contained within the FDC, this thought experiment supports the use of conventional slices along a 0° pitch in the reconstruction of a thick object.

To gain insight into a reason for using reconstruction planes parallel to the detector, it is useful to perform a thought experiment with objects that are occult to tomosynthesis. Based on the Central Slice theorem, an object is occult to tomosynthesis if its Fourier transform is zero at all points inside the FDC. It can be demonstrated from standard properties concerning the Fourier transform that this condition is satisfied by a very thick object. Figure 4.1 illustrates this concept by considering a very thick object whose attenuation coefficient varies sinusoidally along an angle (*i.e.*, “pitch”). The Fourier transform of the object consists of two delta functions along the pitch axis. One can use this object to assess whether individual frequencies are resolvable along various directions in the reconstruction. If one first considers the case in which the pitch is outside the opening angle of the FDC, it follows from the Central Slice Theorem that the reconstruction is zero everywhere [Figure 4.1(c)]. Consequently, a slice that is reconstructed along the pitch of the object cannot resolve the input frequency. By contrast, if the same object has a pitch within the opening angle of the FDC, the test frequency is sampled perfectly in Fourier space [Figure 4.1(d)]. By demonstrating that the object is resolved at pitches within the opening angle of the FDC, this thought experiment supports the use of conventional slices oriented along a 0° pitch. The 0° pitch is always contained within the opening angle of the FDC regardless of the angular range of the scanner.

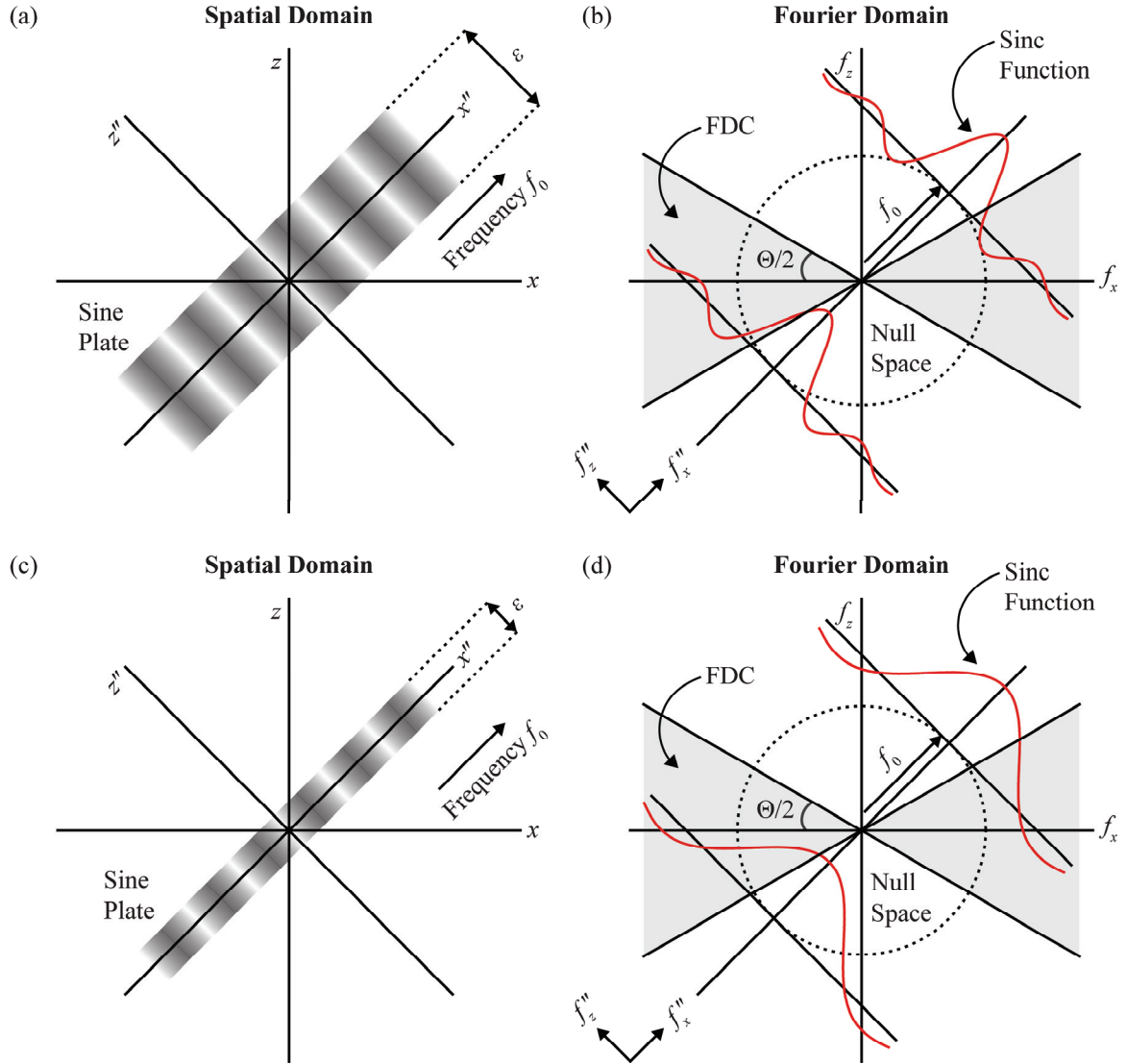
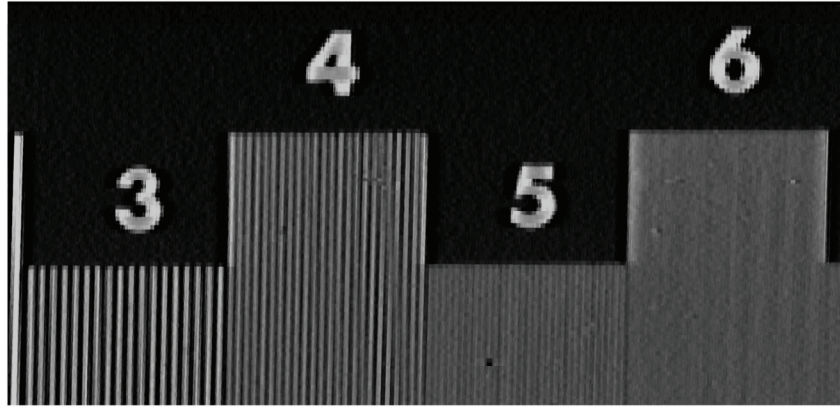


Figure 4.2: Illustration of the effect of thickness on the Fourier transform of a pitched sine plate. To illustrate that a thin object can be visualized in an oblique reconstruction, a test frequency is analyzed at a non-zero pitch. As shown, the Fourier transform of the object consists of two lines modulated by a “sinc” function along the direction perpendicular to the pitch axis. Because the Fourier transform is non-zero within the FDC, a slice that is reconstructed along the pitch of the input frequency is expected to have information that would not otherwise be present for a thick object [Figure 4.1(c)]. The amplitude of the portion of the “sinc” function that intersects the FDC increases as the object thickness is reduced; hence, the modulation in an oblique reconstruction is expected to be largest at small thicknesses.

It is now useful to investigate the effect of reducing the object thickness in the same thought experiment. As shown in Figure 4.2, the Fourier transform of a thin sinusoidal object consists of two lines modulated by a “sinc” function along the direction perpendicular to the pitch axis. Because the Fourier transform has reasonably large modulation within the FDC, a slice along the pitch of the input frequency should not be trivial like the corresponding slice for a thick object.

To investigate whether an oblique reconstruction can indeed resolve a thin object, experimental images of a bar pattern phantom were acquired with a Selenia Dimensions digital breast tomosynthesis system (Hologic, Inc., Bedford, MA). A goniometry stand was used to vary the pitch of frequencies ranging from 1.0 line pair per millimeter (lp/mm) to 10.0 lp/mm in 1.0 lp/mm increments. The technique factors of the scan matched the ones given in our previous work.^{3, 4} Reconstruction was performed in the oblique plane of the bar patterns using a commercial prototype backprojection filtering (BPF) algorithm (BrionaTM, Real Time Tomography, Villanova, PA).⁵ Our previous work showed that frequencies up to 6.0 lp/mm can be resolved if the bar pattern phantom is parallel to the breast support (*i.e.*, 0° pitch). Upon tilting the plane of the bar patterns, reconstructions showed that frequencies up to 5.0 lp/mm and 3.0 lp/mm can be resolved at 30° and 60° pitches, respectively (Figure 4.3). These experimental results indicate that slices in a tomosynthesis reconstruction do not have to be parallel to the breast support as stipulated by convention.

(a) BPF Reconstruction, 30° Pitch



(b) BPF Reconstruction, 60° Pitch

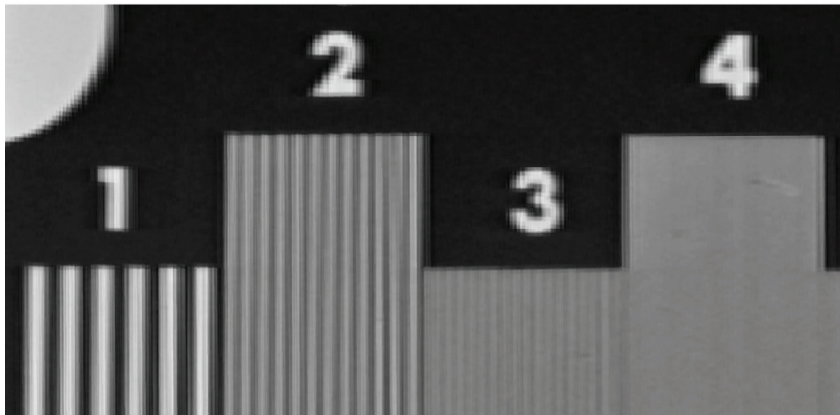


Figure 4.3: Experimental reconstructions of a bar pattern phantom along oblique planes. To investigate the experimental feasibility of oblique reconstructions in a commercial breast tomosynthesis system, a bar pattern phantom was oriented along various pitches using a goniometry stand. The frequencies were pitched at 30° and 60° angles relative to the breast support. BPF reconstructions in the oblique plane of the bar patterns show frequencies up to 5.0 lp/mm and 3.0 lp/mm at the two respective pitches.

In breast tomosynthesis applications,⁶⁻⁸ the objects in the American College of Radiology (ACR) Mammography Accreditation Phantom⁹ give insight into the thickness of clinically important structures. One common attribute of all three objects in the ACR phantom (spheres, rods, and specks) is that they are thin. These objects are designed to simulate masses, spiculations, and calcifications, respectively, in breast images. The

thickness of these objects is comparable to the bar pattern phantom considered in Figure 4.3. For this reason, oblique reconstructions should have clinical applicability in tomosynthesis.

Although the experimental results indicate that thin objects can be resolved in oblique reconstructions, they also demonstrate that high frequency information is lost as the pitch is increased from 0° . To gain more insight into this finding, it is necessary to develop an analytical model of oblique reconstructions in tomosynthesis. To this end, the reconstruction of a pitched sine plate is calculated to determine the visibility of test frequencies in all directions of the reconstruction. From first principles, the optical transfer function (OTF) is also determined by comparing the signal in the image against the attenuation coefficient of the test object at each frequency. The normalized modulus of the OTF yields the modulation transfer function (MTF), which is used to investigate whether modulation is within detectable limits at various pitches and frequencies. A second test object that is simulated in this work is a pitched rod. This object is used to assess whether the length of an object can be correctly estimated along various directions in the reconstruction.

2. METHODS

2.1. Reconstruction Formula for Incomplete Angular Data

From first principles, a general filtered backprojection (FBP) reconstruction formula is now derived for an idealized tomosynthesis system with a parallel-beam geometry. This formula will be used to calculate the reconstruction of a pitched sine

plate and a rod. Although clinical features are 3D, a 2D simulation is developed for a proof-of-principle justification for oblique reconstructions in tomosynthesis.

It is useful to begin this derivation with a review of the Radon Transform. In a parallel beam geometry, the Radon transform is defined by considering the integral of the linear attenuation coefficient of an object over all possible lines $\mathcal{L}(t, \theta)$ in \mathbb{R}^2 . As shown in Figure 4.4, $\mathcal{L}(t, \theta)$ denotes the line that passes through the point $(t \cos \theta, t \sin \theta)$ and that is perpendicular to the unit vector $\mathbf{p} = (\cos \theta)\mathbf{i} + (\sin \theta)\mathbf{k}$, where \mathbf{i} and \mathbf{k} are unit vectors in the x and z directions, respectively, and where $-\infty < t < \infty$ and $-90^\circ < \theta \leq 90^\circ$. Following Hsieh¹⁰ and others, the matrix transformation

$$\begin{pmatrix} x \\ z \end{pmatrix} = \begin{pmatrix} \cos \theta & -\sin \theta \\ \sin \theta & \cos \theta \end{pmatrix} \begin{pmatrix} t \\ s \end{pmatrix} \quad (4.1)$$

provides a parametric representation of the line $\mathcal{L}(t, \theta)$, assuming that (x, z) is a point in \mathbb{R}^2 and that s is a free parameter ranging from $-\infty$ to ∞ . Denoting μ as the linear attenuation coefficient of the input object, the Radon transform can thus be written

$$\mathcal{R}\mu(t, \theta) = \int_{\mathcal{L}(t, \theta)} \mu ds. \quad (4.2)$$

A fundamental relationship between the 1D Fourier transform of $\mathcal{R}\mu(t, \theta)$ and the 2D Fourier transform of $\mu(x, z)$ is established by the Central Slice Theorem^{10, 11}

$$\mathcal{F}_1(\mathcal{R}\mu)(f_r, \theta) = \mathcal{F}_2\mu(f_r \cos \theta, f_r \sin \theta), \quad (4.3)$$

where f_r is radial frequency ranging from $-\infty$ to ∞ . According to Eq. (4.3), each projection samples Fourier space along the angle θ perpendicular to the incident x-ray beam. In tomosynthesis applications for which projections are acquired over a limited

angular range, Figure 4.1(b) shows the corresponding region of Fourier space that is sampled. This region has been termed the FDC in Section 1.

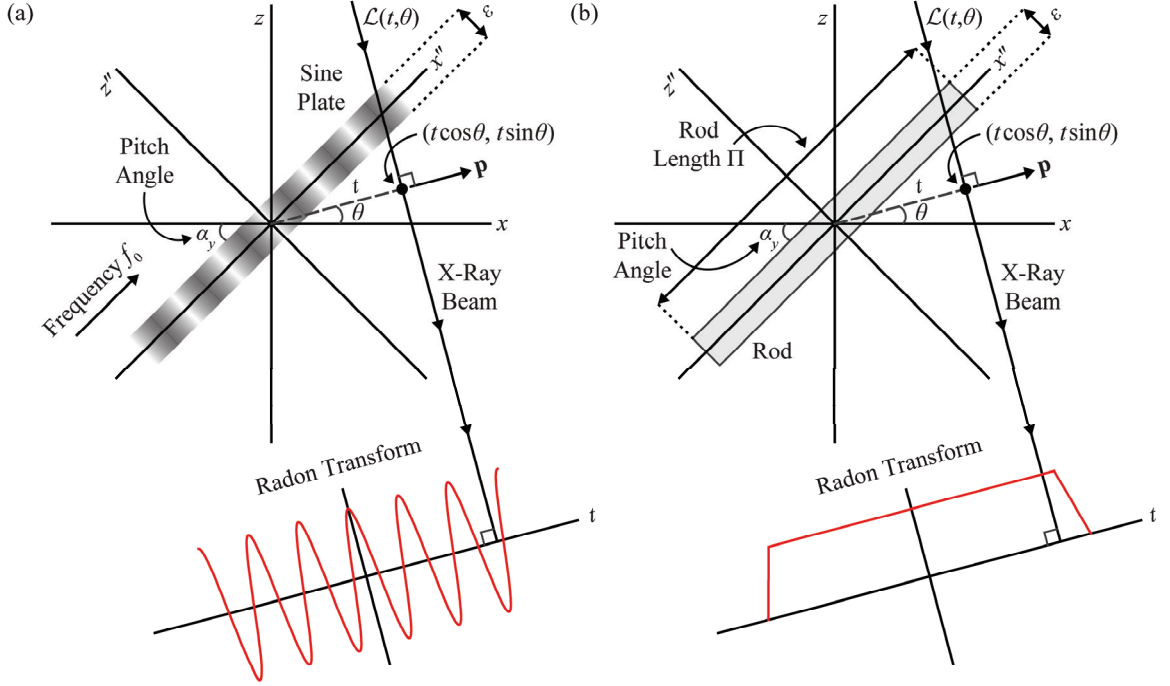


Figure 4.4: Illustration of two test objects and their Radon transforms. In a parallel beam geometry, the Radon transform is defined as the integral of an attenuation coefficient over the line $\mathcal{L}(t, \theta)$. This line intercepts the point $(t \cos \theta, t \sin \theta)$ and is perpendicular to the unit vector $\mathbf{p} = (\cos \theta)\mathbf{i} + (\sin \theta)\mathbf{k}$. At a fixed projection angle θ , the dependency of the Radon transform on the parameter t is illustrated for two test objects. (a) The first object is an infinitely long rectangular prism (thickness ε) whose attenuation coefficient varies sinusoidally along the pitch angle, α_y . (b) The second object is a rod (length Π) that is similarly pitched.

The Central Slice Theorem is now used to derive a formula for the FBP reconstruction of an object in a DBT system with incomplete angular data ranging from $\theta = -\Theta/2$ to $\theta = +\Theta/2$. For the purpose of this derivation, the system is taken to be

noiseless and the angular spacing between projections is infinitesimally small. The FBP reconstruction¹¹ of $\mu(x, z)$ is

$$\mu_{\text{FBP}}(x, z) = \int_{-\Theta/2}^{\Theta/2} (\phi *_{\text{1}} \mathcal{R}\mu)(x \cos \theta + z \sin \theta, \theta) d\theta \quad (4.4)$$

$$= \int_{-\Theta/2}^{\Theta/2} \int_{-\infty}^{\infty} \phi(x \cos \theta + z \sin \theta - \tau) \cdot \mathcal{R}\mu(\tau, \theta) d\tau d\theta, \quad (4.5)$$

where ϕ is the filter and $*_{\text{1}}$ is the 1D convolution operator. Backprojection of $\mathcal{R}\mu(t, \theta)$ to the point (x, z) corresponds to evaluation of the Radon transform at $t = x \cos \theta + z \sin \theta$, as can be deduced from the inverse of the matrix transformation in Eq. (4.1). The transition from Eq. (4.4) to Eq. (4.5) follows directly from the definition of convolution. The 2D Fourier transform¹² of $\mu_{\text{FBP}}(x, z)$ is thus

$$\mathcal{F}_2 \mu_{\text{FBP}}(f_r \cos \zeta, f_r \sin \zeta) = \int_{-\infty}^{\infty} \int_{-\infty}^{\infty} \int_{-\Theta/2}^{\Theta/2} \int_{-\infty}^{\infty} \phi(x \cos \theta + z \sin \theta - \tau) \cdot \mathcal{R}\mu(\tau, \theta) \cdot e^{-2\pi i f_r (x \cos \zeta + z \sin \zeta)} d\tau d\theta dx dz \quad (4.6)$$

where ζ is the polar angle of the 2D frequency vector ($-90^\circ < \zeta \leq 90^\circ$). Eq. (4.6) can be evaluated by changing variables from the (x, z) coordinate system to the (t, s) coordinate system. The differential area element $dx dz$ in Eq. (4.6) should be replaced by $ds dt$, since the Jacobian of the coordinate transformation in Eq. (4.1) is unity.

$$\begin{aligned} \mathcal{F}_2 \mu_{\text{FBP}}(f_r \cos \zeta, f_r \sin \zeta) &= \int_{-\Theta/2}^{\Theta/2} \int_{-\infty}^{\infty} \mathcal{R}\mu(\tau, \theta) \\ &\quad \cdot \left(\int_{-\infty}^{\infty} \phi(t - \tau) \cdot e^{-2\pi i f_r t \cos(\theta - \zeta)} dt \right) \\ &\quad \cdot \left(\int_{-\infty}^{\infty} e^{2\pi i f_r s \sin(\theta - \zeta)} ds \right) d\tau d\theta \end{aligned} \quad (4.7)$$

In Eq. (4.7), the integral over t can be calculated using the Fourier shift theorem¹²

$$\int_{-\infty}^{\infty} \phi(t - \tau) \cdot e^{-2\pi i f_r t \cos(\theta - \zeta)} dt = e^{-2\pi i f_r \tau \cos(\theta - \zeta)} \cdot \mathcal{F}_1 \phi[f_r \cos(\theta - \zeta)], \quad (4.8)$$

and the integral over s can be written in terms of a Dirac delta function.¹³

$$\int_{-\infty}^{\infty} e^{2\pi i f_r s \sin(\theta - \zeta)} ds = \delta[f_r \sin(\theta - \zeta)] \quad (4.9)$$

Eq. (4.9) can be simplified further by noting the composition identity for delta functions.^{13, 14} Assuming that $u(\theta)$ is a function with a finite number of zeros and with no repeated zeros, the identity for the delta function of a composition is

$$\delta[u(\theta)] = \sum_k \frac{\delta(\theta - \theta_{0k})}{|u'(\theta_{0k})|}, \quad (4.10)$$

where θ_{0k} is the k^{th} zero of $u(\theta)$. In evaluating Eq. (4.9), we let $u(\theta) = f_r \sin(\theta - \zeta)$ and hence $\theta_{0k} = k\pi + \zeta$, where $k \in \mathbb{Z}$. Because the only zero of $u(\theta)$ that falls within the integration limits on θ in Eq. (4.7) is θ_{00} , the summation in Eq. (4.10) reduces to the single term for which $k = 0$. Noting that $u'(\theta) = f_r \cos(\theta - \zeta)$, it follows that $u'(\theta_{00}) = f_r$ and Eq. (4.9) simplifies to

$$\delta[f_r \sin(\theta - \zeta)] = \frac{\delta(\theta - \zeta)}{|f_r|}. \quad (4.11)$$

Combining Eqs. (4.7)-(4.11), the 2D Fourier transform of $\mu_{\text{FBP}}(x, z)$ can now be written

$$\begin{aligned} \mathcal{F}_2 \mu_{\text{FBP}}(f_r \cos \zeta, f_r \sin \zeta) &= \int_{-\Theta/2}^{\Theta/2} \left(\int_{-\infty}^{\infty} \mathcal{R} \mu(\tau, \theta) \cdot e^{-2\pi i f_r \tau \cos(\theta - \zeta)} d\tau \right) \\ &\quad \cdot \mathcal{F}_1 \phi[f_r \cos(\theta - \zeta)] \cdot \frac{\delta(\theta - \zeta)}{|f_r|} d\theta. \end{aligned} \quad (4.12)$$

In Eq. (4.12), the integral over τ can be evaluated using the Central Slice theorem [Eq. (4.3)].

$$\begin{aligned} \mathcal{F}_2\mu_{\text{FBP}}(f_r \cos \zeta, f_r \sin \zeta) &= \int_{-\Theta/2}^{\Theta/2} \mathcal{F}_2\mu[f_r \cos(\theta - \zeta) \cos \theta, f_r \cos(\theta - \zeta) \sin \theta] \\ &\quad \cdot \mathcal{F}_1\phi[f_r \cos(\theta - \zeta)] \cdot \frac{\delta(\theta - \zeta)}{|f_r|} d\theta \end{aligned} \quad (4.13)$$

Due to the delta function in Eq. (4.13), this integration is non-trivial only if ζ is between $-\Theta/2$ and $+\Theta/2$; otherwise, the integral vanishes. For this reason, it is important to introduce the function $\text{rect}(\zeta / \Theta)$ in the evaluation of Eq. (4.13), so that

$$\mathcal{F}_2\mu_{\text{FBP}}(f_r \cos \zeta, f_r \sin \zeta) = \frac{1}{|f_r|} \cdot \mathcal{F}_2\mu(f_r \cos \zeta, f_r \sin \zeta) \cdot \mathcal{F}_1\phi(f_r) \cdot \text{rect}\left(\frac{\zeta}{\Theta}\right), \quad (4.14)$$

where

$$\text{rect}(u) \equiv \begin{cases} 1 & , |u| \leq 1/2 \\ 0 & , |u| > 1/2 \end{cases}. \quad (4.15)$$

In Eq. (4.14), the function $\text{rect}(\zeta / \Theta)$ perfectly recovers the FDC whose opening angle is the scan range Θ (Figure 4.1). This result completes the derivation of the general tomosynthesis reconstruction formula.

If one considers the case of complete angular data ($\Theta = 180^\circ$), all of Fourier space is sampled by the projections, and the rectangle function in Eq. (4.14) can be replaced with a constant (unity). By choosing the filter ϕ with the property that $\mathcal{F}_1\phi(f_r) = |f_r|$, it follows directly from Eq. (4.14) that the input object can be reconstructed perfectly. This formula for ϕ is termed the “ramp” filter; it has been previously derived by Hsieh¹⁰ and others for CT applications with complete angular data. This agreement with CT reconstruction theory provides a built-in check on the validity of Eq. (4.14).

With incomplete angular data ($0 < \Theta < 180^\circ$), it is no longer possible to choose a filter ϕ such that there is always agreement between $\mathcal{F}_2\mu_{\text{FBP}}$ and $\mathcal{F}_2\mu$ in Eq. (4.14). In Sections 2.2 and 2.3 of this chapter, Eq. (4.14) is used to calculate the reconstruction of a pitched sine plate and rod in tomosynthesis applications with incomplete angular data.

In determining the reconstruction of the two test objects, an important property to simplify calculations is that the spatial representation of the reconstruction is real-valued. Following the convolution theorem, the spatial representation is

$$\mu_{\text{FBP}}(x, z) = \mu(x, z) *_2 \mathcal{F}_2^{-1} \left[\frac{1}{|f_r|} \cdot \mathcal{F}_1\phi(f_r) \cdot \text{rect}\left(\frac{\zeta}{\Theta}\right) \right] (x, z), \quad (4.16)$$

where $*_2$ denotes the 2D convolution operator. From standard properties, the 2D inverse Fourier transform to the right of the convolution operator must be real-valued if the argument in the rectangular brackets is an even function. Since $1/|f_r|$ and $\text{rect}(\zeta/\Theta)$ are even functions, it follows that the reconstruction is real-valued provided that $\mathcal{F}_1\phi(f_r)$ is also even. This work is limited to filters that satisfy this evenness property.

2.2. Reconstruction of a Pitched Sine Plate

A framework for investigating the reconstruction of a sine plate is now developed by modeling an infinitely long rectangular prism whose attenuation coefficient varies sinusoidally along the pitch α_y . To illustrate that reconstructions are feasible along a broad range of pitches, the angle α_y is taken to be larger than $\Theta/2$, so that the pitch is outside the opening angle of the FDC (Figure 4.1)

$$\mu(x'', z'') = C \cdot \cos(2\pi f_0 x'') \cdot \text{rect}\left(\frac{z''}{\varepsilon}\right), \quad (4.17)$$

where

$$\begin{pmatrix} x'' \\ z'' \end{pmatrix} = \begin{pmatrix} \cos \alpha_y & \sin \alpha_y \\ -\sin \alpha_y & \cos \alpha_y \end{pmatrix} \begin{pmatrix} x \\ z \end{pmatrix}. \quad (4.18)$$

In this formulation, C denotes the maximum value of the attenuation coefficient of the material, f_0 is the input frequency, x'' indicates position along the pitch α_y , and z'' measures position along the thickness (ε) of the sine plate [Figure 4.4(a)]. The transformation matrix given in Eq. (4.18) changes variables between the (x, z) coordinate system and a rotated reference frame whose coordinate axes match the long and short axes of the pitched sine plate, respectively. The subscript y on the variable α_y emphasizes that changing the pitch is equivalent to rotating the x and z axes about the y axis perpendicular to the plane of the parallel projections. For the purpose of this work, it is assumed that $0 \leq \alpha_y \leq 90^\circ$.

To illustrate the calculation of $\mathcal{R}\mu(t, \theta)$, the Radon transform of this object is plotted versus t in Figure 4.4(a) at a fixed projection angle (θ). Appendix A demonstrates from first principles that this plot is sinusoidal with frequency $f_0 \sec(\theta - \alpha_y)$, as shown in the figure.

To calculate the tomosynthesis reconstruction of the sine plate [Eq. (4.14)], it is first necessary to determine the Fourier transform of the sine plate

$$\mathcal{F}_2\mu(f_x, f_z) \equiv \int_{-\infty}^{\infty} \int_{-\infty}^{\infty} \mu(x, z) e^{-2\pi i(f_x x + f_z z)} dx dz \quad (4.19)$$

$$= \int_{-\infty}^{\infty} \int_{-\infty}^{\infty} \mu(x'', z'') e^{-2\pi i(f_x'' x'' + f_z'' z'')} dx'' dz'' . \quad (4.20)$$

In Eq. (4.20), the frequency variables (f_x'', f_z'') are defined by a rotated reference frame analogous to the (x'', z'') coordinate system

$$\begin{pmatrix} f_x'' \\ f_z'' \end{pmatrix} = \begin{pmatrix} \cos \alpha_y & \sin \alpha_y \\ -\sin \alpha_y & \cos \alpha_y \end{pmatrix} \begin{pmatrix} f_x \\ f_z \end{pmatrix}. \quad (4.21)$$

Substituting Eq. (4.17) into Eq. (4.20) yields

$$\mathcal{F}_2 \mu(f_x'', f_z'') = \frac{C\varepsilon}{2} \left[\delta(f_x'' - f_0) + \delta(f_x'' + f_0) \right] \text{sinc}(\varepsilon f_z''), \quad (4.22)$$

where

$$\text{sinc}(u) \equiv \frac{\sin(\pi u)}{\pi u}. \quad (4.23)$$

Using Eq. (4.22) in conjunction with Eq. (4.14), the FBP reconstruction can now be written as the inverse 2D Fourier transform

$$\mu_{\text{FBP}} = \int_{-\infty}^{\infty} \int_{-\infty}^{\infty} \frac{\mathcal{F}_2 \mu}{\sqrt{f_x^2 + f_z^2}} \cdot \mathcal{F}_1 \phi(f_r) \cdot \text{rect}\left(\frac{\zeta}{\Theta}\right) \cdot e^{2\pi i(xf_x + zf_z)} df_x df_z \quad (4.24)$$

$$= \int_{-\infty}^{\infty} \int_{-\infty}^{\infty} \frac{\mathcal{F}_2 \mu}{\sqrt{f_x^2 + f_z^2}} \cdot \mathcal{F}_1 \phi(|f_r|) \cdot \text{rect}\left(\frac{\zeta}{\Theta}\right) \cdot \cos[2\pi(xf_x + zf_z)] df_x df_z. \quad (4.25)$$

The transition from Eq. (4.24) to Eq. (4.25) is justified from *a priori* knowledge that the reconstruction is real-valued. Eq. (4.25) can now be evaluated by changing variables into the (f_x'', f_z'') and (x'', z'') coordinate systems. Combining Eqs. (4.18), (4.21), (4.22) and (4.25) gives

$$\begin{aligned}
\mu_{\text{FBP}} = & \frac{C\varepsilon}{2} \int_{-\infty}^{\infty} \int_{-\infty}^{\infty} \delta(f_x'' + f_0) \cdot \mathcal{F}_1\phi(|f_r|) \cdot \text{rect}\left(\frac{\zeta}{\Theta}\right) \\
& \cdot \frac{\cos\left[2\pi(x''f_x'' + z''f_z'')\right] \text{sinc}(\varepsilon f_z'')}{\sqrt{f_x''^2 + f_z''^2}} df_x'' df_z'' \\
& + \frac{C\varepsilon}{2} \int_{-\infty}^{\infty} \int_{-\infty}^{\infty} \delta(f_x'' - f_0) \cdot \mathcal{F}_1\phi(|f_r|) \cdot \text{rect}\left(\frac{\zeta}{\Theta}\right) \\
& \cdot \frac{\cos\left[2\pi(x''f_x'' + z''f_z'')\right] \text{sinc}(\varepsilon f_z'')}{\sqrt{f_x''^2 + f_z''^2}} df_x'' df_z'' .
\end{aligned} \tag{4.26}$$

In evaluating this expression, the inner integrals over f_x'' can be simplified by substituting the constraints $f_x'' = -f_0$ and $f_x'' = +f_0$ into the terms to the right of the delta function in each respective integrand. This step follows directly from the definition of the delta function. Because of the term $\text{rect}(\zeta/\Theta)$, the outer integral over f_z'' must then be evaluated along integration limits given from the intersection of the FDC with the lines $f_x'' = \pm f_0$. Figure 4.5(a) shows a pitch for which this intersection consists of two line segments. At larger pitches approaching 90° , the intersection consists of infinitely long rays [Figure 4.5(b)]. FBP reconstruction is now calculated separately for these two cases.

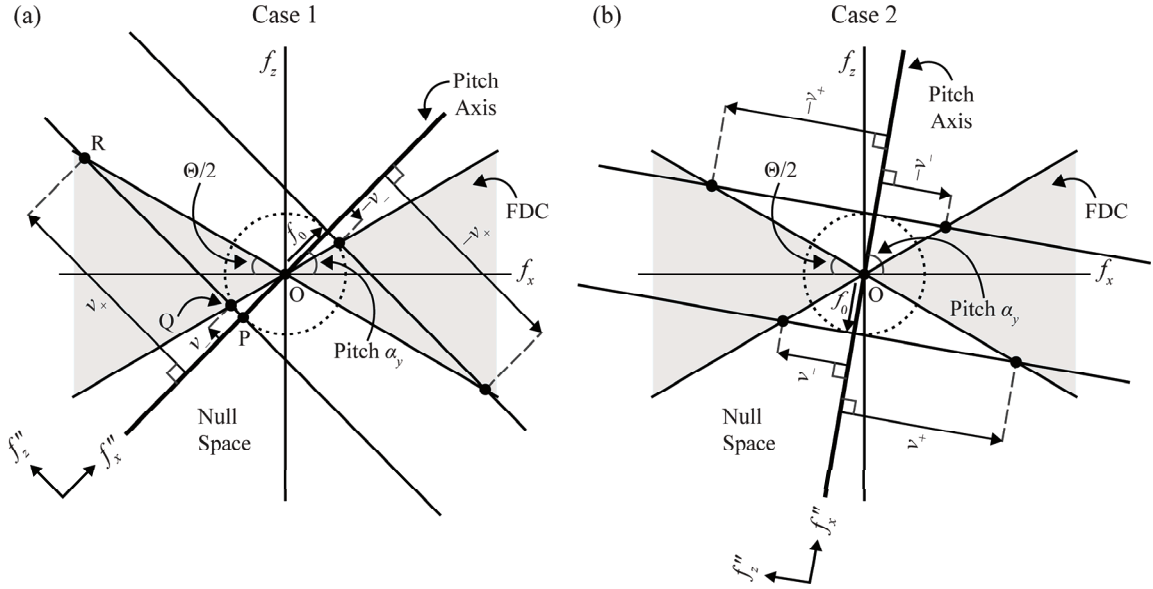


Figure 4.5: Illustration of the sampling of Fourier space for a pitched sine plate. (a) By rotating the coordinate axes of Fourier space by the pitch of the test object, it can be shown that the Fourier transform of a sine plate with frequency f_0 [Figure 4.4(a)] consists of the two lines $f_x'' = \pm f_0$. As shown, these lines intersect the FDC along two line segments. This property holds if $0 \leq \alpha_y < 90^\circ - \Theta/2$. (b) At larger pitches for which $90^\circ - \Theta/2 < \alpha_y \leq 90^\circ$, it can be demonstrated that the Fourier transform of the sine plate intersects the FDC along four rays.

2.2.1. Case 1

Figure 4.5(a) illustrates a pitch for which the FDC intersects the lines $f_x'' = \pm f_0$ along two line segments. The coordinates of the two lines segments are now derived. It is shown in Figure 4.5(a) that, along the line $f_x'' = -f_0$, the first line segment lies along the f_z'' direction with extent between $|\overline{PQ}|$ and $|\overline{PR}|$. In applying trigonometry to the right triangle OPQ, it follows that

$$|\overline{PQ}| = |\overline{OP}| \cdot \tan(\alpha_y - \Theta/2) \quad (4.27)$$

$$= f_0 \tan(\alpha_y - \Theta/2). \quad (4.28)$$

Similarly, in considering the right triangle OPR,

$$|\overrightarrow{PR}| = |\overrightarrow{OP}| \cdot \tan(\alpha_y + \Theta/2) \quad (4.29)$$

$$= f_0 \tan(\alpha_y + \Theta/2). \quad (4.30)$$

In Eq. (4.30), the tangent function tends to infinity if $\alpha_y = 90^\circ - \Theta/2$. For this reason, if the pitch falls between the limits $90^\circ - \Theta/2 < \alpha_y < 90^\circ$, it is no longer true that the FDC intersects the lines $f_x'' = \pm f_0$ along line segments. Instead, the intersection consists of infinitely long rays. This case is considered in Section 2.2.2. To simplify Eqs. (4.28) and (4.30), one can introduce the term ν_\pm

$$\nu_\pm \equiv f_0 \tan(\alpha_y \pm \Theta/2), \quad (4.31)$$

so that Eq. (4.26) can be evaluated as

$$\mu_{\text{FBP}} = \frac{C\varepsilon}{2} \left[\int_{\nu_-}^{\nu_+} \frac{\mathcal{F}_1 \phi \left(\sqrt{f_0^2 + f_z''^2} \right) \cos \left[2\pi(-x''f_0 + z''f_z'') \right] \text{sinc}(\varepsilon f_z'')}{\sqrt{f_0^2 + f_z''^2}} df_z'' + \int_{-\nu_+}^{-\nu_-} \frac{\mathcal{F}_1 \phi \left(\sqrt{f_0^2 + f_z''^2} \right) \cos \left[2\pi(x''f_0 + z''f_z'') \right] \text{sinc}(\varepsilon f_z'')}{\sqrt{f_0^2 + f_z''^2}} df_z'' \right] \quad (4.32)$$

$$\begin{aligned}
&= \frac{C\varepsilon}{2} \left[\begin{aligned} &\cos(2\pi x'' f_0) \left(\int_{v_-}^{v_+} \frac{\mathcal{F}_1 \phi \left(\sqrt{f_0^2 + f_z''^2} \right) \cos(2\pi z'' f_z'') \text{sinc}(\varepsilon f_z'')}{\sqrt{f_0^2 + f_z''^2}} df_z'' \right. \\ &\quad \left. + \int_{-v_+}^{-v_-} \frac{\mathcal{F}_1 \phi \left(\sqrt{f_0^2 + f_z''^2} \right) \cos(2\pi z'' f_z'') \text{sinc}(\varepsilon f_z'')}{\sqrt{f_0^2 + f_z''^2}} df_z'' \right) \\ &+ \sin(2\pi x'' f_0) \left(\int_{v_-}^{v_+} \frac{\mathcal{F}_1 \phi \left(\sqrt{f_0^2 + f_z''^2} \right) \sin(2\pi z'' f_z'') \text{sinc}(\varepsilon f_z'')}{\sqrt{f_0^2 + f_z''^2}} df_z'' \right. \\ &\quad \left. - \int_{-v_+}^{-v_-} \frac{\mathcal{F}_1 \phi \left(\sqrt{f_0^2 + f_z''^2} \right) \sin(2\pi z'' f_z'') \text{sinc}(\varepsilon f_z'')}{\sqrt{f_0^2 + f_z''^2}} df_z'' \right) \end{aligned} \right] \quad (4.33)
\end{aligned}$$

In deriving Eq. (4.32), a symmetry property has been used to determine the integration limits along the line $f_x'' = +f_0$ from knowledge of the analogous limits along the line $f_x'' = -f_0$. The transition from Eq. (4.32) to (4.33) is justified by the angle-sum identity

$$\cos(b_1 + b_2) = \cos(b_1)\cos(b_2) - \sin(b_1)\sin(b_2) \quad (4.34)$$

for the real numbers b_1 and b_2 . Eq. (4.33) can now be simplified by noting that the first and second integrals are equivalent, despite the different integration limits. This result holds because the integrands are an even function of f_z'' , and the two integration intervals are at equivalent distances from $f_z'' = 0$. It can also be shown that the third and fourth integrals in Eq. (4.33) have the same magnitude but opposite sign. This claim follows from the fact that each integrand is an odd function of f_z'' , and the two integration intervals are at the same distance from $f_z'' = 0$. The negative sign preceding the fourth integral yields net equivalence with the third integral, so that

$$\mu_{\text{FBP}} = C\varepsilon \left[\begin{aligned} &\cos(2\pi x''f_0) \int_{\nu_-}^{\nu_+} \frac{\mathcal{F}_1\phi\left(\sqrt{f_0^2 + f_z''^2}\right) \cos(2\pi z''f_z'') \text{sinc}(\varepsilon f_z'')}{\sqrt{f_0^2 + f_z''^2}} df_z'' \\ &+ \sin(2\pi x''f_0) \int_{\nu_-}^{\nu_+} \frac{\mathcal{F}_1\phi\left(\sqrt{f_0^2 + f_z''^2}\right) \sin(2\pi z''f_z'') \text{sinc}(\varepsilon f_z'')}{\sqrt{f_0^2 + f_z''^2}} df_z'' \end{aligned} \right] \quad (4.35)$$

It would be difficult to evaluate the two integrals analytically in Eq. (4.35). Instead, they can be determined numerically using the midpoint formula for integration.¹⁵

$$\mu_{\text{FBP}} \cong C\varepsilon(\nu_+ - \nu_-) \cdot \lim_{J \rightarrow \infty} \frac{1}{J} \left[\begin{aligned} &\cos(2\pi x''f_0) \sum_{j=1}^J \frac{\mathcal{F}_1\phi\left(\sqrt{f_0^2 + f_{z_j}''^2}\right) \cos(2\pi z''f_{z_j}'') \text{sinc}(\varepsilon f_{z_j}'')}{\sqrt{f_0^2 + f_{z_j}''^2}} \\ &+ \sin(2\pi x''f_0) \sum_{j=1}^J \frac{\mathcal{F}_1\phi\left(\sqrt{f_0^2 + f_{z_j}''^2}\right) \sin(2\pi z''f_{z_j}'') \text{sinc}(\varepsilon f_{z_j}'')}{\sqrt{f_0^2 + f_{z_j}''^2}} \end{aligned} \right] \quad (4.36)$$

In applying the midpoint formula to Eq. (4.35), the interval $[\nu_-, \nu_+]$, which corresponds to the integration limits, is evenly partitioned into sub-intervals. The midpoint of the j^{th} sub-interval is

$$f_{z_j}'' \equiv \nu_- + \frac{(j-1/2)(\nu_+ - \nu_-)}{J}, \quad (4.37)$$

where J is the total number of sub-intervals ($J \rightarrow \infty$). The midpoint formula is a valid approximation method provided that the integration limits are finite. This property holds if $0^\circ \leq \alpha_y < 90^\circ - \Theta/2$.

2.2.2. Case 2

In Section 2.2, it was demonstrated that the FDC intersects the lines $f_x'' = \pm f_0$ along infinitely long rays if the pitch satisfies the inequality $90^\circ - \Theta/2 < \alpha_y \leq 90^\circ$.

Figure 4.5(b) shows the four rays of intersection. It follows that

$$\mu_{\text{FBP}} = \frac{C\varepsilon}{2} \left[\begin{aligned} & \int_{-\infty}^{V_+} \frac{\mathcal{F}_1 \phi \left(\sqrt{f_0^2 + f_z''^2} \right) \cos \left[2\pi(-x''f_0 + z''f_z'') \right] \text{sinc}(\varepsilon f_z'')}{\sqrt{f_0^2 + f_z''^2}} df_z'' \\ & + \int_{V_-}^{\infty} \frac{\mathcal{F}_1 \phi \left(\sqrt{f_0^2 + f_z''^2} \right) \cos \left[2\pi(-x''f_0 + z''f_z'') \right] \text{sinc}(\varepsilon f_z'')}{\sqrt{f_0^2 + f_z''^2}} df_z'' \\ & + \int_{-\infty}^{-V_-} \frac{\mathcal{F}_1 \phi \left(\sqrt{f_0^2 + f_z''^2} \right) \cos \left[2\pi(x''f_0 + z''f_z'') \right] \text{sinc}(\varepsilon f_z'')}{\sqrt{f_0^2 + f_z''^2}} df_z'' \\ & + \int_{-V_+}^{\infty} \frac{\mathcal{F}_1 \phi \left(\sqrt{f_0^2 + f_z''^2} \right) \cos \left[2\pi(x''f_0 + z''f_z'') \right] \text{sinc}(\varepsilon f_z'')}{\sqrt{f_0^2 + f_z''^2}} df_z'' \end{aligned} \right] \quad (4.38)$$

$$= C\varepsilon \left[\begin{aligned} & \cos(2\pi x''f_0) \left(\int_{-\infty}^{V_+} \frac{\mathcal{F}_1 \phi \left(\sqrt{f_0^2 + f_z''^2} \right) \cos(2\pi z''f_z'') \text{sinc}(\varepsilon f_z'')}{\sqrt{f_0^2 + f_z''^2}} df_z'' \right. \\ & \quad \left. + \int_{V_-}^{\infty} \frac{\mathcal{F}_1 \phi \left(\sqrt{f_0^2 + f_z''^2} \right) \cos(2\pi z''f_z'') \text{sinc}(\varepsilon f_z'')}{\sqrt{f_0^2 + f_z''^2}} df_z'' \right) \\ & + \sin(2\pi x''f_0) \left(\int_{-\infty}^{V_+} \frac{\mathcal{F}_1 \phi \left(\sqrt{f_0^2 + f_z''^2} \right) \sin(2\pi z''f_z'') \text{sinc}(\varepsilon f_z'')}{\sqrt{f_0^2 + f_z''^2}} df_z'' \right. \\ & \quad \left. + \int_{V_-}^{\infty} \frac{\mathcal{F}_1 \phi \left(\sqrt{f_0^2 + f_z''^2} \right) \sin(2\pi z''f_z'') \text{sinc}(\varepsilon f_z'')}{\sqrt{f_0^2 + f_z''^2}} df_z'' \right) \end{aligned} \right] \quad (4.39)$$

One can justify the transition from Eq. (4.38) to (4.39) by applying steps analogous to the ones used between Eqs. (4.32) and (4.35). Since the integration limits are not all finite, it is no longer acceptable to evaluate these integrals with the midpoint formula. For the purpose of this work, the integrals are evaluated numerically in MATLAB R2012b using the “integral” command.

2.3. Reconstruction of a Pitched Rod

The reconstruction of a pitched rod is now determined by modifying the attenuation coefficient of the input object in Eq. (4.17). The rod is modeled as a rectangle function with length (Π) aligned along the pitch α_y [Figure 4.4(b)].

$$\mu(x'', z'') = C \cdot \text{rect}\left(\frac{x''}{\Pi}\right) \cdot \text{rect}\left(\frac{z''}{\varepsilon}\right) \quad (4.40)$$

Similar to the sine plate, the rod thickness is ε , and the maximum value of the attenuation coefficient is C . The pitch α_y is assumed to be larger than $\Theta/2$, so that the long axis of the rod is not within the opening angle of the FDC. To illustrate the Radon transform of this object, its dependency on t is shown in Figure 4.4(b) at a fixed projection angle (θ). The Radon transform is calculated in Appendix B from first principles.

As discussed in Section 2.2, it is necessary to calculate the Fourier transform of the input object in order to derive the reconstruction. Following Eq. (4.20), this transform can be written

$$\mathcal{F}_2\mu(f_x'', f_z'') = C\Pi\varepsilon \cdot \text{sinc}(\Pi f_x'') \text{sinc}(\varepsilon f_z''). \quad (4.41)$$

The reconstruction can now be determined by substituting Eq. (4.41) into Eq. (4.25).

$$\mu_{\text{FBP}}(x, z) = C\Pi\varepsilon \int_{-\infty}^{\infty} \int_{-\infty}^{\infty} \frac{\text{sinc}(\Pi f_x'') \text{sinc}(\varepsilon f_z'')}{\sqrt{f_x^2 + f_z^2}} \cdot \mathcal{F}_1\phi(|f_r|) \cdot \text{rect}\left(\frac{\zeta}{\Theta}\right) \cdot \cos[2\pi(xf_x + zf_z)] df_z df_x \quad (4.42)$$

$$\begin{aligned} &= C\Pi\varepsilon \int_{-\infty}^0 \int_{f_x \tan(\Theta/2)}^{-f_x \tan(\Theta/2)} \frac{\text{sinc}\left[\Pi(f_x \cos \alpha_y + f_z \sin \alpha_y)\right]}{\sqrt{f_x^2 + f_z^2}} \\ &\quad \cdot \text{sinc}\left[\varepsilon(-f_x \sin \alpha_y + f_z \cos \alpha_y)\right] \mathcal{F}_1\phi(|f_r|) \cos[2\pi(xf_x + zf_z)] df_z df_x \\ &+ C\Pi\varepsilon \int_0^{\infty} \int_{-f_x \tan(\Theta/2)}^{f_x \tan(\Theta/2)} \frac{\text{sinc}\left[\Pi(f_x \cos \alpha_y + f_z \sin \alpha_y)\right]}{\sqrt{f_x^2 + f_z^2}} \\ &\quad \cdot \text{sinc}\left[\varepsilon(-f_x \sin \alpha_y + f_z \cos \alpha_y)\right] \mathcal{F}_1\phi(|f_r|) \cos[2\pi(xf_x + zf_z)] df_z df_x \end{aligned} \quad (4.43)$$

To transition from Eq. (4.42) to Eq. (4.43), the arguments of the sinc functions are transformed into the (f_x, f_z) coordinate system using Eq. (4.21). Also, the limits of the inner integral over f_z are modified to model the FDC. Because it would be difficult to evaluate the inner integrals over f_z in closed form, the midpoint formula¹⁵ can now be used as an approximation technique. Similar to Eq. (4.35), the two intervals of integration in Eq. (4.43) should be evenly partitioned into sub-intervals numbered between $k=1$ and K , so that

$$\begin{aligned} \mu_{\text{FBP}}(x, z) &= C\Pi\varepsilon \int_{-\infty}^0 \lim_{K \rightarrow \infty} \frac{-2f_x \tan(\Theta/2)}{K} \sum_{k=1}^K \frac{\mathcal{F}_1\phi\left(\sqrt{f_x^2 + f_{zk}^2}\right)}{\sqrt{f_x^2 + f_{zk}^2}} \\ &\quad \cdot \text{sinc}(\Upsilon_{1k}^- f_x) \text{sinc}(\Upsilon_{2k}^- f_x) \cos(\pi \Upsilon_{3k}^- f_x) df_x \\ &+ C\Pi\varepsilon \int_0^{\infty} \lim_{K \rightarrow \infty} \frac{2f_x \tan(\Theta/2)}{K} \sum_{k=1}^K \frac{\mathcal{F}_1\phi\left(\sqrt{f_x^2 + f_{zk}^2}\right)}{\sqrt{f_x^2 + f_{zk}^2}} \\ &\quad \cdot \text{sinc}(\Upsilon_{1k}^+ f_x) \text{sinc}(\Upsilon_{2k}^+ f_x) \cos(\pi \Upsilon_{3k}^+ f_x) df_x \end{aligned} \quad (4.44)$$

where

$$f_{zk} \equiv 2f_x \tan\left(\frac{\Theta}{2}\right) \left[\frac{k-1/2}{K} - \frac{1}{2} \right] \quad (4.45)$$

$$\Upsilon_{1k}^{\pm} \equiv \Pi \left[\cos \alpha_y \pm 2 \left(\frac{k-1/2}{K} - \frac{1}{2} \right) \tan\left(\frac{\Theta}{2}\right) \sin(\alpha_y) \right] \quad (4.46)$$

$$\Upsilon_{2k}^{\pm} \equiv \varepsilon \left[-\sin \alpha_y \pm 2 \left(\frac{k-1/2}{K} - \frac{1}{2} \right) \tan\left(\frac{\Theta}{2}\right) \cos(\alpha_y) \right] \quad (4.47)$$

$$\Upsilon_{3k}^{\pm} \equiv 2 \left[x \pm 2z \left(\frac{k-1/2}{K} - \frac{1}{2} \right) \tan\left(\frac{\Theta}{2}\right) \right]. \quad (4.48)$$

The integrals in Eq. (4.44) cannot be evaluated analytically for the most general filter ϕ .

One special case that can be simplified, however, is simple backprojection (SBP) reconstruction for which $\mathcal{F}_1\phi(f_r) = 1$.

$$\begin{aligned} \mathcal{B}(\mathcal{R}\mu)(x, z) = & C\Pi\varepsilon \int_{-\infty}^0 \lim_{K \rightarrow \infty} \frac{-2f_x \tan(\Theta/2)}{K} \\ & \cdot \sum_{k=1}^K \frac{\text{sinc}(\Upsilon_{1k}^- f_x) \text{sinc}(\Upsilon_{2k}^- f_x) \cos(\pi \Upsilon_{3k}^- f_x)}{\sqrt{f_x^2 \left(1 + 4 \tan^2\left(\frac{\Theta}{2}\right) \left[\frac{k-1/2}{K} - \frac{1}{2} \right]^2 \right)}} df_x \\ & + C\Pi\varepsilon \int_0^{\infty} \lim_{K \rightarrow \infty} \frac{2f_x \tan(\Theta/2)}{K} \\ & \cdot \sum_{k=1}^K \frac{\text{sinc}(\Upsilon_{1k}^+ f_x) \text{sinc}(\Upsilon_{2k}^+ f_x) \cos(\pi \Upsilon_{3k}^+ f_x)}{\sqrt{f_x^2 \left(1 + 4 \tan^2\left(\frac{\Theta}{2}\right) \left[\frac{k-1/2}{K} - \frac{1}{2} \right]^2 \right)}} df_x \end{aligned} \quad (4.49)$$

Since

$$\sqrt{f_x^2} = \begin{cases} -f_x, & f_x < 0 \\ +f_x, & f_x \geq 0 \end{cases}, \quad (4.50)$$

it follows that

$$\begin{aligned}
\mathcal{B}(\mathcal{R}\mu)(x, z) &= C\Pi\varepsilon \int_{-\infty}^0 \lim_{K \rightarrow \infty} \frac{-2f_x \tan(\Theta/2)}{K} \\
&\quad \cdot \sum_{k=1}^K \frac{\text{sinc}(\Upsilon_{1k}^- f_x) \text{sinc}(\Upsilon_{2k}^- f_x) \cos(\pi \Upsilon_{3k}^- f_x)}{(-f_x) \sqrt{1 + 4 \tan^2 \left(\frac{\Theta}{2} \right) \left[\frac{k-1/2}{K} - \frac{1}{2} \right]^2}} df_x \\
&\quad + C\Pi\varepsilon \int_0^{\infty} \lim_{K \rightarrow \infty} \frac{2f_x \tan(\Theta/2)}{K} \\
&\quad \cdot \sum_{k=1}^K \frac{\text{sinc}(\Upsilon_{1k}^+ f_x) \text{sinc}(\Upsilon_{2k}^+ f_x) \cos(\pi \Upsilon_{3k}^+ f_x)}{(f_x) \sqrt{1 + 4 \tan^2 \left(\frac{\Theta}{2} \right) \left[\frac{k-1/2}{K} - \frac{1}{2} \right]^2}} df_x \\
&= 2C\Pi\varepsilon \tan(\Theta/2) \cdot \lim_{K \rightarrow \infty} \sum_{k=1}^K \frac{I_{k,\text{SBP}}^- + I_{k,\text{SBP}}^+}{K \sqrt{1 + 4 \tan^2 \left(\frac{\Theta}{2} \right) \left[\frac{k-1/2}{K} - \frac{1}{2} \right]^2}}, \tag{4.51}
\end{aligned}$$

where

$$I_{k,\text{SBP}}^- = \int_{-\infty}^0 \text{sinc}(\Upsilon_{1k}^- f_x) \text{sinc}(\Upsilon_{2k}^- f_x) \cos(\pi \Upsilon_{3k}^- f_x) df_x \tag{4.53}$$

$$I_{k,\text{SBP}}^+ = \int_0^{\infty} \text{sinc}(\Upsilon_{1k}^+ f_x) \text{sinc}(\Upsilon_{2k}^+ f_x) \cos(\pi \Upsilon_{3k}^+ f_x) df_x. \tag{4.54}$$

Using a computer algebra system to evaluate Eqs. (4.53)-(4.54), it can be shown that

$$I_{k,\text{SBP}}^{\pm} = \frac{\left(\begin{aligned} &\left| \Upsilon_{1k}^{\pm} + \Upsilon_{2k}^{\pm} + \Upsilon_{3k}^{\pm} \right| + \left| \Upsilon_{1k}^{\pm} + \Upsilon_{2k}^{\pm} - \Upsilon_{3k}^{\pm} \right| \\ &- \left| \Upsilon_{1k}^{\pm} - \Upsilon_{2k}^{\pm} + \Upsilon_{3k}^{\pm} \right| - \left| \Upsilon_{1k}^{\pm} - \Upsilon_{2k}^{\pm} - \Upsilon_{3k}^{\pm} \right| \end{aligned} \right)}{8 \Upsilon_{1k}^{\pm} \Upsilon_{2k}^{\pm}}, \tag{4.55}$$

completing the derivation of the SBP reconstruction.

3. RESULTS

3.1. Sine Plate

3.1.1. *Visualization of the Reconstruction*

Image acquisition is now simulated for a tomosynthesis system comparable to the Selenia Dimensions DBT unit (Hologic Inc., Bedford, MA) with an angular range (Θ) of 15° , assuming that the sine plate has a thickness (ϵ) of 0.10 mm and a frequency (f_0) of 2.0 lp/mm. Following our previous work, the attenuation coefficient of the sine plate is normalized so that total attenuation is unity for the central projection for which $\theta = 0^\circ$. Accordingly, we let $C = 1/(\epsilon \sec \alpha_y)$. The denominator in this expression is the x-ray path length through the object for the central projection.

In Figure 4.6, SBP reconstruction is displayed as a grayscale image in the xz plane, which is analogous to the plane of the chest wall in a breast application. The two subplots (a) and (b) correspond to two pitches for the sine plate; namely, 0° and 45° . An oscillatory pattern with the frequency of the input object is correctly resolved along both pitches. This finding illustrates that an input frequency with a pitch well outside the opening angle of the FDC can be resolved in tomosynthesis.

Figure 4.6 also shows that the reconstruction greatly overestimates the thickness of the sine plate due to backprojection artifacts. This result is observed at both the 0° and 45° pitches. Similar backprojection artifacts would not be present in an FBP reconstruction for CT with complete angular data ($\Theta = 180^\circ$).

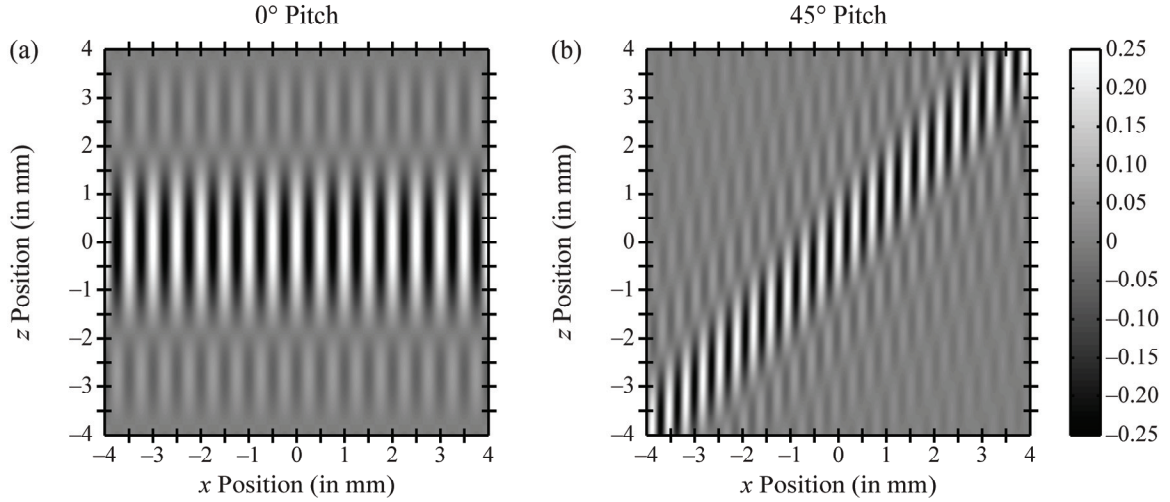


Figure 4.6: Reconstruction of a pitched sine plate in the plane of x-ray tube motion. The simple backprojection (SBP) reconstruction of a sine plate [Figure 4.4(a)] is displayed as a grayscale image in the xz plane, assuming that $\Theta = 15^\circ$, $\varepsilon = 0.10$ mm, and $f_0 = 2.0$ lp/mm. While it is conventional to display the reconstruction with slices oriented along a 0° pitch (that is, with fixed values of z), this figure is useful for showing that an oscillatory pattern can be resolved along the two object pitches, 0° and 45° . The oscillatory pattern has the correct frequency along each pitch. Due to the limited angular range of the projections, backprojection artifacts cause the thickness of the object to be overestimated.

In a clinical application of DBT, the reconstruction is not typically viewed in the xz plane as it is shown in Figure 4.6. Instead, the reconstruction is conventionally displayed as a series of slices oriented along a 0° pitch. In order to simulate the clinical display of a reconstruction more closely, signal should be plotted versus position (x) measured along a 0° pitch, regardless of the pitch of the input object. Figure 4.7(a)-(c) shows this result for a sine plate pitched at a 45° angle similar to Figure 4.6(b). The three plots correspond to three different reconstruction depths (z) given by -3.0 , 0 , and $+3.0$ mm. By viewing these three slices, it is difficult to deduce that the input object is sinusoidal along a 45° pitch. Instead, the object appears as if it were a dampened sine wave whose maximum shifts along the x direction with increasing depth, z . The spacing

between adjacent peaks near the maximum is approximately 0.34 mm, corresponding to a frequency of 2.9 lp/mm. This frequency does not match the input frequency (f_0) of 2.0 lp/mm. It should be noted that the sine plate actually spans a length of $\varepsilon \sec \alpha_y$, or 0.14 mm, within each slice in Figure 4.7(a)-(c). Signal extends across a much broader length than 0.14 mm due to backprojection artifacts, causing the dimension of the object within the slice to be greatly overestimated.

To demonstrate that the same object can be better visualized in an oblique reconstruction, the pitch of the slice is changed to 45° in Figure 4.7(d). This slice is generated at the depth ($z'' = 0$) corresponding to the mid-thickness of the sine plate along the pitch axis. Figure 4.7(d) illustrates that signal is sinusoidal with the correct frequency, 2.0 lp/mm. For this reason, the 45° pitch is the preferred orientation for displaying slices for this object.

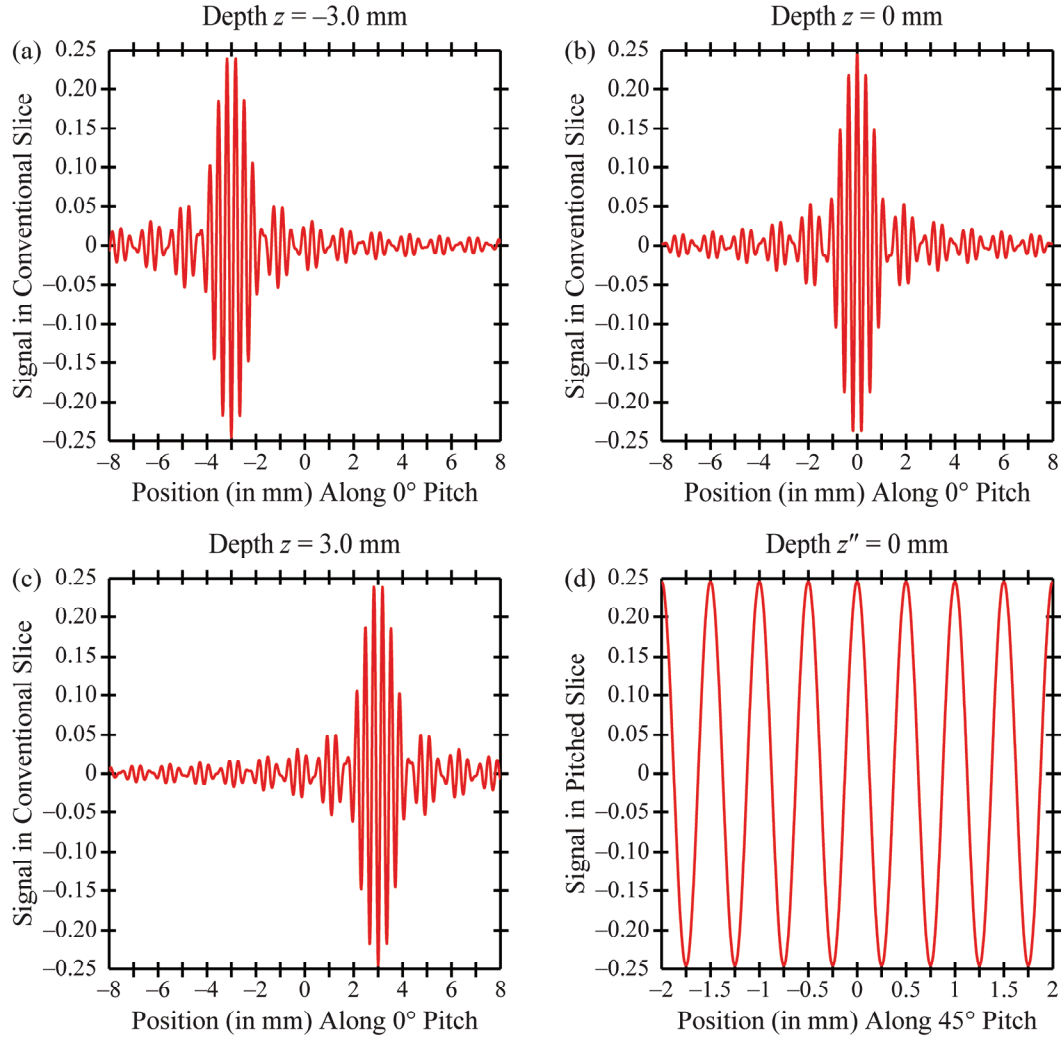


Figure 4.7: Tomographic slices for a pitched sine plate. (a)-(c) Following convention, the reconstruction in Figure 4.6(b) is displayed using slices oriented along a 0° pitch. Each slice corresponds to a fixed depth z . It is difficult to deduce that the test object is sinusoidal along a 45° pitch. (d) In viewing a slice through the mid-thickness of the object at a 45° pitch ($z''=0$), it becomes clear that the attenuation coefficient is sinusoidal along this direction. For this reason, the 45° pitch is the preferred orientation for displaying slices through this object.

3.1.2. Modulation Transfer Function (MTF)

To give further insight into Figure 4.7(d), we now re-examine the formula for the reconstruction derived in the Methods section, and show that signal in a slice along the pitch of the object is always sinusoidal with the correct frequency. According to Eqs. (4.35) and (4.39) giving the formula for the reconstruction, the signal is a linear combination of sinusoidal functions along the x'' direction. This result can be written in terms of one sinusoidal function using the trigonometric identity

$$A_1 \cos(\beta) + A_2 \sin(\beta) = \sqrt{A_1^2 + A_2^2} \cos(\beta + \Phi), \quad (4.56)$$

where

$$\Phi = \arctan\left(\frac{A_2}{A_1}\right) + \begin{cases} -\pi/2, & A_1 < 0 \\ +\pi/2, & A_2 < 0 \end{cases}. \quad (4.57)$$

From Eqs. (4.35) and (4.39), it follows that

$$\mu_{\text{FBP}} = \sqrt{A_1^2 + A_2^2} \cos(2\pi x'' f_0 + \Phi), \quad (4.58)$$

where

$$A_1 = C\varepsilon \begin{cases} \int_{v_-}^{v_+} \frac{\mathcal{F}_1 \phi \left(\sqrt{f_0^2 + f_z''^2} \right) \cos(2\pi z'' f_z'') \text{sinc}(\varepsilon f_z'')}{\sqrt{f_0^2 + f_z''^2}} df_z'', & 0 < \alpha_y \leq 90^\circ - \Theta/2 \\ \left[\int_{-\infty}^{v_+} \frac{\mathcal{F}_1 \phi \left(\sqrt{f_0^2 + f_z''^2} \right) \cos(2\pi z'' f_z'') \text{sinc}(\varepsilon f_z'')}{\sqrt{f_0^2 + f_z''^2}} df_z'' \right. \\ \left. + \int_{v_-}^{\infty} \frac{\mathcal{F}_1 \phi \left(\sqrt{f_0^2 + f_z''^2} \right) \cos(2\pi z'' f_z'') \text{sinc}(\varepsilon f_z'')}{\sqrt{f_0^2 + f_z''^2}} df_z'' \right], & 90^\circ - \Theta/2 < \alpha_y \leq 90^\circ \end{cases}, \quad (4.59)$$

$$A_2 = C\varepsilon \begin{cases} \int_{\nu_-}^{\nu_+} \frac{\mathcal{F}_1 \phi \left(\sqrt{f_0^2 + f_z'^2} \right) \sin(2\pi z'' f_z'') \text{sinc}(\varepsilon f_z'')}{\sqrt{f_0^2 + f_z'^2}} df_z'', & 0 < \alpha_y \leq 90^\circ - \Theta/2 \\ \left[\int_{-\infty}^{\nu_+} \frac{\mathcal{F}_1 \phi \left(\sqrt{f_0^2 + f_z'^2} \right) \sin(2\pi z'' f_z'') \text{sinc}(\varepsilon f_z'')}{\sqrt{f_0^2 + f_z'^2}} df_z'' \right. \\ \left. + \int_{\nu_-}^{\infty} \frac{\mathcal{F}_1 \phi \left(\sqrt{f_0^2 + f_z'^2} \right) \sin(2\pi z'' f_z'') \text{sinc}(\varepsilon f_z'')}{\sqrt{f_0^2 + f_z'^2}} df_z'' \right], & 90^\circ - \Theta/2 < \alpha_y \leq 90^\circ \end{cases} \quad (4.60)$$

Eq. (4.58) provides the desired formula for signal in a slice with the same pitch as the object. This formula proves that the signal is sinusoidal with the correct frequency (f_0). This result holds whether the slice is inside or outside the object.

In the pitched slice described by Eq. (4.58), the signal has a phase shift Φ that does not necessarily match the phase of the input object at each reconstruction depth, z'' . If one considers the special case in which the depth of the slice is aligned with the mid-thickness of the sine plate ($z'' = 0$), it can be shown that Φ vanishes. Hence the phase of the signal matches the object

$$\mu_{\text{FBP}}|_{z''=0} = G(f_0) \cdot C \cos(2\pi x'' f_0), \quad (4.61)$$

where

$$G(f_0) = \begin{cases} \varepsilon \int_{f_0 \tan(\alpha_y - \Theta/2)}^{f_0 \tan(\alpha_y + \Theta/2)} \frac{\mathcal{F}_1 \phi \left(\sqrt{f_0^2 + f_z'^2} \right) \text{sinc}(\varepsilon f_z'')}{\sqrt{f_0^2 + f_z'^2}} df_z'', & 0 < \alpha_y \leq 90^\circ - \Theta/2 \\ \varepsilon \left[\int_{-\infty}^{f_0 \tan(\alpha_y + \Theta/2)} \frac{\mathcal{F}_1 \phi \left(\sqrt{f_0^2 + f_z'^2} \right) \text{sinc}(\varepsilon f_z'')}{\sqrt{f_0^2 + f_z'^2}} df_z'' + \int_{f_0 \tan(\alpha_y - \Theta/2)}^{\infty} \frac{\mathcal{F}_1 \phi \left(\sqrt{f_0^2 + f_z'^2} \right) \text{sinc}(\varepsilon f_z'')}{\sqrt{f_0^2 + f_z'^2}} df_z'' \right], & 90^\circ - \Theta/2 < \alpha_y \leq 90^\circ \end{cases} \quad (4.62)$$

Eq. (4.61) demonstrates that signal in the slice along the mid-thickness of the object is proportional to the attenuation coefficient of the sine plate. The proportionality factor, $G(f_0)$, is by definition the optical transfer function (OTF). The OTF compares the amplitude of signal in the image against the attenuation coefficient of the test object at all frequencies, f_0 . Depending on the sign of the OTF, the phase shift relative to the input object is either 0° or 180° .

To investigate how image quality varies with pitch in an oblique reconstruction, the modulation transfer function (MTF) is now derived from the OTF. The MTF is calculated by normalizing the modulus of $G(f_0)$ to the corresponding limit for which $f_0 \rightarrow 0$.¹⁶ Appendix C shows that this limit can be evaluated in closed form for Case 1 of the Methods section. To demonstrate that modulation is preserved, the MTF should approach unity.

$$\text{MTF}(f_0) = \frac{|G(f_0)|}{\lim_{f_0 \rightarrow 0} G(f_0)} \quad (4.63)$$

In Figure 4.8, the MTF is plotted versus frequency (f_0) and pitch (α_y) for four thicknesses of the sine plate: $\varepsilon = 0.01, 0.10, 1.0$ and 10.0 mm. The reconstruction technique is SBP. As expected, Figure 4.8 demonstrates that the MTF decreases with frequency. This dependency is not quite monotonic at high frequencies exceeding the first zero of the MTF.

Figure 4.8 illustrates that the MTF is highly dependent upon the thickness of the object. If the object is very thin [Figure 4.8(a)], the MTF is close to unity over a broad range of pitches and frequencies. As the object thickness is increased, the MTF decreases. This degradation in MTF is pronounced with increasing pitch and frequency. In accord with the predictions of the analytical model, experimental reconstructions of bar patterns also demonstrate that high frequency information is lost with increasing pitch (Figure 4.3).

It is useful to explain the thickness dependency of the MTF in terms of Fourier theory. Recall that the Fourier transform of a sine plate consists of two lines modulated by a “sinc” function along the direction perpendicular to the pitch axis. Within the sampling cones of Fourier space, it can be shown that the amplitude of the “sinc” function increases as the object thickness is reduced (Figure 4.2). This observation explains why the MTF of a thin object is larger than a thick object in Figure 4.8.

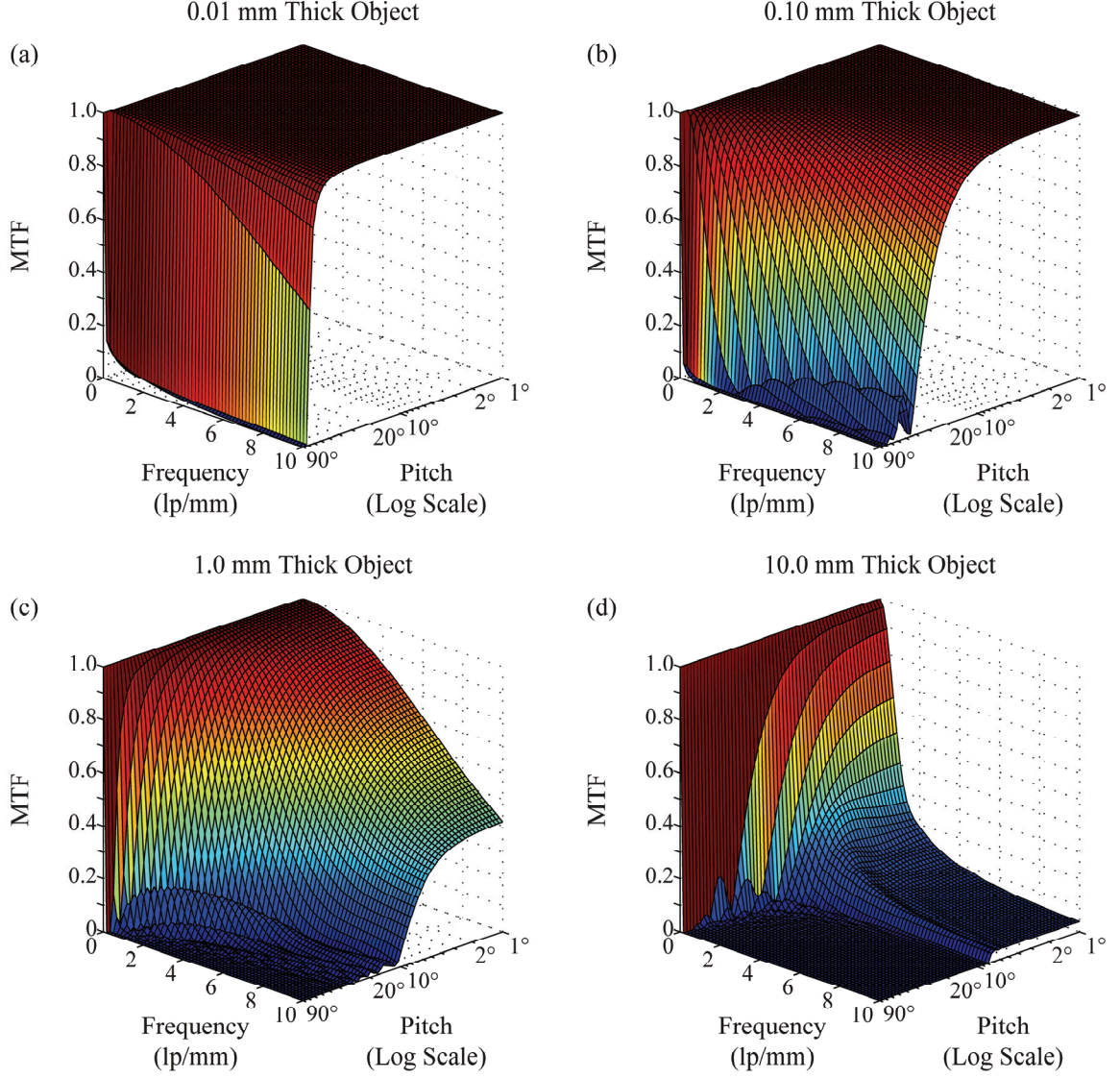


Figure 4.8: Modulation transfer function (MTF) for oblique reconstructions. The dependency of the in-plane MTF on frequency (f_0) and pitch (α_y) is analyzed using surface plots at four object thicknesses ($\varepsilon = 0.01, 0.10, 1.0$, and 10.0 mm). It is demonstrated that modulation is preserved over a broad range of pitches and frequencies if the object is thin. As the object thickness is increased, modulation is degraded. This loss of modulation is pronounced with increasing pitch and frequency. This finding is concordant with experimental images of bar patterns presented earlier in this work (Figure 4.3), which also show that high frequency information is lost with increasing pitch.

3.2. Rod

With a similar acquisition geometry, SBP reconstructions of a rod at 0° and 45° pitches are now simulated (Figure 4.9), assuming a rod length (Π) of 10.0 mm and a thickness (ε) of 0.10 mm. Grayscale images are displayed in the xz plane analogous to Figure 4.6 showing the reconstruction of a sine plate. Due to backprojection artifacts, it is difficult to deduce that the input object is rectangular. However, it can be shown that the rod length is accurately determined from signal along the lines $z = 0$ and $z = x$ for the 0° and 45° pitches, respectively.

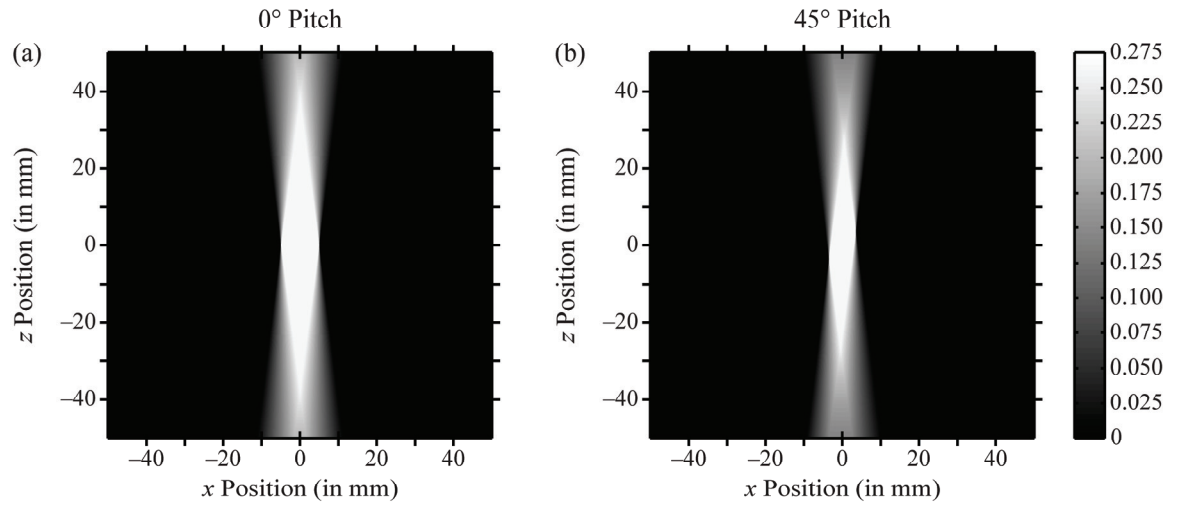


Figure 4.9: Reconstruction of a pitched rod in the plane of x-ray tube motion. The SBP reconstruction of a rod [Figure 4.4(b)] is displayed as a grayscale image in the xz plane, assuming that $\Theta = 15^\circ$, $\varepsilon = 0.10$ mm, and $\Pi = 10.0$ mm. One can show that the rod length of 10.0 mm is correctly determined along the two object pitches, 0° and 45° , by measuring signal along the lines $z = 0$ and $z = x$, respectively. Because projections are acquired over a limited angular range, there are backprojection artifacts that cause the thickness of the rod to be overestimated. In addition, the object does not appear to be rectangular in the reconstruction.

In conventional practice, the reconstruction is not displayed as a grayscale image in the xz plane, but instead, as a series of slices with a 0° pitch. To simulate this convention, signal is plotted versus x in Figure 4.10(a)-(c), assuming that the rod is pitched at a 45° angle. The three plots correspond to three depths within the rod; namely, $z = -3.0, 0$, and $+3.0$ mm. In a perfect reconstruction, each slice should be a rectangle function with length $\varepsilon \sec \alpha_y$, or 0.14 mm. Due to backprojection artifacts, the reconstruction actually appears trapezoidal, and the extent of the rod within each slice is greatly overestimated. At all three depths, the plateau length of the trapezoid is 6.0 mm and the full width at half maximum (FWHM) is 7.0 mm. Consequently, the conventional display of slices is not useful for this object.

The reconstruction more clearly resembles the input object if slices are generated along a 45° pitch, as shown in Figure 4.10(d). In this plot, we simulate a slice at the depth $z'' = 0$, corresponding to the mid-thickness of the rod. As expected, signal is a rectangle function with a plateau length of 10.0 mm. This length matches known ground truth for the rod.

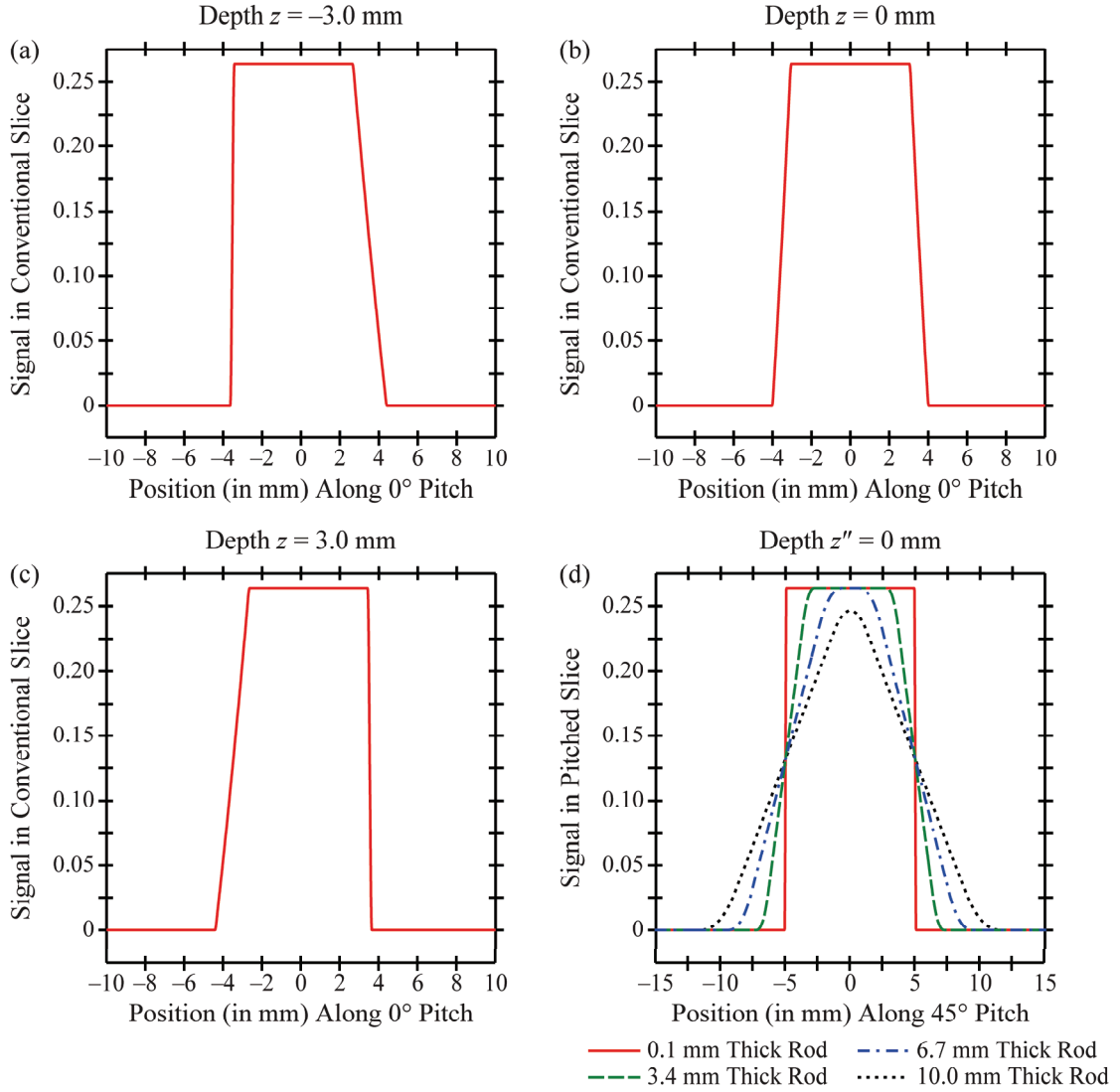


Figure 4.10: Tomographic slices for a pitched rod. (a)-(c) By displaying the reconstruction in Figure 4.9(b) with conventional slices oriented along a 0° pitch, it is difficult to deduce the length of a rod whose long axis is oblique (45° pitch). Due to backprojection artifacts, signal spans a much greater length than expected; signal in each slice should be a rectangle function with length 0.14 mm. (d) The rod length can be correctly determined if slices are generated through the mid-thickness of the object at a 45° pitch ($z'' = 0$). Increasing the thickness of the object causes the edges of the rod to be blurred.

Figure 4.10(d) also investigates how the estimate of rod length is influenced by rod thickness. As the thickness is increased, it is demonstrated that signal appears more

trapezoidal than rectangular, and thus the edge of the rod is blurred. To estimate rod length, one can calculate the FWHM of the trapezoid. With rod thicknesses of 0.1 mm, 3.4 mm, and 6.7 mm, the FWHM is exactly 10.0 mm in agreement with the actual rod length. By contrast, with a rod thickness of 10.0 mm, the FWHM is 10.6 mm. Consequently, the rod length at a 45° pitch is slightly overestimated if its thickness is comparable to its length.

To investigate how the measurement of the size of an object varies along different directions in the reconstruction, the estimate of rod length is plotted versus pitch in Figure 4.11(a). We continue to use the FWHM as the metric for estimating rod length in a pitched slice. Figure 4.11(a) shows that the estimate of rod length is accurate (10.0 mm) over a broad range of pitches if the object is thin. Increasing the rod thickness causes the length estimate to be accurate over a narrower range of pitches; all inaccuracies are overestimates of rod length.

Figure 4.11(b) illustrates the thickness dependency of the maximum pitch at which rod length can be correctly determined. As shown, the maximum pitch decreases with rod thickness. In the special case of an extremely thin rod, the rod length can be correctly determined up to a 90° pitch.

The consequences of permitting error in the estimate of rod length are also explored in Figure 4.11. It is shown that the introduction of error tolerance broadens the range of pitches at which the estimate of rod length is acceptable. For example, if the rod is square, the length estimate is exact up to a pitch of 38° , but is acceptable up to a pitch of 48° with an error tolerance of 15% (Points A and B, respectively, in Figure 4.11).

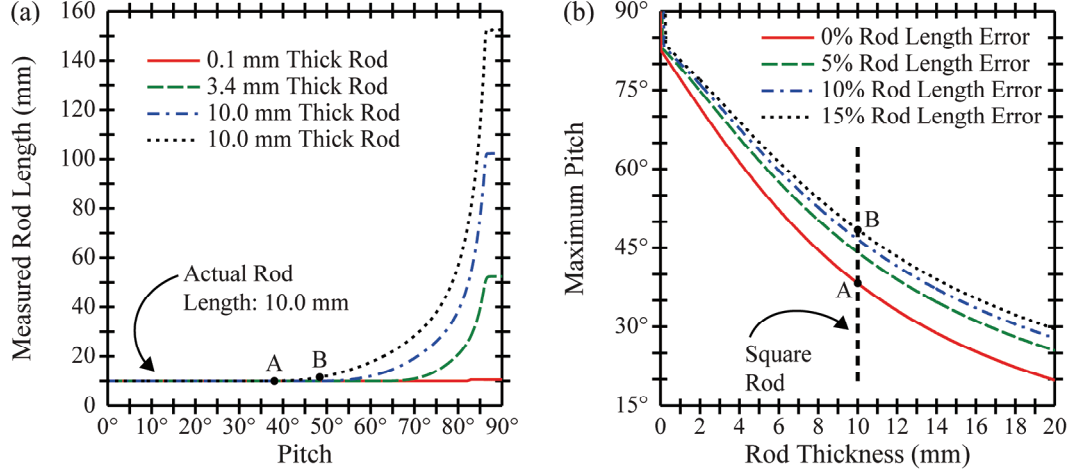


Figure 4.11: Measurement accuracy in oblique reconstructions. (a) The length of a rod is determined at various pitches using oblique reconstructions. The FWHM of signal in pitched slices [Figure 4.10(d)] is the metric used to estimate rod length; the actual length is 10.0 mm. (b) At various rod thicknesses, one can use Figure 4.11(a) to determine the maximum pitch at which rod length can be correctly measured. This maximum pitch is plotted versus rod thickness for different levels of error tolerance in the measurement of rod length. It is demonstrated here that rod length is correctly determined over a broad range of pitches if the object is thin, but over a narrower range of pitches if the object is thick.

4. COMPARISON WITH RESULTS IN THE LITERATURE

In this chapter, the MTF is calculated by comparing the amplitude of the image against the attenuation coefficient of a sinusoidal test object at various frequencies. Previous authors such as Zhao² have proposed a different formulation for MTF in tomosynthesis. Zhao's work draws a distinction between in-plane MTF and 3D MTF. In Zhao's formulation, the in-plane MTF is the integral of the 3D MTF along the z direction. This approach presumes that the z direction is perpendicular to the slice.² To generalize Zhao's calculation of in-plane MTF to oblique planes, we now show that the line integral should be performed along a more general direction perpendicular to the slice. To this

end, one must first deduce the OTF of the entire reconstruction space using the expression for in-plane OTF derived in Eq. (4.62):

$$H(f_x, f_z) = \frac{\mathcal{F}_1 \phi \left(\sqrt{f_x^2 + f_z^2} \right)}{\sqrt{f_x^2 + f_z^2}} \cdot \text{rect} \left(\frac{f_z}{2f_x \tan(\Theta/2)} \right). \quad (4.64)$$

In Eq. (4.64), the rect function models the FDC whose opening angle matches the angular range of the scan [Figure 4.1(b)]. The formula below demonstrates that the in-plane OTF [Eq. (4.62)] can be expressed as a line integral of the OTF of the entire reconstruction space [Eq. (4.64)]:

$$G(f_0) = \int_{-\infty}^{\infty} H(f_x'', f_z'') \big|_{f_x''=f_0} \varepsilon \cdot \text{sinc}(\varepsilon f_z'') df_z'', \quad (4.65)$$

where

$$H(f_x'', f_z'') = \frac{\mathcal{F}_1 \phi \left(\sqrt{f_x''^2 + f_z''^2} \right)}{\sqrt{f_x''^2 + f_z''^2}} \cdot \text{rect} \left(\frac{f_x'' \sin \alpha_y + f_z'' \cos \alpha_y}{2[f_x'' \cos \alpha_y - f_z'' \sin \alpha_y] \tan(\Theta/2)} \right). \quad (4.66)$$

Since the line integral in Eq. (4.65) is performed along a general direction (f_z'') which is perpendicular to the pitch of the slice, this result generalizes Zhao's formulation of in-plane OTF to oblique planes.

Although Zhao does not model the thickness of an object in the reconstruction, this chapter demonstrates that the in-plane MTF is indeed dependent upon the object thickness (Figure 4.8). This property arises from the term $\varepsilon \cdot \text{sinc}(\varepsilon f_z'')$ in the in-plane OTF calculation [Eq. (4.65)]. Recall that this term is the Fourier transform of the function $\text{rect}(z''/\varepsilon)$, which models the object thickness ε along the direction

perpendicular to the slice [Eq. (4.17)]. In summary, this work introduces the object thickness as an additional parameter for quantification of in-plane MTF.

5. DISCUSSION

By convention, a tomosynthesis reconstruction is created with slices parallel to the detector. This work demonstrates from first principles that oblique slices are also justified. To assess how individual frequencies in the MTF are preserved in oblique reconstructions, a sine plate is simulated along various pitches. Although this object is not properly visualized in conventional slices generated along a 0° pitch, the sinusoidal attenuation coefficient is perfectly resolved in slices created along the pitch of the test frequency.

To determine whether the length of an object can be correctly determined along various pitches, the reconstruction of a rod is also simulated. It is shown that backprojection artifacts in conventional slices oriented along a 0° pitch cause the extent of the object to be greatly overestimated with SBP reconstruction. By contrast, backprojection artifacts are minimal in a pitched slice oriented along the length of the rod.

In linear systems theory, the MTF of a single projection image is calculated without making reference to the thickness of the test frequency.¹⁶ This work demonstrates that the in-plane MTF of a reconstruction is indeed dependent upon the object thickness. Previous authors have not introduced the object thickness as a parameter in the MTF calculation.²

According to this work, a very thin object can be reconstructed at large pitches approaching 90° . This property does not hold as the thickness of the object is increased; in particular, it is shown that the MTF is degraded and that the measurement of rod length is inaccurate at large pitches. Because a clinical image consists of objects with a range of thicknesses, a clinical reconstruction is not expected to be valid up to pitches approaching 90° . Future work is merited to determine the range of pitches at which clinical reconstructions are appropriate in tomosynthesis; however, anecdotal results suggest that pitches approaching 45° are viable.

In CT, reconstructions can be generated along any planar or curved surface in the imaging volume using MPR.¹ Although this work on oblique reconstructions is implicitly limited to planar slices, it is reasonable to posit that tomosynthesis reconstructions are also justifiable with curved surfaces. Displaying a blood vessel or a vascular calcification cluster in a single view is a potential application for curved planar reformatting in DBT. It is conceivable that the full extent of these tortuous structures cannot be visualized using conventional slices oriented along a 0° pitch. Justifying the feasibility of MPR along any curved surface would be difficult with analytical modeling. For this reason, future studies should investigate these reconstructions in computer anthropomorphic phantoms and in clinical cases.

This study could also be expanded by considering multiple test objects in the reconstruction. Although this work calculates the backprojection artifacts of a single test object, it does not investigate whether the backprojection artifacts of one object could hide another object. For example, it would be useful to investigate whether the

backprojection artifacts of a mass impact the modulation of a sine plate or the length estimate of a rod (*e.g.*, a spiculation).

This work shows that a pitched slice is the preferred orientation for viewing some test objects in the reconstruction. In theoretical calculations, choosing the optimal pitch for viewing an object is trivial, since the actual pitch of the object is known. Choosing the optimal pitch will be more challenging in clinical cases in which there are out-of-focus artifacts and ground truth is lacking. The development of a framework for determining the optimal pitch for viewing a clinical reconstruction remains the subject of future work. Quantifying the precise size of an asymmetric mass prior to surgical resection is one application where matching the pitch of the reconstruction to the long axis of a lesion is potentially important.

While filtering is modeled in the FBP formulas of Section 2, the reconstructions that are plotted in Section 3 do not apply filtering (Figures 4.6-4.11). Instead, the reconstructions use simple backprojection. Recalling Eq. (4.61), it can be shown that filtering is not critical in displaying a slice through the mid-thickness of a pitched sine plate [Figure 4.7(d)]. According to this expression, signal is sinusoidal with the correct frequency, regardless of filter. Consequently, introducing a filter would not change the relative signal in the pitched slice in Figure 4.7(d).

Although the ramp filter is the basis for image reconstruction in CT,^{2, 17, 18} we now explain why this work suggests that the ramp filter is not optimal for tomosynthesis. In the OTF identity that is derived in Appendix C [Eq. (4.C6)], it is important to note that $G(0)$ is proportional to $\mathcal{F}_1\phi(0)$, or the filter evaluated at zero frequency. In normalizing

$G(f_0)$ by $G(0)$ to calculate the in-plane MTF [Eq. (4.63)], it follows from Appendix C that the quotient is infinite if $\mathcal{F}_1\phi(0) = 0$. Hence, the in-plane MTF is not well-defined if ramp filtering is used. Our previous work on super-resolution in DBT also concluded that the ramp filter is not optimal, since modulation is zero in the reconstruction of a test frequency perpendicular to the plane of x-ray tube motion.⁴ Future work on filter optimization is merited for these reasons. Although this work calculates the in-plane MTF for SBP reconstruction only, it is expected that the result is dependent on the filter [Eq. (4.62)].

Some of the limitations of this work and directions for future analytical modeling are now noted. Although a 2D simulation with a parallel beam geometry was sufficient for a proof-of-principle justification for oblique reconstructions, it will be important to extend this work to a 3D simulation with a divergent beam geometry. In addition, future studies should model the presence of discrete step angles between projections as well as a more general detector that rotates between projections. Finally, the presence of a thin-film transistor array,¹⁹⁻²¹ which samples digital detector signal in pixels, should also be simulated.²²⁻²⁴

6. CONCLUSION

Conventional practice is to generate a tomosynthesis reconstruction using slices parallel to the detector. This work demonstrates that slices can also be generated along oblique directions through the same volume. It is shown that the object must be thin in order to be displayed with high image quality in an oblique reconstruction. In the ACR

Mammography Accreditation Phantom, this thickness constraint is satisfied by the three test objects (spheres, rods, and specks), which have been designed to simulate clinically important structures.

It should be emphasized that the results presented in this chapter are valid in any application of tomosynthesis, not simply breast applications. In addition, although the beam in each projection is presumed to consist of x rays, the calculations in this work are applicable to electromagnetic radiation at any energy, as well as to beams consisting of particles (*e.g.*, neutron tomosynthesis).

7. APPENDIX A: RADON TRANSFORM OF PITCHED SINE PLATE

In Figure 4.4, plots of the Radon transform are shown versus t at a fixed projection angle (θ) for the two test objects. In order to derive the plot for the sine plate [Figure 4.4(a)], we now calculate the Radon transform from first principles. Recall that the 2D Fourier transform of this object is

$$\mathcal{F}_2\mu(f_x, f_z) = \frac{C\mathcal{E}}{2} \left[\begin{array}{c} \delta(f_x \cos \alpha_y + f_z \sin \alpha_y - f_0) \\ + \delta(f_x \cos \alpha_y + f_z \sin \alpha_y + f_0) \end{array} \right] \cdot \text{sinc} \left[\mathcal{E}(-f_x \sin \alpha_y + f_z \cos \alpha_y) \right]. \quad (4.A1)$$

This result follows from Eq. (4.22) using the transformation between the (f_x'', f_z'') and (f_x, f_z) coordinate systems [Eq. (4.21)]. According to the Central Slice Theorem [Eq. (4.3)], this 2D Fourier transform can be related to the Radon transform as follows:

$$\mathcal{R}\mu(t, \theta) = \int_{-\infty}^{\infty} \mathcal{F}_2\mu(f_r \cos \theta, f_r \sin \theta) \cdot e^{2\pi i f_r t} df_r \quad (4.A2)$$

$$= \int_{-\infty}^{\infty} \frac{C\varepsilon}{2} \left(\delta[f_r \cos(\theta - \alpha_y) - f_0] + \delta[f_r \cos(\theta - \alpha_y) + f_0] \right) \cdot \text{sinc}[\varepsilon f_r \sin(\theta - \alpha_y)] \cdot e^{2\pi i f_r t} df_r. \quad (4.A3)$$

In order to simplify Eq. (4.A3), one must assume that $\theta \neq 90^\circ + \alpha_y$, so that the two delta functions can be evaluated with the identity

$$\delta[f_r \cos(\theta - \alpha_y) \pm f_0] = \delta[f_r \pm f_0 \sec(\theta - \alpha_y)] \cdot \sec(\theta - \alpha_y). \quad (4.A4)$$

Due to an infinity in the secant function, Eq. (4.A4) is undefined if $\theta = 90^\circ + \alpha_y$. This constraint corresponds to the projection for which each ray is parallel with the long axis of the sine plate. The Radon transform cannot be written in closed form for this projection, since the total x-ray attenuation is undefined along an infinite path length.

$$\mathcal{R}\mu(t, 90^\circ + \alpha_y) = \begin{cases} \text{undefined}, & -\varepsilon/2 \leq t \leq \varepsilon/2 \\ 0, & \text{otherwise} \end{cases} \quad (4.A5)$$

Although the Radon transform cannot be written in closed form if $\theta = 90^\circ + \alpha_y$, it can indeed be written in closed form for the projection angle illustrated in Figure 4.4(a).

Combining Eqs. (4.A3) and (4.A4) yields

$$\mathcal{R}\mu(t, \theta) = \frac{C\varepsilon}{2} \cdot \sec(\theta - \alpha_y) \text{sinc}[\varepsilon f_0 \tan(\theta - \alpha_y)] \cdot \left(e^{2\pi i f_0 t \sec(\theta - \alpha_y)} + e^{-2\pi i f_0 t \sec(\theta - \alpha_y)} \right) \quad (4.A6)$$

$$= C\varepsilon \sec(\theta - \alpha_y) \text{sinc}[\varepsilon f_0 \tan(\theta - \alpha_y)] \cos[2\pi f_0 t \sec(\theta - \alpha_y)]. \quad (4.A7)$$

This result proves that the Radon transform has sinusoidal dependence on t , as indicated in the figure. Consistent with Eq. (4.A7), the plot has no phase shift relative to the origin, $t = 0$.

8. APPENDIX B: RADON TRANSFORM OF PITCHED ROD

In Figure 4.4(b), the Radon transform of a pitched rod is plotted versus t at a fixed projection angle (θ). To derive this plot, we now calculate the Radon transform from first principles. Using Eqs. (4.21) and (4.41), it can be shown that the 2D Fourier transform of this object is

$$\mathcal{F}_2\mu(f_x, f_z) = C\Pi\varepsilon \cdot \text{sinc}\left[\Pi(f_x \cos\alpha_y + f_z \sin\alpha_y)\right] \cdot \text{sinc}\left[\varepsilon(-f_x \sin\alpha_y + f_z \cos\alpha_y)\right]. \quad (4.B1)$$

From Eq. (4.A2), it follows that

$$\mathcal{R}\mu(t, \theta) = C\Pi\varepsilon \int_{-\infty}^{\infty} \text{sinc}\left[\Pi f_r \cos(\theta - \alpha_y)\right] \cdot \text{sinc}\left[\varepsilon f_r \sin(\theta - \alpha_y)\right] \cdot e^{2\pi i f_r t} df_r. \quad (4.B2)$$

Similar to Appendix A, one must consider two separate constraints in order to evaluate the Radon transform; namely $\theta = 90^\circ + \alpha_y$ and $\theta \neq 90^\circ + \alpha_y$. If one first considers the constraint $\theta = 90^\circ + \alpha_y$, the integral in Eq. (4.B2) simplifies to

$$\mathcal{R}\mu(t, 90^\circ + \alpha_y) = C\Pi\varepsilon \int_{-\infty}^{\infty} \text{sinc}(\varepsilon f_r) \cdot e^{2\pi i f_r t} df_r \quad (4.B3)$$

$$= C\Pi \cdot \text{rect}\left(\frac{t}{\varepsilon}\right). \quad (4.B4)$$

This result corresponds to the projection for which each ray is parallel to the pitch axis (x''). The Radon transform is a rectangular function of t ; the width of this function matches the rod thickness (ε). If one next considers the constraint $\theta \neq 90^\circ + \alpha_y$, the convolution theorem can be used to simplify Eq. (4.B2).

$$\mathcal{R}\mu(t, \theta \neq 90^\circ + \alpha_y) = C\Pi\varepsilon \cdot \mathcal{F}_1^{-1} \text{sinc}\left[\Pi f_r \cos(\theta - \alpha_y)\right] * \mathcal{F}_1^{-1} \text{sinc}\left[\varepsilon f_r \sin(\theta - \alpha_y)\right] \quad (4.B5)$$

$$\begin{aligned}
&= C\Pi\varepsilon \cdot \frac{1}{\Pi \cos(\theta - \alpha_y)} \text{rect} \left[\frac{t}{\Pi \cos(\theta - \alpha_y)} \right] \\
&\quad *_1 \frac{1}{\varepsilon \sin(\theta - \alpha_y)} \text{rect} \left[\frac{t}{\varepsilon \sin(\theta - \alpha_y)} \right].
\end{aligned} \tag{4.B6}$$

In order to analyze the dependency of the Radon transform on t , it is useful to review the equation of an isosceles trapezoid

$$\mathcal{R}\mu(t, \theta \neq 90^\circ + \alpha_y) = B \cdot \text{rect} \left[\frac{t}{(q_1 + q_2)/2} \right] *_1 \frac{1}{(q_2 - q_1)/2} \text{rect} \left[\frac{t}{(q_2 - q_1)/2} \right] \tag{4.B7}$$

$$= B \cdot \begin{cases} 1 & , |t| \leq \frac{q_1}{2} \\ \frac{-1}{(q_2 - q_1)/2} \left(|t| - \frac{q_2}{2} \right) & , \frac{q_1}{2} < |t| \leq \frac{q_2}{2} \\ 0 & , |t| > \frac{q_2}{2} \end{cases}, \tag{4.B8}$$

where B is the height of the plateau, q_1 is the length of the plateau, and q_2 is the length of the base. The trapezoid is symmetric about the origin, $t = 0$. Assuming that $-90^\circ < \theta \leq 90^\circ$ and that $0 \leq \alpha_y \leq 90^\circ$, as stipulated in the body of this work, Eqs. (4.B6)

and (4.B7) can be equated to yield

$$B = \begin{cases} C\varepsilon \sec(\theta - \alpha_y) & , \theta < \alpha_y + \arctan\left(\frac{\Pi}{\varepsilon}\right) \\ C\Pi \csc(\theta - \alpha_y) & , \theta > \alpha_y + \arctan\left(\frac{\Pi}{\varepsilon}\right) \end{cases} \tag{4.B9}$$

$$q_1 = \begin{cases} \Pi \cos(\theta - \alpha_y) - \varepsilon \sin(\theta - \alpha_y) & , \theta < \alpha_y + \arctan\left(\frac{\Pi}{\varepsilon}\right) \\ \varepsilon \sin(\theta - \alpha_y) - \Pi \cos(\theta - \alpha_y) & , \theta > \alpha_y + \arctan\left(\frac{\Pi}{\varepsilon}\right) \end{cases} \tag{4.B10}$$

$$q_2 = \Pi \cos(\theta - \alpha_y) + \varepsilon \sin(\theta - \alpha_y). \tag{4.B11}$$

This result provides a justification for the trapezoidal plot in Figure 4.4(b) showing the Radon transform of the rod at a fixed projection angle (θ).

Although not plotted in Figure 4.4(b), two degenerate cases in the formula for the trapezoid [Eq. (4.B7)] are noted for completeness. One degeneracy occurs if the plateau and base of the trapezoid have the same length ($q_1 = q_2$). Using Eqs. (4.B10) and (4.B11), it can be shown that this property occurs if $\theta = \alpha_y$.

$$\mathcal{R}\mu(t, \alpha_y) = C\varepsilon \cdot \text{rect}\left(\frac{t}{\Pi}\right) \quad (4.B12)$$

This degeneracy corresponds to the projection in which the rays are perpendicular to the pitch axis. It is also useful to examine a second degenerate case in which the length of the plateau of the trapezoid is zero ($q_1 = 0$), while the length of the base is non-zero ($q_2 > 0$). This degeneracy occurs if the lengths of the two rectangle functions in Eq. (4.B6) are equivalent.

$$\mathcal{R}\mu\left(t, \alpha_y + \arctan\left(\frac{\Pi}{\varepsilon}\right)\right) = C\sqrt{\varepsilon^2 + \Pi^2} \cdot \begin{cases} 1 - \frac{|t|\sqrt{\varepsilon^2 + \Pi^2}}{\Pi\varepsilon} & , |t| \leq \frac{\Pi\varepsilon}{\sqrt{\varepsilon^2 + \Pi^2}} \\ 0 & , |t| > \frac{\Pi\varepsilon}{\sqrt{\varepsilon^2 + \Pi^2}} \end{cases} \quad (4.B13)$$

The Radon transform is no longer a trapezoidal function of t but instead is a triangular function of t . Unlike the projection illustrated in Figure 4.4(b), it can be shown that this degenerate case corresponds to the projection in which one of the rays intercepts two corners of the rod. In the projection shown in Figure 4.4(b), a ray that intercepts one corner of the rod does not strike the other corner.

9. APPENDIX C: OPTICAL TRANSFER FUNCTION IDENTITY

In this chapter, the MTF of a pitched reconstruction slice is calculated by normalizing the OTF to its value in the limit $f_0 \rightarrow 0$ [Eq. (4.63)]. It is difficult to evaluate this limit in closed form using Eq. (4.62), since the integration limits both tend toward zero. For this reason, we now provide a more direct method for evaluating $G(0)$ by explicitly calculating the reconstruction of a sine plate with zero frequency. This object is an infinitely long rod whose long axis is oriented along the pitch α_y and whose thickness is ε .

It is first necessary to evaluate the Radon transform of the object by substituting $f_0 = 0$ into Eq. (4.A7).

$$\mathcal{R}\mu(t, \theta) = C\varepsilon \sec(\theta - \alpha_y) \quad (4.C1)$$

As discussed in Appendix A, this result presumes that $\theta \neq 90^\circ + \alpha_y$. Recalling the Methods section, it can be shown that this inequality holds at all projections angles for Case 1 of the reconstruction (Section 2.2.1). Hence

$$\mu_{\text{FBP}}(x, z) = \int_{-\Theta/2}^{\Theta/2} \int_{-\infty}^{\infty} \phi(\tau) \cdot \mathcal{R}\mu(x \cos \theta + z \sin \theta - \tau, \theta) d\tau d\theta \quad (4.C2)$$

$$= \left[\int_{-\infty}^{\infty} \phi(\tau) d\tau \right] \left[\int_{-\Theta/2}^{\Theta/2} \mathcal{R}\mu \cdot d\theta \right]. \quad (4.C3)$$

The transition from Eq. (4.C2) to Eq. (4.C3) is justified because the Radon transform in Eq. (4.C1) is independent of t . The first term in Eq. (4.C3) is the integral of the filter ϕ over all space. From Fourier theory, this integral is equivalent to $\mathcal{F}_1\phi(0)$. The second term in Eq. (4.C3) is

$$\int_{-\Theta/2}^{\Theta/2} \mathcal{R}\mu \cdot d\theta = \int_{-\Theta/2}^{\Theta/2} C\varepsilon \sec(\theta - \alpha_y) d\theta \quad (4.C4)$$

$$= C\varepsilon \ln \left| \frac{\sec(\alpha_y - \Theta/2) - \tan(\alpha_y - \Theta/2)}{\sec(\alpha_y + \Theta/2) - \tan(\alpha_y + \Theta/2)} \right|. \quad (4.C5)$$

Combining Eqs. (4.C3) and (4.C5) yields

$$G(0) = \mathcal{F}_1\phi(0) \cdot \varepsilon \ln \left| \frac{\sec(\alpha_y - \Theta/2) - \tan(\alpha_y - \Theta/2)}{\sec(\alpha_y + \Theta/2) - \tan(\alpha_y + \Theta/2)} \right|, \quad (4.C6)$$

completing the derivation of the OTF identity. If one considers the special case of SBP reconstruction, the substitution $\mathcal{F}_1\phi(f_r) = \mathcal{F}_1\phi(0) = 1$ should be made in Eq. (4.C6).

It would be difficult to perform an analogous derivation of $G(0)$ in considering Case 2 of the Methods section (Section 2.2.2), since the x-ray beam is aligned with the pitch axis of the rod in the projection for which $\theta = 90^\circ + \alpha_y$. At this projection angle, the Radon transform cannot be written in closed form.

$$\mathcal{R}\mu(t, 90^\circ + \alpha_y) = \begin{cases} \infty, & -\varepsilon/2 \leq t \leq \varepsilon/2 \\ 0, & \text{otherwise} \end{cases} \quad (4.C7)$$

Because it would be difficult to evaluate a reconstruction using a Radon transform with an infinity, we evaluate $G(0)$ numerically in considering Case 2. This result can be derived from the integral in Eq. (4.62) in the limit $f_0 \rightarrow 0$.

10. REFERENCES

- ¹Hsieh J. Chapter 4: Image Presentation. Computed Tomography: Principles, Design, Artifacts, and Recent Advances. Bellingham, WA: SPIE Press; 2003. p. 99-111.
- ²Zhao B, Zhao W. Three-dimensional linear system analysis for breast tomosynthesis. Medical Physics. 2008;35(12):5219-32.
- ³Acciavatti RJ, Maidment ADA. Investigating the Potential for Super-Resolution in Digital Breast Tomosynthesis. In: Pelc NJ, Samei E, Nishikawa RM, editors. SPIE Medical Imaging; 2011; Lake Buena Vista, FL: SPIE; 2011. p. 79615K-1 - K-12.
- ⁴Acciavatti RJ, Maidment ADA. Observation of super-resolution in digital breast tomosynthesis. Medical Physics. 2012;39(12):7518-39.
- ⁵Kuo J, Ringer PA, Fallows SG, Bakic PR, Maidment ADA, Ng S. Dynamic Reconstruction and Rendering of 3D Tomosynthesis Images. In: Pelc NJ, Samei E, Nishikawa RM, editors. SPIE Medical Imaging; 2011; Lake Buena Vista, FL: SPIE; 2011. p. 796116-1 - 11.
- ⁶Rafferty EA. Tomosynthesis: New weapon in breast cancer fight. Decisions in Imaging Economics. 2004;17(4).
- ⁷Poplack SP, Tosteson TD, Kogel CA, Nagy HM. Digital breast tomosynthesis: initial experience in 98 women with abnormal digital screening mammography. American Journal of Roentgenology. 2007;189(3):616-23.
- ⁸Park JM, Edmund A, Franken J, Garg M, Fajardo LL, Niklason LT. Breast Tomosynthesis: Present Considerations and Future Applications. RadioGraphics. 2007;27:S231 - S40.
- ⁹ACR. Mammography Quality Control Tests. Mammography Quality Control Manual: American College of Radiology; 1999. p. 231-94.
- ¹⁰Hsieh J. Chapter 3: Image Reconstruction. Computed Tomography: Principles, Design, Artifacts, and Recent Advances. Bellingham, WA: SPIE Press; 2003. p. 37-98.
- ¹¹Barrett HH, Myers KJ. Chapter 4: Series Expansions and Integral Transforms. In: Saleh BEA, editor. Foundations of Image Science. New York, NY: John Wiley & Sons; 2004. p. 175-214.
- ¹²Barrett HH, Myers KJ. Chapter 3: Fourier Analysis. In: Saleh BEA, editor. Foundations of Image Science. New York, NY: John Wiley & Sons; 2004. p. 95-174.
- ¹³Barrett HH, Myers KJ. Chapter 2: Dirac Delta and Other Generalized Functions. In: Saleh BEA, editor. Foundations of Image Science. New York, NY: John Wiley & Sons; 2004. p. 63-94.
- ¹⁴Lea SM. Chapter 6: Generalized Functions in Physics. Mathematics for Physicists. Belmont, CA: Brooks/Cole - Thomson Learning; 2004. p. 287-322.
- ¹⁵Stewart J. Chapter 7: Techniques of Integration. In: Pirtle B, Green S, editors. Calculus: Early Transcendentals. 5e ed. Belmont, CA: Brooks/Cole - Thomson Learning; 2003. p. 474-545.
- ¹⁶Dainty JC, Shaw R. Chapter 6: Fourier Transforms, and the Analysis of Image Resolution and Noise. Image Science. London, England: Academic Press; 1974. p. 190-231.

- ¹⁷Mertelmeier T, Orman J, Haerer W, Dudam MK. Optimizing filtered backprojection reconstruction for a breast tomosynthesis prototype device. In: Flynn MJ, Hsieh J, editors. Physics of Medical Imaging; 2006; San Diego: SPIE; 2006.
- ¹⁸Zhao B, Zhou J, Hu Y-H, Mertelmeier T, Ludwig J, Zhao W. Experimental validation of a three-dimensional linear system model for breast tomosynthesis. Medical Physics. 2009;36(1):240-51.
- ¹⁹Jing T, Goodman CA, Drewery J, Cho G, Hong WS, Lee H, et al. Amorphous silicon pixel layers with cesium iodide converters for medical radiography. IEEE Trans Nucl Sci. 1994;41(4):903-9.
- ²⁰Cowen AR, Kengyelics SM, Davies AG. Solid-state, flat-panel, digital radiography detectors and their physical imaging characteristics. Clin Radiol. 2008;63:487-98.
- ²¹Nagarkar VV, Gupta TK, Miller SR, Klugerman Y, Squillante MR, Entine G. Structured CsI(Tl) scintillators for x-ray imaging applications. IEEE Trans Nucl Sci. 1998;45(3):492-6.
- ²²Albert M, Maidment ADA. Linear response theory for detectors consisting of discrete arrays. Medical Physics. 2000;27(10):2417-34.
- ²³Acciavatti RJ, Maidment ADA. An Analytical Model of NPS and DQE Comparing Photon Counting and Energy Integrating Detectors. In: Samei E, Pelc NJ, editors. SPIE Medical Imaging; 2010; San Diego, CA: SPIE; 2010. p. 76220I-1 - I-12.
- ²⁴Acciavatti RJ, Maidment ADA. A Comparative Analysis of OTF, NPS, and DQE in Energy Integrating and Photon Counting Digital X-ray Detectors. Medical Physics. 2010;37(12):6480-95.

CHAPTER 5

Oblique Reconstructions in Tomosynthesis:

II. Super-Resolution

This chapter expands upon a conference proceedings manuscript published in Lecture Notes in Computer Science **7361**, 737-744 (2012), and is planned for submission to a peer-reviewed journal.

1. INTRODUCTION

In tomosynthesis, a volumetric reconstruction is generated from projection images acquired over a small angular range. Our previous studies proposed a conceptual test object known as a sine plate for assessing image quality in tomosynthesis.¹⁻⁶ This object is a thin strip whose attenuation coefficient varies sinusoidally. Increasing the frequency of the object simulates small closely-spaced structures such as microcalcifications, which are early indicators of cancer. The sine plate has led to the discovery of super-resolution in tomosynthesis (Chapter 3).^{1, 5} Super-resolution is a term which describes the ability to resolve input frequencies higher than the detector alias frequency, or the frequency above which high frequency information is represented as if it were low frequency information in a single projection.⁵

Super-resolution arises because the image of an object is translated in sub-pixel detector element increments between projections. To observe super-resolution, it is necessary to perform the reconstruction with a matrix whose pixel size is much smaller than that of the detector elements. The existence of super-resolution was verified experimentally with a bar pattern phantom^{1, 5} using a commercial digital breast tomosynthesis (DBT) x-ray unit and a commercial prototype reconstruction solution⁷ (BrionaTM, Real Time Tomography, Villanova, PA).

By orienting the long axis of the sine plate along various “pitch” angles relative to the plane of the detector, we have also demonstrated the feasibility of oblique reconstructions in tomosynthesis (Chapter 4). At various frequencies, the modulation transfer function (MTF) was calculated by comparing the amplitude of the reconstruction

against the attenuation coefficient of the sine plate. It was demonstrated that modulation is preserved over a broad range of pitches if the object is thin, but is within detectable limits over a narrower range of pitches if the object is thick.

The previous chapter on oblique reconstructions does not model detector pixelation, and thus does not explicitly show that test frequencies exceeding the detector alias frequency can be reconstructed at various pitches. This current chapter extends our analysis of super-resolution to oblique reconstruction planes. To determine whether the thickness of the object places limits on the feasibility of super-resolution, this chapter also generalizes the MTF calculation to a digital system. For experimental proof of both resolution and super-resolution in oblique reconstructions, projection images of a bar pattern phantom were acquired and subsequently reconstructed.

2. METHODS

2.1. Pitched Sine Plate

A framework for investigating super-resolution in oblique reconstructions for tomosynthesis is now developed. Accordingly, we calculate the reconstruction of a rectangular prism whose linear attenuation coefficient varies sinusoidally along the pitch angle, α_y . As shown in Figure 5.1, the pitch angle corresponds to a rotation of the x and z axes about the y axis perpendicular to the plane of x-ray tube motion (*i.e.*, the xz plane). In DBT, the breast is positioned so that the chest wall lies in the plane of x-ray tube motion, and hence, the y axis is the chest wall-to-nipple direction. The matrix transformation corresponding to the pitch rotation about the y axis is

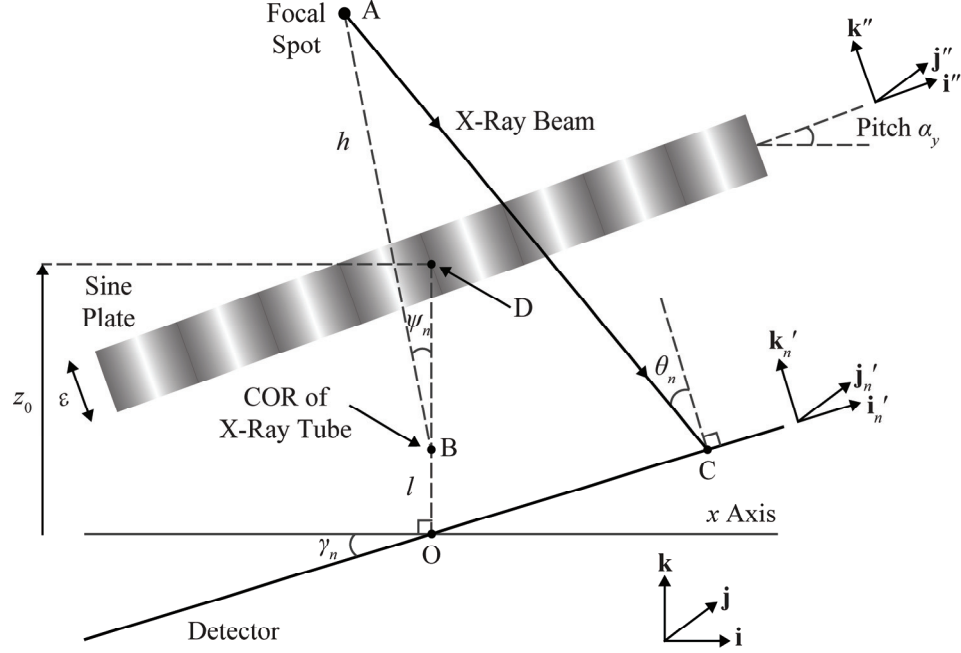


Figure 5.1: Diagram of a pitched sine plate for tomosynthesis reconstruction. A pitched sine plate is used to investigate the potential for super-resolution in oblique reconstructions for tomosynthesis. The pitch axis along the angle α_y relative to the \mathbf{i} direction lies within the plane of x-ray tube motion (*i.e.*, the xz plane). Although a 2D cross section of the object is shown, it is assumed that the object has infinite extent in the $+y$ direction. In acquiring the n^{th} projection image, the x-ray tube rotates about point B at the angle ψ_n relative to the z direction. The detector rotates about the y axis at the angle γ_n relative to the x direction.

$$\begin{pmatrix} \mathbf{i}'' \\ \mathbf{j}'' \\ \mathbf{k}'' \end{pmatrix} = \begin{pmatrix} \cos \alpha_y & 0 & \sin \alpha_y \\ 0 & 1 & 0 \\ -\sin \alpha_y & 0 & \cos \alpha_y \end{pmatrix} \begin{pmatrix} \mathbf{i} \\ \mathbf{j} \\ \mathbf{k} \end{pmatrix}, \quad (5.1)$$

where \mathbf{i} , \mathbf{j} , and \mathbf{k} are orthogonal unit vectors in the x , y , and z directions, respectively, and where \mathbf{i}'' , \mathbf{j}'' , and \mathbf{k}'' are the transformed unit vectors. One can introduce a vector to model the input frequency (f_0) along the pitch angle, α_y . To investigate the potential for super-resolution, this frequency is taken to be higher than the alias frequency of the detector.

$$\mathbf{f}_0 = f_0 \mathbf{i}'' \quad (5.2)$$

$$= f_0 [(\cos \alpha_y) \mathbf{i} + (\sin \alpha_y) \mathbf{k}] \quad (5.3)$$

Figure 5.1 shows a cross section of the input object in the plane of x-ray tube motion. The object has infinite extent in the \mathbf{i}'' and \mathbf{j}'' directions. Defining the origin (O) as the midpoint of the chest wall side of the detector, the attenuation coefficient of the object can thus be written

$$\mu(x, y, z) = C \cdot \cos(2\pi \mathbf{f}_0 \cdot [\mathbf{r} - \mathbf{r}_0]) \cdot \text{rect}\left(\frac{\mathbf{k}'' \cdot [\mathbf{r} - \mathbf{r}_0]}{\varepsilon}\right), \quad (5.4)$$

where \mathbf{r} is a position vector from O to any point (x, y, z) in \mathbb{R}^3 , \mathbf{r}_0 denotes a vector from O to a known point (x_0, y_0, z_0) in the object, C is the maximum value of the attenuation coefficient, ε indicates the object thickness along the \mathbf{k}'' direction, and

$$\text{rect}(u) \equiv \begin{cases} 1 & , |u| \leq 1/2 \\ 0 & , |u| > 1/2 \end{cases}. \quad (5.5)$$

Combining Eqs. (5.1), (5.3), and (5.4) yields

$$\begin{aligned} \mu(x, y, z) = C \cdot \cos\left(2\pi f_0 \left[(x - x_0) \cos \alpha_y + (z - z_0) \sin \alpha_y\right]\right) \\ \cdot \text{rect}\left[\frac{-(x - x_0) \sin \alpha_y + (z - z_0) \cos \alpha_y}{\varepsilon}\right], \end{aligned} \quad (5.6)$$

completing the formalism of the attenuation coefficient.

2.2. Digital Detector Signal

To calculate detector signal for the n^{th} projection, it is useful to perform ray tracing between the focal spot at A and the incident point on the detector at C

(Figure 5.1). The most general tomosynthesis geometry with a divergent x-ray beam and a rotating detector is analyzed. Following our previous work,⁵ the vector from the origin to point C on the detector is written

$$\overrightarrow{OC} = u_1 \mathbf{i}'_n + u_2 \mathbf{j}'_n, \quad (5.7)$$

where u_1 measures detector position within the plane of the x-ray tube motion and u_2 measures position along the perpendicular direction. The unit vectors \mathbf{i}'_n and \mathbf{j}'_n are determined from detector rotation about the y axis at the angle γ_n .

$$\begin{pmatrix} \mathbf{i}'_n \\ \mathbf{j}'_n \\ \mathbf{k}'_n \end{pmatrix} = \begin{pmatrix} \cos \gamma_n & 0 & \sin \gamma_n \\ 0 & 1 & 0 \\ -\sin \gamma_n & 0 & \cos \gamma_n \end{pmatrix} \begin{pmatrix} \mathbf{i} \\ \mathbf{j} \\ \mathbf{k} \end{pmatrix} \quad (5.8)$$

Each projection angle ψ_n relative to the z axis is calculated from the angular spacing between projections ($\Delta\psi$) as

$$\psi_n = n \cdot \Delta\psi, \quad (5.9)$$

so that

$$\gamma_n = \frac{\psi_n}{g}, \quad (5.10)$$

where g denotes the gear ratio of the detector and where the projection number n varies between $-(N-1)/2$ and $+(N-1)/2$. In Chapter 3, the parametric equations for the ray between the focal spot at A and the incident point on the detector at C have been determined.

$$x = w(u_1 \cos \gamma_n + h \sin \psi_n) - h \sin \psi_n \quad (5.11)$$

$$y = wu_2 \quad (5.12)$$

$$z = w(u_1 \sin \gamma_n - l - h \cos \psi_n) + l + h \cos \psi_n \quad (5.13)$$

In these expressions, h is the distance between the focal spot and the center-of-rotation (COR) of the x-ray tube, l is the COR-to-origin distance (Figure 5.1), and w is a free parameter ranging between zero and unity. The x-ray path length \mathcal{L}_n through the input object is now derived from these parametric equations by calculating the points of intersection of the x-ray beam with the planar surfaces of the sine plate. Using Eqs. (5.5) and (5.6), it can be shown that the planar surfaces of the object can be modeled by the expression

$$z_{\pm} = (x - x_0) \tan \alpha_y + z_0 \pm (\varepsilon/2) \sec \alpha_y, \quad (5.14)$$

where the “+” and “-” symbols correspond to the x-ray entrance and exit surfaces, respectively. Denoting x_n^{\pm} and w_n^{\pm} as the values of x and w at these two surfaces, it follows from Eq. (5.11) that

$$w_n^{\pm} = \frac{x_n^{\pm} + h \sin \psi_n}{u_1 \cos \gamma_n + h \sin \psi_n} \quad (5.15)$$

and from Eqs. (5.13)-(5.14) that

$$w_n^{\pm} = \frac{(x_n^{\pm} - x_0) \tan \alpha_y + z_0 \pm (\varepsilon/2) \sec \alpha_y - l - h \cos \psi_n}{u_1 \sin \gamma_n - l - h \cos \psi_n}. \quad (5.16)$$

Eqs. (5.15)-(5.16) provide a system of two equations in two unknowns (x_n^{\pm} and w_n^{\pm}).

Using a computer algebra system (Maple 16, Maplesoft, Waterloo, Ontario) to solve for the two unknowns, w_n^{\pm} can be written in a form that does not depend on x_n^{\pm} .

$$w_n^{\pm} = \frac{z_0 - l - h \cos \psi_n - (x_0 + h \sin \psi_n) \tan \alpha_y \pm (\varepsilon/2) \sec \alpha_y}{u_1 \sin \gamma_n - l - h \cos \psi_n - (u_1 \cos \gamma_n + h \sin \psi_n) \tan \alpha_y} \quad (5.17)$$

Total x-ray attenuation $\mathcal{A}\mu(n)$ for the n^{th} projection is now found by integrating $\mu(x, y, z)$ along \mathcal{L}_n .

$$\mathcal{A}\mu(n) = \int_{\mathcal{L}_n} \mu ds \quad (5.18)$$

From Chapter 3, the differential arc length ds along \mathcal{L}_n is

$$ds = [h \cos(\psi_n - \gamma_n) + l \cos \gamma_n] \sec(\theta_n) \cdot dw, \quad (5.19)$$

where θ_n is the angle of x-ray incidence relative to \mathbf{k}'_n .

$$\theta_n = \arccos \left[\frac{h \cos(\psi_n - \gamma_n) + l \cos \gamma_n}{\sqrt{(u_1 \cos \gamma_n + h \sin \psi_n)^2 + u_2^2 + (l + h \cos \psi_n - u_1 \sin \gamma_n)^2}} \right] \quad (5.20)$$

By combining Eqs. (5.6), (5.11), (5.13), (5.18), and (5.19), the total x-ray attenuation for each projection can now be calculated in closed form

$$\mathcal{A}\mu(n) = \kappa_n \int_{w_n^+}^{w_n^-} \cos \left(2\pi f_0 \left[\frac{(u_1 \cos \gamma_n + h \sin \psi_n) \cos \alpha_y}{+(u_1 \sin \gamma_n - l - h \cos \psi_n) \sin \alpha_y} \right] w + \lambda_n \right) dw \quad (5.21)$$

$$= \frac{\kappa_n \left[\sin \left(2\pi f_0 \left[\frac{(u_1 \cos \gamma_n + h \sin \psi_n) \cos \alpha_y}{+(u_1 \sin \gamma_n - l - h \cos \psi_n) \sin \alpha_y} \right] w_n^- + \lambda_n \right) - \sin \left(2\pi f_0 \left[\frac{(u_1 \cos \gamma_n + h \sin \psi_n) \cos \alpha_y}{+(u_1 \sin \gamma_n - l - h \cos \psi_n) \sin \alpha_y} \right] w_n^+ + \lambda_n \right) \right]}{2\pi f_0 \left[(u_1 \cos \gamma_n + h \sin \psi_n) \cos \alpha_y + (u_1 \sin \gamma_n - l - h \cos \psi_n) \sin \alpha_y \right]}, \quad (5.22)$$

where

$$\kappa_n = C [h \cos(\psi_n - \gamma_n) + l \cos \gamma_n] \sec \theta_n \quad (5.23)$$

$$\lambda_n = 2\pi f_0 [(l + h \cos \psi_n - z_0) \sin \alpha_y - (h \sin \psi_n + x_0) \cos \alpha_y]. \quad (5.24)$$

Using a sum-to-product trigonometric identity for real numbers b_1 and b_2 ,

$$\sin(b_1) - \sin(b_2) = 2 \cos\left(\frac{b_1 + b_2}{2}\right) \sin\left(\frac{b_1 - b_2}{2}\right), \quad (5.25)$$

Eq. (5.22) can be rewritten as

$$\begin{aligned} \mathcal{A}\mu(n) &= \kappa_n (w_n^- - w_n^+) \text{sinc} \left(f_0 \left[\begin{array}{c} (u_1 \cos \gamma_n + h \sin \psi_n) \cos \alpha_y \\ + (u_1 \sin \gamma_n - l - h \cos \psi_n) \sin \alpha_y \end{array} \right] [w_n^- - w_n^+] \right) \\ &\quad \cdot \cos \left(\pi f_0 \left[\begin{array}{c} (u_1 \cos \gamma_n + h \sin \psi_n) \cos \alpha_y \\ + (u_1 \sin \gamma_n - l - h \cos \psi_n) \sin \alpha_y \end{array} \right] [w_n^+ + w_n^-] + \lambda_n \right) \\ &= \left[\frac{\varepsilon \kappa_n \sec \alpha_y}{l + h \cos \psi_n + (u_1 \cos \gamma_n + h \sin \psi_n) \tan \alpha_y - u_1 \sin \gamma_n} \right] \\ &\quad \cdot \text{sinc} \left(\frac{\varepsilon f_0 [u_1 \cos \gamma_n + h \sin \psi_n + (u_1 \sin \gamma_n - l - h \cos \psi_n) \tan \alpha_y]}{l + h \cos \psi_n + (u_1 \cos \gamma_n + h \sin \psi_n) \tan \alpha_y - u_1 \sin \gamma_n} \right) \\ &\quad \cdot \cos \left(\frac{\left(\begin{array}{c} 2\pi f_0 \left[\begin{array}{c} (u_1 \cos \gamma_n + h \sin \psi_n) \cos \alpha_y \\ + (u_1 \sin \gamma_n - l - h \cos \psi_n) \sin \alpha_y \end{array} \right] \cdot [l + h \cos \psi_n + (x_0 + h \sin \psi_n) \tan \alpha_y - z_0] \end{array} \right)}{l + h \cos \psi_n + (u_1 \cos \gamma_n + h \sin \psi_n) \tan \alpha_y - u_1 \sin \gamma_n} + \lambda_n \right) \end{aligned} \quad (5.26)$$

where

$$\text{sinc}(u) \equiv \frac{\sin(\pi u)}{\pi u}. \quad (5.28)$$

Eq. (5.27) gives the signal recorded by the x-ray converter in a detector with no noise or blurring. An amorphous selenium (*a*-Se) photoconductor operated in drift mode is a good approximation for a material with these characteristics. The digitized signal is now found by sampling the total x-ray attenuation using a thin-film transistor (TFT) array

having detector elements with area $a_x \times a_y$. The logarithmically-transformed signal in the \mathbf{m}^{th} detector element for the n^{th} projection is

$$\mathcal{D}\mu(\mathbf{m}, n) = \int_{a_y m_y}^{a_y(m_y+1)} \int_{a_x(m_x-1/2)}^{a_x(m_x+1/2)} \mathcal{A}\mu(n) \cdot \frac{du_1}{a_x} \frac{du_2}{a_y}, \quad (5.29)$$

where m_x and m_y are integers used for labeling detector elements. Detector elements are centered on $u_1 = m_x a_x$ and $u_2 = (m_y + 1/2)a_y$. In the case of square detector elements, it is assumed that $a_x = a_y = a$. Although Eq. (5.29) cannot be evaluated in closed form, this integral can be calculated numerically using the midpoint formula, which is addressed in Chapter 3.⁵

The attenuation coefficient can now be reconstructed using a filtered backprojection (FBP) formula derived in Chapter 3.⁵ It is important to evaluate the reconstruction using pitched slices with extent in the \mathbf{i}'' and \mathbf{j}'' directions [Eq. (5.30)].

$$\begin{pmatrix} x \\ y \\ z \end{pmatrix} = \begin{pmatrix} x_0 \\ y_0 \\ z_0 \end{pmatrix} + \begin{pmatrix} \cos \alpha_y & 0 & -\sin \alpha_y \\ 0 & 1 & 0 \\ \sin \alpha_y & 0 & \cos \alpha_y \end{pmatrix} \begin{pmatrix} x'' \\ y'' \\ z'' \end{pmatrix} \quad (5.30)$$

Within this slice, x'' measures position along the pitch (α_y) and y'' measures position perpendicular to the plane of x-ray tube motion. By contrast, z'' denotes position perpendicular to the slice. All three positions in the double primed coordinate system are measured relative to the point (x_0, y_0, z_0) in the input object.

Following linear systems theory, the net reconstruction filter should be written as the product of ramp (RA) and spectrum apodization (SA) filters in the Fourier domain.

The SA filter is conventionally given by a Hanning window function. The filters are truncated at the frequencies $\pm\xi$ in Fourier space.

2.3. Fourier Transform of the Pitched Reconstruction Slice

To demonstrate that the input object is resolved in the image, the Fourier transform of the pitched reconstruction plane should have a major peak at the test frequency, f_0 . The Fourier transform is now calculated analytically using the FBP reconstruction formula that is derived in Chapter 3 [Eq. (3.65), Acciavatti and Maidment⁵].

$$\mu_{\text{FBP}}(x, y, z) = \sum_{\mathbf{m}, n} \frac{\mathcal{D}\mu(\mathbf{m}, n)}{N} \cdot [\rho_1(t_1)]|_{t_1=\sigma_{1mn}x+\sigma_{2mn}z} \cdot [\rho_2(t_2)]|_{t_2=\sigma_{3mn}x+\sigma_{4mn}y+\sigma_{5mn}z} \quad (5.31)$$

The variables ρ and σ were defined in Chapter 3 to simplify intermediate calculations.⁵

It was demonstrated in that chapter that the 1D Fourier transforms (\mathcal{F}_1) of ρ_1 and ρ_2 are

$$\mathcal{F}_1\rho_1(f_1) = \mathcal{F}_1\phi(f_1) \cdot a_x \cos(\theta_{mn}) \text{sinc}(a_x f_1 \cos \theta_{mn}) e^{-2\pi i m_x a_x f_1 \cos \theta_{mn}} \quad (5.32)$$

$$\mathcal{F}_1\rho_2(f_2) = a_y \cos(\theta_{mn}) \text{sinc}(a_y f_2 \cos \theta_{mn}) e^{-2\pi i (m_y + 1/2) a_y f_2 \cos \theta_{mn}}, \quad (5.33)$$

where $\mathcal{F}_1\phi(f_1)$ is the Fourier representation of the filter and θ_{mn} is the evaluation of θ_n at

the centroid of the \mathbf{m}^{th} detector element. Thus, the 2D Fourier transform (\mathcal{F}_2) of

Eq. (5.31) within the pitched reconstruction slice at the fixed depth z'' is

$$\mathcal{F}_2\mu_{\text{FBP}}(f_x'', f_y'') = \sum_{\mathbf{m}, n} \frac{\mathcal{D}\mu(\mathbf{m}, n)}{N} \cdot \int_{-\infty}^{\infty} \rho_1(\sigma_{1mn}x + \sigma_{2mn}z) \cdot I_{ymn}''(x, z) \cdot e^{-2\pi i f_x'' x} dx'', \quad (5.34)$$

where

$$I''_{y\mathbf{m}n}(x, z) = \int_{-\infty}^{\infty} \rho_2 [\sigma_{3\mathbf{m}n}x + \sigma_{4\mathbf{m}n}(y_0 + y'') + \sigma_{5\mathbf{m}n}z] \cdot e^{-2\pi i f_y'' y''} dy'' . \quad (5.35)$$

In Eq. (5.34), the variables f_x'' and f_y'' are introduced to measure frequency along the x'' and y'' directions, respectively, within the pitched slice. Eq. (5.35) can be evaluated by making the substitution

$$\eta''_{y\mathbf{m}n} = \sigma_{3\mathbf{m}n}x + \sigma_{4\mathbf{m}n}(y_0 + y'') + \sigma_{5\mathbf{m}n}z . \quad (5.36)$$

Since $\sigma_{4\mathbf{m}n} > 0$, one finds

$$I''_{y\mathbf{m}n}(x, z) = \int_{-\infty}^{\infty} \rho_2(\eta''_{y\mathbf{m}n}) e^{\frac{-2\pi i f_y''(\eta''_{y\mathbf{m}n} - \sigma_{3\mathbf{m}n}x - \sigma_{5\mathbf{m}n}z - \sigma_{4\mathbf{m}n}y_0)}{\sigma_{4\mathbf{m}n}}} \frac{d\eta''_{y\mathbf{m}n}}{\sigma_{4\mathbf{m}n}} \quad (5.37)$$

$$= \frac{e^{\frac{2\pi i f_y''(\sigma_{3\mathbf{m}n}x + \sigma_{5\mathbf{m}n}z + \sigma_{4\mathbf{m}n}y_0)}{\sigma_{4\mathbf{m}n}}}}{\sigma_{4\mathbf{m}n}} \int_{-\infty}^{\infty} \rho_2(\eta''_{y\mathbf{m}n}) e^{-2\pi i \left(\frac{f_y''}{\sigma_{4\mathbf{m}n}}\right) \eta''_{y\mathbf{m}n}} d\eta''_{y\mathbf{m}n} \quad (5.38)$$

$$= \frac{e^{\frac{2\pi i f_y''(\sigma_{3\mathbf{m}n}x + \sigma_{5\mathbf{m}n}z + \sigma_{4\mathbf{m}n}y_0)}{\sigma_{4\mathbf{m}n}}}}{\sigma_{4\mathbf{m}n}} \mathcal{F}_1 \rho_2 \left(\frac{f_y''}{\sigma_{4\mathbf{m}n}} \right). \quad (5.39)$$

Hence, from Eq. (5.34), it follows that

$$\mathcal{F}_2 \mu_{\text{FBP}}(f_x'', f_y'') = \sum_{\mathbf{m}, n} \frac{\mathcal{D}\mu(\mathbf{m}, n)}{N} \frac{I''_{x\mathbf{m}n}}{\sigma_{4\mathbf{m}n}} \mathcal{F}_1 \rho_2 \left(\frac{f_y''}{\sigma_{4\mathbf{m}n}} \right), \quad (5.40)$$

where

$$I''_{x\mathbf{m}n} = \int_{-\infty}^{\infty} \rho_1(\sigma_{1\mathbf{m}n}x + \sigma_{2\mathbf{m}n}z) e^{-2\pi i \left[f_x'' x'' - \frac{(\sigma_{3\mathbf{m}n}x + \sigma_{5\mathbf{m}n}z + \sigma_{4\mathbf{m}n}y_0) f_y''}{\sigma_{4\mathbf{m}n}} \right]} dx'' \quad (5.41)$$

$$= \int_{-\infty}^{\infty} \rho_1 \left[\left(\sigma_{1\mathbf{m}n} \cos \alpha_y + \sigma_{2\mathbf{m}n} \sin \alpha_y \right) x'' + \sigma_{1\mathbf{m}n} x_1 + \sigma_{2\mathbf{m}n} z_1 \right] \cdot e^{-2\pi i \left[\left(f_x'' \left[\frac{\sigma_{3\mathbf{m}n} \cos \alpha_y + \sigma_{5\mathbf{m}n} \sin \alpha_y}{\sigma_{4\mathbf{m}n}} \right] f_y'' \right) x'' - \frac{(\sigma_{3\mathbf{m}n} x_1 + \sigma_{5\mathbf{m}n} z_1 + \sigma_{4\mathbf{m}n} y_0) f_y''}{\sigma_{4\mathbf{m}n}} \right]} dx'' \quad (5.42)$$

and where

$$x_1 = x_0 - z'' \sin \alpha_y \quad (5.43)$$

$$z_1 = z_0 + z'' \cos \alpha_y. \quad (5.44)$$

Eq. (5.30) justifies the transition from Eq. (5.41) to Eq. (5.42). In Eqs. (5.43)-(5.44), the variables x_1 and z_1 are introduced to simplify intermediate calculations. To evaluate Eq. (5.42), it is necessary to perform the change of variables

$$\eta''_{xmn} = \left(\sigma_{1mn} \cos \alpha_y + \sigma_{2mn} \sin \alpha_y \right) x'' + \sigma_{1mn} x_1 + \sigma_{2mn} z_1, \quad (5.45)$$

giving

$$I''_{xmn} = \int_{-\infty}^{\infty} \frac{\rho_1(\eta''_{xmn})}{\left| \sigma_{1mn} \cos \alpha_y + \sigma_{2mn} \sin \alpha_y \right|} \cdot e^{-2\pi i \left[f_x'' \frac{\left[\sigma_{3mn} \cos \alpha_y + \sigma_{5mn} \sin \alpha_y \right] f_y''}{\sigma_{4mn}} \left(\frac{\eta''_{xmn} - \sigma_{1mn} x_1 - \sigma_{2mn} z_1}{\sigma_{1mn} \cos \alpha_y + \sigma_{2mn} \sin \alpha_y} \right) - \frac{(\sigma_{3mn} x_1 + \sigma_{5mn} z_1 + \sigma_{4mn} y_0) f_y''}{\sigma_{4mn}} \right]} d\eta''_{xmn} \quad (5.46)$$

$$= \frac{e^{2\pi i \left[f_x'' \frac{\left[\sigma_{3mn} \cos \alpha_y + \sigma_{5mn} \sin \alpha_y \right] f_y''}{\sigma_{4mn}} \left(\frac{\sigma_{1mn} x_1 + \sigma_{2mn} z_1}{\sigma_{1mn} \cos \alpha_y + \sigma_{2mn} \sin \alpha_y} \right) + \frac{(\sigma_{3mn} x_1 + \sigma_{5mn} z_1 + \sigma_{4mn} y_0) f_y''}{\sigma_{4mn}} \right]}}{\left| \sigma_{1mn} \cos \alpha_y + \sigma_{2mn} \sin \alpha_y \right|} \quad (5.47)$$

$$\cdot \int_{-\infty}^{\infty} \rho_1(\eta''_{xmn}) e^{-2\pi i \left(\frac{\sigma_{4mn} f_x'' - \left[\sigma_{3mn} \cos \alpha_y + \sigma_{5mn} \sin \alpha_y \right] f_y''}{\sigma_{4mn} \left[\sigma_{1mn} \cos \alpha_y + \sigma_{2mn} \sin \alpha_y \right]} \right) \eta''_{xmn}} d\eta''_{xmn}$$

$$= \frac{e^{2\pi i \left[f_x'' \frac{\left[\sigma_{3mn} \cos \alpha_y + \sigma_{5mn} \sin \alpha_y \right] f_y''}{\sigma_{4mn}} \left(\frac{\sigma_{1mn} x_1 + \sigma_{2mn} z_1}{\sigma_{1mn} \cos \alpha_y + \sigma_{2mn} \sin \alpha_y} \right) + \frac{(\sigma_{3mn} x_1 + \sigma_{5mn} z_1 + \sigma_{4mn} y_0) f_y''}{\sigma_{4mn}} \right]}}{\left| \sigma_{1mn} \cos \alpha_y + \sigma_{2mn} \sin \alpha_y \right|} \quad (5.48)$$

$$\cdot \mathcal{F}_1 \rho_1 \left(\frac{\sigma_{4mn} f_x'' - \left[\sigma_{3mn} \cos \alpha_y + \sigma_{5mn} \sin \alpha_y \right] f_y''}{\sigma_{4mn} \left(\sigma_{1mn} \cos \alpha_y + \sigma_{2mn} \sin \alpha_y \right)} \right)$$

Substituting Eq. (5.48) into Eq. (5.40) yields the final expression for the 2D Fourier transform.

$$\begin{aligned}
\mathcal{F}_2 \mu_{\text{FBP}}(f_x'', f_y'') = \sum_{\mathbf{m}, n} \frac{\mathcal{D}\mu(\mathbf{m}, n)}{N} \frac{e}{\left| \sigma_{1m} \cos \alpha_y + \sigma_{2m} \sin \alpha_y \right| \sigma_{4m}} & \cdot \mathcal{F}_1 \rho_1 \left(\frac{\sigma_{4m} f_x'' - \left[\sigma_{3m} \cos \alpha_y + \sigma_{5m} \sin \alpha_y \right] f_y''}{\sigma_{4m} (\sigma_{1m} \cos \alpha_y + \sigma_{2m} \sin \alpha_y)} \right) \\
& \cdot \mathcal{F}_1 \rho_2 \left(\frac{f_y''}{\sigma_{4m}} \right)
\end{aligned} \quad (5.49)$$

An important special case of Eq. (5.49) occurs with $f_y'' = 0$.

$$\begin{aligned}
\mathcal{F}_2 \mu_{\text{FBP}}(f_x'', 0) = \sum_{\mathbf{m}, n} \frac{\mathcal{D}\mu(\mathbf{m}, n)}{N} \frac{e}{\left| \sigma_{1m} \cos \alpha_y + \sigma_{2m} \sin \alpha_y \right| \sigma_{4m}} & \cdot \mathcal{F}_1 \rho_1 \left(\frac{f_x''}{\sigma_{1m} \cos \alpha_y + \sigma_{2m} \sin \alpha_y} \right)
\end{aligned} \quad (5.50)$$

This special case is useful for analyzing an input frequency oriented along the pitch, α_y , such as the input frequency given in Eq. (5.2). To analyze an input frequency oriented along a 0° pitch ($\alpha_y = 0$), one can introduce the equation $z = z_0$ to define the plane of reconstruction. It follows directly from Eqs. (5.1) and (5.30) that the following properties hold for this reconstruction plane: $x_0 = z'' = 0$ and $f_x'' = f_x$. If one makes these substitutions in Eq. (5.50), one can recover the Fourier transform of a conventional reconstruction plane that was derived in Chapter 3 [Eq. (3.86), Acciavatti and

Maidment⁵]. This agreement with our previous work provides a built-in check on the validity of Eq. (5.50).

3. THEORETICAL RESULTS

3.1. Projection Images

Projection images are now simulated for a Selenia Dimensions DBT system (Hologic Inc., Bedford, MA), assuming an object thickness (ε) of 0.05 mm, an object pitch (α_y) of 20° , and an object displacement (x_0) of 0 mm along the direction parallel to the chest wall side of the breast support. The acquisition parameters for this system are detailed in Chapter 3.⁵ The centroid of the sine plate (point D in Figure 5.1) is simulated at the depth $z_0 = 50.0$ mm. This depth corresponds to the mid-thickness of a typical breast size (50.0 mm thick), assuming that the breast support is 25.0 mm above the detector. In order to investigate super-resolution in this system with $140 \mu\text{m}$ detector elements, the test frequency (f_0) is chosen to be 5.0 lp/mm. This input frequency is higher than the detector alias frequency (3.6 lp/mm).

The total attenuation of a zero frequency object is now calculated in order to normalize the amplitude C of the attenuation coefficient of the input waveform. From Eqs. (5.23) and (5.27), it follows that

$$C = \left[\frac{1}{N} \sum_n \frac{\varepsilon [h \cos(\psi_n - \gamma_n) + l \cos \gamma_n] \sec(\theta_n) \sec(\alpha_y)}{l + h \cos \psi_n + [u_1(n) \cos \gamma_n + h \sin \psi_n] \tan \alpha_y - u_1(n) \sin \gamma_n} \right]^{-1}, \quad (5.51)$$

where

$$u_1(n) = \frac{x_0(l + h \cos \psi_n) + z_0 h \sin \psi_n}{x_0 \sin \gamma_n + (l - z_0) \cos \gamma_n + h \cos(\psi_n - \gamma_n)} \quad (5.52)$$

$$u_2(n) = \frac{y_0 [l \cos \gamma_n + h \cos(\psi_n - \gamma_n)]}{x_0 \sin \gamma_n + (l - z_0) \cos \gamma_n + h \cos(\psi_n - \gamma_n)}. \quad (5.53)$$

This calculation assumes that rays for each projection pass through the point (x_0, y_0, z_0) , giving rise to x-ray attenuation. Concordant with Chapter 3, Eqs. (5.52) and (5.53) are derived from the equations [Eqs. (5.11)-(5.13)] for the ray between the focal spot and the point (u_1, u_2) on the detector. Although $u_2(n)$ is not a coordinate listed directly in Eq. (5.51), it is calculated in Eq. (5.53) as a necessary substitution in the formula for θ_n [Eq. (5.20)].

In Figure 5.2(a) and 5.2(b), a cross section of signal is plotted versus detector position u_1 for the central projection ($n = 0$) and an oblique projection ($n = 7$). The signal is calculated at the distance $u_2 = 30.0$ mm from the chest wall side of the breast support. Following Chapter 3,⁵ this u_2 displacement is chosen to simulate a position approximately halfway between the chest wall and nipple in a typical breast size (450 ml). To illustrate that oblique x-ray incidence introduces a translational shift in the image of the object on the detector, Figure 5.2(b) shows the shift in the oblique projection [Eq. (5.52)], assuming that $h = 70.0$ cm as would be characteristic of the Selenia Dimensions system. The analogous shift in the central projection is zero [Figure 5.2(a)].

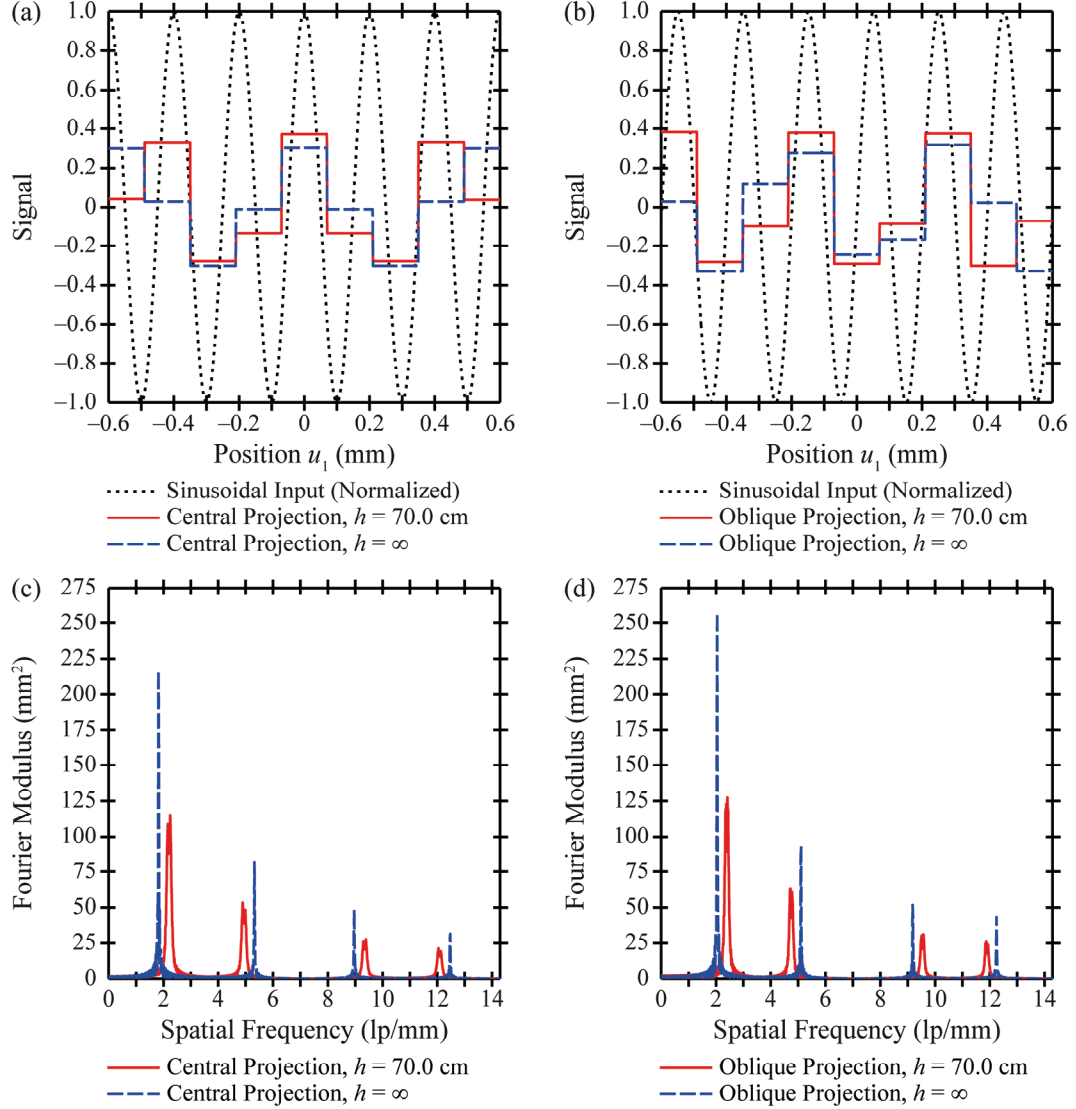


Figure 5.2: Simulated projections of a pitched sine plate. (a)-(b) Two projection images of a pitched sine plate are shown, assuming $\alpha_y = 20^\circ$, $f_0 = 5.0$ lp/mm, $\varepsilon = 0.05$ mm, $x_0 = 0$ mm, and $z_0 = 50.0$ mm. Signal is plotted versus detector position u_1 at the fixed distance (u_2) of 30.0 mm from the plane of x-ray tube motion. The presence of each detector element ($a = 0.14$ mm) is modeled by a rectangle function. (c)-(d) The Fourier transforms of each projection show classical signs of aliasing. The major Fourier peak does not occur at the input frequency (5.0 lp/mm) but instead at a frequency less than the detector alias frequency, 3.6 lp/mm.

Although detector signal is a discrete function in a digital system, it is represented graphically as a continuous function in Figure 5.2(a) and 5.2(b). The presence of each

detector element is modeled by a rectangle function whose width matches the detector element length (0.14 mm). The projection images do not have the appearance of the input waveform, but instead are step-like due to the detector element sampling.

To illustrate the presence of aliasing in the two projection images, the Fourier transform of detector signal is also calculated in Figure 5.2. Chapter 3 has demonstrated that this Fourier transform is

$$\mathcal{F}_2(\mathcal{S}\mu)(f_1, f_2) = a^2 \text{sinc}(af_1) \text{sinc}(af_2) \cdot \sum_{\mathbf{m}} \mathcal{D}\mu(\mathbf{m}, n) \cdot e^{-2\pi i a [m_x f_1 + (m_y + 1/2) f_2]}, \quad (5.54)$$

where $\mathcal{S}\mu$ denotes the detector signal, and f_1 and f_2 measure frequency along the u_1 and u_2 directions, respectively. Figure 5.2(c) and 5.2(d) show the Fourier transform versus f_1 , assuming $f_2 = 0$. The major peak of the Fourier transform does not occur at the input frequency (5.0 lp/mm), but instead at a frequency less than the detector alias frequency (3.6 lp/mm). This finding is concordant with Chapter 3 studying a similar test frequency at a 0° pitch in place of the 20° pitch.

Although the source-to-COR distance (h) is 70.0 cm in the Selenia Dimensions system, it is useful to consider projections at an infinite value of h . This limiting case corresponds to a parallel beam geometry. As illustrated in Figure 5.2(c) and 5.2(d), the positions of the Fourier peaks for each projection are dependent on h . For a parallel beam geometry ($h = \infty$), Figure 5.3 illustrates how to calculate the frequencies of the Fourier peaks in the central projection. The period T of the test frequency projects onto the x-ray converter as $T \cos \alpha_y$. Hence, the projected frequency is $f_0 \sec \alpha_y$, or 5.3 lp/mm. This frequency gives the first minor Fourier peak in Figure 5.2(c). Sampling by the thin-film transistor (TFT) array aliases the input frequency to 1.8 lp/mm, yielding

the major Fourier peak. The two largest Fourier peaks in Figure 5.2(c) are equidistant from the detector alias frequency $0.5a^{-1}$ (3.6 lp/mm). As shown in the figure, two additional Fourier peaks occur at 9.0 lp/mm and 12.5 lp/mm. These peaks are similarly equidistant from the frequency $1.5a^{-1}$ (10.7 lp/mm).

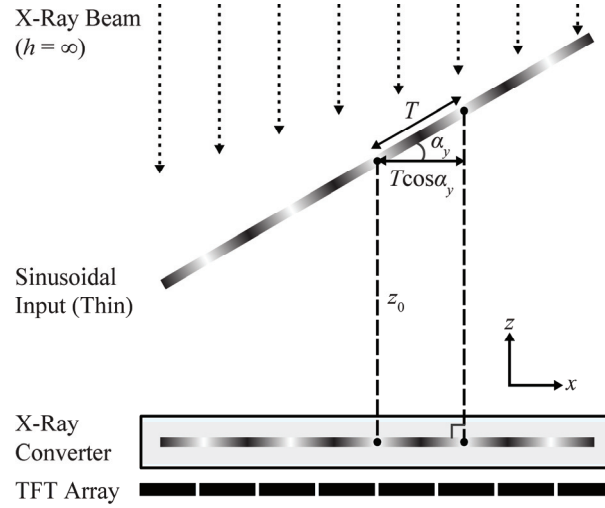


Figure 5.3: Illustration of the projection of a pitched sine plate onto the detector. The projection of a pitched sine plate onto the detector is illustrated using a parallel x-ray beam geometry ($h = \infty$). As shown, the period T of the input waveform is projected onto the x-ray converter as $T \cos \alpha_y$ in the central projection. Hence, the frequency detected by the x-ray converter is $f_0 \sec \alpha_y$, or 5.3 lp/mm assuming $f_0 = 5.0$ lp/mm and $\alpha_y = 20^\circ$. This frequency corresponds to the first minor Fourier peak in Figure 5.2(c) in the acquisition geometry for which $h = \infty$.

Unlike a parallel beam geometry, a divergent beam geometry ($h = 70.0$ cm) magnifies the object that is projected onto the x-ray converter. Denoting M as the magnification

$$M = \frac{h}{h - z_0}, \quad (5.55)$$

it follows from Figure 5.3 that the test frequency f_0 projects onto the x-ray converter as $M^{-1} \cdot f_0 \sec \alpha_y$, or 4.9 lp/mm. This frequency corresponds to the first minor Fourier peak in Figure 5.2(c). The major peak at 2.2 lp/mm and the first minor peak are equidistant from the alias frequency, 3.6 lp/mm. As expected, additional Fourier peaks occur at 9.3 lp/mm and 12.1 lp/mm with equal distance relative to the frequency $1.5a^{-1}$ (10.7 lp/mm).

3.2. SBP and FBP Reconstruction

In Figure 5.4(a), SBP reconstruction is shown in a slice with signal measured in the x'' direction along a 20° pitch, assuming that $y''=0$ and $z''=0$ [Eq. (5.30)]. Although a single projection is not capable of resolving the test frequency, the pitched reconstruction is capable of resolving 5.0 lp/mm properly. The corresponding SBP Fourier transform [Eq. (5.50)] shows that the major peak occurs at the input frequency [Figure 5.4(c)]. These results generalize our previous work on super-resolution at a 0° pitch (Chapter 3) to an oblique pitch.

FBP reconstructions and their Fourier transforms are also plotted in Figure 5.4 using either the RA filter alone or the RA and SA filters together. Following Chapter 3 on super-resolution, the filter truncation frequency (ξ) is 14.3 lp/mm, corresponding to the second zero of the modulation transfer function (MTF) of the detector sampling process

$$\text{MTF}(f_1, f_2) = |\text{sinc}(af_1)\text{sinc}(af_2)|. \quad (5.56)$$

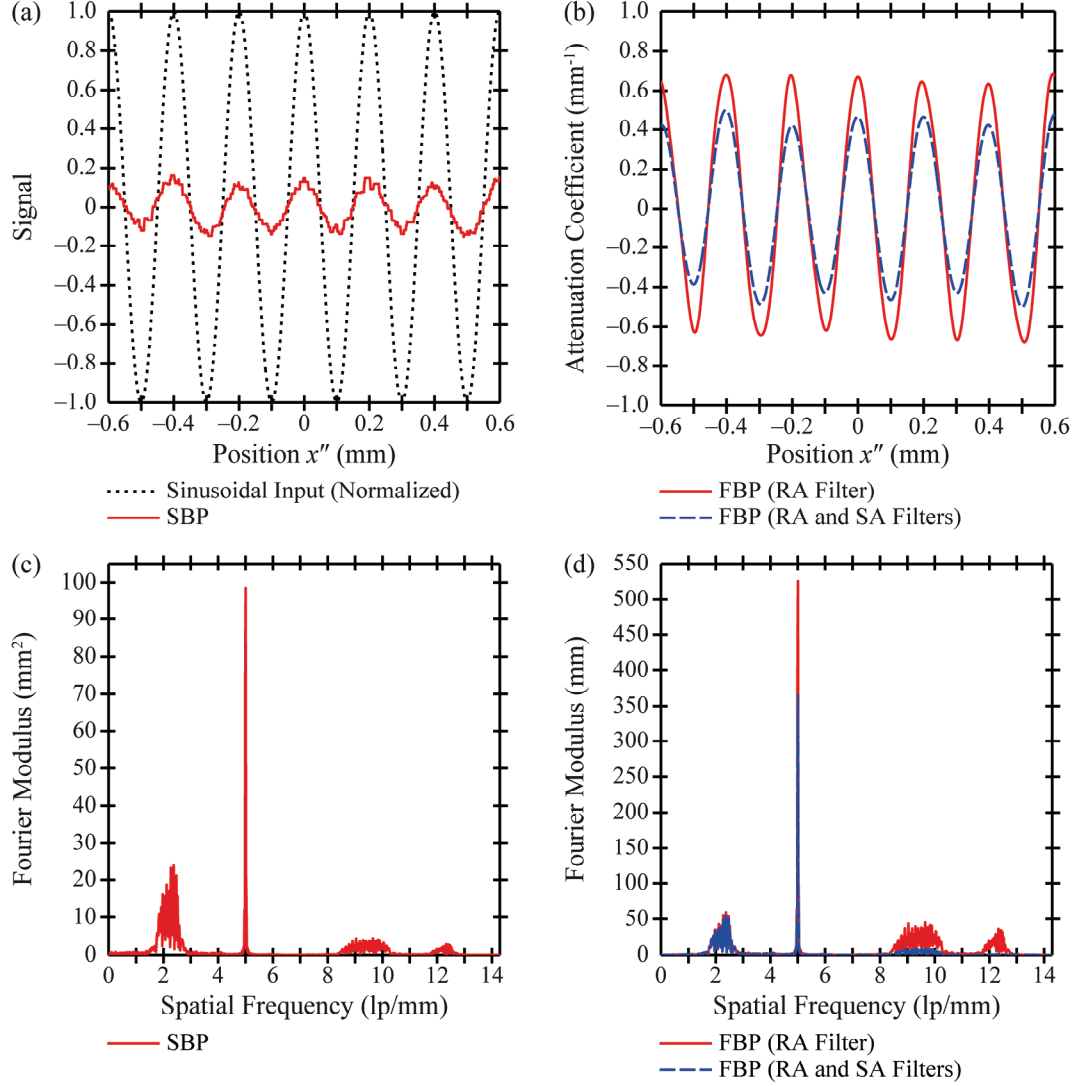


Figure 5.4: Simulated reconstruction of a pitched sine plate. SBP and FBP reconstructions are performed using a slice with signal measured in the x'' direction along the 20° pitch of the input object, assuming $y'' = 0$ and $z'' = 0$. Unlike a single projection (Figure 5.2), the reconstructions can resolve the high frequency object. The corresponding Fourier transforms have a major peak at the input frequency (5.0 lp/mm), demonstrating that our earlier work on super-resolution at a 0° pitch (Chapter 3) can be generalized to oblique reconstructions.

This value of ξ is chosen to correspond with the second zero of the MTF measured along the f_1 direction, assuming that $f_2 = 0$. Figure 5.4 demonstrates that like SBP, the Fourier transforms of FBP reconstructions possess their major peak at the input frequency,

5.0 lp/mm. Filtering provides an improvement over SBP reconstruction by smoothing pixelation artifacts in the spatial domain. The two FBP reconstructions differ in that reconstruction with the RA filter alone has greater modulation than reconstruction with the RA and SA filters together. This finding is expected, since the SA filter places more relative weight on low frequencies to reduce high frequency noise. The drawback of reconstructing with the RA filter alone is the increased amplitude of high frequency spectral leakage in the Fourier domain. Figures 5.4(b) and 5.4(d) are qualitatively concordant with the results at a 0° pitch in Chapter 3.

3.3. Effect of Object Thickness on the Modulation Transfer Function (MTF)

Section 3.2 has demonstrated the existence of super-resolution in oblique reconstructions using a relatively thin input object ($\epsilon = 0.05$ mm). Based on Chapter 4 modeling a non-pixelated detector, one would expect the MTF in an oblique reconstruction to be substantially degraded at large object thicknesses. For this reason, we now investigate the thickness dependency of super-resolution in oblique reconstructions.

In Figure 5.5, the dependency of the MTF on object thickness and frequency is investigated with surface plots at two pitches (0° and 20°), assuming SBP reconstruction. Following convention, the MTF is found by normalizing the amplitude of the reconstruction at each test frequency f_0 against the corresponding value for a zero-frequency object ($f_0 = 0$). As Figure 5.4 illustrates, the amplitude of the reconstruction can be determined by the value at $x'' = 0$, corresponding to signal at the point (x_0, y_0, z_0) .

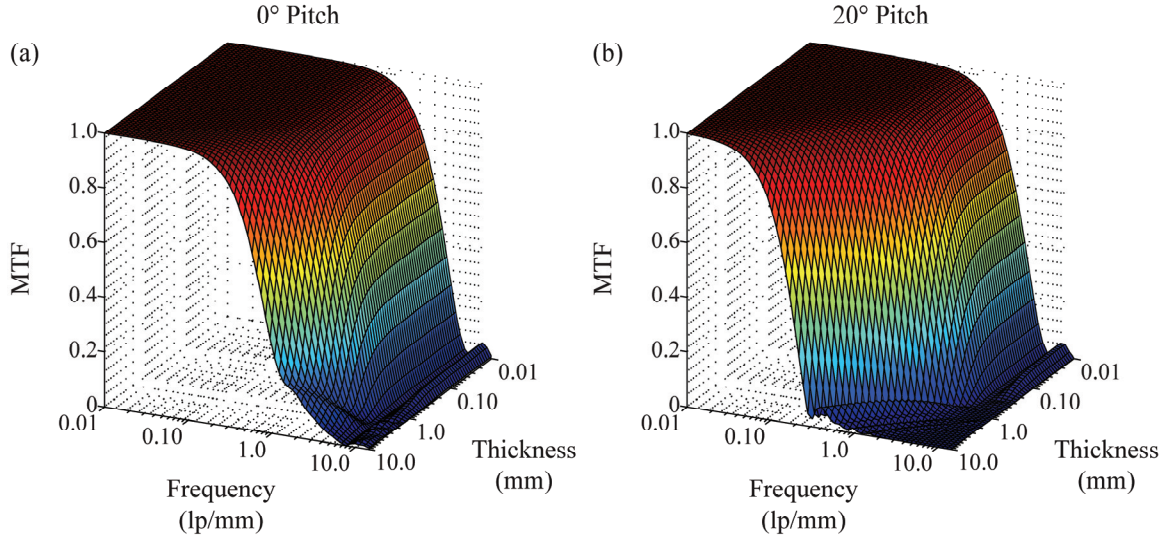


Figure 5.5: Dependency of the modulation transfer function (MTF) on frequency and object thickness. Using SBP reconstruction, the dependency of the MTF on frequency and object thickness is investigated at two pitches (0° and 20°). If the object is thin, the MTF does not differ considerably between the two pitches. However, if the object is thick, the loss in modulation at high frequencies is much more pronounced at the 20° pitch than at the 0° pitch.

In the case of a very thin object ($\epsilon = 0.01$ mm), Figure 5.5 demonstrates that there is minimal difference in MTF between the 0° and 20° pitches. It is typically assumed that the object is detectable if the MTF exceeds 10.0%. Using this threshold, one can show that frequencies up to 5.7 and 5.4 lp/mm are visible at the 0° and 20° pitches, respectively. These frequencies exceed the detector alias frequency, 3.6 lp/mm. Consequently, super-resolution is achievable at either pitch.

Turning next to the case of a thick object, Figure 5.5 shows that the MTF is more sharply degraded with increasing frequency. The resolution loss at high frequencies is much more pronounced at the 20° pitch than at the 0° pitch. For example, if the object is 1.0 mm thick, the highest detectable frequencies at the 0° and 20° pitches are 5.4 and 2.5 lp/mm, respectively, assuming that the limit of resolution is an MTF of 10.0%. This

finding illustrates that super-resolution is only achievable in an oblique reconstruction if the object is thin. Super-resolution is feasible at a 0° pitch over a much broader range of object thicknesses.

In the reconstruction of a thick object, Figure 5.5 demonstrates that low frequencies have detectable modulation over a broader range of pitches than high frequencies. To illustrate this concept, Figure 5.6(a)-(b) shows the reconstruction of a relatively thick object ($\varepsilon = 1.0$ mm) at 2.0 and 5.0 lp/mm with either the 0° or 20° pitch. Modulation is detectable at both pitches for the low frequency object, but is detectable only at the 0° pitch for the high frequency object.

In Figure 5.6(b), the reconstruction of the 5.0 lp/mm frequency at a 20° pitch shows a 180° phase shift that is not observed in the other plots in the figure. This result can be explained from the fact that the optical transfer function (OTF) is negative. Recall that the MTF is the normalized modulus of the OTF. The OTF attains negative values at frequencies just exceeding the first zero of the MTF (Figure 5.5).

3.4. Limiting Resolution of an Oblique Reconstruction

3.4.1. Loss of Resolution with Increasing Object Thickness

Using an MTF of 10.0% as the limit of resolution, Figure 5.6(c) explicitly studies the thickness dependence of the highest frequency with detectable modulation. As expected, it is demonstrated that modulation is within detectable limits over a broad range of frequencies if the object is thin. Modulation is detectable over a narrower range of frequencies if the object is thick.

It is also shown in Figure 5.6(c) that the highest frequency with detectable modulation decreases with pitch. If the object is very thin (0.01 mm thick), the highest frequencies with detectable modulation are 5.7, 5.5, 5.0, 4.0, 2.9, and 1.5 lp/mm at 0°, 15°, 30°, 45°, 60°, and 75° pitches, respectively. As expected, the highest frequency with detectable modulation does not exceed the frequency corresponding to 10.0% detector MTF (6.5 lp/mm), which can be calculated from Eq. (5.56) assuming that $f_2 = 0$. Figure 5.6(c) illustrates that super-resolution is not achievable at pitches approaching 90°, regardless of object thickness. However, modulation of lower frequency objects is preserved even at high obliquity.

3.4.2. Aliasing at Large Object Thicknesses

In Figure 5.6(c), the thickness range is truncated at an intermediate value (3.8 mm) for the 0° pitch. Unlike the other pitches in the plot, it can be demonstrated that frequencies exceeding the detector alias frequency have detectable modulation at thicknesses exceeding 3.8 mm. We now show that these high frequencies are aliased based on a metric developed in Chapter 3.⁵ Using the Fourier transform of the SBP reconstruction of a sine plate [Figure 5.4(c)], this metric is the ratio (r) of the amplitude of the highest peak less than the detector alias frequency (3.6 lp/mm) to the amplitude at the input frequency (5.0 lp/mm). Super-resolution is present if $r < 1$, while aliasing is present if $r \geq 1$. Figure 5.6(d) shows that the r -factor exceeds unity at thicknesses greater than 3.8 mm for a 0° pitch. Because Figure 5.6(d) demonstrates the existence of aliasing at these thicknesses, the corresponding thickness range is truncated in Figure 5.6(c).

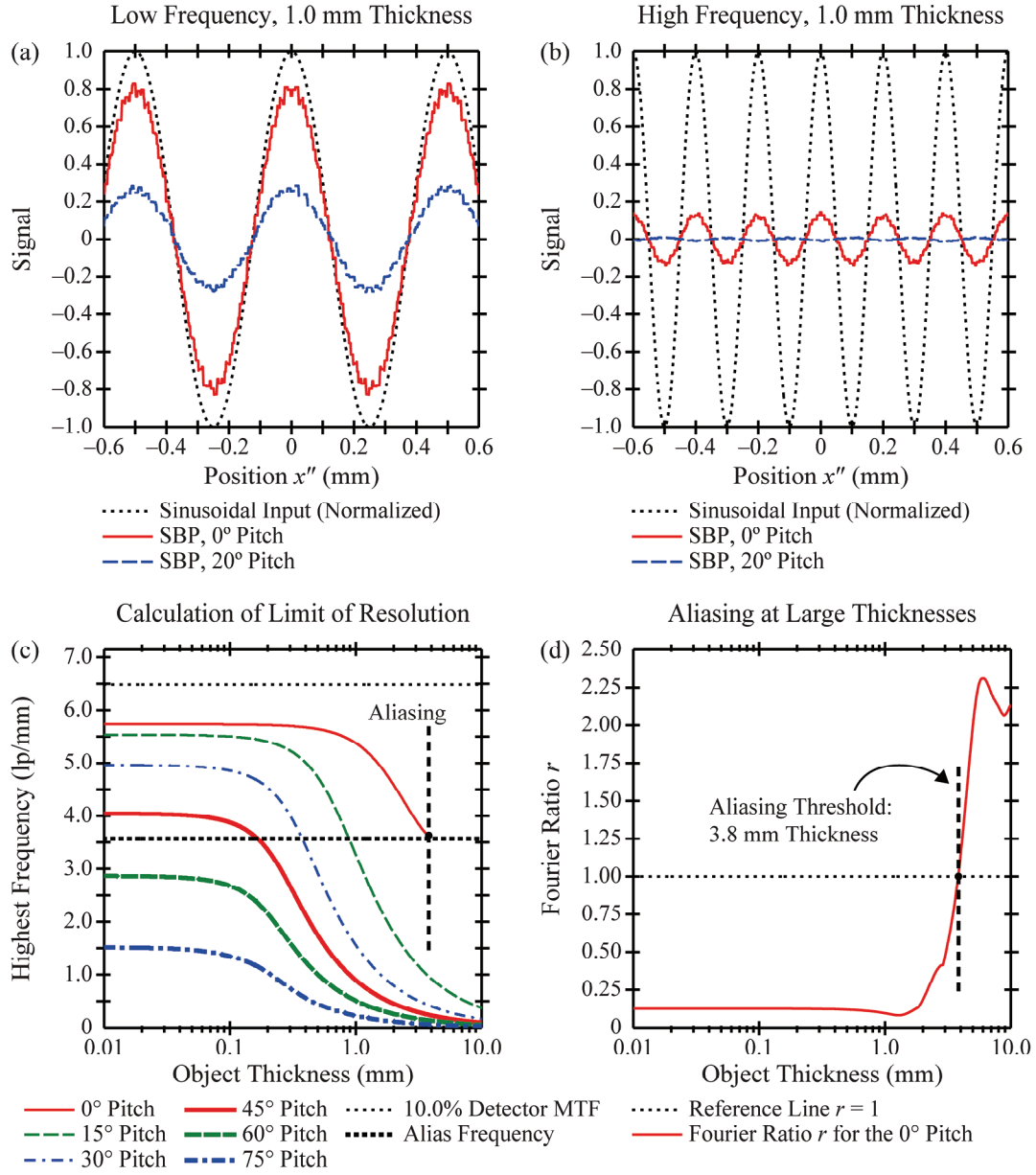


Figure 5.6: Effect of object thickness on the limit of resolution. (a) In the SBP reconstruction of a 1.0 mm thick object with a 2.0 lp/mm input frequency, modulation is detectable at both the 0° and 20° pitches. (b) In the analogous reconstruction at a 5.0 lp/mm input frequency, modulation is detectable only at the 0° pitch. (c) Using an MTF threshold of 10.0% as the limit of resolution of SBP reconstruction, the highest frequency with detectable modulation is plotted versus object thickness. At various pitches, this figure shows that the object must be thin in order to maximize the range of frequencies with detectable modulation. (d) At a 0° pitch, super-resolution is not achievable at thicknesses exceeding 3.8 mm ($r \geq 1$).

To further illustrate that aliasing is present at thicknesses exceeding 3.8 mm, the SBP reconstruction of a 5.0 mm thick sine plate is shown in Figure 5.7 for the 0° pitch. As expected from Figure 5.6(d), this object is not resolved since the peaks and troughs in the reconstruction do not properly match the input frequency. The r -factor is 2.0 at this thickness.

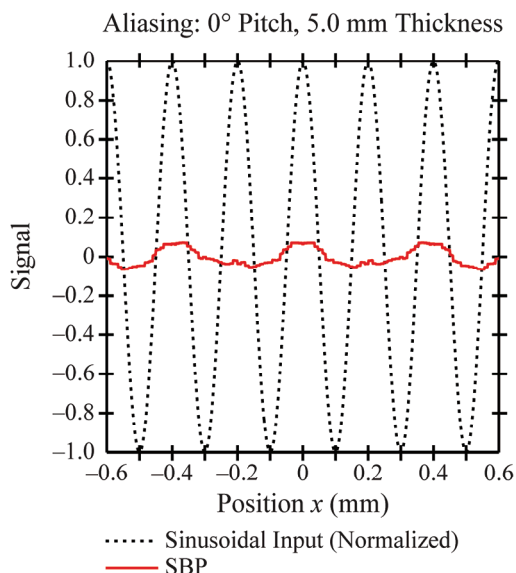


Figure 5.7: Aliasing in the reconstruction of a thick sine plate. At a 0° pitch, the SBP reconstruction of a very thick object ($\varepsilon = 5.0$ mm) shows aliasing for a 5.0 lp/mm input frequency. This result illustrates that the thickness of the test object places a constraint on the feasibility of super-resolution, as expected from Figure 5.6(d) using the r -factor.

3.5. Depth Dependence of Super-Resolution

Using the r -factor, Chapter 3 showed that the existence of super-resolution is dependent on depth (z_0) in the reconstruction. For frequency measurements along the x direction, it was demonstrated that various depths in the plane $x = 0$ do not exhibit super-resolution. The plane $x = 0$ was termed the mid PA/SS plane in Chapter 3, since this

plane has extent in the posteroanterior (PA) and source-to-support (SS) directions in breast applications. Figure 5.8 investigates whether the depth-dependency of the r -factor continues to hold in oblique reconstructions. The detector field-of-view (FOV) used for calculating the Fourier transforms is $42.1 \text{ mm} \times 42.1 \text{ mm}$ and is centered on the mid PA/SS plane. The detector element indices m_x and m_y range from -150 to $+150$ and 0 to 301 , respectively; this range matches the one used in Figure 5.6(d). At the two smallest pitches investigated in Figure 5.8 (0° and 2.5°), r exceeds unity at eight depths, which are comparable to the results presented in Chapter 3.⁵ At these eight peaks, the image of the sine plate is translated in approximately integer multiples of detector element length between projections. Super-resolution is not achievable since the translational shifts between projections do not maximize sub-pixel sampling gain.

Turning next to the 5.0° pitch, Figure 5.8 shows that the r -factor continues to peak at eight depths in the reconstruction, but does not exceed unity. Super-resolution is technically achievable at all depths in the reconstruction. Since r exceeds 0.5 at these eight peaks, the quality of super-resolution is not optimal.

By increasing the pitch further to 7.5° , 10.0° , or 20.0° , Figure 5.8 shows that the peaks in the value of r have much lower amplitude. Hence, super-resolution with reasonably good quality can be achieved at all depths for these pitches.

Although the r -factor can be used to analyze the existence of super-resolution, it does not demonstrate whether modulation is within detectable limits. Unpublished experimental work has shown that modulation is indeed within detectable limits at all

depths in the reconstruction. Future work will further explore the calculation of modulation at various reconstruction depths.

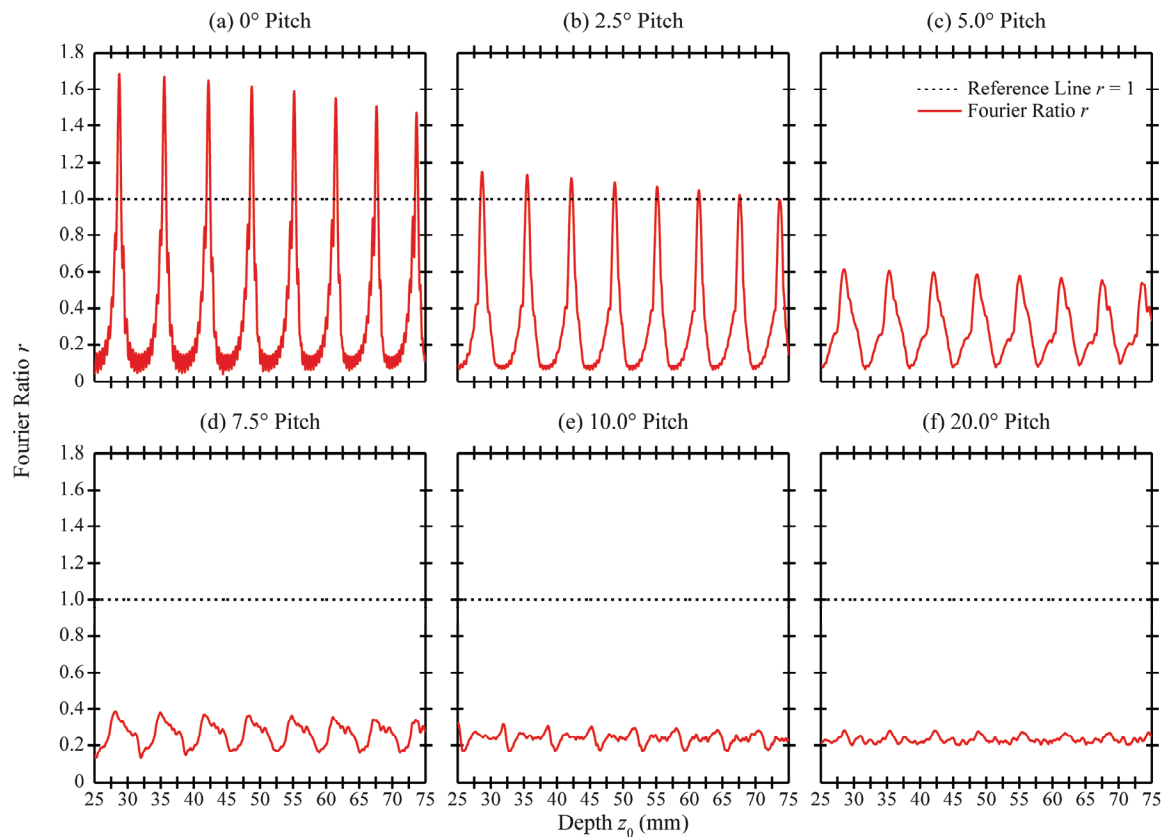


Figure 5.8: Depth dependency of super-resolution in oblique reconstructions. The depth dependency of super-resolution is investigated for measurements made in the mid PA/SS plane ($x = 0$) using a 5.0 lp/mm input frequency. At a 0° or 2.5° pitch, super-resolution is not achievable at various reconstruction depths for which $r \geq 1$. By increasing the pitch, it is demonstrated that the peaks in the value of r have much lower amplitude. For high quality super-resolution, r should approach zero. All subplots in this figure implicitly share a common legend.

4. EXPERIMENTAL RESULTS

In order to validate the analytical model, a goniometry stand was used to vary the pitch of a relatively thin ($\varepsilon = 0.05$ mm) bar pattern phantom (Model 07-515, Fluke Biomedical, Cleveland, OH). Projection images were acquired on a Selenia Dimensions DBT system, and reconstruction was performed in the oblique plane of the bar patterns using a commercial prototype backprojection filtering (BPF) algorithm⁷ (BrionaTM, Real Time Tomography, Villanova, PA). The technique factors of the image acquisition matched the ones given in Chapter 3. The long axis of the phantom, which was centered on the mid PA/SS plane, was positioned at a fixed depth, $z_0 = 10.8$ cm above the detector, for all pitches. Although this depth corresponds to a position outside the breast in a typical 5.0 cm thickness under compression, it was the only depth supported by the goniometry stand and is presented for the purpose of experimental validation of oblique reconstructions.

To illustrate that a single projection image cannot resolve frequencies exceeding the detector alias frequency, the central projection of the bar pattern phantom at a 0° pitch is shown in Figure 5.9. The projection misrepresents frequencies higher than 3.6 lp/mm. For example, at 4.0 lp/mm, Moiré patterns are present. At 5-7 lp/mm, the line pairs have an erroneous orientation and are imaged as if they were a lower frequency.

As expected from Chapter 3 on super-resolution, a reconstruction at a 0° pitch [Figure 5.10(a)] is capable of resolving higher frequencies than a single projection. Frequencies up to 5.75 lp/mm can be resolved. This estimate of the highest detectable frequency is approximated to the nearest multiple of 0.25 lp/mm, since it is determined

by visual inspection. The reconstruction grid was specified to have 10-times smaller pixelation ($14.0\text{ }\mu\text{m}$) than the detector in order to support super-resolution. At a 30° pitch, the reconstruction in the plane of the bar patterns [Figure 5.10(b)] also shows super-resolution, as frequencies up to 4.75 lp/mm have detectable modulation. This experimental result verifies that our earlier work on super-resolution (Chapter 3) can be generalized to an oblique reconstruction plane.

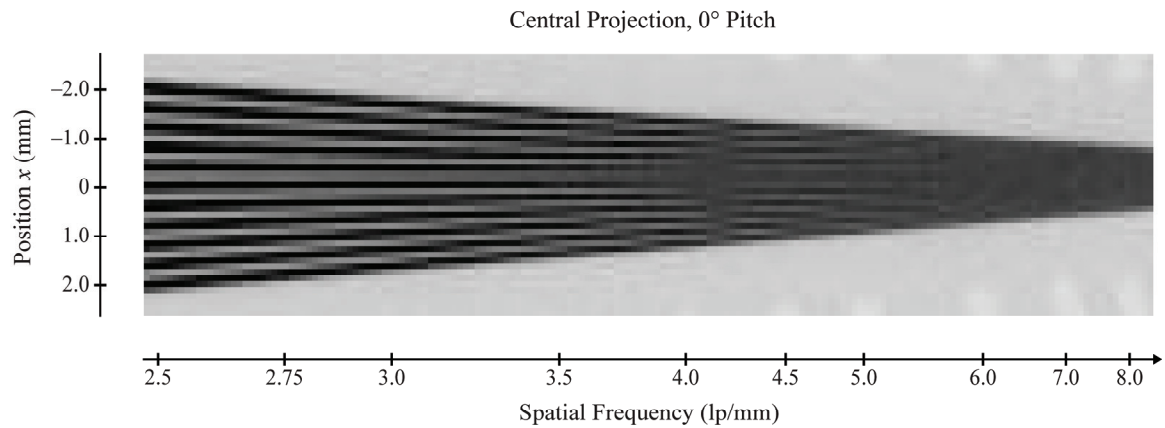


Figure 5.9: Experimental image of a bar pattern phantom in a plane parallel to the breast support. A bar pattern phantom was positioned parallel to the breast support (*i.e.*, at a 0° pitch) of a Selenia Dimensions DBT system. It is shown here that the central projection cannot resolve frequencies higher than the detector alias frequency, 3.6 lp/mm , for $140\text{ }\mu\text{m}$ detector elements.

Concordant with the analytical model, the experimental images demonstrated that super-resolution is not achievable at pitches approaching 90° . To illustrate this concept, Figure 5.10(c) shows the reconstruction of the bar pattern phantom at a 60° pitch. The highest frequency with detectable modulation is 3.0 lp/mm .

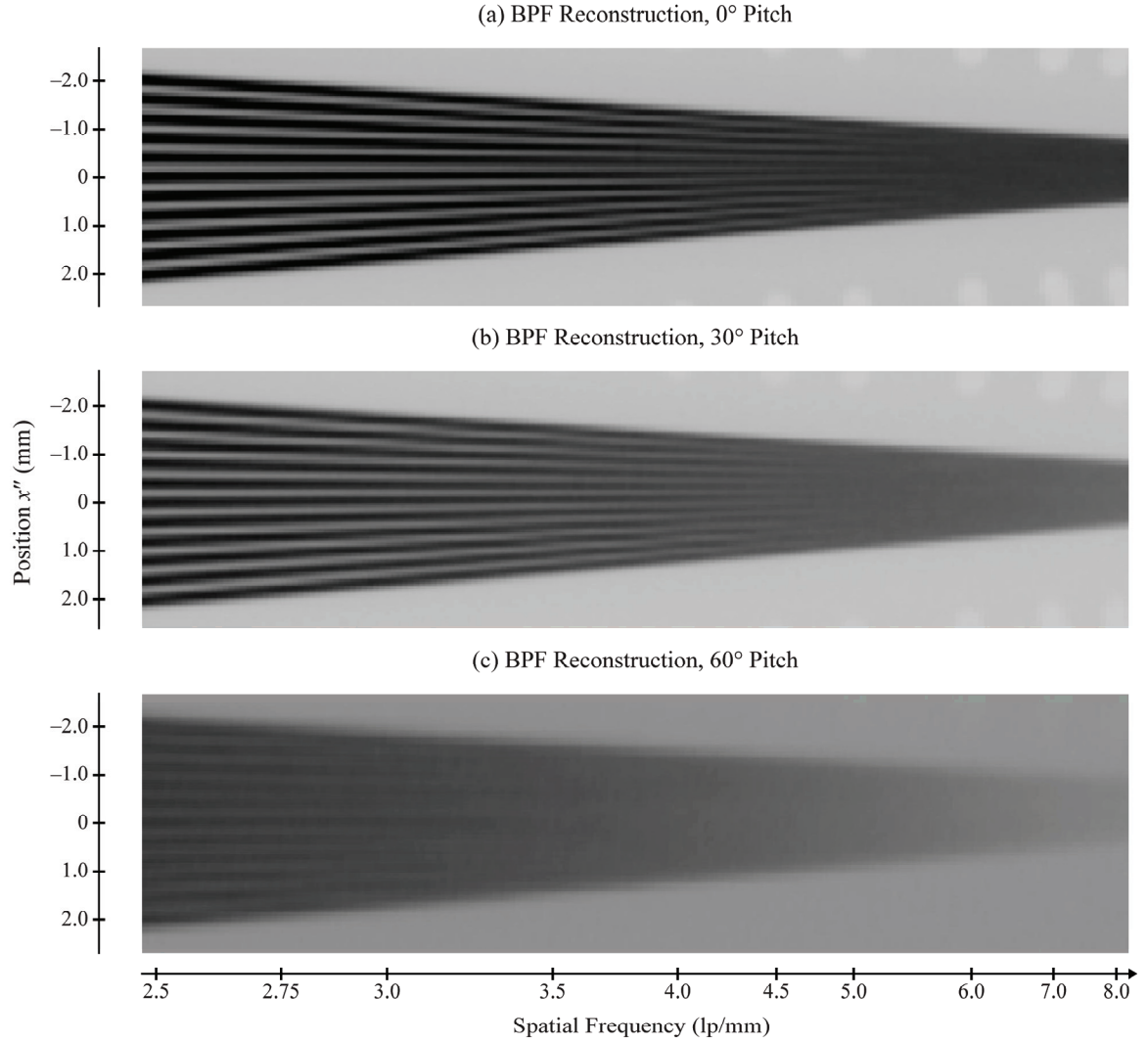


Figure 5.10: Experimental reconstructions of a bar pattern phantom along various pitches. (a) A BPF reconstruction, which is performed on a grid with much smaller pixelation than the detector, is capable of resolving higher frequencies than a single projection. As shown here at the 0° pitch, the highest frequency with detectable modulation is approximately 5.75 lp/mm. This frequency is higher than the detector alias frequency, 3.6 lp/mm. (b) A reconstruction in the oblique plane of the bar patterns at a 30° pitch also shows super-resolution, with visibility of frequencies up to 4.75 lp/mm. (c) At a 60° pitch, the highest frequency with detectable modulation is 3.0 lp/mm. This result illustrates that super-resolution is not achievable at pitches approaching 90° .

Although Figure 5.10 only shows reconstructions at 0° , 30° , and 60° pitches, images of bar patterns at additional pitches were also obtained experimentally. By

visually inspecting the reconstruction at each pitch, the highest frequency with detectable modulation was determined. The estimate was approximated to the nearest multiple of 0.25 lp/mm. In Figure 5.11, these results are compared against the predictions of the analytical model. Because there is no absolute threshold for detectable modulation, we consider MTF thresholds of 5.0%, 10.0%, and 15.0% in the analytical model. Figure 5.11 demonstrates that the highest frequency with detectable modulation decreases with pitch. The experimental data are in good agreement with the analytical model.

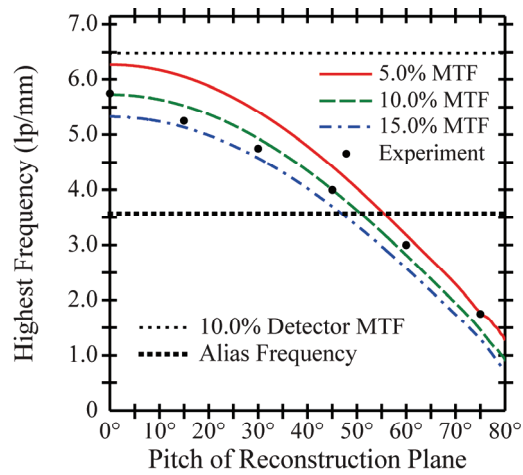


Figure 5.11: Effect of pitch on the limit of resolution. Using the experimental reconstructions, the highest frequency with detectable modulation is plotted versus the pitch of the bar pattern phantom. In addition, the analogous results derived from the analytical model are shown using MTF thresholds of 5.0%, 10.0%, and 15.0%. The experimental results show good agreement with the analytical model.

The highest frequency that can be resolved in a single projection is the alias frequency of the detector. Using Figure 5.11, one can calculate the pitch at which the highest frequency with detectable modulation exactly matches the alias frequency of the detector (3.6 lp/mm). For an MTF threshold of 10.0%, this pitch is 51°. This result

suggests that a 51° angle is a practical upper limit for the pitch at which a reconstruction should be generated. Figure 5.11 presumes that the object is relatively thin (0.05 mm thick). Because a clinical reconstruction consists of objects with various thicknesses, future work is necessary to determine the range of pitches at which clinical reconstructions are appropriate.

5. CLINICAL RESULTS

In breast imaging, super-resolution has application in the visualization of fine structural details, such as microcalcifications. This concept is illustrated in Figure 5.12 which builds upon a clinical example presented in Chapter 3.⁵ Figure 5.12(a) is created by magnifying a slice at a 0° pitch using $140\text{ }\mu\text{m}$ voxels matching the detector element size. The net result has $35\text{ }\mu\text{m}$ voxels. By contrast, Figure 5.12(b) is a reconstruction using much smaller pixelation than the detector, yielding a sharper image that supports super-resolution. In Figure 5.12(c), a slice is generated at a 30° pitch using the same pixelation as Figure 5.12(b). Figure 5.12(c) demonstrates that the visibility of the lower cluster of calcifications is not considerably different from Figure 5.12(b). The impact of super-resolution is evident in the oblique reconstruction plane.

The upper left cluster of calcifications is not visible at the 30° pitch in Figure 5.12(c), as it is out of the reconstruction plane. Visualization is improved by orthogonally translating the reconstruction plane by 5.0 mm [Figure 5.12(d)]. The calcifications are sharper in Figure 5.12(d) than in Figure 5.12(a), reflecting the effect of super-resolution.

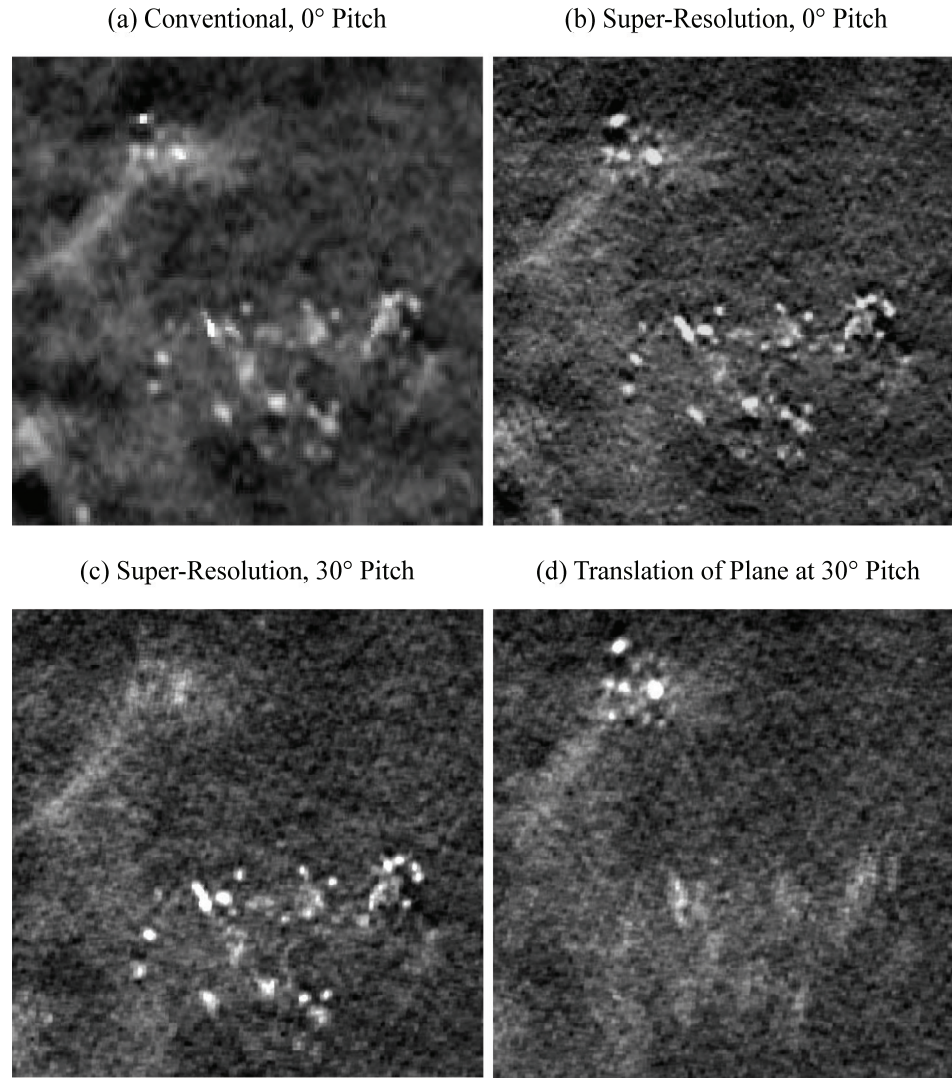


Figure 5.12: An anecdotal clinical image of microcalcifications using oblique reconstructions. In breast imaging, the concepts studied in this chapter have applications in the visualization of microcalcifications. (a) A slice at a 0° pitch in a BPF reconstruction is initially created using pixels matching the detector element size ($140\ \mu\text{m}$), and the result is magnified to give the image displayed. (b) A slice at a 0° pitch is generated using a reconstruction grid with much smaller pixelation than the detector. (c) Using the same reconstruction grid size as image (b), the pitch of the reconstruction plane is changed to 30° . (d) The oblique reconstruction plane in image (c) is orthogonally translated by 5.0 mm to bring the upper left cluster of calcifications into focus. Images (b), (c), and (d) support super-resolution, unlike image (a).

Although the lower cluster of calcifications spans the same area in Figure 5.12(c) as in Figure 5.12(b), the upper left cluster spans a larger area in Figure 5.12(d) than in Figure 5.12(b). This result might indicate that the upper cluster is obliquely pitched relative to the breast support and is best visualized in an oblique reconstruction plane (Figure 5.13). While it would be reasonable to assume that a reconstruction is optimally viewed along the actual pitch of the calcification cluster, it is not possible to determine this optimal pitch due to the lack of ground truth in clinical images. The development of a framework for determining the optimal pitch for viewing a clinical reconstruction is beyond the scope of this work, but should be the subject of future studies.

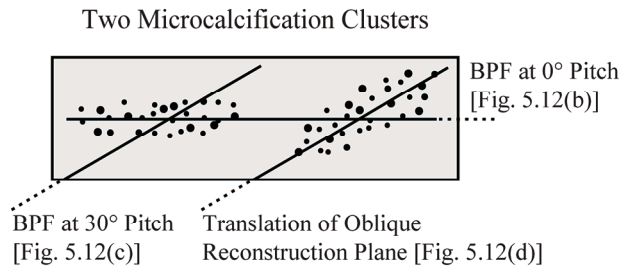


Figure 5.13: Illustration of microcalcifications oriented along various pitches. A sketch of microcalcification clusters at two orientations is shown. It is posited that the calcification cluster in Figure 5.12(d) is obliquely pitched relative to the breast support, unlike the cluster in Figure 5.12(c).

Oblique reconstructions also have application in quantifying the size of a complex cancer. Figure 5.14 shows the reconstruction of a clinical example using slices at 0° and 38° angles relative to the breast support. It appears that the full extent of the lesion can be seen more clearly in the oblique plane than in the plane parallel to the breast support. It also appears that the tumor margins are defined more precisely in the oblique plane. A

future clinical study is merited to quantify the clinical impact of oblique reconstructions in tomosynthesis.

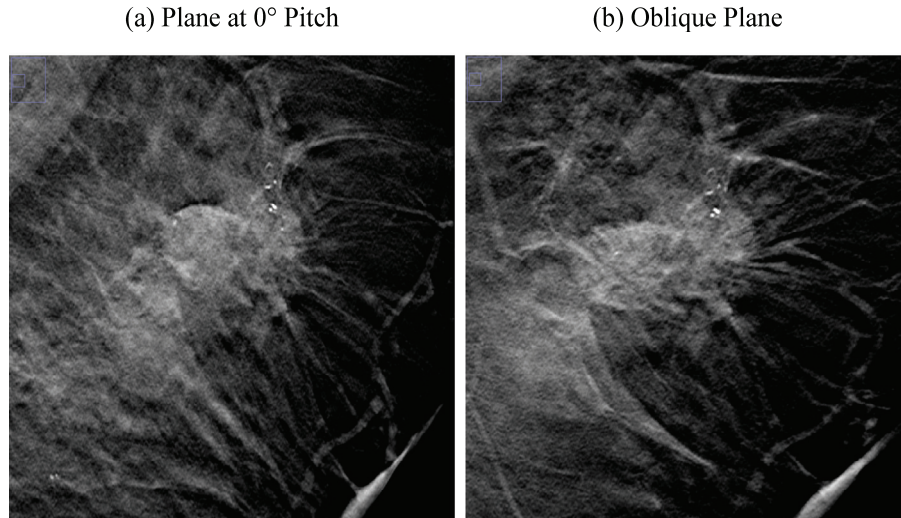


Figure 5.14: Visualization of a complex cancer using oblique reconstructions. (a) A reconstruction plane at a 0° angle relative to the breast support does not show the full extent of a complex cancer in this anecdotal example. (b) A plane at a 38° relative to the breast support appears to show the full extent of the lesion more clearly and to define the borders of the tumor more precisely.

6. DISCUSSION

Chapter 4 gave a proof-of-principle justification for oblique reconstructions in tomosynthesis. Because simplifying assumptions about the acquisition geometry were made in that chapter, it was not explicitly demonstrated that oblique reconstructions are capable of super-resolution. By modeling detector pixelation and additional features of the acquisition geometry, this current chapter shows that input frequencies exceeding the detector alias frequency are indeed resolvable in an oblique reconstruction. The features

of the acquisition geometry that are modeled in this chapter, but not in the preceding chapter, are summarized in Table 5.1.

SUMMARY OF DESIGN FEATURES MODELED IN TWO CHAPTERS ON OBLIQUE RECONSTRUCTIONS FOR TOMOSYNTHESIS	
Chapter 4	Chapter 5
Non-pixelated detector	Pixelated detector
Stationary detector	Rotating detector
2D Reconstruction Space	3D Reconstruction Space
Parallel X-Ray Beam Geometry	Divergent X-Ray Beam Geometry
Infinitesimally small angular spacing between projections	Discrete step angles between projections

Table 5.1: Summary of the modeling assumptions in chapters 4 and 5. In simulating the reconstruction of a pitched sine plate (Figure 5.1), this chapter models features of the tomosynthesis acquisition geometry that were not modeled in the preceding chapter. The most important feature for demonstrating the existence of super-resolution is detector pixelation.

In order for a test frequency to be visualized in an image, it is necessary for the MTF to exceed the detectability limit (10.0%). This chapter demonstrates that an object must be thin for frequencies exceeding the detector alias frequency to have detectable MTF in an oblique reconstruction. This constraint does not hold for low frequency objects, which are detectable in oblique reconstructions at larger thicknesses.

The r -factor was investigated as a metric for assessing the depth dependency of super-resolution. In oblique reconstruction planes centered about the mid PA/SS plane, it was demonstrated that the depth dependency of the r -factor is minimized with increasing

pitch. Thus, one benefit of increasing the pitch of the reconstruction plane is minimizing the anisotropies in super-resolution.

The existence of super-resolution in oblique reconstructions was validated with a commercial DBT system by analyzing a bar pattern phantom. Super-resolution is achievable up to a 51° pitch in the Selenia Dimensions geometry, assuming that the input object is thin. As we noted in Chapter 3,⁵ the feasibility of super-resolution is not necessarily unique to the commercial DBT system analyzed or to the commercial reconstruction algorithm used. A necessary constraint is that the reconstruction algorithm supports finer sampling than the detector. The range of pitches at which super-resolution is achievable is dependent upon the design of the acquisition geometry.

By using modulation as the metric of detectability, this chapter implicitly assumes that noise does not influence the visibility of an object. This assumption is valid for a high contrast bar pattern phantom, as was the case in the experimental images. If one were to consider low contrast signals, the relative signal-to-noise would be a more useful metric of detectability. Future work should expand the analytical model to simulate quantum noise at various radiation dose levels, as well as other noise sources.⁸ The highest detectable frequency in an oblique reconstruction plane [Figures 5.6(c), 5.11] could then be calculated as a function of the radiation dose.

Although the 2D MTF for a slice in the reconstruction is used as a metric of image quality in this chapter (Figure 5.5), Chapter 4 demonstrated that 3D MTF can also be used as a metric of image quality. In Chapter 4, we showed that the 3D MTF is non-zero within a region resembling a double cone in the f_x - f_z planes of Fourier space (Figure 4.1).

The opening angle of the sampling cones matches the angular range of the scan. Since the 0° pitch is contained within the sampling cones in a parallel beam geometry, conventional practice is to create slices along this pitch. It is important to note that the 0° pitch is not necessarily contained within the sampling cones in a divergent beam geometry. At the corner of the detector opposite the chest wall, for example, the incident angle (θ_n) varies over 15 projections between 22.9° and 26.3° in the Selenia Dimensions system with a $24.0 \text{ cm} \times 29.0 \text{ cm}$ detector FOV. In this example, an important distinction must be drawn between the 3D MTF and the in-plane MTF. Although the 3D MTF is zero along the 0° pitch of Fourier space, the 2D MTF of a slice along this pitch is non-zero. This property arises because the in-plane MTF is the integral of the 3D MTF along the direction perpendicular to the slice.

In order to view a reconstruction using an oblique plane, this chapter assumes that the conventional reconstruction planes perpendicular to the z axis are rotated about the y axis, or the chest wall-to-nipple direction in a breast application. Oblique reconstruction planes can also be generated by a rotation about the x axis, or the direction parallel to the chest wall side of the breast support. Using the conventional definition of Euler angles, the latter rotation is termed a “roll” instead of a “pitch”. Roll rotations were not modeled in this chapter, although we have successfully investigated these experimentally (images not shown). Roll rotations should be investigated in future work to generalize the calculation of the highest detectable frequency [Figures 5.6(c) and 5.11] to various pitch and roll combinations.

A few additional directions for more complete modeling in future work are now noted. Future work should simulate blurring in the x-ray converter, so that total attenuation in Eq. (5.27) is convolved with a point spread function (PSF). Blurring in the x-ray converter is most pronounced at the edges and corners of the detector due to increasing deviation in the angle of x-ray incidence relative to the normal to the detector. Previous studies have calculated the MTF degradation due to oblique x-ray incidence.⁹⁻¹⁶

Detector lag and ghosting are additional concepts that would be useful to model in future studies.¹⁷⁻¹⁹ Although this chapter implicitly assumes the presence of a monoenergetic x-ray beam, polyenergetic x-ray spectra²⁰⁻²² should also be simulated in future work. Finally, the MTF degradation due to the finite size of the focal spot,²³ as well as focal spot motion during a continuous scan of x-ray projections,²⁴⁻²⁶ should be simulated. While these subtleties of the acquisition geometry were not modeled directly in this chapter, the simulations showed reasonably good agreement with experimental results for the purpose of this work.

7. CONCLUSION

This chapter demonstrates the existence of super-resolution in oblique reconstructions for tomosynthesis. We show that test frequencies exceeding the detector alias frequency can be resolved in an oblique plane created with pixelation smaller than the detector element size. The test object must be thin in order for high frequencies to have detectable modulation.

Experimental images of a thin bar pattern phantom verified the existence of super-resolution in oblique reconstructions. In good agreement with the predictions of the analytical model, the range of frequencies with detectable modulation decreased with increasing pitch, so that only low frequency objects could be detected at pitches approaching 90° . This limiting case corresponds to a test frequency perpendicular to the breast support in the DBT system used for experimental validation. In breast imaging, super-resolution has application in the visualization of microcalcifications and other subtle signs of cancer.

8. REFERENCES

- ¹Acciavatti RJ, Maidment ADA. Investigating the Potential for Super-Resolution in Digital Breast Tomosynthesis. In: Pelc NJ, Samei E, Nishikawa RM, editors. SPIE Medical Imaging; 2011; Lake Buena Vista, FL: SPIE; 2011. p. 79615K-1 - K-12.
- ²Acciavatti RJ, Maidment ADA. Optimization of Continuous Tube Motion and Step-and-Shoot Motion in Digital Breast Tomosynthesis Systems with Patient Motion. In: Pelc NJ, Nishikawa RM, Whiting BR, editors. SPIE Medical Imaging; 2012; San Diego, CA: SPIE; 2012. p. 831306-1 - 12.
- ³Acciavatti RJ, Maidment ADA. Proposing an Acquisition Geometry That Optimizes Super-Resolution in Digital Breast Tomosynthesis. Lecture Notes in Computer Science. 2012;7361:386-93.
- ⁴Acciavatti RJ, Mein SB, Maidment ADA. Investigating Oblique Reconstructions with Super-Resolution in Digital Breast Tomosynthesis. Lecture Notes in Computer Science. 2012;7361:737-44.
- ⁵Acciavatti RJ, Maidment ADA. Observation of super-resolution in digital breast tomosynthesis. Medical Physics. 2012;39(12):7518-39.
- ⁶Acciavatti RJ, Bakic PR, Maidment ADA. Proposing a New Velocity Profile for Continuous X-Ray Tube Motion in Digital Breast Tomosynthesis. In: Nishikawa RM, Whiting BR, Hoeschen C, editors. SPIE Medical Imaging; 2013; Lake Buena Vista, FL: SPIE; 2013. p. 86680F-1 - F-10.
- ⁷Kuo J, Ringer PA, Fallows SG, Bakic PR, Maidment ADA, Ng S. Dynamic Reconstruction and Rendering of 3D Tomosynthesis Images. In: Pelc NJ, Samei E, Nishikawa RM, editors. SPIE Medical Imaging; 2011; Lake Buena Vista, FL: SPIE; 2011. p. 796116-1 - 11.
- ⁸Barrett HH, Myers KJ. Chapter 12: Noise in Detectors. In: Saleh BEA, editor. Foundations of Image Science. New York, NY: John Wiley & Sons; 2004. p. 701-800.
- ⁹Que W, Rowlands JA. X-ray imaging using amorphous selenium: Inherent spatial resolution. Medical Physics. 1995;22(4):365-74.
- ¹⁰Hajdok G, Cunningham IA. Penalty on the detective quantum efficiency from off-axis incident x rays. In: Yaffe MJ, Flynn MJ, editors. Medical Imaging 2004: Physics of Medical Imaging; 2004; San Diego, CA: SPIE; 2004. p. 109-18.
- ¹¹Mainprize JG, Bloomquist AK, Kempston MP, Yaffe MJ. Resolution at oblique incidence angles of a flat panel imager for breast tomosynthesis. Medical Physics. 2006;33(9):3159-64.
- ¹²Acciavatti RJ, Maidment ADA. Calculation of OTF, NPS, and DQE for Oblique X-Ray Incidence on Turbid Granular Phosphors. Lecture Notes in Computer Science. 2010;6136:436-43.
- ¹³Freed M, Park S, Badano A. A fast, angle-dependent, analytical model of CsI detector response for optimization of 3D x-ray breast imaging systems. Medical Physics. 2010;37(6):2593-605.
- ¹⁴Freed M, Park S, Badano A. Erratum: "A fast, angle-dependent, analytical model of CsI detector response for optimization of 3D x-ray breast imaging systems" [Med. Phys. 37, 2593-2605 (2010)]. Medical Physics. 2011;38(4):2307.

- ¹⁵Badano A, Freed M, Fang Y. Oblique incidence effects in direct x-ray detectors: A first-order approximation using a physics-based analytical model. *Medical Physics*. 2011;38(4):2095-8.
- ¹⁶Acciavatti RJ, Maidment ADA. Optimization of phosphor-based detector design for oblique x-ray incidence in digital breast tomosynthesis. *Medical Physics*. 2011;38(11):6188-202.
- ¹⁷Bloomquist AK, Yaffe MJ, Mawdsley GE, Hunter DM. Lag and ghosting in a clinical flat-panel selenium digital mammography system. *Medical Physics*. 2006;33(8):2998-3005.
- ¹⁸Siewerdsen JH, Jaffray DA. A ghost story: Spatio-temporal response characteristics of an indirect-detection flat-panel imager. *Medical Physics*. 1999;26(8):1624-41.
- ¹⁹Zhao W, DeCrescenzo G, Kasap SO, Rowlands JA. Ghosting caused by bulk charge trapping in direct conversion flat-panel detectors using amorphous selenium. *Medical Physics*. 2005;32(2):488-500.
- ²⁰Tucker DM, Barnes GT, Chakraborty DP. Semiempirical model for generating tungsten target x-ray spectra. *Medical Physics*. 1991;18(2):211-8.
- ²¹Boone JM, Fewell TR, Jennings RJ. Molybdenum, rhodium, and tungsten anode spectral models using interpolating polynomials with application to mammography. *Medical Physics*. 1997;24(12):1863-74.
- ²²Blough MM, Waggener RG, Payne WH, Terry JA. Calculated mammographic spectra confirmed with attenuation curves for molybdenum, rhodium, and tungsten targets. *Medical Physics*. 1998;25(9):1605-12.
- ²³Johns HE, Cunningham JR. Chapter 16: Diagnostic Radiology. *The Physics of Radiology*. 4th ed. Springfield, IL: Charles C Thomas; 1983. p. 557-669.
- ²⁴Zhao B, Zhao W. Three-dimensional linear system analysis for breast tomosynthesis. *Medical Physics*. 2008;35(12):5219-32.
- ²⁵Ren B, Ruth C, Stein J, Smith A, Shaw I, Jing Z. Design and performance of the prototype full field breast tomosynthesis system with selenium based flat panel detector. In: Flynn MJ, editor. *SPIE*; 2005; San Diego, CA: SPIE; 2005. p. 550-61.
- ²⁶Shaheen E, Marshall N, Bosmans H. Investigation of the effect of tube motion in breast tomosynthesis: continuous or step and shoot? In: Pelc NJ, Samei E, Nishikawa RM, editors. *SPIE Medical Imaging*; 2011; Lake Buena Vista, FL: SPIE; 2011. p. 79611E-1 - E-9.

GLOSSARY OF TERMS:

Chapters 3, 4, and 5

LIST OF SYMBOLS

Symbol	Meaning
\bullet	Dot product operator.
$*$	Convolution operator (subscript denotes dimension).
\times	Cross product operator.
\in	Set membership.
$A\mu(n)$	Total attenuation for the n^{th} projection.
$\tilde{A}\mu(n)$	A useful approximation for total attenuation [Eqs. (3.32)-(3.33)].
\mathcal{B}	Backprojection operator.
$\mathcal{D}\mu(\mathbf{m}, n)$	Signal in the \mathbf{m}^{th} detector element for the n^{th} projection.
\mathcal{F}	Fourier transform operator (subscript denotes dimension).
\mathcal{L}_n	Path length through the input for the n^{th} projection.
$\mathcal{L}(t, \theta)$	Line that intercepts the point $(t \cos \theta, t \sin \theta)$ and that is perpendicular to the unit vector $\mathbf{p} = (\cos \theta)\mathbf{i} + (\sin \theta)\mathbf{k}$.
\mathcal{R}	Radon transform operator.
\mathbb{R}^2	Euclidean 2-space.
\mathbb{R}^3	Euclidean 3-space.
$\mathcal{S}\mu(u_1, u_2)$	Raw signal at coordinate (u_1, u_2) on the rotated detector.
\mathcal{X}	X-ray transform operator.
\mathbb{Z}	Set of integers.
\mathbb{Z}^*	Set of non-negative integers.

α_y	Pitch angle, corresponding to a rotation about the y axis.
β	Real number used to illustrate a trigonometric identity [Eq. (4.56)].
γ_n	Angle of rotation of the detector relative to the x axis for the n^{th} projection.
Γ_{mn}	Angle of backprojection within the plane of the detector [Eqs. (3.53)-(3.54)].
δ	Delta function.
$\Delta\psi$	Angular spacing between projections.
$\Delta u_j(n_1, n_2)$	Translational shift in u_j coordinate of incident ray comparing projection numbers n_1 and n_2 , where j varies between 1 and 2.
ε	Thickness of sine plate [Figures 3.1, 4.2(a), 4.2(c), 4.4(a), and 5.1] or rod [Figure 4.4(b)].
ζ	Polar angle of 2D frequency vector.
η''_{xmn}	A term defined by Eq. (5.45) to simplify intermediate calculations.
η''_{ymn}	A term defined by Eq. (5.36) to simplify intermediate calculations.
θ	Projection angle (defined in Figure 4.4).
θ_n	Angle of x-ray incidence relative to the normal to the detector (θ_{mn} denotes the special case at the centroid of the \mathbf{m}^{th} detector element for the n^{th} projection).
Θ	Angular range of tomosynthesis scan.
κ_n	A quantity defined by Eqs. (3.25) and (5.23).

λ_n	A quantity defined by Eq. (3.26) for the pitch angle $\alpha_y = 0$; this result is generalized to arbitrary pitch angles in Eq. (5.24).
Λ	A quantity defined by Eq. (3.A4).
μ	X-ray linear attenuation coefficient of test object.
μ_{Se}	X-ray linear attenuation coefficient of <i>a</i> -Se photoconductor.
ν_{\pm}	A quantity defined by Eq. (4.31) to simplify intermediate calculations (Figure 4.5).
ξ	Truncation frequency of reconstruction filter.
Π	Rod length [Figure 4.4(b)].
ρ_1, ρ_2	Quantities defined by Eqs. (3.66)-(3.67).
σ_{jmn}	Terms defined by Eqs. (3.68)-(3.72) used to simplify intermediate calculations, where <i>j</i> varies from 1 to 5.
Υ_{jk}^{\pm}	Terms defined by Eqs. (4.46)-(4.48) used to simplify intermediate calculations, where <i>j</i> varies from 1 to 3.
ϕ	Reconstruction filter.
Φ	A quantity defined by Eq. (4.57) used to simplify intermediate calculations.
ψ_n	Nominal projection angle.
A_1, A_2	Quantities defined by Eqs. (4.59)-(4.60) used to simplify intermediate calculations.
ACR	American College of Radiology.

a_x, a_y	Detector element dimensions in the x and y directions; if the x and y subscripts are removed, the detector element is square ($a_x = a_y = a$).
B	Height of plateau of trapezoid used for calculating the Radon transform of a pitched rod [Eq. (4.B7)].
b_1, b_2	Real numbers used to illustrate trigonometric identities [Eqs. (3.27), (4.34), and (5.25)].
BPF	Backprojection filtering.
C	Maximum value of attenuation coefficient of sine plate or rod.
CC	Cranial-caudal.
COR	Center-of-rotation of x-ray tube motion.
CT	Computed tomography.
d_n	Distance between points G and O (Figure 3.2) calculated in Eq. (3.50).
DBT	Digital breast tomosynthesis.
DM	Digital mammography.
f	Spatial frequency (subscript denotes direction of measurement).
f_0	Input frequency of a sine plate.
f_{zj}''	A quantity defined by Eq. (4.37) used to simplify intermediate calculations.
f_{zk}	A quantity defined by Eq. (4.45) used to simplify intermediate calculations.
FBP	Filtered backprojection.
FDC	Fourier double cone (defined by Figure 4.1).
FOV	Field-of-view.

FWHM	Full width at half maximum.
g	Gear ratio of detector.
$G(0)$	In-plane OTF evaluated at zero frequency.
$G(f_0)$	In-plane OTF evaluated at the frequency f_0 [Eq. (4.62)].
h	Source-to-COR distance for rotating x-ray tube.
$H(f_x, f_z)$	OTF of the reconstruction [Eq. (4.64)].
i	Imaginary unit given as $\sqrt{-1}$.
$I_{k,SBP}^{\pm}$	An integral defined by Eqs. (4.53)-(4.54).
I_{xmn}	An integral defined by Eq. (3.81).
I''_{xmn}	An integral defined by Eq. (5.41).
$I_{ymn}(x)$	An integral defined by Eq. (3.76).
$I''_{ymn}(x, z)$	An integral defined by Eq. (5.35).
l	Distance between the COR and the midpoint of the chest wall side of the detector (Figures 3.1, 3.2, and 5.1).
L	Thickness of a -Se photoconductor in Eq. (3.94).
lp	Line pairs.
\mathbf{m}	A doublet with coordinates (m_x, m_y) used for labeling detector elements.
M	Magnification.
MLO	Mediolateral oblique.
MRI	Magnetic resonance imaging.

MTF	Modulation transfer function.
n	Projection number.
N	Total number of projections.
OTF	Optical transfer function.
\mathbf{p}	Unit vector given by $(\cos \theta)\mathbf{i} + (\sin \theta)\mathbf{k}$ (Figure 4.4).
PA	Posteroanterior (in breast x-ray imaging, the direction perpendicular to the chest wall).
PA/SS	Descriptive acronym for a plane with extent along the posteroanterior (PA) and source-to-support (SS) directions.
PSF	Point spread function.
q_1	Length of plateau of trapezoid used for calculating the Radon transform of a pitched rod [Eq. (4.B7)].
q_2	Length of base of trapezoid used for calculating the Radon transform of a pitched rod [Eq. (4.B7)].
r	Ratio of the amplitude at the highest Fourier peak less than the detector alias frequency ($0.5a^{-1}$) to the amplitude at the input frequency (<i>e.g.</i> , 5.00 lp/mm) in reconstructing a high frequency sine plate (Figure 3.1, 5.1).
RA	Ramp filter.
s	Free parameter ranging between $-\infty$ and ∞ used in the parametric representation of the line $\mathcal{L}(t, \theta)$ [Eq. (4.1)].
SA	Spectrum apodization filter.

SBP	Simple backprojection.
SID	Source-to-image distance (commonly measured between the focal spot and the midpoint of the chest wall side of the detector in the central projection).
SNR	Signal-to-noise ratio.
SS	Source-to-support (defined to be synonymous with the z direction).
t	Affine parameter of Radon transform [Eq. (4.1)].
t_1, t_2	Affine parameters of the x-ray transform [Eqs. (3.38)-(3.39)].
T	Period of input waveform (Figure 5.3).
TFT	Thin-film transistor.
u_1, u_2	Position in the plane of the rotated detector (parallel and perpendicular to the chest wall, respectively).
w	Parameter ranging between 0 and 1 in the equation of the x-ray beam between the focal spot and the incident point on the detector [Eq. (3.16) and Eqs. (5.11)-(5.13)].
w_n^\pm	Value of w at the entrance (w_n^+) and exit (w_n^-) points of the x-ray beam through the sine plate (Figure 3.1, 5.1) for the n^{th} projection.
x	Position parallel to the chest wall side of the breast support; rotation by the angle γ_n about the y axis yields x'_n .
x''	Position along the pitch angle α_y of an oblique reconstruction plane relative to the point (x_0, y_0, z_0) in Eq. (5.30).

x_0	Translational shift in the input waveform along the x direction [Eqs. (3.1) and (5.6)] or in the centroid of an oblique reconstruction plane [Eq. (5.30)].
x_n^\pm	Value of x at the entrance (x_n^+) and exit (x_n^-) points of the x-ray beam through the sine plate (Figure 5.1) for the n^{th} projection.
y	Position perpendicular to the chest wall; it is equivalent to y'_n .
y''	Position perpendicular to the plane of x-ray tube motion relative to the point (x_0, y_0, z_0) in Eq. (5.30).
y_0	Translational shift in the input waveform along the y direction [Eq. (3.A1)] or in the centroid of an oblique reconstruction plane [Eq. (5.30)].
z	Position perpendicular to the plane of the breast support; rotation by the angle γ_n about the y axis yields z'_n .
z''	Position perpendicular to an oblique reconstruction plane relative to the point (x_0, y_0, z_0) in Eq. (5.30).
z_0	Central height of the input object relative to the midpoint of the chest wall side of the detector (Figures 3.1 and 5.1).

CHAPTER 6

Thesis Summary and Future Work

1. THESIS SUMMARY

In the development of Zhao's model of image quality for DBT, simplifying assumptions about the system were made in order to keep the mathematics tractable.¹ In the following section, I summarize how each chapter in the body of this thesis has led to a more complete model of image quality by addressing the limitations found in Zhao's work.

1.1. Chapter 2

One assumption made in Zhao's work is that the transfer functions of each projection can be approximated by their value at normal incidence. In order to model the image quality of each projection more carefully, I extended Swank's calculations of the transfer functions of x-ray fluorescent screens to oblique incidence in Chapter 2. The modulation transfer function (MTF) and noise power spectra (NPS) were derived using the diffusion approximation to the Boltzmann equation to model optical scatter within the phosphor. The detective quantum efficiency (DQE) was then determined from the Nishikawa formulation, where it was written as the product of the x-ray quantum detection efficiency, the Swank factor, and the Lubberts fraction. I calculated the transfer functions for both front- and back-screen configurations, which differ by positioning the photocathode at the exit or entrance point of the x-ray beam, respectively.

In the front-screen configuration, I found that the MTF and DQE have considerable angular dependence, while the NPS varies minimally with projection angle. The high frequency MTF and DQE are degraded substantially at large angles. By

contrast, all transfer functions for the back-screen configuration have the advantage of significantly less angular dependence. Using these models, I investigated the possibility for optimizing the design of DBT detectors. As an example optimization strategy, the phosphor thickness which maximizes the DQE at a fixed frequency was analyzed. I demonstrated that the optimal phosphor thickness for the front-screen is angularly dependent, shifting to lower thickness at higher angles. Conversely, the back-screen is not optimized by a single thickness but instead attains reasonably high DQE values over a large range of thicknesses. Although the back-screen configuration is not suited for current detectors using a glass substrate, it may prove to be preferred in future detectors using newly proposed plastic thin-film transistor (TFT) substrates.

1.2. Chapter 3

An additional assumption made in Zhao's work is that the pixel size in the reconstruction grid is the same as the detector elements. Under this assumption, the highest frequency that can be resolved in the plane of reconstruction is the alias frequency of the detector. In Chapter 3, I investigated the feasibility of reconstruction grids with much smaller pixelation in order to visualize higher frequencies. Although Zhao does not model the translational shifts in the image of an object with each increasing projection angle, I demonstrated that these translational shifts give rise to super-resolution, or higher resolution in the reconstruction than in each 2D projection. For analytical proof of super-resolution, I calculated the reconstruction of a conceptual

test object known as a “*sine plate*”. Increasing the frequency of the sine plate simulates small, closely-spaced objects, such as microcalcifications.

Using the theoretical model of the sine plate, I showed that a single projection cannot resolve frequencies greater than the detector alias frequency. The Fourier transform of each projection is maximized at a lower frequency than the input as evidence of aliasing. By contrast, a reconstruction can resolve the input, and its Fourier transform is correctly maximized at the input frequency.

I also demonstrated that the existence of super-resolution is dependent on position in the reconstruction and on the directionality of the input frequency. Although super-resolution is achievable over a broad range of positions if the test frequency is oriented along the tube travel direction (x), it is feasible at far fewer positions if the test frequency is oriented along the chest wall-to-nipple direction (y). Consistent with the analytical results, experimental reconstructions of bar patterns showed visibility of frequencies greater than the detector alias frequency. Super-resolution was observed at positions predicted from analytical modeling.

1.3. Chapter 4

Zhao’s work presumes that slices in a DBT reconstruction should only be created on planes parallel to the breast support. Prior to this thesis, it has not been demonstrated that slices can be generated along oblique directions through the same volume, analogous to multiplanar reconstructions in CT. In Chapter 4, I investigated the feasibility of oblique reconstructions by calculating the reconstruction of a pitched sine plate in a 2D

parallel beam geometry. I also determined the in-plane MTF for a slice along the pitch of the object by comparing signal in the reconstruction against the attenuation coefficient of the object at each frequency. A second test object that I modeled was a rod whose long axis is pitched similar to the sinusoidal input. The rod was used to assess whether the length of an object can be correctly estimated in oblique reconstructions.

To simulate the conventional display of the reconstruction, I analyzed slices along a 0° pitch. This direction is perpendicular to the rays of the central projection. I showed that the input frequency of a pitched sinusoidal object cannot be determined using these slices, but can be properly determined in slices which match the pitch of the object. In addition, I found that the in-plane MTF is within detectable limits over a broad range of pitches if the object is thin, but is detectable over a narrower range of pitches if the object is thick. Turning next to the second test object, I showed that the length of a pitched rod can be correctly determined in oblique reconstructions. Concordant with the behavior of the MTF, the length estimate is accurate over a broad range of pitches if the object is thin, but is correct over a narrower range of pitches if the object is thick.

1.4. Chapter 5

In Chapter 5, I demonstrated that the feasibility of super-resolution can be generalized to oblique reconstruction planes. Unlike the previous chapter on oblique reconstructions, the simulation of the acquisition geometry includes detector pixelation and other features which are necessary for investigating super-resolution. From first principles, I calculated the reconstruction of a sine plate and determined the MTF in

oblique planes. For experimental validation of super-resolution, I used a goniometry stand to orient a bar pattern phantom along various pitches in a commercial DBT system.

With theoretical modeling, I showed that a single projection cannot resolve a sine input whose frequency exceeds the detector alias frequency. By contrast, the high frequency input is correctly visualized in an oblique reconstruction plane using a slice along the pitch of the test frequency. Using the MTF to determine if modulation is detectable, I demonstrated that the object must be thin in order for super-resolution to be achievable in oblique reconstructions.

Consistent with the theoretical results, experimental images of a thin bar pattern phantom showed super-resolution in oblique reconstructions. The range of frequencies with detectable modulation varied with the pitch of the bar patterns, and exhibited good agreement with the predictions of the analytical model. I demonstrated that super-resolution is not achievable if the pitch of the object approaches 90° , corresponding to the case in which the test frequency is perpendicular to the breast support. Only low frequency objects are detectable at pitches close to 90° .

2. AREAS FOR FUTURE RESEARCH

Although the potential benefits of DBT over DM have been identified, a rigorous platform for optimizing the design of DBT systems has not yet been established. Should DBT one day be offered on a large scale as an upgrade or adjunct to DM in screening centers across the United States, the development of this optimization platform will be critical; otherwise, radiologists run the risk of applying a higher radiation dose than

absolutely necessary to achieve a desired level of image quality. In this section, I discuss areas for future research focusing on the optimization of image quality in DBT.

2.1. Points of Future Investigation with Super-Resolution

2.1.1. Quantifying the Clinical Benefits of Super-Resolution

Although DBT has the ability to detect cancers which are mammographically occult due to tissue superposition, one hurdle to widespread dissemination of DBT is reduced visibility of microcalcifications. Early clinical trials have shown that the benefits of DBT over DM are limited to noncalcification findings.²⁻⁵ Based on the results of this thesis, I project that super-resolution is the mechanism for improving the visibility of microcalcifications. In a sample clinical case in Chapter 3, super-resolution appeared to produce a sharper image of microcalcifications showing more detail (Figure 3.12). To determine whether super-resolution should be translated into clinical practice, the diagnostic benefits of super-resolution should be quantified in future work using a clinical trial.

2.1.2. Development of an Acquisition Geometry that Optimizes Super-Resolution

In Chapter 3, I showed that super-resolution is achievable over a broad range of positions for frequencies along the tube travel direction (x), but is feasible at far fewer positions for frequencies along the posteroanterior (PA) direction (y). To optimize super-resolution, I propose two strategies for investigation in future studies: (1) translate the detector in the PA direction during the scan time; and (2) modify the trajectory of the

x-ray tube to have extension in the PA direction. Either strategy should promote sub-pixel sampling gain in the PA direction by increasing translational shifts in the image between projections.

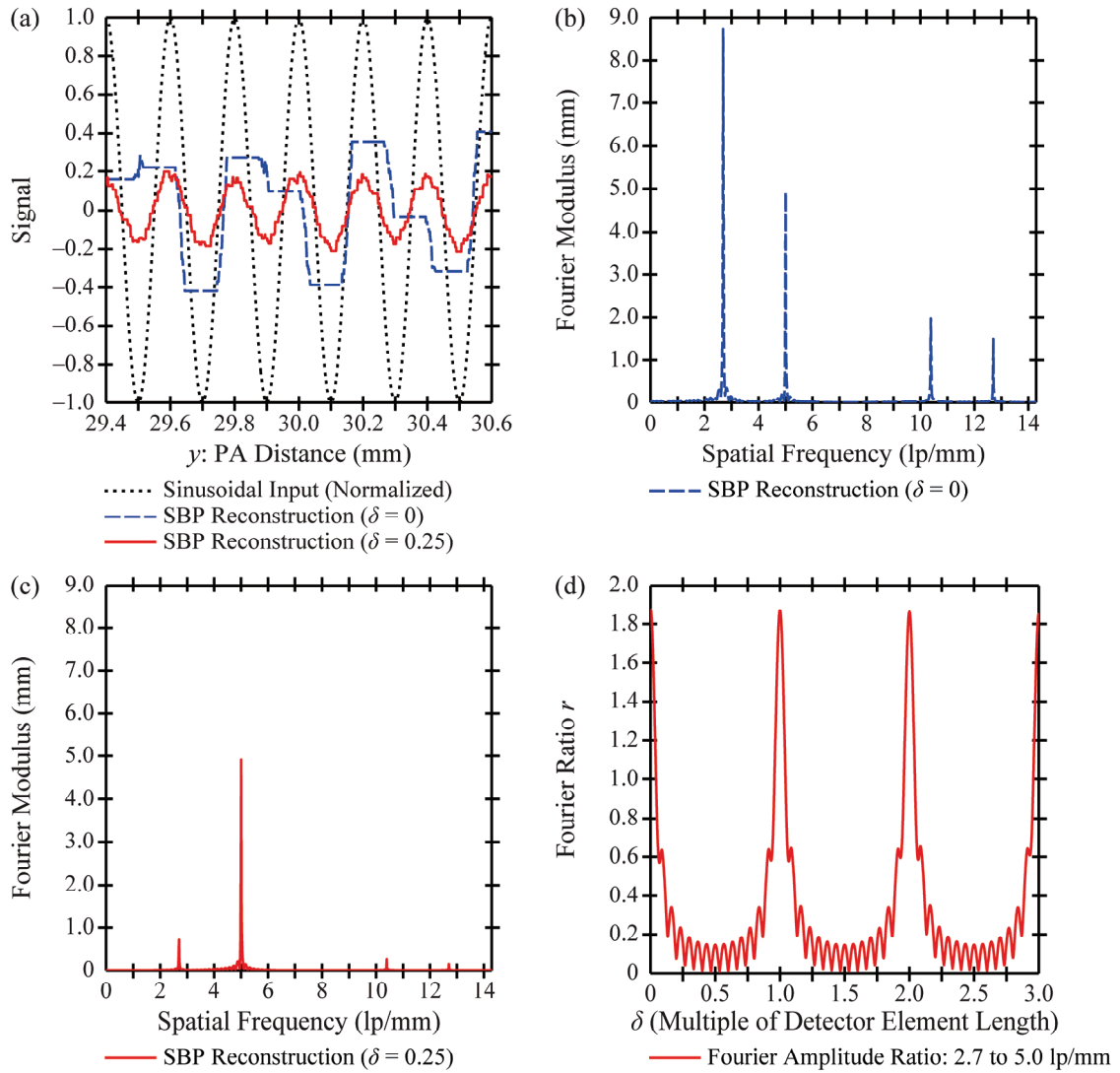


Figure 6.1: Optimization of super-resolution along the posteroanterior (PA) direction using a newly proposed acquisition geometry. By translating the detector between projections, super-resolution is achievable in the chest wall-to-nipple direction.

To illustrate that detector translation during the scan time has the potential to optimize super-resolution, a reconstruction of the 5.0 lp/mm input frequency is shown in Figure 6.1.⁶ Detector translations of 25% of detector element length (35 μm) between projections are simulated along the chest wall-to-nipple direction. As expected from Chapter 3, the reconstruction in a conventional acquisition geometry resembles a single projection in which signal varies with position in a step-like manner [Figure 6.1(a)]. As evidence of aliasing, the corresponding Fourier transform [Figure 6.1(b)] has a major peak at 2.7 lp/mm, which is clearly less than the input frequency, 5.0 lp/mm. By contrast, the reconstruction with the newly proposed geometry has the overall appearance of a sine wave whose peaks and troughs match the input frequency perfectly. For analytical proof of super-resolution, the major peak of the Fourier transform [Figure 6.1(c)] correctly occurs at the input frequency, 5.0 lp/mm.

Using the Fourier transforms in Figure 6.1, one can calculate the r -factor as a metric of the quality of super-resolution. Recall from Chapters 3 and 5 that this metric is the ratio of the amplitude of the Fourier peaks at 2.7 to 5.0 lp/mm. Super-resolution is present if $r < 1$ and is absent if $r \geq 1$. In Figure 6.1(d), the dependency of r on the increment (δ) of detector translation is analyzed. The symbol δ is simply a parameter which expresses the detector translation between projections as a multiple of detector element length. Super-resolution is not feasible ($r > 1$) if detector translation between projections occurs in integer multiples of detector element length. To maximize sub-pixel sampling gain between projections, there is a range of δ values over which r is sufficiently less than unity for high quality super-resolution. For example, if the detector

translation between each projection lies between 24% and 76% of detector element length, the ratio of the amplitude of the Fourier peaks at 2.7 to 5.0 lp/mm is less than 1:5 (*i.e.*, 20%). Using the *r*-factor as a metric for assessing the quality of super-resolution, future work should determine precise bounds on the detector translations that yield optimal image quality.⁶

A DBT detector may be designed with either discrete or continuous translations during the scan time. Although Figure 6.1 considers discrete translations, continuous translations should also show super-resolution, since the detector translation during the exposure time of each projection should be significantly smaller than the detector element length. The feasibility of continuous detector translations should be investigated rigorously in future studies.

In conventional acquisition geometries, the x-ray tube traces a circular arc in the plane of the chest wall during the scan time. To optimize super-resolution in future work, one can also consider x-ray tube trajectories with a component of motion along the PA direction. Using the *r*-factor described previously, one can determine the x-ray tube translations along the PA direction that are necessary for high quality super-resolution.

After using theoretical modeling to identify the acquisition geometries which optimize super-resolution, the benefits of the new geometries can be tested further with a virtual clinical trial (VCT). The Maidment lab has developed a simulation platform for anthropomorphic phantoms in DBT.⁷ Future work should investigate the reconstructions of phantoms with realistic microcalcification clusters using current DBT geometries and the newly proposed super-resolution geometries. A VCT can demonstrate the potential

clinical benefits of the optimized geometries in a cost-effective manner and provide guidance for the design of the next generation of DBT systems.

2.1.3. Geometric Accuracy Requirements for Super-Resolution

Although the acquisition geometry is known exactly in the theoretical model of image quality developed in this thesis, this is not necessarily the case in clinical practice. The precise positions of the focal spot, center-of-rotation of the x-ray tube, and angle of rotation of the detector are not known exactly in a clinical system. In calculating the reconstruction, geometric imprecision yields small errors in the backprojection of rays from the detector to the focal spot. Future work should investigate whether the feasibility of super-resolution is limited by such imprecisions. The r -factor can be used as a metric to quantify super-resolution at various levels of imprecision. This future research can be used to inform manufacturers of tolerance limits in the design specifications for a system.

In the preceding section, I gave preliminary evidence that detector translations can be used to optimize super-resolution along the PA direction (Figure 6.1). It will be important to investigate whether imprecision in the detector translation places limits on super-resolution along the PA direction. The effect of small imprecisions can be tested in a VCT with anthropomorphic phantoms using observer studies.

2.1.4. Effect of Reducing the Detector Element Size

As discussed in Chapter 3, the FDA-approved Hologic system employs binning when switching between DM and DBT imaging modes. While the DM detector element

dimensions are $70\ \mu\text{m} \times 70\ \mu\text{m}$, the DBT detector element dimensions are $140\ \mu\text{m} \times 140\ \mu\text{m}$. Hologic is now working toward $70\ \mu\text{m}$ pixelation for DBT. This design modification should improve resolution by increasing the detector alias frequency ($0.5a^{-1}$) from 3.6 lp/mm to 7.1 lp/mm.

In Chapters 3 and 5, I found that the first zero of the detector MTF places a limit on the frequencies with detectable modulation in a reconstruction with super-resolution. Figure 6.2 illustrates this concept by plotting the detector MTF [Eq. (1.7)] versus frequency in multiples of a^{-1} (inverse detector element length). Since the first zero of the detector MTF corresponds to the frequency a^{-1} , the current Hologic geometry is capable of super-resolution at frequencies approaching 7.1 lp/mm. According to Figure 6.2, a system with $70\ \mu\text{m}$ pixelation should show super-resolution at frequencies approaching 14.3 lp/mm. Future work should determine whether the visibility of microcalcifications is improved in a system with $70\ \mu\text{m}$ detector pixelation due to the visibility of higher frequencies.

Although the benefits of reducing the detector element size are evident in a theoretical model, it will be important to determine whether design imprecisions place a practical limit on the visibility of frequencies approaching 14.3 lp/mm in a $70\ \mu\text{m}$ system. Using the r -factor to quantify super-resolution, future work should investigate how the tolerance limits in the system design vary with the detector element size.

While Hologic uses an α -Se detector, other manufactures use phosphor-based detectors. Because phosphor-based systems exhibit more blurring, the detector MTF shows more degradation at high frequencies. Figure 6.2 illustrates this concept by

approximating the MTF of the phosphor blur as a Gaussian. Recent research by Freed *et al.* has verified that the Gaussian is a valid approximation for the MTF of a thick CsI:Tl phosphor irradiated at normal incidence.⁸

$$\text{MTF}(f_x, f_y) = e^{-2\pi^2\sigma^2(f_x^2 + f_y^2)} \left| \text{sinc}(a_x f_x) \text{sinc}(a_y f_y) \right| \quad (6.1)$$

As shown in Figure 6.2, the modulation at high frequencies is degraded with increased blurring in the phosphor, as measured by increased standard deviation (σ) in the Gaussian. This plot assumes that frequency is measured along the x direction ($f_y = 0$). Future work should investigate whether the MTF of a phosphor places an inherent limit on the visibility of high frequencies that cannot be surmounted by reducing the detector element size.

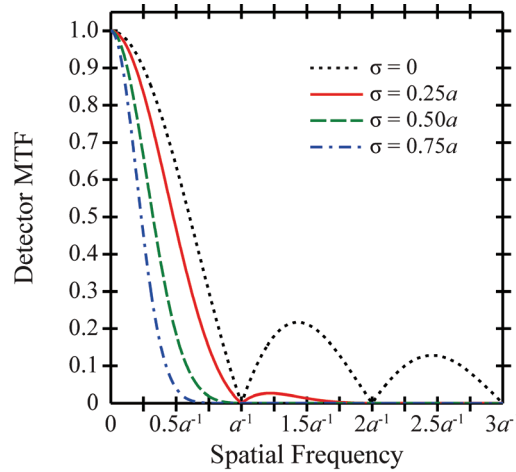


Figure 6.2: Modulation transfer function (MTF) for various phosphor blurring parameters. The MTF of the detector is plotted versus frequency measured along the x direction ($f_y = 0$) for four blurring parameters (σ), assuming that detector elements are square with sides of length a . The first zero of the MTF places a limit on the frequencies with detectable modulation.

2.2. Development of Optimal Design Strategies for Continuous X-Ray Tube Motion

2.2.1. Optimization of Scan Time

Throughout this thesis, I have modeled a system whose focal spot is stationary during each projection. In order to develop a more complete model of image quality, future studies should simulate continuous x-ray tube motion during the scan. Although continuous tube motion has the benefit of reducing patient motion by lowering scan time, it has the drawback of introducing blurring artifacts due to focal spot motion. My preliminary work on this topic has shown that continuous x-ray tube motion yields a loss of modulation in the reconstruction. These theoretical results were presented in my proceedings manuscript for the 2012 SPIE Medical Imaging conference.⁹

In this preliminary work on continuous x-ray tube motion, I investigated the trade-offs of long and short scan time in a system with patient motion, and found that an intermediate scan time optimizes modulation. With objects velocities of 30 and 60 $\mu\text{m/s}$, I demonstrated that the optimal scan times for continuous tube motion are 3.3 and 2.4 s, respectively, assuming an input frequency of 2.0 lp/mm and an exposure time of 30.0 ms. This work assumed that the sine plate is translated with constant velocity during the scan time. Future studies should investigate additional velocity profiles (*e.g.*, pulsatile motion of structures lying along blood vessels).

In DM, it has been demonstrated that the scan time should be less than 2.0 s to minimize patient motion. Currently, no such guideline for DBT has been developed. My SPIE manuscript considered an object velocity between 30 and 60 $\mu\text{m/s}$, which was chosen to be comparable to the value observed in a clinical case presented in the paper.

Since this case is not necessarily representative of the most significant extent of patient motion, additional cases should be analyzed in future work to develop guidelines for scan time in DBT.

2.2.2. Optimization of the X-Ray Tube Velocity

In existing systems with continuous tube motion, manufacturers configure the x-ray tube with constant angular velocity during the scan time. In my 2013 SPIE paper, I investigated a different angular velocity profile in order to optimize continuous tube motion.¹⁰ The velocity profile approaches zero during projections and is larger between projections. Importantly, the velocity profile is smooth, so that there is no abrupt start-and-stop motion that would make a fast acquisition time prohibitive.

To assess the improvements in image quality with the newly proposed tube velocity, I calculated modulation at various frequencies. I showed that modulation in the newly proposed system differs minimally from a system with step-and-shoot motion. This technical innovation should allow a system with continuous tube motion to have short scan time and hence less patient motion than a step-and-shoot system, but no longer have the trade-off of focal spot blurring during each projection. In future studies, the benefits of the newly proposed design should be validated with a VCT comparing calcification visibility in systems with different forms of x-ray tube motion. In addition, the newly proposed design is being investigated as a tool for shortening scan time and thus minimizing patient motion.

3. THESIS CONCLUSION

DBT is being investigated as a 3D alternative to conventional mammography with potentially increased sensitivity and specificity for cancer detection. Although the benefits of DBT over conventional mammography have been identified, DBT is still in its early stages of development, and a rigorous platform for optimizing image quality has not yet been established. In this thesis, I developed a more complete model of image quality by addressing the limitations found in Zhao's linear systems model. One assumption made by Zhao is that the image quality in each projection can be approximated from the transfer functions at normal incidence. In order to model the effect of oblique x-ray incidence in each projection, I extended Swank's calculations of the transfer functions of x-ray fluorescent screens to a general incident angle. I demonstrated that the resolution loss due to oblique incidence can be modeled in closed form. In later work, I introduced a conceptual test object known as a sine plate to analyze the consequences of oblique x-ray incidence in the reconstruction. Since the image of an object is translated in sub-pixel increments with each increasing projection angle, I showed that a reconstruction is capable of super-resolution, or sub-pixel resolution. In addition, by orienting the sine plate along various angles relative to the breast support, I demonstrated that reconstructions can be performed along oblique planes. The theoretical results derived from the sine plate were verified with experimental images of bar patterns and with anecdotal clinical examples. Quantifying the clinical benefits of super-resolution and oblique reconstructions is an exciting area for future research.

DBT appears to have a bright future in medical imaging. In demonstrating the potential benefits of super-resolution and oblique reconstructions, I have shown that DBT reconstructions are capable of much higher image quality than previously thought in the literature. In the future, my model of image quality will play a role in optimizing the design of DBT systems.

4. REFERENCES

- ¹Zhao B, Zhao W. Three-dimensional linear system analysis for breast tomosynthesis. *Medical Physics*. 2008;35(12):5219-32.
- ²Poplack SP, Tosteson TD, Kogel CA, Nagy HM. Digital breast tomosynthesis: initial experience in 98 women with abnormal digital screening mammography. *American Journal of Roentgenology*. 2007;189(3):616-23.
- ³Gur D, Abrams GS, Chough DM, Ganott MA, Hakim CM, Perrin RL, et al. Digital Breast Tomosynthesis: Observer Performance Study. *American Journal of Roentgenology*. 2009;193:586-91.
- ⁴Teertstra HJ, Loo CE, Bosch MAAJvd, Tinteren Hv, Rutgers EJT, Muller SH, et al. Breast tomosynthesis in clinical practice: initial results. *European Radiology*. 2010;20:16-24.
- ⁵Gur D, Bandos AI, Rockette HE, Zuley ML, Sumkin JH, Chough DM, et al. Localized Detection and Classification of Abnormalities on FFDM and Tomosynthesis Examinations Rated Under an FROC Paradigm. *American Journal of Roentgenology*. 2011;196:737-41.
- ⁶Acciavatti RJ, Maidment ADA. Proposing an Acquisition Geometry That Optimizes Super-Resolution in Digital Breast Tomosynthesis. *Lecture Notes in Computer Science*. 2012;7361:386-93.
- ⁷Bakic PR, Zhang C, Maidment ADA. Development and characterization of an anthropomorphic breast software phantom based upon region-growing algorithm. *Medical Physics*. 2011;38(6):3165-76.
- ⁸Freed M, Miller S, Tang K, Badano A. Experimental validation of Monte Carlo (MANTIS) simulated x-ray response of columnar CsI scintillator screens. *Medical Physics*. 2009;36(11):4944-56.
- ⁹Acciavatti RJ, Maidment ADA. Optimization of Continuous Tube Motion and Step-and-Shoot Motion in Digital Breast Tomosynthesis Systems with Patient Motion. In: Pelc NJ, Nishikawa RM, Whiting BR, editors. *SPIE Medical Imaging*; 2012; San Diego, CA: SPIE; 2012. p. 831306-1 - 12.
- ¹⁰Acciavatti RJ, Bakic PR, Maidment ADA. Proposing a New Velocity Profile for Continuous X-Ray Tube Motion in Digital Breast Tomosynthesis. In: Nishikawa RM, Whiting BR, Hoeschen C, editors. *SPIE Medical Imaging*; 2013; Lake Buena Vista, FL: SPIE; 2013. p. 86680F-1 - F-10.